

ANNUAL REPORT

2023

and list of publications



Bayerisches Forschungsinstitut
für Experimentelle Geochemie und Geophysik
Universität Bayreuth

Bayerisches Geoinstitut
Universität Bayreuth
95440 Bayreuth
Germany

Telephone: +49-(0)921-55-3700
Telefax: +49-(0)921-55-3769
e-mail: bayerisches.geoinstitut@uni-bayreuth.de
www: <https://www.bgi.uni-bayreuth.de>

Editorial compilation by: Florian Heidelberg and Petra Buchert
Section editors: Andreas Audétat, Tiziana Boffa Ballaran, Audrey Bouvier,
Johannes Buchen, Leonid Dubrovinsky, Dan Frost, Florian Heidelberg,
Gregor Golabek, Tomoo Katsura, Hans Keppler, Nobuyoshi Miyajima,
Gerd Steinle-Neumann, Tony Withers



Staff and guests of the Bayerisches Geoinstitut in **June 2023**:

Die Mitarbeiter und Gäste des Bayerischen Geoinstituts im **Juni 2023**:

first row, from left (1. Reihe, v. links) Laura Czekay, Catherine McCammon, Florian Heidelberg, Eun Jeong Kim, Narangoo Purevjav, Dorothea Wiesner, Tiziana Boffa Ballaran, Amrita Chakraborti, Meredith Calogero

second row, from left (2. Reihe, v. links) Kui Han, Gerald Bauer, Sven Linhardt, Greta Rustioni, Petra Buchert, Janina Scharnagel, Jinia Sikdar, Rebecka Matthäus, Ulrike Trenz

third row, from left (3. Reihe, v. links) Da-Peng Zhu, Muhammad Ilham Hamadi, Melanie Pöppelbaum, Giacomo Criniti, Cristian Timoner Bosch, Heinz Fischer

fourth row from left (4. Reihe, v. links) Audrey Bouvier, Pedro Validiva Munoz, Marco Beltrame, Matej Hlede, Dan Frost, Anthony Withers, Arne Spang, Stefan Übelhack

back rows, from left (hintere Reihen, v. links) Raphael Njul, Guoliang Niu, Britany Kulka, Anna Dinius, Jonathan Dolinschi, Nobuyoshi Miyajima, Ran Zhao, Andrea Piccolo, Gerd Steinle-Neumann, Lianjie Man, Detlef Krauß, Jyotirmoy Paul, Jia Chang, Adrien Néri, Hans Keppler, Andreas Audétat, Oliver Rausch

Absent (Es fehlten) Fariia Akbar, Daria Andreieva, Andrii Aslandukov, Alena Aslandukova, Dmitry Bondar, Daniela Bubmann, Johannes Buchen, Artem Chanyshev, Laura Cialdella, Leonid Dubrovinsky, Gregor Golabek, Tomo Katsura, Holger Kriegl, Edith Kubik, Alexander Kurnosov, Dominic Langhammer, Naira Martirosyan, Anastasiia Minchenkova, Edna Obengo, Sergey Ovsyannikov, Anke Potzel, Alexander Rother, David Rubie, Marcel Thielmann, Fei Wang, Lin Wang, Liang Yuan

Contents

Foreword/Vorwort	9/I
1. Advisory Board and Directorship	11
1.1 Advisory Board	11
1.2 Leadership	11
2. Staff, Funding and Facilities	13
2.1 Staff	13
2.2 Funding	13
2.3 Laboratory and office facilities	18
2.4 Experimental and analytical equipment	18
3. Forschungsprojekte – Zusammenfassung in deutscher Sprache	III
3. Research Projects	21
3.1 <i>Earth and Planetary Structure and Dynamics</i>	21
a. Magma oceanography of the dense, ultrashort-period sub-Earth GJ 367b (G.J. Golabek, T. Lichtenberg/Groningen and P.J. Tackley/Zurich)	22
b. The origin and impact history of ordinary chondrite melt breccia Northwest Africa 12520 (R. Zhao and A. Bouvier; M. Trieloff, W.H. Schwarz and T. Ludwig/Heidelberg)	23
c. 4.46 Ga zircons anchor chronology of lunar magma ocean (J. Greer and P.R. Heck/Chicago, B. Zhang/Los Angeles, D. Isheim and D.N. Seidman/ Evanston, A. Bouvier)	25
d. Numerical models of North China craton destruction (J. Paul, A. Spang and A. Piccolo)	27
e. Slab tearing velocities controlled by trench curvature and upper mantle rheology: Insights from 3D numerical experiments (A. Piccolo, M. Thielmann and A. Spang)	29
f. The effects of slab detachment and tearing on the foreland basins architecture, insights from geodynamic and stratigraphic forward modelling (L.H.J. Eskens and N. Andrić-Tomašević/Karlsruhe, A. Piccolo and M. Thielmann, B. Claussmann and M. Lejri/Oslo, T.A. Ehlers/Glasgow)	30
g. Electrical and thermal conductivities of fcc and hcp iron under conditions of the Earth's core from ab initio simulations (U. Kleinschmidt, M. French and R. Redmer/Rostock, G. Steinle-Neumann)	32
3.2 <i>Geochemistry</i>	34
a. Al-Mg and U-Pb chronological records of Erg Chech 002 ungrouped achondrite meteorite (A. Bouvier, P.M. Reger/London, Canada; Y. Roebbert and S. Weyer/Hannover; W. Neumann, W.H. Schwarz, T. Ludwig and M. Trieloff/Heidelberg; A. Gannoun/Clermont-Ferrand and M. Regelous/ Erlangen)	37

b.	Sulphide inventory in the meteorite Ksar El Goraane (H5): A window on the formation conditions of ordinary chondrites (S. Arif and H. Chennaoui Aoudjehane/Casablanca, A. Bouvier)	39
c.	Effect of S on Fe isotopic fractionation between metal and silicate: Preliminary results and implications for Mars' core light element budget (E. Kubik, in collaboration with S. Rabin/Brussels)	41
d.	Evolution of the experimental metal-silicate iron isotopic fractionation with pressure: Implications for core formation on large terrestrial planets (E. Kubik and A. Bouvier, P.A. Sossi/Zurich)	43
e.	Testing the feasibility of ⁴⁰ K as a heat producing element in planetary cores based on K metal-silicate partitioning experiments (J. Sikdar and E. Kubik)	44
f.	Tracing the origin of volatile elements with core formation experiments and sulphur isotopes (L.M. Calvo/Paris, E. Kubik, J. Labidi/Paris and J. Siebert/Paris)	46
g.	Fluxes and reservoirs in the deep Earth oxygen cycle (M.M. Hirschmann)	47
h.	An experimental investigation of the role of NiS in controlling the O content of sulphide melts in the Earth's upper mantle (M.I. Hamadi, S. Abeykoon, A. Néri and D.J. Frost)	51
i.	Peridotite–carbonatite reaction experiments: Testing the validity of chemical fingerprinting of mantle metasomatism (C. Shaw/Fredericton)	52
j.	The effect of phengite and apatite on the mobility of trace elements in subduction zones (G. Rustioni, A. Audétat and H. Keppler)	53
k.	The gold content of mafic to felsic potassic magmas (J. Chang and A. Audétat, in collaboration with T. Pettke/Bern)	54
l.	Common anhydrite saturation in Laramide-age arc magmas in southwestern USA (A. Audétat and J. Chang)	56
m.	An experimental study on the partitioning of gallium in felsic magmatic systems (M. Hlede and H. Keppler)	58
n.	Experimental investigation of the stability of calcite in rhyolitic melts (C. Timoner and A. Audétat)	59
o.	Sn isotope fractionation of cassiterite during magmatic-hydrothermal processes (J. Wu and H. Li/Changsha, R. Mathur/Huntingdon, A. Bouvier, W. Powell/Brooklyn, K. Yonezu/Fukuoka and D. Zhu)	62
3.3	<i>Mineralogy, Crystal Chemistry and Phase Transformations</i>	64
a.	Exploring the lithospheric mantle beneath central Mongolia: Constraints from spinel-bearing peridotite xenoliths and high-pressure experiments (M. Beltrame/Trieste and C.A. McCammon, in collaboration with L. Ziberna/Trieste, M. Masotta/Pisa and A. De Min/Trieste)	66
b.	Alumina solubility in periclase determined to lower mantle conditions and implications for ferropericlase inclusions in diamonds (L. Man, H. Fei, E.J. Kim, A. Néri, L. Xie and D.J. Frost)	68

c.	Cr incorporation in post-spinel Fe ²⁺ -Fe ³⁺ oxides (K. Schumann, L. Uenver-Thiele and A.B. Woodland/Frankfurt a. M.; C. Melai and T. Boffa Ballaran)	70
d.	Cr incorporation in post-spinel Mg-Fe ³⁺ oxides (A.B. Woodland, L. Uenver-Thiele and K. Rosbach/Frankfurt a. M.; C. Melai and T. Boffa Ballaran)	72
e.	High-pressure phase relations of Al-bearing magnetite (L. Uenver-Thiele and A.B. Woodland/Frankfurt a. M.; N. Miyajima and T. Boffa Ballaran)	73
f.	Post-spinel phase transition in Mg ₂ SiO ₄ -Fe ₂ SiO ₄ system (A. Chanyshv, F. Wang, N. Martirosyan, K. Han, R. Farla/Hamburg and T. Katsura)	75
g.	Experiments on the stability of whewellite, an organic mineral, in subduction zone fluids (L. Czekay and H. Keppler)	76
h.	Synthesis of magnesium (II) orthocarbonate, Mg ₂ CO ₄ , from different precursors (L.S. Dubrovinsky, T. Fedotenko/Hamburg, S. Khandarkhaeva, A. Aslandukov, A. Aslandukova, Y. Yin/Bayreuth, K. Glazyrin/Hamburg, D. Laniel/Edinburgh and N.A. Dubrovinskaia/Bayreuth)	77
i.	Fe oxidation state of garnet and clinopyroxene in grospydite xenoliths from the Zagadochnaya pipe (Yakutia, Russia) (G. Marras/Rome, V. Stagno/Rome, C.A. McCammon and D. Mikhailenko)	79
j.	Pressure dependence of Fe ³⁺ /ΣFe in bridgmanite (F. Wang, L. Wang, H. Fei, N. Miyajima, C.A. McCammon, D.J. Frost and T. Katsura)	80
k.	Crystallographic features of omphacite in lawsonite-eclogite xenolith from Colorado Plateau (R. Fukushima and T. Tsujimori/Sendai, N. Miyajima, T. Boffa Ballaran, G. Criniti and C.A. McCammon)	81
l.	The electron diffraction pattern of quenched davemaoite and the unit cell volume at ambient pressure (N. Miyajima, L. Wang and T. Katsura)	82
3.4	<i>Physical Properties of Minerals</i>	85
a.	The effect of faceting on olivine wetting properties (Y. Huang/Guangzhou, T. Nakatani and S. Sawa/Sendai, G. Wu/Guangzhou and Beijing, M. Nakamura/Sendai and C.A. McCammon)	86
b.	Compressibility of N-bearing talc and insights into the deep nitrogen cycle (A. Minchenkova, D.J. Frost, T. Boffa Ballaran, A. Kurnosov, G. Criniti and C. Melai, in collaboration with W. Zhou and M. Hanfland/Grenoble)	88
c.	The elastic behaviour of Mg-sursassite (B. Chrappan and M. Merlini/Milan, in collaboration with G. Criniti, T. Boffa Ballaran and A. Kurnosov)	90
d.	Effect of chemistry on the compressibility and structural evolution of CaFe ₂ O ₄ -type aluminous phases (G. Criniti, T. Boffa Ballaran, A. Kurnosov and D.J. Frost, in collaboration with T. Ishii/Misasa, K. Glazyrin/Hamburg and T. Fedotenko/Hamburg)	91
e.	Thermal equation of state of an Fe ²⁺ -rich aluminous bridgmanite (G. Criniti, T. Boffa Ballaran, A. Kurnosov and D.J. Frost, in collaboration with T. Ishii/Misasa and K. Glazyrin/Hamburg)	93

f.	Elasticity of Martian ringwoodite (A. Kurnosov, T. Boffa Ballaran, G. Criniti and D.J. Frost)	94
g.	Reproducing iron-rich phase textures in primitive achondrites: Overcoming surface tension in solids (A. Néri, E. Kubik, G.J. Golabek and A. Bouvier, in collaboration with N.P. Walte/Garching)	96
3.5	<i>Fluids, Melts and their Interaction with Minerals</i>	99
a.	A major nitrogen reservoir near the core mantle boundary (G. Rustioni, M. Wiedenbeck/Potsdam, N. Miyajima, A. Chanyshhev and H. Keppler)	100
b.	Hydrogen distribution between the Earth's inner and outer core (L. Yuan and G. Steinle-Neumann)	102
c.	Fingerprints for coupled substitutions of H and trivalent elements in olivine from polarised infrared spectroscopy (A.C. Withers)	104
d.	The temperature dependence of H ₂ O solubility in Al-free stishovite (N. Purevjav, H. Fei, T. Ishii, G. Criniti, Y. Lin, H.K. Mao/Beijing and T. Katsura)	106
e.	The permeability of water in mantle minerals at subduction zone conditions (M. Pöppelbaum, A. Néri and D.J. Frost)	107
f.	The diffusivity of hydrogen through olivine assemblages at high pressure and temperature (M. Pöppelbaum and D.J. Frost)	111
g.	Melting of primitive peridotite under mid-mantle conditions (N.S. Martirosyan, A.D. Chanyshhev, H. Fei and T. Katsura)	112
h.	The pure melt viscosity of andesitic magmas: Understanding the effect of nanocrystallization and iron oxidation in the laboratory (P. Valdivia Munoz, A. Zandonà and J. Löschmann/Clausthal, C. McCammon, A. Kurnosov, T. Boffa Ballaran, D. Di Fiore and C. Romano/Rome, J. Deubener/Clausthal and D. Di Genova/Rome)	113
i.	Combining a synthetic data approach with an artificial neural network to determine the viscosity of volcanic melts (D. Langhammer, D. Di Genova/Rome and G. Steinle-Neumann)	115
3.6	<i>Rheology</i>	118
a.	1D numerical models of rapid ductile strain localization (A. Spang and M. Thielmann, in collaboration with D. Kiss/Mainz)	119
b.	Modelling nucleation and propagation of ductile ruptures (A. Spang and M. Thielmann)	120
c.	The dual mechanism of transformational faulting and thermal runaway for deep earthquakes: A numerical study (M.I. Hamadi, A. Spang and M. Thielmann)	121
d.	Negligible effect of grain size dependent viscosity in the Earth's lower mantle (J. Paul, G.J. Golabek, T. Katsura, H. Fei/Zhejiang, A. Rozel and P. Tackley/Zürich)	122

e.	Investigation of the rheology of the Earth's lower mantle due to ferropericlasite morphology (A. Chakraborti, H. Fei/Zhejiang, Y. Nishihara and W. Wu/Matsuyama, M. Thielmann, A. Chanyshv, F. Heidelbach, N. Tsujino/Sayo and T. Katsura)	125
f.	Si self-diffusion in bridgmanite accounts for the viscosity and seismic anisotropy of the mid-mantle (L. Wang, J. Wang/Washington D.C., F. Couffignal/Potsdam, R. Dohmen/Bochum, H. Fei/Zhejiang, M. Wiedenbeck/Potsdam and T. Katsura)	126
g.	Reaction-enhanced deformability of the eclogite-facies metagranitoids in the Sesia Zone, Western Alps: Revisit with advanced electron microscopy (S. Wen/Oxford and N. Miyajima)	128
3.7	<i>Materials Science</i>	130
a.	Electronic properties of Fe ₄ O ₅ (S.V. Ovsyannikov, F. Wilhelm/Grenoble, A. Rogalev/Grenoble and L.S. Dubrovinsky)	131
b.	High-pressure oC16-YBr ₃ polymorph recoverable to ambient conditions: From 3D framework to layered material (A. Aslandukova, A. Aslandukov, F.I. Akbar, L.S. Dubrovinsky, N.A. Dubrovinskaia/Bayreuth; S. Chariton and V. Prakapenka/Chicago; A. Pakhomova and M. Hanfland/Grenoble)	133
c.	Novel high-pressure rare-earth metal carbides with diverse carbon atoms arrangements (F.I. Akbar, A. Aslandukova, A. Aslandukov, N.A. Dubrovinskaia/Bayreuth, L.S. Dubrovinsky, Y. Yin/Linköping, E. Bykova and M. Bykov/Frankfurt a. M., D. Laniel/Edinburgh)	134
d.	Stabilization of the CN ₃ ⁵⁻ anion in recoverable high-pressure Ln ₃ O ₂ (CN ₃) (Ln = La, Eu, Gd, Tb, Ho, Yb) oxoguanidates (A. Aslandukov, A. Aslandukova, A. Chanyshv, Y. Yin/Bayreuth, F.I. Akbar, S. Khandarkhaeva, N.A. Dubrovinskaia/Bayreuth, L.S. Dubrovinsky, P.L. Jurzick and M. Bykov/Köln, D. Laniel/Edinburgh, T. Fedotenko and K. Glazyrin/Hamburg, S. Chariton and V. Prakapenka/Chicago, F. Wilhelm, A. Rogalev, D. Comboni and M. Hanfland/Grenoble)	135
e.	High-pressure behaviour of anthracene up to 42 GPa (W. Zhou/Bayreuth, L.S. Dubrovinsky, N.A. Dubrovinskaia/Bayreuth and M. Hanfland/Grenoble)	136
f.	Pressure-induced structural transformations in (1-x)·Na _{0.5} Bi _{0.5} TiO ₃ -x·BaTiO ₃ at the morphotropic phase boundary (C. Rösche/Hamburg, T. Boffa Ballaran and B. Mihailova/Hamburg)	137
3.8	<i>Methodological Developments</i>	140
a.	Cyclic loading experiments of polycrystalline aggregates at high pressures (J. Buchen; B. Wang, N. Satta and V. Trautner/Oxford; G. Criniti; A.S.J. Méndez and H.-P. Liermann/Hamburg and H. Marquardt/Oxford)	141

b.	Insights on the orientation and chemical distribution of laser heated ringwoodite single crystals (F. Heidelbach, A. Kurnosov, T. Boffa Ballaran and G. Criniti)	142
c.	Thermodynamic model for the activity of Fe in solid and molten FePt alloys for use as fO_2 sensors at extreme temperatures and pressures (M.M. Hirschmann and H.L. Zhang/Beijing)	144
d.	Lawsonite and epidote as novel sensors of redox and intraslab mass transfer (D.L. Whitney/Minneapolis, M. Wilke/Potsdam and F. Heidelbach)	146
e.	Relations between the secondary ion mass spectrometry and elastic recoil detection analyses of hydrogen in various silicate glasses (D. Bondar, A.C. Withers, D. Di Genova, M. Wiedenbeck/Potsdam, H. Bureau/Paris, H. Khodja/Paris-Saclay, F. Couffignal/Potsdam, H. Fei and T. Katsura)	148
f.	Sub-micrometer quantitative high-resolution chemical analysis of Al-bridgmanite and Fe-bearing minerals using low voltage SEM-EDS (C. Timoner and N. Miyajima)	150
g.	The effect of iron content on the electrical conductivity of Al-bearing bridgmanite (K. Han and T. Katsura)	152
h.	Thermal gradient measurements in box furnace 25/15 assemblies designed for high-temperature experiments (E. Kubik, A. Néri/Lille and R. Hin/Milan)	153
i.	<i>In situ</i> stress measurement of San Carlos olivine at high pressure and temperature using two methods (J.D. Dolinschi, L. Man, A. Chakraborti, L. Wang, R. Farla/Hamburg and D.J. Frost)	154
j.	Setup and start of commissioning of the SAPHiR helium-3 detector systemat FRM II (A. Howard, K. Zeitelhack and N. Walte/Garching and H. Keppler)	157
4.	Publications, Conference Presentations, Seminars	161
4.1	Publications (published)	161
a)	Refereed international journals	161
b)	Non peer-reviewed publications	169
4.2	Publications (submitted, in press)	169
4.3	Presentations at scientific institutions and at congresses	172
4.4	Lectures and seminars at Bayerisches Geoinstitut	182
4.5	Conference organization	184
5.	Visiting Scientists	187
5.1	Visiting scientists funded by the Bayerisches Geoinstitut	187
5.2	Visiting scientists supported by other externally funded BGI projects	189
5.3	Visitors (externally funded)	189
6.	Additional Scientific Activities	191
6.1	Theses	191

6.2	Honours and awards	191
6.3	Editorship of scientific journals	191
6.4	Membership of scientific advisory bodies	192
7.	Scientific and Technical Personnel	195
	Index	198

Foreword

The Bayerisches Geoinstitut maintains an enormous collection of high-pressure and analytical equipment, which requires frequent updating to provide the most advanced scientific possibilities. While the high-pressure equipment is relatively long-lived, analytical facilities need to be regularly replaced. We are therefore very happy that in 2023, we were able to purchase and install a new electron microprobe, which was co-funded by DFG. The instrument will offer improved spatial resolution and lower detection limits, in particular for light elements. The new clean rooms and mass spectrometers for cosmochemistry also entered routine operation in this year. They greatly enhance our analytical capabilities, not only for experimental samples, but also for planetary materials. Through the generosity of NASA, we have obtained some lunar samples from the Apollo 16 and 17 missions, which will be studied with the most advanced analytical methods in order to better understand processes occurring in the early solar system.

As in every year (except during the covid pandemic), the institute hosted numerous scientists from all over the world that came here to use our experimental facilities. We were particularly pleased to host Marc Hirschmann from the University of Minnesota, who arrived with the support of a prestigious Alexander von Humboldt research award. Some of the work he did in Bayreuth is described in later sections of this Annual Report. During the summer, our new Junior Professor in Geomaterials Johannes Buchen also started his appointment.

In 2023, the Bayerisches Geoinstitut maintained a broad portfolio of experimental studies at high pressure, complemented by geodynamic and atomistic modelling and occasional studies of natural samples. As it often happens in science, the most unexpected and accidental observations were sometimes also the most interesting ones. A very nice example is the study by Rustioni and coworkers on page 100 ff. This study was originally designed to measure nitrogen solubility in bridgmanite, the most abundant mineral in the lower mantle. Minor amounts of magnesiowüstite (Fe,Mg)O also formed during the experiments. When Greta Rustioni measured these crystals by SIMS (secondary ion mass spectrometry), she observed incredibly high count rates for nitrogen. Detailed studies then showed that nitrogen solubility in these crystals increases by orders of magnitude with the Fe/Mg ratio, from a few ppm at low Fe contents to more than 10 wt. % in Fe-rich samples, apparently due to some solid solution between FeO and FeN. Geochemically, this is an extremely interesting observation. According to seismic data, layers of Fe-rich magnesiowüstite probably exist in the lowermost mantle just above the core. They are likely the result of the fractional crystallization of a deep magma ocean. Some rough calculations indicate that according to the new data obtained here, they may contain several times more nitrogen than currently resides in the atmosphere. This implies that nitrogen is not anomalously depleted on Earth, as is often believed. This apparent nitrogen depletion is just caused by most nitrogen residing in a very deep reservoir that is extremely poorly sampled.

New methodological developments are a particular strength of the Bayerisches Geoinstitut. For understanding the structure of the Earth and of other planets, it is essential to translate seismic data into mineralogical models. For this, elastic constants need to be determined at high pressure and high temperature. While measuring these data at high pressure and room temperature is rather straightforward, measurements at combined high pressure and high temperature conditions are still extremely difficult. The contribution on page 94 ff. investigated the elastic properties of a relatively Fe-rich ringwoodite, which is believed to be a main constituent of the mantle of Mars – and for Mars, seismic data are now available from the NASA InSight Lander. In this study, Kurnosov and coworkers managed to measure Brillouin spectra in a laser-heated diamond cell to 21 GPa and 1950 K, which is an extremely impressive technical achievement.

While BGI is primarily an institute for high pressure experimentation, we sometimes also look at natural samples. A nice example is the contribution by Chang and Audéat on page 54 ff. Modern technology relies on a constant supply of all kinds of raw materials, in particular metals. Satisfying the industrial demand becomes increasingly difficult and finding new deposits requires a fundamental understanding of the processes that enrich trace metals to industrial grade ore deposits. One interesting observation here is that magmatic gold deposits are often associated with alkaline igneous rocks. This has led to the suggestions that these magmas may be particularly gold-rich from the beginning. This is not so easy to test. The concentrations are exceedingly low and normal rock samples may have lost their original gold content by weathering and other processes. To solve this problem, Chang and Audéat looked at melt inclusions – droplets of magma trapped inside growing crystals – from a worldwide suite of samples. The melt inclusions are shielded from subsequent modification by the surrounding crystals. Laser-ablation mass spectrometry analyses of these tiny samples gave an unambiguous result: They contain only 2 to 7 ppb (nanogram/gram) of gold, comparable to other magmas. The association of gold with the alkaline magmas must therefore have other reasons that are likely related to processes in the later crystallization of these magmas.

On the behalf of my colleagues, I would like to thank the *Free State of Bavaria* as represented by the *Bavarian State Ministry of Science, Research and Art*, as well as the *Advisory Board for High-Pressure Research in Geoscience of the Bavarian Academy of Sciences* for their continuing support and strong commitment to the Bayerisches Geoinstitut. I would further like to thank the *President and Leadership of the University of Bayreuth* for their high regard of our institute. We also gratefully acknowledge generous support from external funding agencies, in particular the *Alexander von Humboldt Foundation*, the *European Union*, the *German Science Foundation*, and the *Federal Ministry of Education and Research*, which continue to contribute greatly to the further development and success of the Geoinstitut.

Bayreuth, March 2024

Hans Keppler

Vorwort

Das Bayerische Geoinstitut unterhält einen enormen Gerätepark für Hochdruckexperimente und für die Untersuchung von Proben. Während die Hochdruckapparaturen recht langlebig sind, müssen die analytischen Einrichtungen regelmäßig erneuert werden. Wir freuen uns daher sehr, dass wir im Jahr 2023 eine neue Elektronen-Mikrosonde beschaffen und in Betrieb nehmen konnten, die von der DFG mitfinanziert wurde. Das Gerät bietet eine verbesserte Auflösung und niedrigere Nachweisgrenzen insbesondere für leichte Elemente. Die neuen Reinräume und Massenspektrometer für Kosmochemie wurden ebenfalls in diesem Jahr in vollen Betrieb genommen. Mit ihnen werden unsere analytischen Fähigkeiten enorm erweitert, sowohl für Proben aus Hochdruckexperimenten als auch für extraterrestrische Materialien. Die NASA hat uns großzügigerweise Proben der Apollo 16- und 17-Missionen zur Verfügung gestellt, die hier mit modernsten analytischen Methoden untersucht werden, um Prozesse im frühen Sonnensystem besser zu verstehen.

Wie in jedem Jahr (außer während der Corona-Pandemie) war das Institut Gastgeber für zahlreiche Wissenschaftler, die aus der ganzen Welt nach Bayreuth gekommen sind, um unsere experimentellen Einrichtungen zu nutzen. Wir haben uns besonders über den Aufenthalt von Marc Hirschmann von der University of Minnesota gefreut, der mit einem prestigeträchtigen Alexander-von-Humboldt-Forschungspreis nach Bayreuth gekommen ist. Im Sommer hat auch Johannes Buchen, unser neuer Junior-Professor für Geomaterialien seinen Dienst angetreten.

Im Jahr 2023 wurde am Bayerischen Geoinstitut ein breites Spektrum von Hochdruckexperimenten durchgeführt, ergänzt durch geodynamische und atomistische Modellierung und durch die Untersuchung natürlicher Proben. Wie oft in der Wissenschaft waren gerade die unerwarteten und zufälligen Beobachtungen manchmal am interessantesten. Ein schönes Beispiel ist hier der Bericht von Rustioni und Mitarbeitern auf Seite 100 ff. In diesem Projekt sollte eigentlich die Löslichkeit von Stickstoff in Bridgmanit untersucht werden, dem wichtigsten Mineral im unteren Erdmantel. In den Experimenten entstanden aber auch kleinere Mengen von Magnesiowüstit (Fe,MgO). Als Greta Rustioni diese Kristalle mit SIMS (Sekundärionen-Massenspektrometrie) untersuchte, beobachtete sie unglaublich hohe Zählraten von Stickstoff. Genauere Untersuchungen zeigten dann, dass die Löslichkeit von Stickstoff in diesen Kristallen mit dem Fe/Mg-Verhältnis um Größenordnungen ansteigt, von wenigen ppm bei niedrigen Eisen-Gehalten zu über 10 Gew. % in Eisen-reichen Proben. Grund dafür ist offenbar die Bildung von Mischkristallen zwischen FeO und FeN. Für die Geochemie ist das eine höchst interessante Beobachtung. Seismische Daten zeigen, dass sich im untersten Mantel, direkt über dem Erdkern lokal wahrscheinlich Lagen von Eisen-reichem Magnesiowüstit befinden. Diese Lagen wurden wohl dadurch gebildet, dass Kristalle von Magnesiowüstit aus einem tiefen Magmenozean auskristallisierten und sich dann über dem Erdkern abgelagert haben. Überschlägige Rechnungen auf Basis der hier erhaltenen neuen Daten zeigen, dass diese Lagen wahrscheinlich das Mehrfache der Menge an Stickstoff enthalten, der sich heute in der Atmosphäre befindet. Dies würde dann auch bedeuten, dass Stickstoff auf der Erde nicht anomal verarmt ist, wie oft angenommen wird. Diese scheinbare Verarmung wird nur dadurch vorgetäuscht, dass sich der größte Teil des Stickstoffs in einem sehr tiefen Reservoir befindet, das kaum beprobt wird.

Neue methodische Entwicklungen sind eine besondere Stärke des Bayerischen Geoinstituts. Um die Struktur der Erde und anderer Planeten zu verstehen, müssen seismische Daten in mineralogische Modelle übersetzt werden. Hierzu müssen die elastischen Eigenschaften von Mineralen unter hohem Druck und hoher Temperatur bestimmt werden. Entsprechende Messungen bei hohem Druck und Raumtemperatur sind relativ einfach durchzuführen, Experimente bei hohem Druck und gleichzeitig hoher Temperatur sind aber immer noch extrem schwierig. In dem Beitrag auf Seite 94 ff. werden die elastischen Eigenschaften von relativ Eisen-reichem Ringwoodit untersucht. Dieses Mineral ist wahrscheinlich ein Hauptbestandteil des Mantels von Mars und für Mars gibt es mittlerweile seismische Daten aus der NASA InSight Lander-Mission. In dem genannten Projekt konnten Kurnosov und Mitarbeiter Brillouin-Spektren in Laser-geheizten Diamantstempel-Zellen bis zu 21 GPa und 1950 K messen, was eine enorme technische Leistung darstellt.

Obwohl das BGI primär ein Institut für experimentelle Hochdruckforschung ist, untersuchen wir gelegentlich auch natürliche Proben. Ein schönes Beispiel ist der Beitrag von Chang und Audétat auf Seite 54 ff. Unsere moderne Zivilisation benötigt einen kontinuierlichen Nachschub von zahlreichen Rohstoffen, insbesondere auch Metallen. Es wird zunehmend schwieriger, diesen Bedarf zu decken und die Erschließung neuer Lagerstätten erfordert ein grundlegendes Verständnis der Prozesse die in der Natur Spurenelemente bis zu nutzbaren Vorkommen anreichern. Eine interessante Beobachtung ist hier, dass magmatische Gold-Lagerstätten oft an alkalischen Magmen gebunden sind. Es wird daher diskutiert, dass diese Magmen vielleicht von Anfang an besonders reich an Gold sind. Diese Frage ist nicht einfach zu beantworten, denn die Konzentrationen sind extrem niedrig und normale Gesteinsproben können ihr Gold nachträglich durch Verwitterung oder andere Prozesse verloren haben. Um dieses Problem zu lösen, haben Chang und Audétat in einem Satz von Proben aus aller Welt Schmelzeinschlüsse untersucht – kleine Tröpfchen von Magma, die in wachsende Kristalle eingeschlossen wurden. Die Kristalle schirmen die Einschlüsse gegen nachträgliche Veränderungen ab. Untersuchungen mit Laser-Ablations-Massenspektrometrie an diesen winzigen Proben ergaben ein eindeutiges Resultat: der Gold-Gehalt liegt zwischen 2 und 7 ppb (Nanogramm/Gramm), vergleichbar mit anderen Magmen. Die Verknüpfung von Gold mit alkalischen Magmen muss daher andere Gründe haben, die wahrscheinlich etwas mit Prozessen bei der späteren Kristallisation dieser Magmen zu tun hat.

Meine Kollegen und ich möchten dem *Freistaat Bayern*, vertreten durch das *Bayerische Staatsministerium für Wissenschaft, Forschung und Kunst*, und dem *Beirat für Geowissenschaftliche Hochdruckforschung der Bayerischen Akademie der Wissenschaften* unseren Dank für ihre fortwährende Unterstützung des Bayerischen Geoinstituts aussprechen. Darüber hinaus möchten wir dem Präsidenten und der Hochschulleitung der Universität Bayreuth ausdrücklich für ihre zuverlässige und kontinuierliche Unterstützung unseres Instituts danken. Wir sind auch für die großzügige Förderung durch externe Geldgeber dankbar, insbesondere der *Alexander-von-Humboldt-Stiftung*, der *Europäischen Union* und der *Deutschen Forschungsgemeinschaft*, die ebenfalls wesentlich zur Entwicklung und zum Erfolg des Bayerischen Geoinstituts beigetragen haben.

Bayreuth, im März 2024

Hans Keppler

1. Advisory Board and Directorship

1.1 Advisory Board

The *Beirat für Geowissenschaftliche Hochdruckforschung der Bayerischen Akademie der Wissenschaften* advises on the organisation and scientific activities of the institute. Members of this board are:

Prof. Dr. Ulrich CHRISTENSEN	Emeritus, Max-Planck-Institut für Sonnensystemforschung, Göttingen
Prof. Dr. Rudolf GROSS (Vice Chairman)	Walther-Meißner-Institut für Tieftemperaturforschung (WMI), Garching
Prof. Dr. Francois HOLTZ	Institut für Mineralogie der Leibniz Universität Hannover
Prof. Dr. Klaus MEZGER	Institut für Geologie der Universität Bern
Prof. Dr. Herbert PALME	Emeritus, Institut für Mineralogie und Geochemie der Universität zu Köln – Senckenberg Forschungsinstitut und Naturmuseum Frankfurt/M.
Prof. Dr. Markus RIEDERER (Chairman)	Julius-von-Sachs-Institut für Biowissenschaften, Würzburg
Prof. Dr. Ekhard SALJE, FRS, FRSA	Emeritus, Department of Earth Sciences, University of Cambridge
Prof. Dr. Christine THOMAS	Institut für Geophysik der Westfälischen Wilhelms-Universität Münster

1.2 Leadership

Prof. Dr. Hans KEPPLER (Director)
Prof. Dr. Dan FROST (Deputy Director)
Prof. Dr. Tomoo KATSURA
Prof. Dr. Audrey BOUVIER

2. Staff, Funding and Facilities

2.1 Staff

At the end of 2023 the following staff positions existed in the Institute:

- Scientific staff: **15**
- Technical staff: **14**
- Administrative staff: **2**
- Administrative officer: **1***

* The administrative officer is employed on 40 % of a full position provided by the central administration.

During 2023, 26 scientific positions (249 months) were funded by grants raised externally by staff members of the institute. In addition, 5 scientific positions (20 months) were funded by the resources of the BGI Visiting Scientists' Programme (see Sect. 8), which also supported short-term visits for discussing future projects or presenting research results (see Sect. 5). 8 student assistants (65.5 months) were funded by externally raised grants. 8 scientists and 3 PhD students (101 months) were supported by personal grants or stipends.

A position (72 months) for a tenure-track junior professorship was funded by BMBF and provided by courtesy of Bayreuth University.

2.2 Funding

In 2023, the following financial resources were available from the Free State of Bavaria:

- Visiting Scientists' Programme: 156.000 €
- Consumables: 622.000 €

The total amount of national/international external funding ("*Drittmittel*") used for ongoing research projects in 2023 was 3.421.000 € (positions: 2.049.000 €; equipment, consumables and travel grants: 1.372.000 €).

	positions	equipment, consum- ables, travel grants	total
• AvH	67.000 €	1.000 €	68.000 €
• DFG	1.195.000 €	980.000 €	2.175.000 €
• EU	691.000 €	374.000 €	1.065.000 €
• Others	96.000 €	17.000 €	113.000 €
	2.049.000 €	1.372.000 €	3.421.000 €

(AvH = Alexander von Humboldt Foundation; DFG = German Science Foundation; EU = European Union; Others: DAAD, Chinese Science Council, Japanese Society for the Promotion of Science, Swiss National Science Foundation)

In the following list, only the BGI components of the funding are listed in cases where joint projects involved other research institutions. Principal investigators and the duration of the grants are listed in brackets. Total project funding refers to the funding over the entire duration of this project.

Funding institution	Project, Funding	Total Project Funding
AvH	Project SEPARATION (E. Kubik – 3/23-2/25) "Segregation efficiency of planetary cores addressed through the isotopes of nickel" Positon: 24 months 70.000 € Consumables: 19.200 €	89.200 €
DFG	AU 314/6-1 (A. Audétat – 1/21-7/23) "Bestimmung der Faktoren, die das Cu-Au Mineralisationspotenzial von Magmen in Kollisionszonen kontrollieren" Positions: E 13 (100 %), 24 months 151.000 € Consumables: 35.800 € Overhead: 41.100 €	227.900 €
DFG	BO 2550/10-1 (T. Boffa Ballaran, B. Mihailova – 7/21-6/24) "Mehrskaliges Hochdruckverhalten der bleifreien ferroelektrischen Perowskitmischkristalle (1-x)Na _{0,5} BiTiO _{3-x} BaTiO ₃ " Positions: student assistant 15.000 € Consumables: 6.900 € Overhead: 4.800 €	26.700 €
DFG	DI 2751/2-1 (D. Di Genova – 10/21-9/24) "Rheology of nanocrystal-bearing natural silicate melts" Positions: E 13 (75 %), 36 months 160.900 € student assistant 4.846 € Equipment: 18.000 € Overhead: 40.400 €	224.146 €
DFG	DU 393/13-2 (L.S. Dubrovinsky – 7/20-6/23) "Mantel-formende Materialien von Super-Erden bei statischen Drücken von über 500 GPa und hohen Temperaturen" Positions: E 13 (75 %), 36 months 158.600 € student assistant 7.000 € Equipment: 32.250 € Overhead: 43.500 €	241.350 €
DFG	FR 1555/11-1 (D.J. Frost – 3/16-2/23) Gottfried Wilhelm Leibniz-Preis 2016	2.500.000 €

DFG	INST 91/455-1 (A. Bouvier) Major Research Instrumentation Individual Proposal for a Laser Ablation – Multi-collector Inductively Coupled Plasma Mass Spectrometer with collision reaction cell. 50 % from institution (UBT and BGI) – 50% from DFG. Total from DFG:	615.000 €
DFG	INST 91/463-1 FUGG (H. Keppler – 2022-2023) Co-financing for a new electron microprobe. Total DFG funding (50 % of total costs):	611.000 €
DFG	INST 91/467-1 FUGG (D. Frost – 2022-2024) Co-financing for a microfocus single-crystal X-ray diffractometer. Total DFG funding (50 % of total costs):	390.000 €
DFG	KA3434/19-1 (T. Katsura – 02/21-08/23) "Evaluation of the aspect ratio of ferropericlase under lower-mantle conditions" Positions: E13, 24 months 152.200 € Consumables: 50.000 € Overhead: 44.400 €	246.600 €
DFG	KA 3434/20-1 (T. Katsura – 9/21-8/23) "Accurate determination of the melting relations of primitive peridotite under lower-mantle conditions up to 35 GPa using advanced multi-anvil techniques" Positions: E13, 24 months 154.100 € Consumables: 50.000 € Overhead: 44.900 €	249.000 €
DFG	KA 3434/24-1 (T. Katsura – 10/23-9/26) "H ₂ O solubilities in Al-free and Al-bearing high-pressure silica polymorphs as a function of pressure and temperature: H ₂ O storage in the lower mantle" Positions: E13, 36 months 246.800 € student assistant 5.000 € Consumables: 78.000 € Overhead: 72.600 €	402.400 €
DFG	KE 501/16-1 (H. Keppler – 2020-2024) "Cassiterite solubility, tin partitioning, and the origin of porphyry tin deposits" Total funding:	242.288 €
DFG	KE 501/18-1 (H. Keppler – 2022-2025) "Stability of organic molecules in subduction zone fluids" Total funding:	259.555 €
DFG	KE 501/19-1 (H. Keppler – 2023-2027) "Subduction fluids and the source of metals in porphyry deposits" Total funding:	259.603 €

DFG	KU 3447/1-2 (A. Kurnosov – 1/22-12/24) "Einkristall-Elastizität von Mars-Mineralen und ein flexibles CO ₂ Laserheizsystem" Position: E 13, 36 months 237.100 € student assistant 10.000 € Consumables and travel funding: 23.550 € Overhead: 59.500 €	330.150 €
DFG	MC 3/20-2 (C.A. McCammon – 1/18-3/24) DFG FOR 2125 (CarboPaT) "Elastic properties of carbonates at high pressure and high temperature" Position: E 13 (67 %), 36 months: 132.800 € Equipment, consumables and travel funding: 27.750 € Overhead: 35.300 €	195.850 €
DFG	MI 1721/3-1 (N. Miyajima – 9/19-2/23) "Al, Si-Interdiffusion in Bridgmanit und die Viskosität des unteren Mantels" Position: E 13 (75 %), 36 months: 149.500 € E 13 (75 %), 6 months extension 26.900 € student assistant 7.500 € Consumables and travel funding: 29.500 € Overhead: 41.000 € Overhead extension: 5.900 €	260.300 €
DFG	OV 110/3-3 (S.V. Ovsyannikov – 11/23-10/25) "High-pressure synthesis and properties of novel simple oxides with unusual stoichiometries" Position: E 13, 24 months: 159.900 € Consumables and travel funding: 36.000 € Overhead: 43.100 €	239.000 €
DFG	STE 1105/13-2 (G. Steinle-Neumann – 7/20-6/24) "Thermodynamic properties of silicate solids and liquids and iron to the TPa range from <i>ab initio</i> calculations" Positions: E 13 (75%), 36 months 158.600 € student assistant 7.000 € Consumables: 8.250 € Overhead: 38.200 €	212.050 €
DFG	STE 1105/15-1 (G. Steinle-Neumann – 7/23-6/26) "The role of light elements at the core-mantle boundary – partitioning, demixing and transport " Positions: E 13 (75%), 36 months 172.100 € student assistant 7.000 € Consumables: 10.250 € Overhead: 41.657 €	231.007 €

DFG	TH 2076/7-1 (M. Thielmann – 6/21-5/24) "Quantifizierung des Oberflächensignals durch Lithosphärenablösung in den Alpen" Positions: 244.700 € Consumables: 17.050 € Overhead: 57.600 €	319.350 €
DFG	TH 2076/8-1 (M. Thielmann – 11/21-10/24) "Identifizierung der Entstehungsprozesse tiefer Erdbeben" (Emmy-Noether-Programm) Positions: 670.913 € Consumables: 60.580 € Workshops: 5.000 € Overhead: 162.000 €	898.496 €
DFG	WI 5383/1-1 (A. Withers, A.B. Woodland – 04/20-03/23) "Gescherte Peridotite: Deformation, Metasomatose und beginnende Destabilisierung von Kratonen" Positions: student assistant 7.500 € Overhead: 1.700 €	9.200 €
DFG	YU 358/1-1 (L. Yuan, G. Steinle-Neumann – 2/22-1/25) "Partitionierung flüchtiger Elemente im tiefen Magma Ozean der Erde" Positions: E 13, 36 months 232.900 € student assistant 10.000 € Consumables: 14.250 € Overhead: 56.600 €	313.750 €
EU	European Research Council (ERC) Advanced Grant No. 787 527 (T. Katsura – 10/18-9/23) "Chemistry and transport properties of bridgmanite controlling lower-mantle dynamics" ("UltraLVP") Positions (post docs): 860.144 € Travel funding: 187.380 € Equipment: 49.250 € Consumables: 997.722 € In-kind contributions: 24.000 € Overhead: 523.624 €	2.642.120 €
EU	European Research Council (ERC) Grant No. 949 417 (R. Hin – 1/21-12/25) "The chemical consequences of vapour loss during planetary accretion (VapLoss)" ("HORIZON 2020") Positions: 756.169 € Travel funding: 44.781 € Consumables: 129.403 € Equipment: 153.802 € Internally Goods and Services: 173.235 € Overhead: 314.348 €	1.571.738 €

2.3 Laboratory and office facilities

The institute occupies an area of

ca. 1470 m² laboratory space

ca. 480 m² infrastructural areas (machine shops, computer facilities, seminar room, library)

ca. 520 m² office space

in a building which was completed in 1994.

2.4 Experimental and analytical equipment

The following major equipment is available at the Bayerisches Geoinstitut:

I. High-pressure apparatus

15 MN/1500 tonne Kawai-type multianvil high-pressure apparatus (50 GPa, 3000 K)

6 x 8 MN/6x800 tonne independently acting-anvil press (40 GPa, 3000 K)

50 MN/5000 tonne multianvil press (25 GPa, 3000 K)

12 MN/1200 tonne multianvil press (25 GPa, 3000 K)

10 MN/1000 tonne multianvil press (25 GPa, 3000 K)

5 MN/500 tonne multianvil press (20 GPa, 3000 K)

5 MN/500 tonne press with a deformation DIA apparatus

5 piston-cylinder presses (4 GPa, 2100 K)

Cold-seal vessels (700 MPa, 1100 K, H₂O), TZM vessels (300 MPa, 1400 K, Ar), rapid-quench cold-seal vessels (400 MPa, 1200 K, H₂O)

Internally-heated autoclave (1 GPa, 1600 K)

High-pressure gas loading apparatus for DAC

II. Structural and chemical analysis

1 X-ray powder micro-diffractometer

1 X-ray powder diffractometer with furnace and cryostat

2 automated single-crystal X-ray diffractometers

High-brilliance X-ray system

Single crystal X-ray diffraction with super-bright source

1 Mössbauer spectrometer (1.5 - 1300 K)

3 Mössbauer microspectrometers

2 FTIR spectrometers with IR microscope

FEG transmission electron microscope (TEM), 200 kV analytical, with EDS

FEG scanning TEM, 80-200 kV analytical, with 4-SDDs EDS and post-column energy filter (EFTEM/EELS)

FEG scanning electron microscope (SEM) with BSE detector, EDS, EBSD and CL

Dual beam device, focused ion beam (FIB) and FEG SEM. In situ easy-lift manipulator,
 STEM, EDS and EBSD detectors, and beam deceleration option
 3 Micro-Raman spectrometers with ultraviolet and visible lasers
 Tandem-multipass Fabry-Perot interferometer for Brillouin scattering spectroscopy
 Two electron microprobes; fully-automated with 14 resp. 12 crystals, 5 spectrometer
 configuration, EDX, capability for light elements, CL
 193 nm Excimer Laser-Ablation ICP-MS
 Water content determination by Karl-Fischer titration
 GC/MS-MS for organic analyses
 Confocal 3D surface measurement system
 1.4 Tesla sweepable ESR magnet
 Solid state 300 MHz NMR spectrometer
 ESI NWRGEO 193 nm Excimer Laser Ablation system
 Thermo Scientific iCAP triple quadrupole ICPMS for solution or in-situ LA- isotopic
 analysis
 Thermo Scientific Neoma MS/MS multi-collector ICPMS for solution or in-situ LA- high-
 resolution isotopic ratio measurements
 Isotope Cosmochemistry & Geochemistry Laboratory ISO 6 cleanrooms equipped with ISO
 4 exhaust laminar flow cabinets for sample preparation
 500 Hz 193 nm Excimer Laser Ablation system
 Triple quadrupole ICPMS for solution or in-situ LA-isotopic analysis
 Multi-collector ICPMS/MS for solution or in-situ LA-isotopic analysis

III. *In situ* determination of properties

Diamond anvil cells for powder and single crystal X-ray diffraction, Mössbauer, IR, Raman,
 optical spectroscopy, NMR spectroscopy, electrical resistivity measurements over 200
 GPa
 Facility for in situ hydrothermal studies in DAC
 Externally heated DACs for in situ studies at pressures to 100 GPa and 1200 K
 1-atm furnaces to 1950 K, gas mixing to 1600 K, zirconia fO₂ probes
 1-atm high-temperature creep apparatus
 Megahertz ultrasonic interferometer
 2 freezing-heating stages for fluid inclusion analysis (80-870 K; 300-1900 K)
 Impedance/gain-phase analyser for electrical conductivity studies
 Apparatus for in situ measurements of thermal diffusivity at high P and T
 Laser-heating facility for DAC
 Portable pulsed laser heating system for DAC

The Geoinstitut maintains a well equipped machine shop, an electronic workshop and sample preparation laboratories. It has access to supercomputing resources at the University and Leibniz computer centres.

3. Forschungsprojekte

3.1 Struktur und Dynamik der Erde und Planeten

Mit fast 5600 bekannten Exoplaneten und dem Beginn hochauflösender Beobachtungen durch das neue James Webb Space Telescope (JWST) wird es möglich, verschiedene Stadien der Planetenentwicklung im Detail zu untersuchen. Im ersten Beitrag verwenden Golabek und Kollegen numerische Modelle auf globaler Ebene, um die Entwicklung des Magmaozeans auf dem gebunden rotierenden Super-Merkur GJ 367 b zu untersuchen. Die Ergebnisse können mit den JWST-Beobachtungen dieses Planeten verglichen werden. Dadurch können Erkenntnisse über das ansonsten unzugängliche Magmaocean-Stadium junger terrestrischer Planeten erlangt werden.

Die Bildung von Einschlagskratern ist der wichtigste geologische Prozess, der auf den meisten Planetenoberflächen im Sonnensystem zu beobachten ist. Bei planetaren Körpern mit einem Durchmesser von weniger als etwa 100 km ist die Bildung von Einschlagskratern praktisch der einzige Prozess, der seit ihrer Entstehung auf der Oberfläche stattgefunden hat. Selbst auf größeren Körpern wie dem Mond, auf dem es erhebliche vulkanische Aktivität gegeben hat, dominieren Einschlagbecken die großräumige Topografie. Die Entschlüsselung der Geschichte der Planetenentstehung und der Einschlagsereignisse ist eine Herausforderung, da die Methoden der radiometrischen Datierung auf dem Isotopengleichgewicht zum Zeitpunkt des Ereignisses beruhen. Die Spuren planetarer Prozesse wie der magmatischen Kristallisation können durch sekundäre Ereignisse wie hochenergetische Planeteneinschläge beeinflusst werden. Die meiste Energie bei Einschlägen wird schnell deponiert und führt in erster Linie zu mechanischer Verformung und physikalischer Verschiebung von Materialien, was möglicherweise keine isotopischen Auswirkungen hat. Im zweiten Beitrag untersuchen Zhao und Kollegen einen gewöhnlichen Chondriten mit Schmelzbrekzien, der große und langsam abgekühlte Bruchstücke von Einschlagsschmelzen enthält. In der gesamten Brekzie wurde eine Schockverformung festgestellt, was auf mehrere Einschläge hindeutet. Anhand von geochemischen und Sauerstoff-isotopischen Analysen stellen die Autoren fest, dass sich diese Bruchstücke durch vollständiges Aufschmelzen des chondritischen Materials gebildet haben und anschließend auf dem Meteoriten-Mutterkörper zusammengemischt wurden. Die Pb-Pb-Alter der Phosphate, die nur im chondritischen Material gefunden wurden, erlauben keine Unterscheidung zwischen thermischer Metamorphose oder einem frühen Impaktereignis. Im dritten Beitrag setzen Greer und Kollegen die Atomsonden-Tomographie ein, um die Auswirkungen des Schocks auf die Pb-Isotopenverteilung auf der Nanoskala zu untersuchen, was das Pb-Pb-Alter von geschockten Zirkonen verändern kann.

Die ältesten Teile der Erdoberfläche sind Kratone, und die meisten von ihnen sind seit mehreren Milliarden Jahren unverformt geblieben. Ein seltenes Beispiel für die Zerstörung eines Kratons ist das nordchinesische Kraton. Im vierten Beitrag verwenden Paul und Kollegen numerische 2D-Modelle auf regionaler Ebene, um verschiedene Szenarien für die Zerstörung von Kratonen

zu testen. Sie zeigen, dass die Freisetzung von Wasser aus einer subduzierenden Platte, die Metasomatose und das Absinken des tiefen Teils der Lithosphäre verursacht, ein Kraton schwächen und schließlich zerstören kann.

Kontinent-Kontinent-Kollisionen, die zum Beispiel für die Entstehung des Himalayas und der Alpen verantwortlich sind, führen oft zum Abbrechen von Platten. Dieses tektonische Ereignis verursacht an der Oberfläche erhebliche topografische Veränderungen und die Verfüllung von Becken durch Sedimente. Eskens und Kollegen kombinieren geodynamische Modelle auf regionaler Ebene mit Sedimentmodellen, um dies für das österreichische Vorlandbecken zu untersuchen, wobei sie eine gute Übereinstimmung mit den verfügbaren seismischen Daten für diese Region nachweisen. In einer verwandten Studie untersuchen Piccolo und Kollegen die physikalischen Prozesse, die das Abbrechen der Platte kontrollieren. Sie zeigen, dass die Krümmung der Platte einen wichtigen Einfluss auf die Zeitskala der Abtrennung hat und dass sich anhand von Oberflächenbeobachtungen verschiedene Abtrennungsszenarien unterscheiden lassen.

Sowohl die Zusammensetzung als auch der physikalische Zustand der Planetenkerne beeinflussen die Erzeugung des Magnetfelds, das die Planetenoberfläche vor solarer und galaktischer kosmischer Strahlung schützt. Im siebten Beitrag verwenden Kleinschmidt und Kollegen *ab initio*-Simulationen, um sowohl die elektrische als auch die thermische Leitfähigkeit von Eisenphasen unter Bedingungen des Erdkerns zu ermitteln. Sie stellen Diskrepanzen zwischen ihren Simulationen und den experimentellen Daten fest, die mit Druck und Temperatur zunehmen, und vielleicht durch die in einigen der Experimente verwendete Probengeometrie verursacht werden. Sie schließen aus ihren Ergebnissen, dass die Wärmeleitfähigkeit des inneren Kerns viel höher ist als im äußeren Kern, so dass im festen inneren Erdkern wahrscheinlich keine Konvektion stattfindet.

3.2 Geochemie

Die erste Studie in diesem Abschnitt beschreibt die radiometrische Datierung eines differenzierten Meteoriten, der aus der magmatischen Kruste eines früh entstandenen Planetesimals stammt. Die magmatische Differenzierung und Krustenbildung auf solchen Planetesimalen wurde durch die Zerfallswärme des kurzlebigen radiogenen Isotops ^{26}Al angetrieben. Die Halbwertszeit des ^{26}Al von etwa 0,7 Millionen Jahren bedeutet, dass es jetzt nicht mehr vorhanden ist. Der radioaktive Zerfall erzeugte aber einen erkennbaren Überschuss des Tochterisotops ^{26}Mg in früh gebildeten Mineralen, der mit dem verbleibenden stabilen Isotop ^{27}Al korreliert. Dieser Überschuss kann zur Bestimmung des Alters von Planetesimal-Krusten herangezogen werden. Die größte Unsicherheit ist dabei das ursprüngliche Verhältnis von $^{26}\text{Al}/^{27}\text{Al}$. Ohne Kenntnis dieses Wertes kann das Alter nur relativ zu den frühesten Objekten im Sonnensystem, den so genannten Kalzium-Aluminium-reichen Einschlüssen (CAI), angegeben werden. In dieser Studie werden die absoluten Alter auch mit Hilfe der

langlebigen Uran-Blei-Isotope datiert. Durch diese Kreuzkalibrierung kann ein ursprüngliches $^{26}\text{Al}/^{27}\text{Al}$ -Verhältnis bestimmt werden, was darauf hindeutet, dass ^{26}Al im frühen Sonnensystem gleichmäßig verteilt gewesen zu sein scheint. Die Ergebnisse zeigen auch, dass sich das betreffende Planetesimal nur 1,8 Millionen Jahre nach den ersten Mineralen im Sonnensystem (den CAIs) gebildet hat und damit das älteste bekannte magmatische Gestein ist.

In der folgenden Studie werden Sulfidminerale in einem gewöhnlichen Chondrit-Meteoriten untersucht, dessen Einschlag vor etwa fünf Jahren in Marokko beobachtet wurde. Gewöhnliche Chondrite sind, wie der Name schon sagt, die bei weitem häufigste Meteoritenklasse. Die Proben innerhalb dieser Klasse unterscheiden sich sowohl im Gesamteisengehalt und Redoxzustand, als auch im Ausmaß der thermischen und schockbedingten Metamorphose. Sulfidische Minerale neigen dazu, sich mit zunehmender Temperatur durch Diffusions- und schließlich Schmelzprozesse zu homogenisieren. Der fragliche Meteorit wurde thermisch metamorph überprägt, so dass die Untersuchung der Sulfidminerale dazu beiträgt, die ursprünglichen Prozesse der Entmischung des Kerns und Mantels zu verstehen.

In den nächsten beiden Studien wird untersucht, wie sich das Verhältnis der stabilen Eisenisotope ^{56}Fe und ^{54}Fe während der Kernbildung auf der Erde und dem Mars verändert haben könnte. In der ersten Studie wird die Auswirkung von Schwefel in der metallischen Schmelze für Zusammensetzungen und Bedingungen untersucht, die wahrscheinlich typisch für die Kernbildung auf dem Mars waren. Im Gegensatz zu früheren Studien, die bei niedrigem Druck durchgeführt wurden, wird bei schwefelhaltigen Metallschmelzen keine signifikante Fraktionierung von ^{56}Fe und ^{54}Fe beobachtet, was mit dem scheinbar unfraktionierten Eisenisotopenverhältnis des Marsmantels im Vergleich zu primitiven Meteoriten übereinstimmt. In der zweiten Studie wird die Auswirkung des Drucks für Metallzusammensetzungen ohne Schwefel untersucht. Bei Drücken zwischen 8 und 15 GPa wird eine Fraktionierung beobachtet, wodurch der Mantel an dem schwereren Eisenisotop verarmt würde. Dies steht sowohl im Widerspruch zu früheren Vorhersagen als auch zum tatsächlichen Zustand des Erdmantels. Bei höheren Drücken wird jedoch nur eine sehr geringe Fraktionierung beobachtet. Durch solche Messungen könnten daher wichtige Hinweise auf die Druckbedingungen der Gleichgewichtseinstellung zwischen Kern und Mantel erhalten werden.

Falls Kalium während der Kernbildung in den Erdkern gelangte, würde dies eine wichtige zusätzliche Wärmequelle zur Aufrechterhaltung des Magnetfelds darstellen. Die in der nächsten Studie dieses Abschnitts durchgeführten Experimente sollen dies klären, indem die Verteilung von Kalium zwischen Metall und Silikat bei hohem Druck und hohen Temperaturen untersucht wird. Die bisherigen Ergebnisse zeigen, dass die Verteilungskoeffizienten, die unter den gleichen Bedingungen gemessen wurden, in Abhängigkeit von der Versuchszeit variieren. Dies könnte auf Gleichgewichtsprobleme zurückzuführen sein, aber auch auf Schwierigkeiten bei der Analyse der sehr flüchtigen Kalium-Komponente in der abgeschreckten metallischen Phase.

Die Auswirkung der Kernbildung auf das Schwefelisotopenverhältnis $^{34}\text{S}/^{32}\text{S}$ sind Gegenstand der folgenden Studie. Es wird oft angenommen, dass der Schwefelgehalt des Erdmantels der Erde erst spät, nach Abschluss der Kernbildung, hinzugefügt wurde. Ansonsten hätte der meiste Schwefel als metallliebendes Element in den Kern extrahiert worden sein müssen. Das $^{34}\text{S}/^{32}\text{S}$ -Verhältnis des Erdmantels ist jedoch leichter als das der primitiven Meteoriten. Es ist daher denkbar, dass ein Teil des spät hinzugekommenen Schwefels noch in den Kern gelangt sein könnte. Vorläufige experimentelle Ergebnisse zeigen in der Tat, dass das schwerere Isotop offenbar bei hohem Druck im Eisen-Metall angereichert wird. Die Frage des Schwefelverlustes aus den experimentellen Kapseln muss jedoch noch geklärt werden. Außerdem muss noch das Erreichen des Isotopengleichgewichts getestet werden, bevor konkrete Schlussfolgerungen gezogen werden können.

Im Bericht von Hirschmann wird der Redox-Austausch zwischen der Erdoberfläche und dem Erdmantel analysiert. Das Redox-Budget quantifiziert die oxidierende oder reduzierende Kapazität eines geochemischen Reservoirs auf der Grundlage des Anteils und des Oxidationszustands der wichtigsten Elemente mit variabler Wertigkeit, im Wesentlichen Fe, C und S. Der Wert wird relativ zum vorherrschenden Redox-Zustand im Erdmantel angegeben und ist positiv, wenn ein Reservoir stärker oxidiert ist als der Erdmantel, und negativ, wenn es stärker reduziert ist. Aus dieser Analyse ergeben sich eine Reihe interessanter Erkenntnisse. Das Redox-Budget des Erdmantels ist deutlich größer als das der Oberfläche, aber die Stofftransporte in den und aus dem Erdmantel scheinen sich im Rahmen der Unsicherheiten die Waage zu halten. Die Basalterruptionen der ozeanischen Inseln scheinen jedoch eine stärker oxidierte Quelle im Mantel zu haben, die wahrscheinlich zu groß ist, um durch Subduktion zugeführt worden zu sein, da dies den Redoxhaushalt der Erdoberfläche erschöpft hätte. Dies scheint darauf hinzudeuten, dass es ein primordiales oxidiertes Reservoir gibt, das sich wahrscheinlich im tiefen Mantel befindet.

Die folgende Studie untersucht den Sauerstoffgehalt von Sulfidschmelzen bei hohen Drücken und Temperaturen. Eisen-Nickel-Sulfide sind häufige Einschlüsse in Diamanten, und es wäre nützlich, wenn ihre Zusammensetzung zur Interpretation ihrer Entstehungsbedingungen herangezogen werden könnte. Für einige Sulfideinschlüsse in Diamanten wurden Sauerstoffgehalte angegeben, die darauf hindeuten, dass sie aus Sulfidschmelzen kristallisiert sind. Eine frühere Studie hat gezeigt, dass der Sauerstoffgehalt solcher Schmelzen von der Temperatur und dem Eisenoxidgehalt der koexistierenden Silikate abhängig ist. In dieser Studie wird die Auswirkung des Ni-Gehalts der Sulfidschmelze untersucht und es wird festgestellt, dass er nur einen sehr geringen Einfluss auf den Sauerstoffgehalt hat. Dies ist merkwürdig, da viele Sulfideinschlüsse mit hohem Ni-Gehalt in Diamanten auch einen hohen Sauerstoffgehalt aufweisen. Weitere Untersuchungen der Diamanteinschlüsse selbst sind wahrscheinlich die einzige Möglichkeit, diese Diskrepanz zu klären.

Die Studie von Calvo *et al.* untersucht, ob die Schwefelisotopensignatur des Erdmantels allein durch die Zugabe von außerirdischem Material während des sogenannten 'late veneer'

Ereignisses erklärt werden kann oder ob eine Isotopenfraktionierung zwischen Erdkern und Silikatmantel beteiligt war. Zu diesem Zweck wurden Hochdruck-Experimente zur Fraktionierung von Schwefel-Isotopen zwischen Metall- und Silikat-Schmelzen in Vielstempel-Pressen durchgeführt. Die Ergebnisse sind aufgrund möglicher Ungleichgewichtsprobleme bisher nicht schlüssig.

Es ist immer noch unklar, ob die Mantelmetasomatose in der Lithosphäre durch Silikatschmelzen, Karbonatitschmelzen oder wässrige Fluide verursacht wird. Im Projekt von Shaw wurden Kolben-Zylinder-Experimente durchgeführt, bei denen Spinellperidotite und einzelne Mantelminerale mit Karbonatitschmelzen umgesetzt wurden. Vorläufige Ergebnisse deuten darauf hin, dass das Ca/Al-Verhältnis in Klinopyroxen nicht in der Lage ist, zwischen Karbonatit- und Silikatschmelze als metasomatischem Agens zu unterscheiden.

Rustioni *et al.* untersuchten in Kolben-Zylinder-Experimenten, ob das Vorhandensein von geringen Mengen Phengit und Apatit im Eklogit die Verteilung von Rb, Cs, Sr, Ba und LREE zwischen Gestein und wässrigen Fluiden signifikant beeinflusst. Die Ergebnisse bestätigen, dass sich Rb, Cs, Sr, Ba in Phengit und LREE in Apatit stark anreichern. Die modalen Häufigkeiten dieser beiden Minerale Eklogiten mit MORB-Zusammensetzung sind aber zu gering, um die Verteilungskoeffizienten zwischen Gestein und Fluid signifikant zu beeinflussen.

Die letzten fünf Beiträge befassen sich mit Prozessen in der Erdkruste, insbesondere mit der Bildung von magmatisch-hydrothermalen Erzlagerstätten. Aufgrund der häufigen Verbindung von K-reichen Magmen mit Au-reichen porphyrisch-epithermalen Erzlagerstätten wurde vorgeschlagen, dass K-reiche Magmen entweder ungewöhnlich Au-reich sind oder hohe Au/Cu-Verhältnisse besitzen. Um diese Hypothese zu prüfen, wurde der Metallgehalt von Schmelzeinschlüssen in unterschiedlich entwickelten K-reichen Gesteinen aus mehr als einem Dutzend Vorkommen weltweit mit einem hochempfindlichen LA-ICP-MS-System analysiert. Es stellte sich heraus, dass sowohl die absoluten Au-Gehalte als auch die Au/Cu-Verhältnisse in diesen Schmelzen mit denen von MORB-Schmelzen vergleichbar sind, was die obige Hypothese widerlegt. Wahrscheinlich sind die Au-reichen Erze entweder durch eine bevorzugte Au-Verteilung zwischen Fluid und Schmelze oder eine selektive Metallausfällung aus den hydrothermalen Fluiden entstanden sind.

Porphyrische Cu-(Au, Mo)-Lagerstätten stellen auch große geochemische Schwefelanomalien dar. Der ursprüngliche Schwefelgehalt von Magmen lässt sich jedoch nur schwer rekonstruieren, da der meiste Schwefel in magmatischen Sulfiden und/oder Anhydrit enthalten war. Diese Minerale zersetzen sich oft während der Kristallisation der Magmen. Audétat & Chang zeigen, wie das frühere Vorhandensein von Anhydritkristallen in porphyrischem Gestein anhand von Hohlräumen erkannt werden kann, die räumlich mit Apatit-Mikrokristallen assoziiert sind. Solche Hohlräume wurden in porphyrischen Cu-verwandten Gesteinen im Südwesten der USA sehr häufig gefunden. Es ist jedoch noch unklar, ob das Vorhandensein

von magmatischem Anhydrit ein charakteristisches Merkmal von mineralisierten Systemen oder von Inselbogen-Magmen im Allgemeinen ist.

Gallium wird derzeit ausschließlich als Nebenprodukt aus Sphalerit- und Bauxiterzen gewonnen. Um zu prüfen, ob dieses Element bei magmatisch-hydrothermalen Prozessen signifikant angereichert werden kann, untersuchten Hlede & Keppler die Löslichkeit von Ga in Rhyolithschmelzen und seine Verteilung zwischen Schmelze und Fluid. Die Ergebnisse deuten darauf hin, dass weder die magmatische Fraktionierung noch die Fluid-Schmelze-Verteilung zu einer signifikanten Anreicherung von Ga führt, was wenig Hoffnung auf die Entdeckung magmatisch-hydrothermalen Ga-Lagerstätten lässt. Im Gegensatz dazu wird Zinn fast ausschließlich in magmatisch-hydrothermalen Erzlagerstätten abgebaut. Um die Anreicherung von Zinn besser zu verstehen, untersuchten Wu *et al.* die Sn-Isotopensignatur verschiedener Generationen von Kassiterit in der großen Xianghualing Sn-Lagerstätte in China. Die beobachteten Isotopenvariationen sind wohl hauptsächlich auf eine kinetische Ungleichgewichts-Fraktionierung zurückzuführen. Die Isotopenfraktionierungsfaktoren zwischen Kassiterit und Fluid sind jedoch nicht gut bekannt, weshalb derzeit Experimente in Hydrothermal-Autoklaven durchgeführt werden, um weitere Daten zu erhalten.

3.3 Mineralogie, Kristallchemie und Phasenübergänge

Minerale passen sich an Veränderungen in ihrer geologischen Umgebung an, indem sie ihre chemische Zusammensetzung und im Extremfall ihre Kristallstruktur ändern. Die Mineralchemie und die kristallografischen Merkmale spiegeln daher die physikalisch-chemischen Bedingungen wider, unter denen das Mineral entstanden ist. Um diese Informationen auslesen zu können, ist eine detaillierte Untersuchung natürlicher Proben notwendig. Außerdem muss durch Experimente geklärt werden, welchen Einfluss Druck, Temperatur, Sauerstoffugazität und andere Faktoren auf die Mineraleigenschaften haben. In diesem Abschnitt werden Forschungsprojekte vorgestellt, in denen Mineralproben aus natürlichen Hochdruckgesteinen untersucht oder Hochdruckexperimente durchgeführt wurden. Mit diesen Untersuchungen sollen letztlich Prozesse im Erdinneren besser verstanden werden.

Die ersten Beiträge in diesem Abschnitt befassen sich mit der Kristallchemie von Oxidmineralen und der Post-Spinell-Phasenumwandlung. Die Untersuchung von Xenolithen aus dem Erdmantel ermöglicht wertvolle Einblicke in das Erdinnere. Beltrame *et al.* untersuchen Mineralreaktionen unter Beteiligung von Spinell, um ein neues Geobarometer für Spinell-Peridotit-Xenolithe zu entwickeln. Natürliche Diamanten und ihre Einschlüsse öffnen ein Fenster in den tieferen Erdmantel. Der Gehalt an dreiwertigen Elementen wie Aluminium und Chrom in Oxidphasen wie Ferropiklas und Magnetit kann Aufschluss über die Temperatur und die Bildungstiefe des Wirt-Einschluss-Paares geben. Man *et al.* beschreiben die Löslichkeit von Aluminiumoxid in Periklas, um die Entstehungsbedingungen von sub-lithosphärischen Diamanten zu verstehen, die als Informationsquelle für kohlenstoffhaltige Fluide oder Schmelzen im Erdmantel dienen können.

Hochdruck-Mg-Fe-Oxide der Stöchiometrien M_4O_5 und M_5O_6 können Einschlüsse in Diamanten bilden, zerfallen jedoch bei Druckentlastung in Gemische aus Spinell und anderen Phasen. Die Eisen-Endglieder Fe_4O_5 und Fe_5O_6 enthalten Eisenkationen in zwei Wertigkeitsstufen und könnten als akzessorische Phasen zur Mineralogie des Erdmantels beitragen. Schumann *et al.* beobachteten, dass Fe_4O_5 mehr Chrom einbauen kann als Fe_5O_6 . In Gesteinen mit typischen Cr-Gehalten des Erdmantels würden sich also eher Mischkristalle der Zusammensetzung $Fe^{2+}_2(Fe^{3+},Cr)_2O_5$ bilden. Die Mg-haltigen Gegenstücke dieser Phasen wurde von Woodland *et al.* mit dem ähnlichen Ergebnis untersucht, dass Chrom die M_4O_5 -Phase stark gegenüber der M_5O_6 -Phase bevorzugt. Neben anderen Phasen lässt sich auch Magnetit in Diamanteinschlüssen finden. Die Auswirkungen von Aluminium auf die Stabilität von Magnetit und dessen verwandte Phasen bei hohen Drücken sind jedoch nicht gut erforscht. Uenver-Thiele *et al.* haben experimentell die Phasenbeziehungen für Al-haltige Magnetit-Zusammensetzungen bestimmt. Das daraus resultierende Phasendiagramm hilft, die Mikrostrukturen in Magnetit-führenden Diamanteinschlüssen zu erklären.

In einer Tiefe von 660 km ändern sich die seismischen Wellengeschwindigkeiten im Erdmantel innerhalb eines sehr kurzen Tiefenintervalls erheblich. Diese Diskontinuität in den seismischen Wellengeschwindigkeiten wird häufig mit der Post-Spinell-Phasenumwandlung erklärt, d. h. mit der Dissoziation von Ringwoodit mit Spinellstruktur in die Minerale Bridgmanit und Ferroperiklas des unteren Erdmantels. Die genaue Tiefe der Diskontinuität variiert jedoch mit der geografischen Lage, vermutlich als Funktion der Temperatur des Erdmantels. Durch den Einsatz modernster Hochdruckexperimente gekoppelt mit Synchrotron-Röntgenbeugungsmethoden konnten Chanyshv *et al.* die Phasengrenze der Post-Spinell-Phasenumwandlung sowie dessen Steigung im Druck-Temperatur-Diagramm mit hoher Präzision bestimmen. Sie stellten fest, dass die Steigung für das System FeO-MgO-SiO₂ deutlich steiler ist als für das Fe-freie System MgO-SiO₂. Demzufolge können die Tiefenvariationen der seismischen Diskontinuität in 660 km Tiefe tatsächlich durch Variationen der Manteltemperatur erklärt werden.

Die Stabilität bestimmter Minerale kann Aufschluss über die geochemischen Kreisläufe flüchtiger Elemente wie etwa Kohlenstoff geben. Das organische Mineral Whewellit könnte beispielsweise auf das Vorhandensein abiotisch gebildeter organischer Moleküle in den Fluiden von Subduktionszonen hinweisen. Czekay & Keppler haben die Lösung und Kristallisation von Whewellit in Wasser unter hohen Drücken untersucht, um die Bedingungen zu bestimmen, bei denen Whewellit in Fluiden von Subduktionszonen ausgefällt werden könnte. In seiner oxidierten Form kann Kohlenstoff auch in Karbonaten gebunden sein, von denen viele bei den Drücken und Temperaturen des tiefen Erdmantels stabil bleiben können. Während die Kristallstrukturen der meisten Karbonatminerale auf planaren CO₃²⁻-Gruppen basieren, berichten Dubrovinsky *et al.* über die Synthese und Kristallstruktur einer Magnesiumkarbonatphase, Mg₂CO₄, mit tetraedrischen CO₄⁴⁻-Gruppen. Diese Mg-reiche Tetracarbonat-Phase wurde in Experimenten mit Diamantstempelzellen bei Drücken über 100 GPa beobachtet und könnte Kohlenstoff bei Drücken binden, die denen im unteren Erdmantel entsprechen.

Der Oxidationszustand des Kohlenstoffs und damit die Stabilität der Kohlenstoff-haltigen Minerale im Erdmantel hängen entscheidend von der vorherrschenden Sauerstoff-Fugazität ab. Xenolithe in Kimberliten liefern einzigartige Proben des Erdmantels, mit denen die Sauerstoff-Fugazität während ihrer Entstehung in der Tiefe abgeschätzt werden kann. Marras *et al.* haben die Kristallchemie von Granaten und Klinopyroxenen in xenolithischen Eklogiten analysiert. Auf der Grundlage von Messungen der $\text{Fe}^{3+}/\Sigma\text{Fe}$ -Verhältnisse schließen sie auf eine ungewöhnlich hohe Sauerstoff-Fugazität, die auch durch die Abwesenheit von Diamanten in den Xenolithen untermauert wird und die Variabilität der Sauerstoff-Fugazität im Erdmantel demonstriert. Deutlich tiefer im Erdmantel ist das meiste dreiwertige Eisen vermutlich im Mineral Bridgmanit gebunden. Wang *et al.* untersuchten die Auswirkung des Drucks auf den Gehalt von Eisen(III) in Bridgmanit und stellten fest, dass andere Faktoren wie die Sauerstoff-Fugazität, die Temperatur und der Aluminiumgehalt einen stärkeren Einfluss auf den Gehalt an dreiwertigem Eisen in Bridgmanit haben könnten als der Druck.

Die Bedingungen, unter denen sich ein Mineral gebildet hat, können sich auch in Strukturen auf der Nano- und Mikroskala niederschlagen. Durch den Vergleich von Röntgen- und Elektronenbeugungsmustern von Omphacit-Kristallen aus einem eklogitischen Xenolith entdeckten Fukushima *et al.* Hinweise auf eine unvollständige Kationenordnung, die die komplexe thermische Geschichte des Wirtsgesteins widerspiegeln könnte. Einige Mineralphasen, wie z. B. der Kalziumsilikat-Perowskit Davemaoit, konnten bei Normalbedingungen noch nie beobachtet werden, da sie sich bei Dekompression leicht in amorphe Phasen umwandeln. Dennoch gelang es Miyajima *et al.*, eine Davemaoit-Probe synthetisch herzustellen und zu konservieren, um die Symmetrie- und Gitterparameter bei Normalbedingungen mit Hilfe der Transmissions-Elektronenmikroskopie zu bestimmen. Die konservierten Davemaoit-Domänen behielten ihre kubische Symmetrie und wurden wahrscheinlich durch die sie umgebenden amorphen Ränder und starren Bridgmanit-Körner vor einer Umwandlung geschützt.

3.4 Physikalische Eigenschaften von Mineralen

Die physikalischen Eigenschaften von Mineralien bestimmen eine Vielzahl von Prozessen, die wir auf der Erde und in extraterrestrischen Systemen beobachten können. Hierzu gehören etwa der Transport von Stoffen ins tiefe Erdinnere, das Verhalten von Gesteinen unter mechanischen Spannungen und die Ausbreitung seismischer Wellen in einem Planeten. Die Beiträge in diesem Abschnitt beschreiben das Verhalten von Mineralen in der Erde, auf dem Mars und in den Mutterkörpern achondritischer Meteorite.

Im ersten Beitrag wurden die Grenzflächenwinkel im Olivin-Fluid-System als Funktion von Druck, Temperatur und Fluidzusammensetzung untersucht. Hiermit kann die Geometrie der Poren und die Mobilität von Fluiden im Erdmantel besser bestimmt werden. Der Anteil der facettierten Grenzflächen im Olivin-Fluid-System scheint unabhängig von Druck, Temperatur

und Fluidzusammensetzung zu sein. Tendenziell vergrößert die Facettierung die Grenzwinkel, so dass der für die Perkolation notwendige Fluidanteil zunimmt.

Die nächsten beiden Beiträge untersuchen das Hochdruckverhalten von Mineralen, die flüchtige Stoffe im Erdmantel speichern können. In Beitrag **b** wurden Hochdruckexperimente zur Untersuchung des Stickstoff-Einbaus in Antigorit durchgeführt. Das resultierende Produkt bestand aus einer Mischung aus Olivin, Enstatit und einer N-haltigen Phase, die ein Mischkristall aus Talk und Tobelit zu sein scheint. Diese Phase hat einen kleineren Kompressionsmodul und eine größere Anisotropie als Talk. In Beitrag **c** wurde die Schallwellengeschwindigkeit in Mg-Sursassit untersucht, der sich unmittelbar nach der Destabilisierung von Chlorit in subduzierten ozeanischen Platten bilden kann. Die Messungen wurden mittels Brillouin-Streuung in einem Einkristall durchgeführt, wobei sich eine signifikante Anisotropie der longitudinalen Wellengeschwindigkeit bei Raumdruck zeigte.

Um aus seismischen Beobachtungen Informationen über die Zusammensetzung und Temperaturschwankungen im unteren Erdmantel zu erhalten, sind genaue Daten über das Hochdruckverhalten von Mineralen erforderlich. Der vierte Beitrag dieses Abschnitts beschreibt die Kompressibilität von Natrium-reichen, Aluminium-haltigen Silikaten mit der Ca-Ferrit-Struktur, die eine Hauptphase in subduzierten Metabasalten im unteren Erdmantel sein könnte. Die Studie zeigt, dass der Mg- und Fe-Gehalt den isothermen Kompressionsmodul relativ zum $\text{NaAlSi}_3\text{O}_8$ -Endglied erhöht und dass oberhalb von 25 GPa ein Spin-Übergang in Fe-haltigen Proben auftritt. Im fünften Beitrag wurden Einkristalle von Fe^{2+} -reichem Bridgmanit mittels Röntgenbeugung bei gleichzeitig hohem Druck und hoher Temperatur untersucht, um die thermische Zustandsgleichung dieser Hauptkomponente des unteren Erdmantels zu bestimmen.

Die Geschichte der Erde steht in engem Zusammenhang mit der Geschichte der anderen Planeten und Asteroiden in unserem Sonnensystem. Daher wurden Anstrengungen unternommen, neben den Eigenschaften von Materialien in der Erde auch die Zusammensetzung und Bildung extraterrestrischer Objekte zu verstehen. In den letzten beiden Beiträgen wurden experimentelle Untersuchungen durchgeführt, um die Zusammensetzung des Mars und die Bildung rätselhafter Texturen in den Fe-reichen Phasen der Achondrite aufzuklären. In Beitrag **f** wurden Einkristalle eines synthetischen Fe-reichen Ringwoodits mit einer im Marsmantel erwartbaren Zusammensetzung mittels Brillouin-Streuung in Verbindung mit einem CO_2 -Laserheizsystem untersucht. Die gemessenen akustischen Wellengeschwindigkeiten können verwendet werden, um die seismische Signatur dieses Materials mit den Daten zu vergleichen, die vom Seismometer des NASA-InSight-Landers aufgezeichnet werden. Im letzten Beitrag wurde die in einem vereinfachten analogen System (Olivin, Troilit und Gold) bei hoher Temperatur und hohem Druck erzeugte Textur mit der von Fe-reichen Phasen in primitiven Achondriten verglichen. Dies zeigt, dass solche Texturen nicht auf ein Gleichgewicht bei hoher Temperatur zurückzuführen sind, sondern auf Erholungsprozesse während der langsamen Abkühlung der Asteroiden, von denen die Achondriten stammen.

3.5 Fluide, Schmelzen und ihre Wechselwirkung mit Mineralen

Luft besteht überwiegend aus Stickstoff (78 % N₂) und lange Zeit wurde angenommen, dass die Atmosphäre das größte Stickstoff-Reservoir auf der Erde ist. Dies würde dann auch bedeuten, dass Stickstoff relativ zu anderen leichtflüchtigen Elementen, wie Wasserstoff oder Kohlenstoff auf der Erde anomal verarmt ist. Arbeiten am Bayerischen Geoinstitut haben in den letzten Jahren jedoch gezeigt, dass Stickstoff im unteren Erdmantel stark angereichert sein könnte. Nur weil dieses Reservoir so unzugänglich ist, entsteht vielleicht der Eindruck einer Verarmung von Stickstoff auf der Erde, die möglicherweise gar nicht existiert. Der erste Beitrag in diesem Kapitel beschreibt neue Ergebnisse, die diese These unterstützen. In Hochdruckexperimenten, in denen eigentlich die Löslichkeit von Stickstoff in Bridgmanit untersucht werden sollte, wurde auch etwas Eisen-reicher Magnesiowüstit (Fe,Mg)O gebildet. Chemische Analysen zeigten dann spektakulär hohe Stickstoff-Gehalte in diesem Mineral, mit Werten bis über 10 Gew. %. Anscheinend gibt es bei den hohen Drücken in diesen Experimenten eine ausgedehnte Mischkristallbildung zwischen (Fe,Mg)O und FeN. In der frühen Erdgeschichte hat dieser Effekt möglicherweise zu einer starken Anreicherung von Stickstoff im untersten Mantel geführt, unmittelbar oberhalb der Kern-Mantel-Grenze. Hier existieren Bereiche von extrem niedrigen seismischen Geschwindigkeiten, die wahrscheinlich mit Eisen-reichem Magnesiowüstit angereichert sind, der bei der Kristallisation eines tiefen Magmenozeans hier abgelagert wurde. Dies wäre daher ein Mechanismus, durch den der größte Teil des Stickstoffs auf der Erde in einer dünnen Lage oberhalb des Erdkerns konzentriert worden sein könnte.

Neben dem Mantel könnte der Kern auch ein wichtiges Reservoir von flüchtigen Elementen im Erdinnern sein. Entsprechende Experimente unter den Druck- und Temperatur-Bedingungen des Kerns sind jedoch extrem schwierig. Der nächste Beitrag in diesem Kapitel nutzt daher molekular-dynamische Simulationen unter Verwendung von zwischenatomaren Potentialen aus neuronalen Netzwerken, um die Verteilung von Wasserstoff zwischen dem festen inneren Kern und dem flüssigen äußeren Kern zu bestimmen. Die Daten zeigen, dass Wasserstoff in der Schmelze relativ zum Feststoff nur etwa um einen Faktor zwei angereichert ist. Wasserstoff könnte daher sowohl im inneren als auch im äußeren Kern zu dem bekannten Dichtedefizit beitragen.

Im Erdmantel liegt "Wasser" überwiegend als OH-Defekte in Mineralen vor. Obwohl diese Defekte nur in geringen Konzentrationen vorkommen, stellen sie doch ein erhebliches Wasser-Reservoir dar und beeinflussen die physikalischen Eigenschaften des Mantels. Zwei Beiträge untersuchen daher Wasser in Mantel-Mineralen. Olivin ist das häufigste Mineral im oberen Mantel und zeigt oft komplexe Infrarot-Spektren, die auf mehrere verschiedene Typen von OH-Gruppen in der Struktur hindeuten. Die "Gruppe-II-Banden" zwischen 3250 und 3400 cm⁻¹ wurden oft OH-Defekten zugeordnet, die mit Fe³⁺ assoziiert sind. Diese Interpretation ist aber etwas problematisch, da man diese Banden auch in Proben sehen kann, die unter stark reduzierenden Bedingungen gebildet wurden. Hier sollte die Konzentration von Fe³⁺ im Olivin verschwindend gering sein. In einem Projekt wurden nun die Infrarot-Spektren von Olivin-

Kristallen gemessen, die mit unterschiedlichen Spurenelementen dotiert wurden. Die Resultate zeigen, dass die "Gruppe-II-Banden" von OH-Gruppen verursacht werden, die an Cr^{3+} gekoppelt sind. Ein weiterer Beitrag beschäftigt sich mit der Löslichkeit von Wasser in Al-freiem Stishovit und stellt fest, dass dieses Mineral wahrscheinlich nur wenig zum Transport von Wasser in den tiefen Mantel beiträgt.

Die Entwässerung von wasserhaltigen Mineralen in subduzierten Platten setzt Fluide frei, die dann nach oben wandern und die Bildung von Schmelzen im Mantel-Keil verursachen. Auf welche Art und wie schnell sich diese Fluide bewegen, ist aber wenig untersucht. Zwei Beiträge liefern hier neue experimentelle Resultate. Multi-Anvil-Experimente wurden so ausgeführt, dass sich auf einer Seite einer Probe eine Fluid-Quelle befand, auf der anderen Seite ein Absorber. Permeabilitäts-Messungen mit dieser Methode zeigen, dass Wasser sich entlang der Korngrenzen eines polykristallinen Olivin-Aggregats nur langsam bewegt, über Entfernungen von nur etwa einem Meter während einer Million Jahre und bei einer Temperatur von $700\text{ }^{\circ}\text{C}$. Sehr wahrscheinlich ist eine Art von fokussiertem Fließen erforderlich, um die Fließgeschwindigkeit in der Natur zu erhöhen. Vorläufige Experimente zeigen jedoch auch, dass Wasserstoff (H_2) unter stärker reduzierenden Bedingungen wesentlich mobiler ist.

Die (wasserfreie) Schmelztemperatur des oberen Mantels ist ziemlich gut bekannt. Im Vergleich dazu sind die Phasenbeziehungen im mittleren Teil des Mantels wesentlich weniger gesichert. In einem Projekt wurden technische Neuentwicklungen, wie Öfen mit verschwindend geringem Temperaturgradienten benutzt, um Solidustemperaturen im mittleren Mantel mit Multi-Anvil-Experimenten zu bestimmen. Die gemessenen Werte sind 45 bis $60\text{ }^{\circ}\text{C}$ niedriger als bisher angenommen. Die letzten beiden Beiträge in diesem Kapitel beschäftigen sich mit der Viskosität von Silikatschmelzen. Frühere Messungen der Viskosität von Andesit-Schmelzen waren möglicherweise fehlerhaft, da während der Messung nano-Kristalle von Eisen-Titan-Oxiden gebildet wurden. Existierende Modelle für die Viskosität natürlicher Schmelzen haben oft das Problem, dass es eine Lücke gibt im Bereich der Viskositäten, die im Labor gemessen werden können. Diese Lücke wurde nun geschlossen mit Hilfe von "synthetischen Daten", die durch ein künstliches neuronales Netzwerk erzeugt wurden. Neue Modelle, die mit diesen Daten kalibriert wurden, können nun auch physikalisch plausible Viskositäten in einem Bereich vorhersagen, der durch direkte Messungen nicht zugänglich ist.

3.6 Rheologie und Metamorphose

Die Rheologie von Gesteinen und Mineralen unter den hohen Temperaturen und Drücken des Erdinneren ist für das Verständnis der dynamischen Prozesse in unserem Planeten von entscheidender Bedeutung. Die kritischen rheologischen Parameter Spannung und Verformungsgeschwindigkeit bestimmen die Fließgesetze und die Viskosität des Gesteins. Sie stellen jedoch eine experimentelle Herausforderung dar, da es schwierig ist, den Umschließungsdruck und die deviatorischen Spannungen separat zu bestimmen (siehe auch

Methodische Entwicklungen). Daher wurden am BGI im letzten Jahr auch alternative Ansätze verfolgt, wie z. B. geodynamische Simulationen verschiedener Deformationsprozesse oder auch die experimentelle Bestimmung der Selbstdiffusion als Geschwindigkeits-bestimmender Prozess während der Verformung.

In den ersten drei Beiträgen dieses Kapitels werden 1- und 2-dimensionale Computermodelle verwendet, um die schnelle duktile Verformungslokalisierung in Kombination mit thermischer Rückkopplung ('thermal runaway') in Olivin als möglichen Erdbebenmechanismus in großen Tiefen zu verstehen. Hier sind die Temperaturen zu hoch, um die für Erdbeben charakteristische spröde Verformung zuzulassen. Die Simulationen zeigen, dass eine Störung durch eine solche thermische Rückkopplung erzeugt werden kann, sofern ein bestimmter Festigkeitskontrast zwischen der gestörten Region und dem umgebenden Gestein entsteht. Darüber hinaus kann ein großer Erdbebenherd durch denselben thermischen Prozess erzeugt werden, indem sich eine Serie kleiner gestörter Regionen aneinanderreicht. In den gestörten Regionen verformt sich das Material dabei vorwiegend durch Versetzungskriechen, während im umgebenden Gestein Niedertemperatur-Plastizität vorherrscht. Im dritten Beitrag wird das Potenzial eines Phasenübergangs zwischen Olivin und Ringwoodit für die Auslösung eines Erdbebens durch thermische Rückkopplung rechnerisch als Funktion verschiedener Parameter untersucht. Die Simulationen zeigen, dass eine lokale Überhitzung bei hohen Anfangsspannungen, schnellen Reaktionszeiten, höheren Temperaturen und kleineren Korngrößen nach dem Phasenübergang wahrscheinlicher wird.

Im vierten Beitrag wurde die Mantelkonvektion über die letzten 4,5 Ga seit der Entstehung der Erde in einem geodynamischen Modell simuliert. Hierbei wurde der Einfluss der Korngrößenentwicklung im oberen und unteren Mantel sowie das Diffusionskriechen als dominierender Deformationsmechanismus berücksichtigt. Die Ergebnisse zeigen, dass zumindest für lange Zeitskalen die Korngröße einen bemerkenswert geringen Einfluss auf die Gesamtviskosität, Temperatur und Mobilität des konvektiven Mantels hat.

In den beiden folgenden Beiträgen werden experimentelle Ergebnisse vorgestellt, die tiefgreifende Konsequenzen für die Rheologie des unteren Erdmantels haben. Im fünften Beitrag wird die statische Erholung der experimentell verformten Kornstruktur der Mantelparagenese Bridgmanit-Magnesiowüstit untersucht, um festzustellen, ob Bridgmanit oder Magnesiowüstit die Festigkeit des Gesteins bestimmen. Die Ergebnisse deuten darauf hin, dass der vermutlich festere Bridgmanit ein die Spannung übertragendes Gerüst bildet und somit die Viskosität des unteren Mantels bestimmt. Im folgenden Projekt wurde die Diffusionsgeschwindigkeit von Silizium in Bridgmanit unter Bedingungen des unteren Erdmantels gemessen. Sie hat einen entscheidenden Einfluss auf die Fließgesetze für dieses Mineral, da wahrscheinlich die Diffusion von Silizium der geschwindigkeitsbegrenzende Faktor beim Hochtemperatur-Kriechen ist. Die resultierenden Diffusivitäten und daraus abgeleiteten Viskositäten für Bridgmanit stimmen gut mit denen aus geophysikalischen Daten überein.

Der letzte Beitrag zeigt die Komplexität des Zusammenspiels von Gesteinsverformung und Mineralreaktionen an dem natürlichen Beispiel eines Hochdruck-Mylonits aus der Sesia-Zone in den südlichen Alpen. Sehr detaillierte mikrostrukturelle Untersuchungen demonstrieren, dass der Reaktionsverlauf eng mit der plastischen Verformung (und umgekehrt) verbunden ist, was die Interpretation der tatsächlichen p,T-Verformungsgeschichte des Gesteinskomplexes erschwert.

3.7 Materialwissenschaften

Eine Kombination aus Hochdrucktechnologie, modernen Einrichtungen zur Probencharakterisierung und hoher Fachkompetenz ermöglicht anspruchsvolle Forschung in Materialphysik und Materialchemie am Bayerischen Geoinstitut. In diesem Abschnitt des Jahresberichts werden Studien über eine Vielfalt neuartiger Materialien vorgestellt, die unter extremen Bedingungen synthetisiert wurden und interessante Veränderungen im chemischen Verhalten aufweisen.

Eisen bildet eine Serie von Oxiden mit gemischtem Oxidationszustand. Der erste Beitrag untersucht die Eigenschaften eines dieser Oxide, Fe_4O_5 , das aus geologischer, chemischer und physikalischer Sicht von großem Interesse ist. Anhand von Röntgenabsorptionsspektren wird gezeigt, dass Fe_4O_5 eine halbmetallische Leitfähigkeit aufweist, die eine für Metalle typische hohe Ladungsträgerkonzentration mit einer für Halbleiter charakteristischen niedrigen elektrischen Leitfähigkeit kombiniert. Yttriumbromid YBr_3 ist ein weiterer Halbleiter, der unter Hochdruck- und Hochtemperaturbedingungen synthetisiert wurde. Bei Dekompression verwandelt sich dessen 3D-Gerüst in eine Schichtstruktur mit Halbleitereigenschaften und niedriger Exfoliationsenergie. Diese YBr_3 Phase erweitert die Liste und unser Verständnis von geschichteten dreiwertigen Halogeniden auf Basis von Seltenerdmetallen und zeigt, wie hoher Druck strukturelle Motive und physikalische Eigenschaften verändern kann.

Auch Karbide kommen regelmäßig im materialwissenschaftlichen Teil des Jahresberichts vor. Der dritte Beitrag berichtet über neuartige Hochdruck-Dysprosiumkarbide mit verschiedenen Stöchiometrien und einzigartigen Kohlenstoffanordnungen. Diese Seltenerdkarbide wurden in einer Diamantstempelpresse hergestellt und weisen vielfältige Strukturen mit unterschiedlichen Bindungen auf, die unser Verständnis der Karbidchemie erheblich erweitern. Obwohl sie noch nicht zu Umgebungsbedingungen stabilisiert werden konnten, deuten Berechnungen mit Hilfe der Dichtefunktionaltheorie auf eine dynamische Stabilität dieser Dysprosiumkarbide bei Umgebungsdruck hin, was eine Abschreckung zu Normalbedingungen möglich erscheinen lässt. Kohlenstoff spielt auch im vierten Beitrag eine wichtige Rolle. Hier ermöglicht die Hochdruck-Synthese die Stabilisierung des CN_3^{5-} (Guanidinat) Anions, was zu einer neuen Klasse von anorganischen ternären Metall-Kohlenstoff-Stickstoff-Verbindungen führt: Mehrere isostrukturelle Lanthanit (Ln)-Oxoguanidinate $\text{Ln}_3\text{O}_2(\text{CN}_3)$ wurden erfolgreich synthetisiert. Ihre Kristallstrukturen wurden mit Einkristall-Röntgenbeugung am Synchrotron

bestimmt, unterstützt durch Röntgenabsorptionsmessungen und Elektronenstrukturberechnungen. Außerdem kann das CN_3^{5-} Guanidinat-Anion in diesen Verbindungen bei Normaldruck erhalten werden. Der nächste Beitrag über ein kohlenstoffbasiertes Material macht den Schritt zu einer organischen Verbindung, C_{14}H_8 -Anthracen und untersucht deren Hochdruckverhalten. Hier wird die molekulare Fischgrätenstruktur bis zu ~ 42 GPa beibehalten. Oberhalb von diesem Druck deutet das Fehlen eines Beugungsmusters in der Einkristall-Röntgenuntersuchung auf Amorphisierung hin.

Strukturelle Umwandlungen im Mischkristall $(1-x)\cdot\text{Na}_{0.5}\text{Bi}_{0.5}\text{TiO}_3-x\cdot\text{BaTiO}_3$ (NBT- x BT) mit Perowskit-Struktur, einem bleifreien Ferroelektrikum von potenziellem industriellem Interesse, wurden an einer rhomboedrischen/tetragonalen Phasengrenze untersucht. Subtile strukturelle Veränderungen können bei hohem Druck verstärkt werden und deren Charakterisierung kann dazu beitragen, die allgemeinen Prozesse beim Übergang zu erhellen. Im letzten Beitrag werden Daten aus der Hochdruck-Röntgenbeugung und Raman-Spektroskopie für den oben genannten Mischkristall mit $x = 0.048$ vorgestellt, die signifikante Veränderungen im Kompressionsmechanismus der Struktur aufzeigen. Dies schließt mehrere Umwandlungen ein, die für das Verständnis der Elastizität und strukturellen Stabilität von NBT- x BT wichtig sind.

3.8 Methodische Entwicklungen

Seit seiner Gründung im Jahr 1986 ist das Bayerische Geoinstitut (BGI) stets führend in der Entwicklung und Verbesserung von Methoden zur Erforschung des Erdinneren gewesen. Dazu gehören die Erfindung neuer experimenteller Geräte und Techniken sowie wesentliche Verbesserungen bestehender Methoden. Diese Fortschritte haben sich tiefgreifend auf unser Verständnis des Erdinneren ausgewirkt und die Untersuchung von Geomaterialien unter extremen Bedingungen ermöglicht, die zuvor unerreichbar waren.

Die ersten beiden Studien konzentrieren sich auf die Messung der Elastizität von Mineralen bei hohem Druck unter Verwendung von Diamant-Stempelzellen. Buchen *et al.* zeigen, dass auch unter hohem Druck die aus der Röntgenbeugung abgeleitete elastische Verformung von Mineralaggregaten direkt mit einer angelegten Spannung bei seismischen Frequenzen korreliert werden kann. Dadurch können die seismischen Eigenschaften solcher Aggregate deutlich besser bestimmt und mit geophysikalischen Daten aus dem Erdinneren verglichen werden. Heidelberg *et al.* untersuchen die Auswirkungen extremer p,T-Bedingungen auf die Orientierung und chemische Homogenität von Ringwoodit-Einkristallen und zeigen, dass die Messung elastischer Eigenschaften mithilfe der Brillouin-Spektroskopie in der Diamant-Stempelzelle an Einkristallen bei hohen Temperaturen und Drücken sinnvoll durchführbar ist.

Die folgenden Studien befassen sich mit der Bestimmung der Sauerstoff-Fugazität in experimentellen und natürlichen Umgebungen mithilfe von Legierungen oder Mineralen. Hirschmann & Zhang stellen eine neue Kalibrierung für die Aktivität von Fe in festen und

geschmolzenen FePt-Legierungen vor, die üblicherweise als Sensoren für die Sauerstoff-Fugazität in Hochdruck-Temperaturexperimenten verwendet werden. Diese Kalibrierung ist für Experimente anwendbar, bei dem eine geschmolzene FePt-Legierung mit einer eisenhaltigen Silikatschmelze unter extremen Bedingungen ins Gleichgewicht gebracht wird. Whitney *et al.* untersuchen die Rolle von Lawsonit- und Epidotmineralen beim Redox- und Intraplatten-Massentransfer. Sie weisen darauf hin, dass die Orientierung ein wichtiger Parameter bei der XANES-Analyse bestimmter Minerale für die Bestimmung des $\text{Fe}^{3+}/\Sigma\text{Fe}$ -Verhältnisses und folglich der Sauerstoff-Fugazität ist.

Die beiden folgenden Beiträge befassten sich mit der Analyse von Proben, die mit Vielstempelpressen bei hohem Druck und hoher Temperatur hergestellt werden. Bondar *et al.* vergleichen die Sekundärionen-Massenspektrometrie (SIMS) und die elastische Rückstoßdetektionsanalyse (ERDA) für die Messung von Wasserstoff in verschiedenen Silikatgläsern. Sie unterstreichen in ihrem Beitrag den ausgeprägten Matrixeffekt bei der SIMS-Analyse. Timoner *et al.* setzten SEM-EDS mit besonders niedrigen Beschleunigungsspannungen für die hochauflösende chemische Analyse von Al-Bridgmanit und Fe-haltigen Mineralen ein, wobei eine räumliche Auflösung erreicht wurde, die der von Elektronenmikrosonden überlegen ist. Diese Technik ist besonders vorteilhaft für die experimentelle geowissenschaftliche Forschung, wo die geringe Kristallgröße von Hochdruckproben oft eine große analytische Herausforderung darstellt.

In den drei nächsten Beiträgen werden verbesserte Hochdruckzellen für Experimente mit Vielstempelpressen beschrieben. Han & Katsura schlagen eine neue Konstruktion für die Messung der elektrischen Leitfähigkeit bei den extremen Drücken und Temperaturen des unteren Erdmantels vor. Kubik *et al.* rekalibrierten die Temperaturen in sogenannten Kastenofen-Experimenten in der Vielstempelpresse und konnten so die thermischen Gradienten erheblich reduzieren, was besonders für Experimente zur Kalibrierung chemischer Reaktionen wichtig ist. Dolinski *et al.* zeigen, dass die Verwendung von Piezokristallen als Spannungssensoren in Hochdruck-Verformungsexperimenten mit der Sechstempel-Presse quantitative Resultate liefert, die mit denen aus der *in situ* Röntgenbeugung an Synchrotronanlagen vergleichbar sind. Der letzte Beitrag von Howard *et al.* dokumentiert die Fortschritte beim Aufbau einer Hochdruck-Neutronenstrahlanlage am Forschungsreaktor FRM II in Garching. Eine komplexe Anordnung von 2D-Detektorbänken in einem möglichst breiten Bereich von Streuwinkeln wurde eingerichtet und kalibriert, um eine optimale Nutzung der eingesetzten Neutronen sicher zu stellen.

3. Research Projects

3.1 Earth and Planetary Structure and Dynamics

With almost 5600 known exoplanets and the advent of high-resolution observations enabled by the new James Webb Space Telescope (JWST), it becomes possible to observe and study various stages of planetary evolution in detail. In the first contribution, Golabek and colleagues use global-scale numerical models to study the magma ocean evolution on tidally locked super-Mercury GJ 367 b. Results can be compared with the JWST observations of this planet, providing insight into the otherwise inaccessible magma ocean stage of young terrestrial planets.

Impact cratering is the predominant geological process observed on most planetary surfaces in the Solar System. For planetary bodies smaller than approximately 100 km in diameter, impact cratering is virtually the only surface process that has occurred since their formation. Even on larger bodies like the Moon, which has experienced significant volcanic activity, impact basins dominate the large-scale topography. Deciphering the history of planetary formation and impact events is challenging because radiometric geochronology methods are based on isotopic equilibrium at the time of the event. The records of planetary processes, such as igneous crystallisation, may be affected by secondary events such as high-energy planetary impacts. Most of the energy involved in impacts is rapidly deposited and primarily contributes to processes like mechanical deformation and physical displacement of materials, which appear not to affect isotopic records. In the second contribution, Zhao and colleagues investigate an ordinary chondrite melt breccia meteorite containing large and slowly cooled impact melt clasts. Shock deformation is also identified throughout the breccia suggesting several impact events. Using geochemistry and oxygen isotopic analyses, the authors establish that these clasts formed from complete melting of the chondritic host and that they were subsequently mixed together on the meteorite parent body. The Pb-Pb ages of phosphates only found in the chondrite host do not permit to discriminate between thermal metamorphism or an early impact event. In the third contribution, Greer and colleagues employ the atom probe tomography technique to investigate the effects of shock on the Pb isotope distribution at the nanoscale, which may modify the Pb-Pb ages of shocked zircons.

The oldest parts of the Earth's lithosphere are cratons and most of them have remained undeformed for several billion years; a rare example of craton destruction is the North China craton. In the fourth contribution, Paul and colleagues use 2D regional-scale numerical models to test various craton destruction scenarios and conclude that water release from a subducting slab that causes metasomatism and lithospheric dripping is an efficient way to weaken and finally destroy a craton.

Continent-continent collisions, responsible, for example, for the Himalayan and Alpine orogeny, involve a stage of slab detachment. This tectonic event causes significant topographic

changes at the surface and sedimentary infill of basins. In the fifth contribution, Eskens and colleagues combine regional-scale geodynamic models with sedimentary models to study the case of the Austrian foreland basin, demonstrating a good fit with available seismic data for this region. In a related study, Piccolo and colleagues use 3D regional-scale models to study the physical processes controlling slab detachment and show that the slab curvature has an important effect on the detachment timescale. Finally, the authors show that different detachment scenarios can be distinguished based on surface observations.

Both the composition and physical condition of planetary cores influence the magnetic field generation, shielding the planetary surface from solar and galactic cosmic rays. In the final contribution, Kleinschmidt *et al.* use *ab initio* simulations to constrain the electrical and thermal conductivities of iron phases at conditions of the Earth's core. They find discrepancies between their simulations and experimental data that increase with pressure and temperature and that may be linked to sample geometry used in some of the experiments. They deduce that as the thermal conductivity of the inner core is significantly larger than in the outer core, heat is conducted efficiently, and the Earth's solid inner core is likely not convecting.

a. *Magma oceanography of the dense, ultrashort-period sub-Earth GJ 367b (G.J. Golabek, T. Lichtenberg/Groningen and P.J. Tackley/Zurich)*

The dawn of high-resolution observations with the James Webb Space Telescope will enable spatially resolved observations of ultrashort-period rocky exoplanets. Some of these planets orbit so closely to their star that they lack an atmosphere, which gives direct access to their surfaces and opens a window to infer their geodynamics. The physical parameters of the ultrashort-period sub-Earth GJ 367b have been observationally constrained to a planetary radius of about 0.72 to 0.75 Earth-radii and a mass between 0.48 and 0.55 Earth-masses, implying a density of 6200 to 8500 kg/m³, which puts this planet in a Mercury-like interior regime with a thin mantle overlying a fractionally large core.

The dayside temperature ranges between 1500 to 1800 K, thus suggesting the presence of a permanent magma ocean or dayside magma pond on the surface, induced by stellar irradiation. The large uncertainty on the age of the stellar system, between 30 Myr and about 8 Gyr, however, introduces severe uncertainties related to the compositional and thermal evolution of the planetary mantle. We performed global 2D spherical annulus StagYY simulations of solid-state mantle convection and surface melting to constrain the geometric and compositional properties of the planet. Constraining the spatial dimensions of thermodynamic properties of partially molten, atmosphere-less planets like GJ 367b offers unique opportunities to constrain the compositional fractionation during magma ocean epochs and provides avenues to constrain the delivery and loss cycle of atmophile elements on strongly irradiated exoplanets.

b. The origin and impact history of ordinary chondrite melt breccia Northwest Africa 12520 (R. Zhao and A. Bowvier; M. Trierloff, W.H. Schwarz and T. Ludwig/Heidelberg)

Northwest Africa (NWA) 12520 is an LL6 ordinary chondrite melt breccia. The meteorite consists of unmelted chondritic material and centimeter-size impact melt rock (IMR) clasts (Fig. 3.1-1A), the origin of which is unknown. Shock-induced melt veins were identified within a chondritic clast and in between the chondrite and impact melt lithologies. These veins contain relict olivine and low Ca-pyroxene. High-pressure polymorphs (*e.g.*, ringwoodite, majorite) were not identified in the shock veins in the matrix of the chondritic clast. The strong mosaicism and planar deformation fractures in olivine and the partially isotropic plagioclase in the chondritic clast matrix suggest that the shock stage of the chondritic clast should be S4 (on a scale of S1 to S6).

The composition of olivine in the chondrite host is homogeneous with $Fa_{30.2\pm 0.3}$. The olivine in the impact melt clast is chemically zoned from core to rim (Fig. 3.1-1B) with corresponding compositional variations from $Fa_{15.0\pm 1.5}$ to $Fa_{33.6\pm 2.8}$, respectively. The triple oxygen isotopic compositions of olivine were measured by SIMS Cameca 1280-HR at Heidelberg University. The olivine analyses in the impact melt clast ($n=23$) have on average $\delta^{18}O=+4.45$ (2SE= $\pm 0.13\%$), $\delta^{17}O=+3.52$ (2SE= $\pm 0.10\%$), $\Delta^{17}O=+1.17$ (2SE= $\pm 0.05\%$). The chondrite clast olivines ($n=11$) have on average $\delta^{18}O=+5.90$ (2SE= $\pm 0.10\%$), $\delta^{17}O=+4.44$ (2SE= $\pm 0.08\%$), $\Delta^{17}O=+1.33$ (2SE= $\pm 0.06\%$). These oxygen isotopic compositions combined with elemental geochemistry indicate that the impactor has modified the oxygen isotopic composition of the protolith (if similar to the host rock).

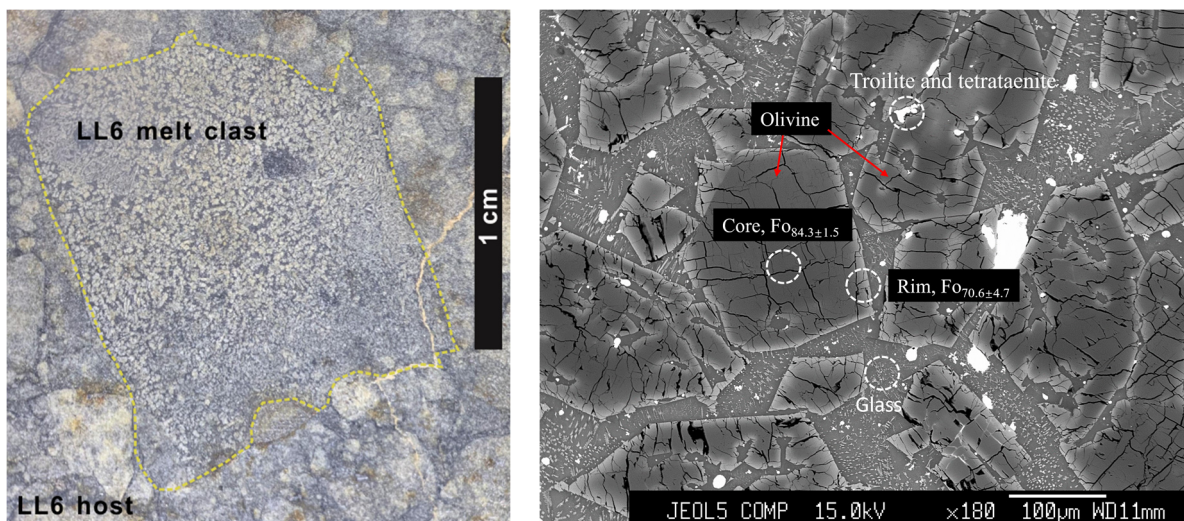


Fig. 3.1-1: (left) Hand specimen of NWA 12520 showing the impact melt clast and host LL6 ordinary chondrite melt breccia. (right) High magnification backscattered electron image of the impact melt rock clast. Fo number of core and rim of olivine are 84.3 ± 1.5 ($n=10$) and 70.6 ± 4.7 ($n=9$), respectively, n is the number of analyses using EPMA.

We also measured by SIMS the Pb-Pb ages of Ca-phosphates (apatites and merrillites) found in the chondrite host and near shock veins. We find an average age of 4547 ± 13 Ma (2SE) (Fig. 3.1-2), which is older than the Ar-Ar impact ages of 0.20 to 4.42 Ga of LL ordinary chondrite breccias reported in the literature. This age could therefore be associated with thermal

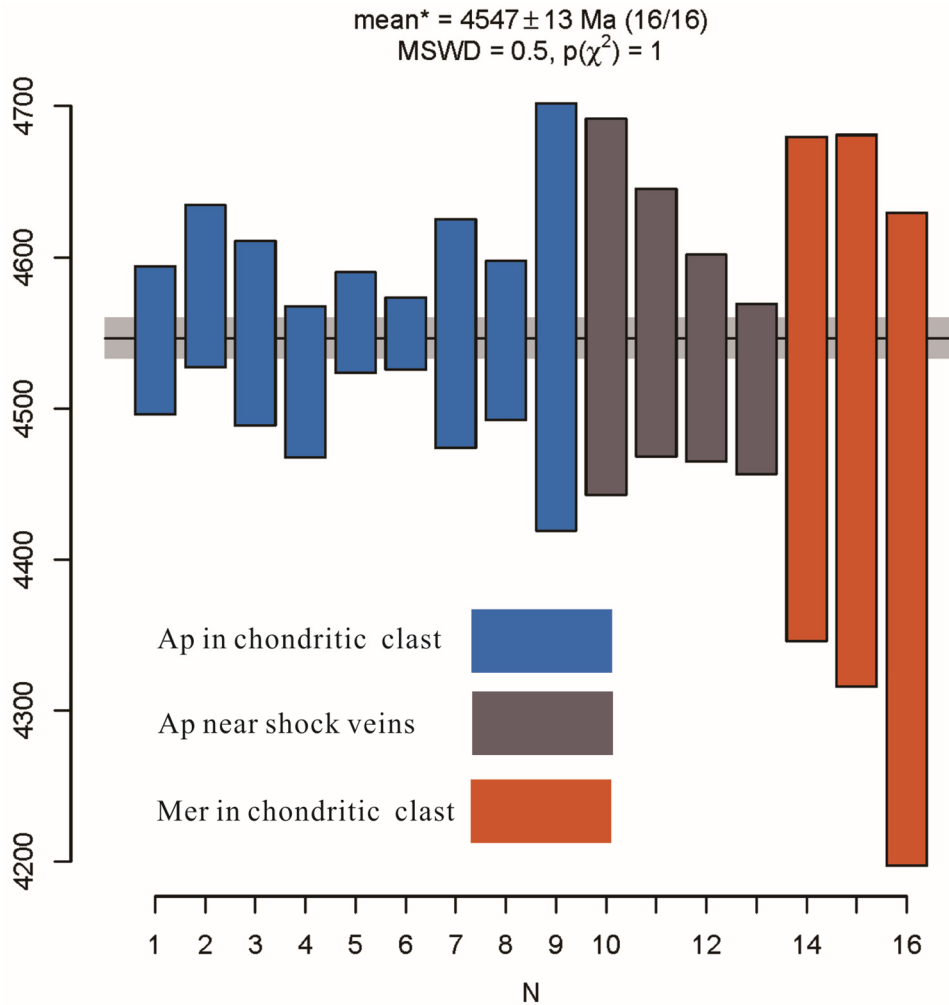


Fig. 3.1-2: ^{207}Pb - ^{206}Pb age distribution of apatite and merrillite in LL6 chondrite melt breccia NWA 12520 and their weighted mean age. Ap = apatite, Mer = merrillite.

metamorphism on the chondrite parent body before impact metamorphism and melting. Three main shock events were identified in NWA 12520 (Fig. 3.1-3). During the first shock event, parts of the parent body were completely melted and then cooled to form the olivine-bearing impact melt rock. In a subsequent shock event, chondritic rock and impact melt rock clast were shocked, fragmented, and mixed together. A third shock event formed the melt veins found locally and crossing in both the chondritic clasts and between the chondritic and impact melt rock clasts. Additional mass-independent isotopic analyses and chronological data may shed light on the source reservoir of the impactor and timing of the shock events, respectively.

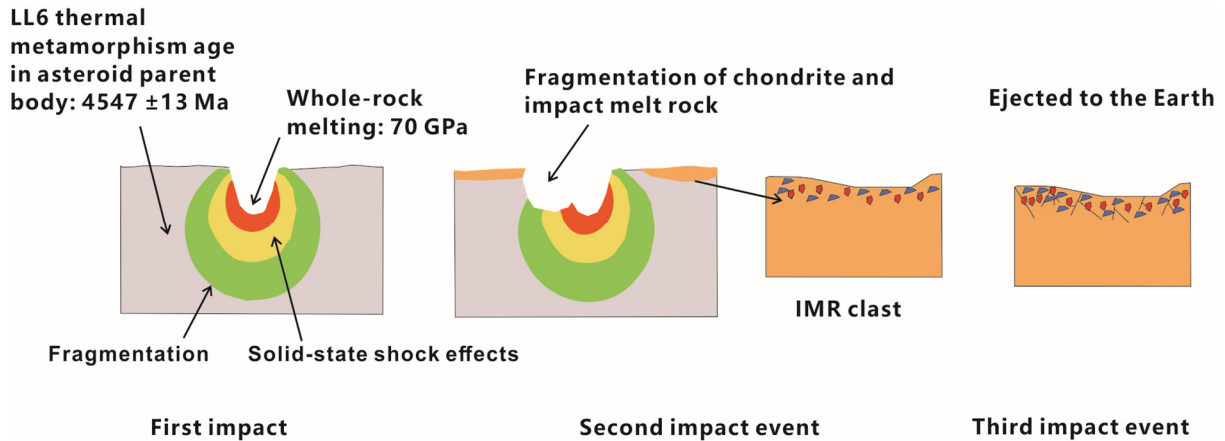


Fig.: 3.1-3: Schematic cross-section of part of impact crater on parent body of LL6 chondrite. At least three shock events were recorded in NWA 12520 melt breccia.

c. 4.46 Ga zircons anchor chronology of lunar magma ocean (J. Greer and P.R. Heck/Chicago, B. Zhang/Los Angeles, D. Isheim and D.N. Seidman/Evanston, A. Bouvier)

Uranium-lead geochronology of zircons is an important tool for constraining the timescales of planetary processes. Lead mobility during secondary processes has been shown to create spurious U-Pb and Pb-Pb ages. Six NanoSIMS analyses of micro-zircon from the Civet Cat norite clast in Apollo 17 impact melt breccia 72255 yielded an average $^{207}\text{Pb}/^{206}\text{Pb}$ age of 4453 ± 34 Ma. This is the oldest lunar zircon age dated so far but it could be the result of unsupported radiogenic Pb clusters at sub-micrometer scale. We used atom-probe tomography (APT) to investigate the nanoscale distribution of trace elements Pb, Y, and Hf in one of the oldest zircons in 72255 (Fig. 3.1-4) to better understand the nanoscale features of this zircon and provide further constraints on the significance of the Pb-Pb age of the zircons. In APT, atoms are field-evaporated from the surface of a sample and analysed by a position-sensitive time-of-flight mass spectrometer, allowing for the detection of individual isotopes, as well as the position of ions in three dimensions. The technique has previously been used to study extraterrestrial and terrestrial zircons, e.g., from other Apollo 17 samples, Martian meteorites and the Jack Hills conglomerate from Western Australia.

A $1 \mu\text{m}$ by $10 \mu\text{m}$ lamella was lifted out from zircon Z14 of Apollo 17 thin section 72255,123 (Z14 pit #1 = 4457 ± 47 Ma, pit #2 = 4399 ± 46 Ma), encompassing the pits left by SIMS analysis that did not overlap with metamict zones (based on CL images). Five nanotips, prepared using established APT sample preparation methods were analysed with the LEAP 5000XS tomograph at the NUCAPT facility of Northwestern University. Instrumental conditions were chosen to maximize sample stability as well as minimize thermal noise due to laser heating.

Three of the five nanotips yielded data (Fig. 3.1-5), for a total of ~ 50 M ions and a length of ~ 500 nm. These three nanotips are all sourced from the same SIMS pit #2, and are laterally

separated by about 1 μm . In two of the nanotips, large thermal tails in the mass spectra resulted in a detection limit of ~ 1 at. %. In nanotip A, less abundant species were detected, including ^{89}Y , $^{176-180}\text{Hf}$, ^{208}Pb , and ^{232}Th . We determine the ^{208}Pb concentration to be 170 at. ppm. Isotopes ^{206}Pb and ^{207}Pb were below our detection limits with reported concentrations of 28 and 16 wt. ppm, respectively, whereas Y in pit #2 was reported at 203 wt. ppm with SIMS and was detected with APT. Several different methods were used to survey for heterogeneity in the nanotips. Density isosurface analysis and nearest-neighbor distribution analysis of Pb and Y do not show any clusters. These elements are homogeneously distributed through the zircon and there is no difference between the spacing of Pb atoms in the nanotip and a model of Pb atoms randomly distributed.

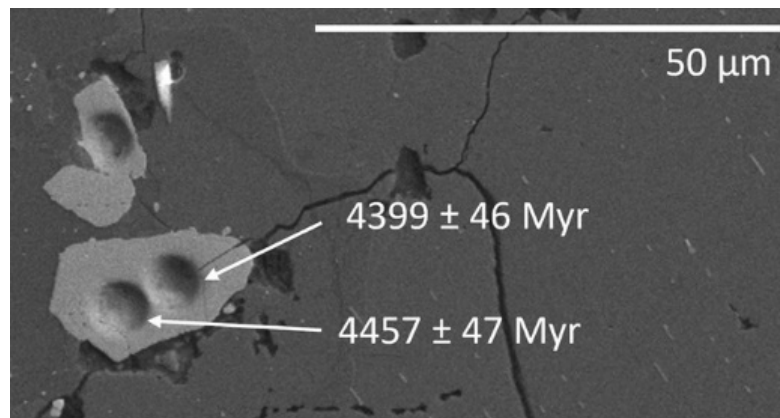


Fig. 3.1-4: Secondary electron images of zircon Z14 showing SIMS pits and corresponding Pb-Pb ages.

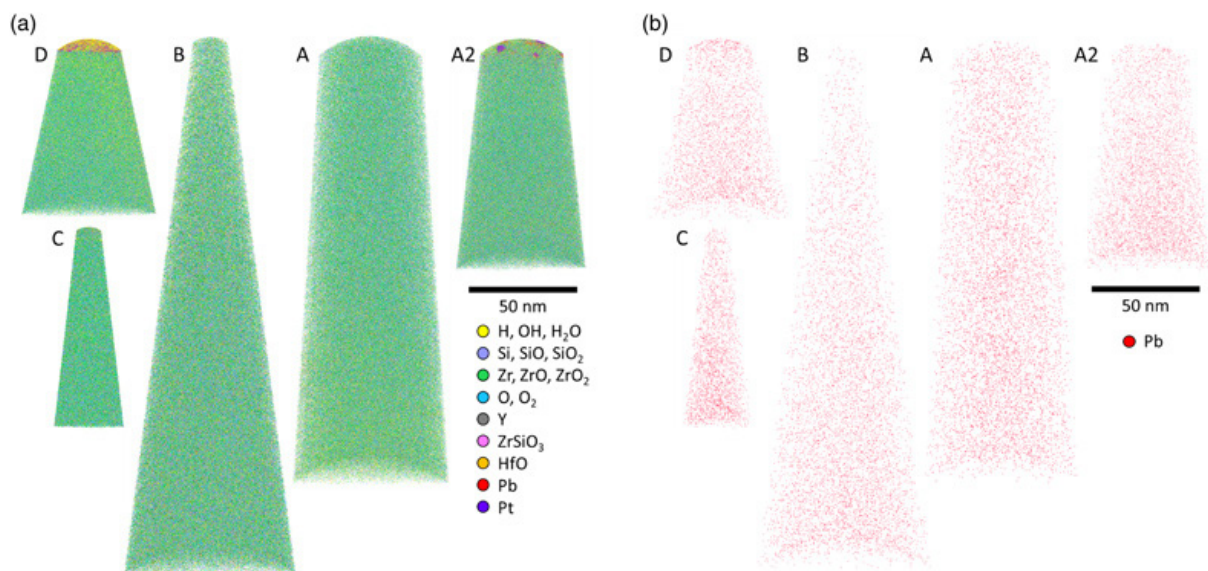


Fig. 3.1-5: APT reconstructions of the nanotips. Panel (a) shows the major ionic species present, with each ion identified as an individual point and colour-coded, and Panel (b) shows just $^{208}\text{Pb}^{++}$ in red.

The ancient age of 4453 ± 34 for the Civet Cat norite zircons could either be induced by nanoscale Pb clusters or record an authentic crystallization age with normal Pb loss. If radiogenic Pb clusters occurred in these grains, their intercluster distance must be larger than 500 nm. Trace element mobility in zircons has been previously documented on the nanoscale in volumes that are of the same scale as what was measured in this study. Although we could not obtain $^{207}\text{Pb}/^{206}\text{Pb}$ distribution and corresponding ages, the absence of ^{208}Pb and trace-element clusters likely indicates that no significant Pb clustering occurred within Z14 pit #2. This provides evidence that the old age reported by NanoSIMS Pb-Pb dating – 4453 ± 47 Ma – is the true age of crystallization of this zircon, and the younger age of pit #2 results from normal Pb loss. Our study demonstrates how important APT analysis is to survey Pb mobility and to establish the significance of U-Pb and Pb-Pb ages obtained from ion-microprobe data.

Our results push the timing of the solidification of the lunar crust to within at least the first 100 Myr of the formation of the solar system and provide a minimum age for the giant impact event that formed the Earth-Moon system. Altogether, the old age places an age bracket on the timing of the giant impact, subsequent lunar magma ocean crystallization, and the onset of Mg-suite magmatism to between 4.51 and 4.46 Ga. This period also corresponds to when the Moon began recording a history of bombardments.

d. Numerical models of North China craton destruction (J. Paul, A. Spang and A. Piccolo)

Cratons, traditionally viewed as the most stable components of continental lithosphere, have endured since the Archean. However, certain geological conditions may lead to their destruction. While controversies surround the destruction of some cratons (*e.g.*, Indian craton destruction), the North China craton (NCC) destruction hypothesis is well established. Geochemical proxies indicate that a flat slab subducted on the eastern flank of the NCC, releasing significant water that could metasomatize and weaken the cratonic root. The recent hypothesis of the presence of carbonatite melt metasomatism adds another potential factor for lithospheric weakening. The weakened lithospheric root under the NCC could have been eroded later when the slab started to roll back into the mantle.

We test this geological scenario in numerical models. We develop models in a 2-D cartesian box using an open-source finite-difference code LaMEM. In our models, we incorporate a 200 km thick craton and a flat slab subduction at the eastern edge of the craton. The flat extent of the slab hypothetically divides the craton into the western and eastern parts (Fig. 3.1-6 a-b). The eastern part of the craton, which lies above the flat slab, is gradually weakened with time. As the slab rolls back, it perturbs the mantle beneath the craton, leading to the formation of lithospheric drips at the base. Depending on the craton's 'available buoyancy', these drips become large and unstable, eventually detaching from the craton (Fig 3.1-6a-b). Our results highlight the crucial roles of both density and viscosity in craton removal. Only a dense or solely weakened craton does not undergo destruction, whereas a weak and dense craton can be destroyed within 20-30 million years, aligning with geochemical observations.

We explore alternative hypotheses for NCC destruction, such as eclogitization of the lower crust and the presence of a weak mid-lithospheric discontinuity (MLD). Our models, however, reveal that while eclogites are indeed dense, the thick and viscous nature of the cratonic root prevents the development of top-to-bottom deformation within the craton. As a result, the dense layer fails to induce the craton destruction (Fig. 3.1-6 c-d). In contrast, the presence of an MLD does promote the delamination of the craton; however, the flat slab protects the eastern side of the craton. In this model, the western part delaminates first, leading to a geologically unrealistic outcome (Fig. 3.1-6 e-f).

Our comprehensive assessment points towards flat-slab-induced metasomatic weakening as the primary driving force behind the destruction of the North China Craton. This conclusion agrees with the observed geological and geochemical features, providing valuable insights into the complex processes influencing the evolution of cratons under specific geological conditions.

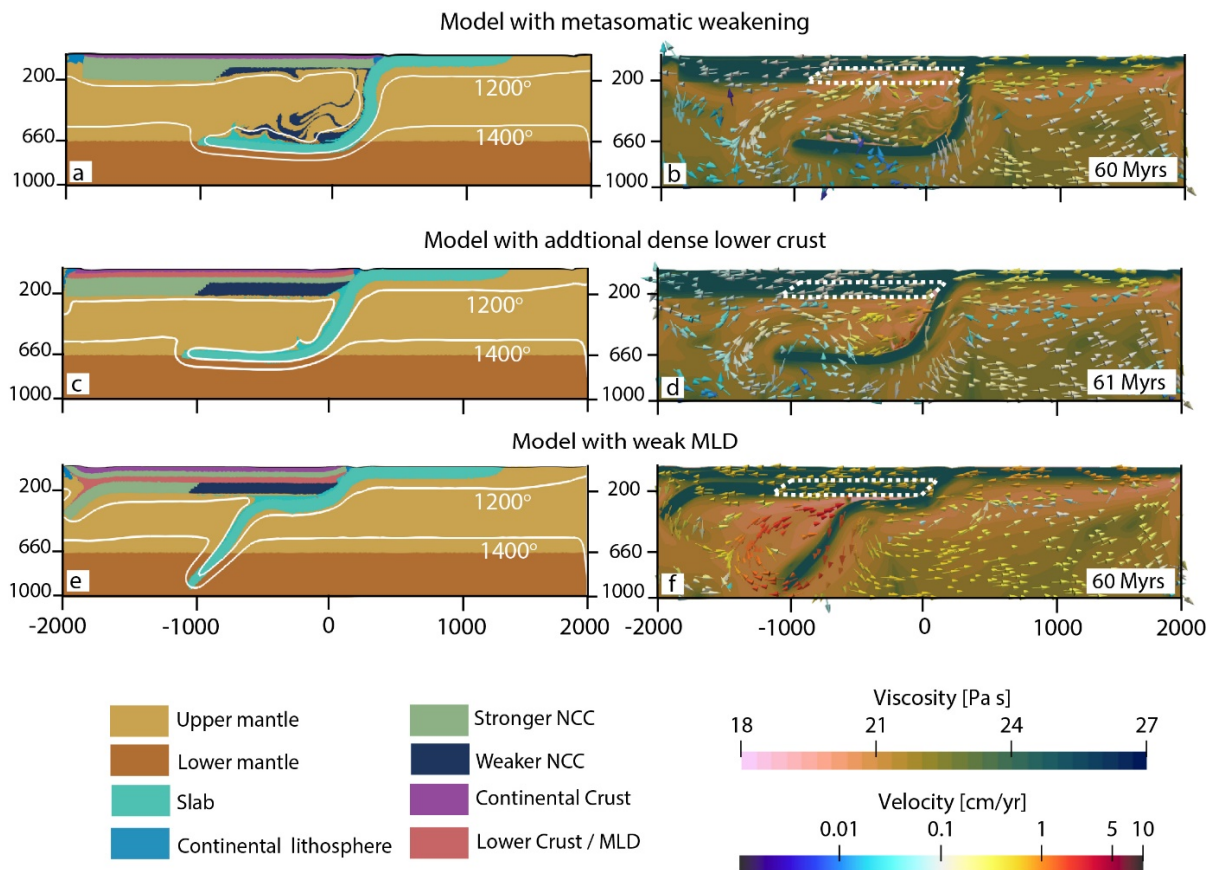


Fig. 3.1-6: a-b: Snapshot of the destruction of the North China craton due to slab-induced metasomatism, c-d: Craton fails to destroy due to dense lower crust, e-f: Unrealistic destruction of craton due to weak mid-lithospheric discontinuity. The background colors in the left panel represent different materials (*e.g.*, crust, upper and lower mantle, craton, slab, *etc.*), with light brown indicating mantle and blue colors representing craton, with darker shades for the eastern part. The exact location of the eastern block in our models is marked by a white dashed line. Temperature is presented by isosurface lines. The right panel shows background colors indicating viscosity, with velocity vectors plotted on top of it, where the vector colors represent the magnitude of velocity.

e. Slab tearing velocities controlled by trench curvature and upper mantle rheology: Insights from 3D numerical experiments (A. Piccolo, M. Thielmann and A. Spang)

Slab detachment and slab tearing are processes that have been invoked to explain rapid uplift, deep seismicity, and magmatic activity in several active orogens (e.g., Alps, Himalaya). However, the link between slab detachment and these phenomena has not yet been sufficiently quantified. Thus, deciphering the physical processes controlling detachment and tearing is important to understand its impact on the post-collisional evolution of orogens. Here, we study these processes using numerical modelling. Due to the three-dimensional nature of the tearing process, we employ three-dimensional numerical models to investigate the impact of the nonlinear coupling between the detaching slab and the surrounding mantle. As slabs are rarely straight, we also investigate the impact of slab curvature on the tearing process.

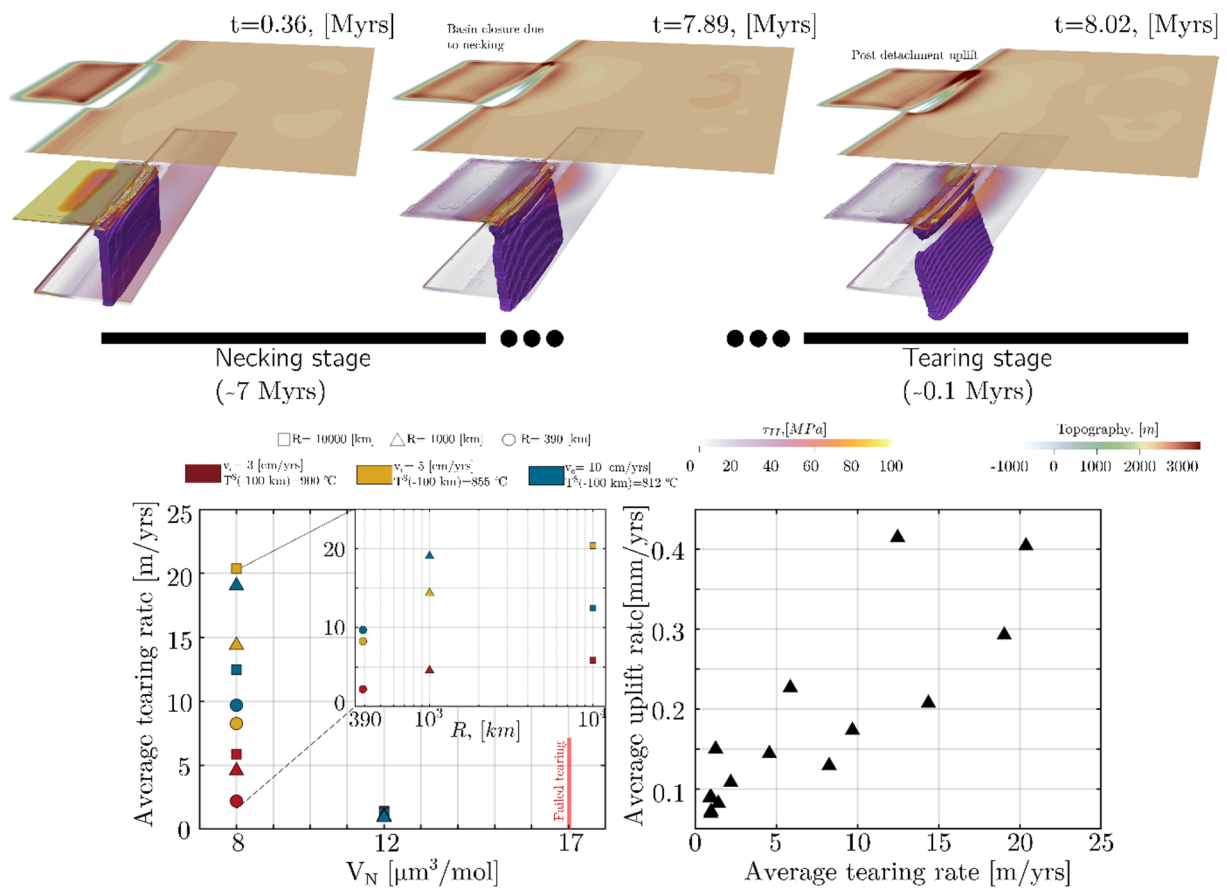


Fig. 3.1-7: The top panel represents the typical evolution of linear trench slab experiments. We can divide the experiments into two stages: the necking stage, in which the slab starts developing a necking instability along the entire strike of the slab, and the tearing stage, in which the lateral propagation of the detachment happens. The lower left picture represents the sensitivity of the tearing velocity with respect to the main input parameters, and the lower right picture shows the correlation between the average uplift velocities and the tearing velocity.

We systematically varied the radius of curvature of the trench, the temperature structure of the slab and the rheological parameters of the slab and the surrounding mantle. Simulation results show that a highly curved slab exhibits slower detachment and tearing whereas straight slabs detach almost instantaneously (see Fig. 3.1-7 upper panel). Onset times of detachment are controlled by the thermal structure of the slab. While detachment starts earlier in hotter and weaker slabs, tearing velocities are lower. In the case of cold and stiffer slabs, detachment onset times are delayed, but tearing velocities are increased. In both cases, detachment and tearing are significantly affected by upper mantle rheology, where a strong upper mantle may completely inhibit the detachment process (see Fig. 3.1-7 left lower panel).

To determine how different detachment scenarios can be distinguished by surface observations, we also computed the topographic response and uplift velocities. Results show that these two surface observables correlate with tearing velocities (see Fig. 3.1-7 lower right panel). This correlation therefore allows us to infer slab and mantle rheology from surface observations, thus providing an additional constraint on these parameters.

f. *The effects of slab detachment and tearing on the foreland basins architecture, insights from geodynamic and stratigraphic forward modelling (L.H.J. Eskens and N. Andrić-Tomašević/Karlsruhe, A. Piccolo and M. Thielmann, B. Claussmann and M. Lejri/Oslo, T.A. Ehlers/Glasgow)*

In all of the peripheral pro-foreland basins the architecture of the basin is changing drastically during the transition between underfilled and overfilled conditions (flysch to molasse transition). The evolution of architecture depends on several external forces spanning from climate or tectonic processes. In particular, the evolution of the adjacent orogen and the consequent flexure of the lithosphere due to the load imposed by the thrust belts can have an important effect on the evolution of the basin. Therefore, by studying the sedimentary history of the basin it is possible to retrieve valuable information on the tectonic evolution of the surrounding areas. For example, it has been proposed that slab break-off can drive the flysch-molasse transition in Alps and other active orogens. However, this hypothesis has not yet been proven quantitatively and it is based on the temporal and spatial correlation of the flysch-molasse transition with other geological events associated with break-off. However, the signal of the tectonic processes can be overprinted by other surface dynamics, so it is necessary to isolate the effects of break-off on the basin's overall evolution.

To understand the effects of break-off on the basins, we decided to conjugate two different forward modelling techniques: geodynamic modelling and stratigraphic modelling using LaMEM and GPM software (SLB) (see Fig. 3.1-8 for two case studies). The geodynamic forward modelling was used to generate different scenarios of break-off to retrieve the topography evolution with time, while stratigraphic forward modelling creates synthetic basin architectures from these data. We tested the effects of the bending angle, thermal structure, and

rheology of the slab on the uplift rates and deduced what the main outcomes on the evolution of the sedimentary basins are. Our preliminary results indicate that vertical uplift due to isostatic rebound in the pro-foreland basin (1.5-7 cm /yr, where fast necking of steep slabs yields higher values) decreases the accommodation space, leading to a stratigraphic upward shallowing. Furthermore, isostatic rebound of the adjacent mountain range (2-5 cm/yr, same relationship with slab dynamics as pro-foreland basin) results in up to 2.5x increased rates of sediment supply with small lag, adding to the stratigraphically upward shallowing. Lastly, the facies of the flysch to molasse transition in our synthetic seismic looks like that observed on the seismic of the Austrian Molasse, which occurred coeval with slab breakoff under the Eastern Alps.

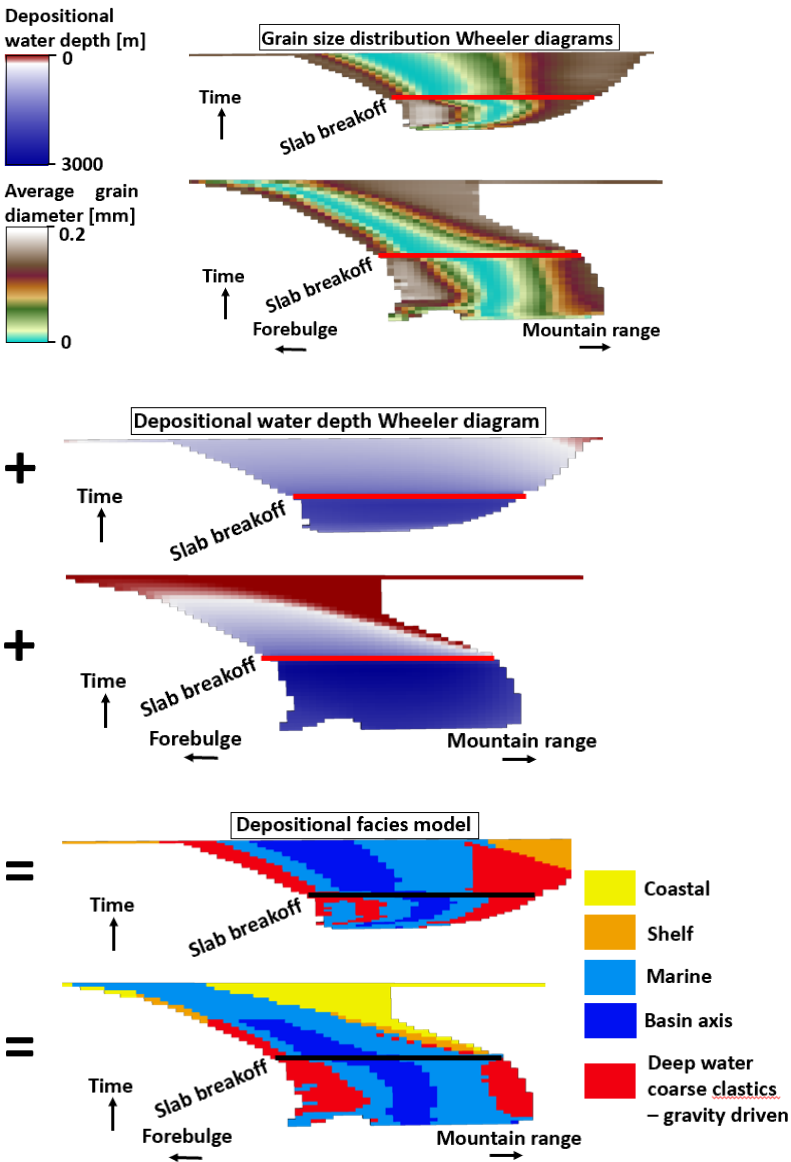


Fig. 3.1-8: Typical forward sedimentary simulations of two slab-break-off scenarios. In the top column, we plotted the grain size evolution, in the central column where depth of deposition of the sediments w.r.t. the water level, and the bottom column represents the sedimentary facies predicted by the model.

g. Electrical and thermal conductivities of fcc and hcp iron under conditions of the Earth's core from ab initio simulations (U. Kleinschmidt, M. French and R. Redmer/Rostock, G. Steinle-Neumann)

The electrical (σ) and thermal conductivities (λ) of iron play an important role in the stability and evolution of planetary magnetic fields. Liquid iron dominates the dynamo-active outer core (OC) in terrestrial planets, and solid phases in the inner core (IC) may influence the generation of magnetic fields, at least for Earth and Mercury, for which inner cores have been observed. At the high pressure (P) of planetary interiors, experiments show that close-packed phases exist along the melting curve, with the triple point between the face-centred cubic (fcc), the hexagonal close-packed (hcp) phases, and the liquid located at $P = 90 - 110$ GPa and temperature $T = 2800 - 3400$ K. The past decade has seen significant advances in both experimental and computational studies on high- P conductivities of iron and some of its alloys, but no study has systematically investigated the effect of crystal structure on electronic transport. Here we compare σ and λ of the fcc and hcp phases by performing molecular dynamics (MD) simulation on fcc and hcp iron over a wide density (ρ) and T range using finite-temperature density functional theory (FT-DFT). From the equilibrated MD simulations, we take 10-30 uncorrelated ionic configurations and run static FT-DFT calculations to compute σ and λ , both dominated by electronic transport in the metal.

Electrical conductivity decreases with T and increases with ρ for both hcp and fcc iron, and values for fcc are larger than for hcp by up to $\sim 25\%$ (Fig. 3.1-9), consistent with the general trend in experiments. A more detailed comparison with data reveals a complex picture: At $P < 150$ GPa our results agree with some of the literature data, but not with others. The discrepancy between our results and experimental data, as well as between different experiments increases with P and T . The large discrepancies between different experimental data sets may originate from P -induced changes of sample geometry, and a published semiquantitative reanalysis suggests that the discrepancy between the measurements decreases when this effect is considered. Thermal conductivity increases with T and ρ for both phases, and – as for σ – the values for fcc iron are systematically larger by up to $\sim 25\%$ (Fig. 3.1-9). Some experimental data overlap with our results at low P (< 50 GPa) and T (1800-200 K). Strangely, these and other experiments show no increase in λ with P , unlike our FT-DFT-MD results. For further analysis and comparison, we turn to the Lorenz number $L = \lambda / (\sigma T)$, which is a constant $L_0 = 2.44 \cdot 10^{-8}$ W Ω /K 2 in the fully degenerate electron gas (Wiedemann-Franz law). While L computed from our results differs from L_0 , the simultaneous increase in λ and decrease of σ with T is compensated by T in the denominator to first order, and we do not observe a substantial or systematic P dependence of L . However, if the experimental P dependence of σ and λ are combined semi-quantitatively, L would be lower by a factor of 2-3 than L_0 . Such a deviation would require a special theoretical explanation, in particular as the degeneracy of electrons becomes larger with P which increasingly favors a Lorenz number *converging* to the Wiedemann-Franz limit, not *diverging* from it.

At the IC boundary of the Earth – 330 GPa and ~ 6350 K – the hcp phase with $\sigma = 1.65$ MS/m and $\lambda = 295$ W/(Km) is juxtaposed with liquid iron with $\sigma = 1.60$ MS/m and $\lambda = 230$ W/(Km). The discontinuity in σ is small and insignificant, while the difference in thermal conductivity with $\Delta\lambda = 70$ W/(Km) between the liquid and solid is geophysically important, with direct consequences on the thermal state and deformation regime of the IC. With a significantly larger value of λ than in the OC, the IC is likely not in a convective regime as heat is conducted very efficiently along an adiabat, counteracting the buildup of a superadiabatic T profile that could form as a consequence of a thermal memory effect during its solidification history.

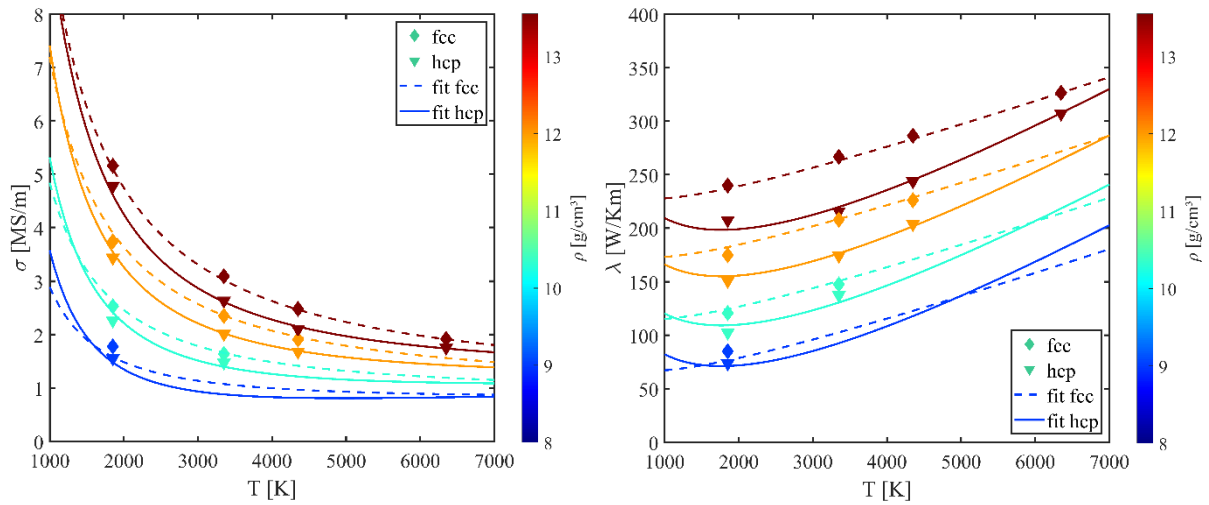


Fig. 3.1-9: Electrical (left) and thermal conductivity (right) of fcc and hcp iron at high density and temperature. Direct results from the FT-DFT-MD simulations are shown by the symbols and global fits by the solid (hcp) and dashed (fcc) lines.

3.2 Geochemistry

The first study in this section describes radiometric dating of a differentiated meteorite, which was part of the magmatic crust of an early formed planetesimal. Magmatic differentiation and crust formation on such planetesimals were driven by heating resulting from the decay of the short-lived radiogenic isotope ^{26}Al . The half-life of ^{26}Al , of approximately 0.7 million years, means that it is now extinct but it produced recognisable excesses of the daughter isotope ^{26}Mg in the earliest formed objects, that correlate with the remaining stable isotope ^{27}Al . These excesses can be used to determine the age of such planetesimal crusts but the main uncertainty is the initial $^{26}\text{Al}/^{27}\text{Al}$ ratio. Without some knowledge of this value, ages are normally reported relative to the earliest formed objects in the solar system, so called calcium aluminium inclusions (CAIs). In this study absolute ages are also determined by using the long-lived uranium-lead isotope dating technique. Through this age cross calibration an initial $^{26}\text{Al}/^{27}\text{Al}$ ratio can be constrained, which when compared to other types of meteorites, indicates that ^{26}Al appears to have been evenly distributed throughout the early solar system. The results also show that the planetesimal in question formed only 1.8 million years after the first materials in the solar system (CAIs), making it the oldest known magmatic rock.

The following study examines sulphide minerals in an ordinary chondrite meteorite that was observed to fall in Morocco about five years ago. Ordinary chondrites, as the name suggests, are by far the most common class of meteorite but samples within this class vary both in total iron content and redox state and also in the extent of thermal and shock induced metamorphism. Sulphide mineral phases will tend to homogenize and amalgamate with increasing temperature through diffusive and eventually melting processes. The meteorite in question has been thermally metamorphosed, so the study of the sulphide minerals should help to understand the initial processes of core mantle segregation.

The next two studies examine how the stable iron isotope ratio $^{56}\text{Fe}/^{54}\text{Fe}$ may have fractionated between metal and silicate during core formation on Earth and Mars. In the first of these, the effect of sulphur in the metallic melt is examined using compositions and conditions that were likely typical for core formation on Mars. In contrast to previous studies performed at low pressure, no significant fractionation is observed for sulphur bearing metallic melts, which is consistent with the seemingly unfractionated iron isotope ratio of the Martian mantle, compared to primitive meteorites. In the second study the effect of pressure is examined for metal compositions without sulphur. At pressures between 8 and 15 GPa a positive fractionation factor is observed, which would have left the mantle depleted in the heavier iron isotope. This is both contrary to previous predictions and to the actual state of the Earth's mantle. At higher pressures, however, very little fractionation is observed, which raises the possibility that important constraints can be placed on the pressures of core-mantle equilibration through such measurements.

If potassium entered the Earth's core during core formation this would provide an important additional heat source to sustain the magnetic field. Experiments performed in the next study

in this section seek to clarify this by examining the high-pressure and -temperature metal silicate partitioning of potassium. The results obtained so far, show a variation in partitioning values collected at the same conditions as a function of time. This may be due to equilibration problems but it could also result from difficulties in analysing the very volatile potassium component in the quenched metallic phase.

The effect of core formation on the sulphur isotope ratio $^{34}\text{S}/^{32}\text{S}$ is the subject of the following study. It is often considered that the sulphur content of the mantle was added late to the Earth, after core formation had completed, otherwise as a metal loving element most sulphur would have been extracted to the core. However, the $^{34}\text{S}/^{32}\text{S}$ ratio of the Earth's mantle is lighter than that of primitive meteorites, raising the possibility that some of the late arriving sulphur may have still been partitioned into the core. Preliminary experimental results indeed show the heavier isotope apparently preferentially entering iron metal at high pressures. However, an issue concerning sulphur loss from the capsules must be resolved and a test for the attainment of isotopic equilibrium needs to be performed before firm conclusions can be made.

The report by Hirschmann is an analysis of the so-called redox budget exchange between the surface and the mantle. Redox budget quantifies the oxidizing or reducing capacity of a reservoir based on its proportion and oxidation state of major variably valent elements, essentially Fe, C and S. The value is reported relative to the dominant redox state for the element in the mantle and is positive when a reservoir is more oxidized than the mantle and negative when more reducing. A number of interesting insights are obtained from this analysis. The redox budget of the mantle is estimated to be significantly larger than that of the surface but the fluxes into and out of the mantle appear, within the uncertainty, to be balanced. However, ocean island basalt eruptions appear to have a more oxidized source in the mantle, which is probably too large to have been supplied through subduction, as this would have left the surface strongly depleted in redox budget. This seems to indicate that there is a primordial oxidized reservoir, most likely in the deep mantle.

The following study is aimed at understanding the oxygen content of sulphide melts at high pressures and temperatures. Iron-nickel sulphides are the most dominant type of inclusion found in diamonds and it would be useful if their compositions could be used to interpret their formation conditions. Oxygen contents have been reported for some sulphide inclusion assemblages in diamonds, which seem to imply that they crystallized from sulphide melts. A previous study has shown that the oxygen contents of such melts are sensitive to temperature and the iron oxide content of coexisting silicates. In this study the effect of sulphide melt Ni content is examined and is found to have very little influence on the oxygen content. This seems odd because many high Ni content sulphide inclusions in diamonds also have high reported oxygen contents. Further study of the diamond inclusions themselves is probably the only way to resolve this discrepancy.

The study of Calvo *et al.* aims at resolving the question of whether the sulphur isotopic signature of the mantle can be explained solely by the addition of extra-terrestrial material during the late

veener event, or whether isotopic fractionation between the Earth's core and silicate mantle was involved. For this purpose, metal–silicate melt fractionation experiments have been performed using multianvil presses. The results are not conclusive so far due to potential disequilibrium problems.

There is an ongoing debate of whether the agents responsible for mantle metasomatism in the lithosphere are composed dominantly of silicate melts, carbonatite melts, or aqueous-carbonic fluids. In order to test the validity of published agent-sensitive trace element indicators in clinopyroxene, Shaw performed piston cylinder experiments during which spinel peridotites and individual mantle minerals were reacted with carbonatite melts. Preliminary results suggest that the proposed Ca/Al discriminant in clinopyroxene is not able to differentiate between carbonatitic vs. silicate melt metasomatic agent.

Rustioni *et al.* performed piston-cylinder diamond-trap experiments on a K- and P-doped MORB starting material to check whether the presence of accessory phengite and apatite in eclogite significantly affects the bulk rock–fluid partition coefficient of Rb, Cs, Sr, Ba and LREE. The results confirm that Rb, Cs, Sr, Ba partition into phengite and that LREE partition into apatite, but the modal abundances of these two minerals in MORB-derived eclogites are too small to significantly affect the bulk rock–fluid partition coefficients.

The last five contributions deal with processes operating in the Earth's crust, in particular ones related to the formation of magmatic-hydrothermal ore deposits. Based on the common association of K-rich magmas with Au-rich porphyry-epithermal ore deposits it has been proposed that potassic magmas are either unusually Au-rich or contained high Au/Cu ratios. To test this hypothesis, the metal content of melt inclusions in variously evolved potassic rocks from more than a dozen locations worldwide was analysed using a highly sensitive LA-ICP-MS system. It turns out that both absolute Au contents as well as Au/Cu ratios in these melts are comparable to those of MORB melts, which disproves the above hypothesis and instead suggests that the Au-rich ores resulted from preferential Au fluid–melt partitioning or selective metal precipitation from the hydrothermal fluids.

Porphyry Cu (Au, Mo) deposits represent huge geochemical anomalies of sulphur. However, original sulphur contents of magmas are difficult to reconstruct because most of the sulphur may have been present in magmatic sulphides and/or anhydrite, phases which typically decompose during magma solidification. Audétat & Chang demonstrate how the former presence of anhydrite phenocrysts in porphyritic rocks can be recognized on the basis of cavities that are spatially associated with apatite microphenocrysts. Such cavities were found to be very common in porphyry Cu-related rocks in southwestern USA. However, due to the lack of a comparative sample set from barren magma systems it is not clear yet whether the presence of magmatic anhydrite is a characteristic feature of mineralized systems or of arc magmas in general.

Gallium is currently recovered exclusively as a byproduct from sphalerite and bauxite ores. In order to test whether this element may become significantly enriched during magmatic-

hydrothermal processes, the solubility of Ga in rhyolite melts and its partitioning between melt and fluid was investigated by Hlede & Keppler by means of cold-seal pressure vessel and piston cylinder experiments. The results suggest that neither magmatic fractionation nor fluid–melt partitioning leads to significant enrichment of Ga, leaving little hope to discover magmatic-hydrothermal Ga deposits.

In contrast, tin is mined almost exclusively from magmatic-hydrothermal ore deposits. In order to gain insights into the processes that lead to economic ore grades of this element, Wu *et al.* investigated the Sn isotopic signature of various generations of cassiterite in the large Xianghualing Sn deposit of China. The data suggest that the observed isotopic variation is mostly due to kinetic disequilibrium fractionation. However, the isotopic fractionation factors between cassiterite and fluid are not well constrained, for which reason cold-seal pressure vessel experiments are currently being conducted to obtain more data.

a. *Al-Mg and U-Pb chronological records of Erg Chech 002 ungrouped achondrite meteorite (A. Bouvier, P.M. Reger/London, Canada; Y. Roebbert and S. Weyer/Hannover; W. Neumann, W.H. Schwarz, T. Ludwig and M. Trieloff/Heidelberg; A. Gannoun/Clermont-Ferrand and M. Regelous/Erlangen)*

The use of radiometric dating has been a cornerstone of unravelling the events surrounding the formation and early evolution of the Solar System. Of the various chronometers, the long-lived, absolute U-corrected Pb-Pb chronometer and the short-lived, relative ^{26}Al - ^{26}Mg (half-life of $\sim 717\,000$ yr) chronometer have been particularly useful in dating extra-terrestrial materials. The ^{26}Al - ^{26}Mg chronometer can resolve events within $\sim 30,000$ years, while the U-corrected Pb-Pb chronometer can reach a time resolution of about 300,000 years for events that took place more than 4.56 billion years ago. More specifically, when comparing the isotopic systematics of the short-lived ^{26}Al - ^{26}Mg chronometer anchored to absolute U-corrected Pb-Pb ages, inferences about the distribution of ^{26}Al in the protoplanetary disk can be evaluated.

Achondrite meteorites are remnants of the earliest planetary differentiation processes in the Solar System. They have been used to anchor short-lived radiochronometers to absolute ages determined from long-lived radiochronometers. Erg Chech 002 is a recent meteorite find with an unusual chemistry and mineralogy: (1) the whole-rock composition is comparable to terrestrial andesites in silica and alkaline element concentrations and (2) it contains large (up to 9 cm) orthopyroxene megacrysts in a groundmass of sodic plagioclase, pigeonite and silica (Fig. 3.2-1). Geochemically, EC 002 exhibits a distinct trace element pattern compared to other andesitic meteorites, with no significant anomalies in alkali and high field-strength elements relative to CI chondrites. Highly siderophile elements show fractionation between the compatible and incompatible elements that suggest metal-silicate separation occurred on the parent body of EC 002. Mass-independent O, Cr, and Nd isotope anomalies of the whole-rock indicate accretion of the EC 002 parent body in the non-carbonaceous reservoir.

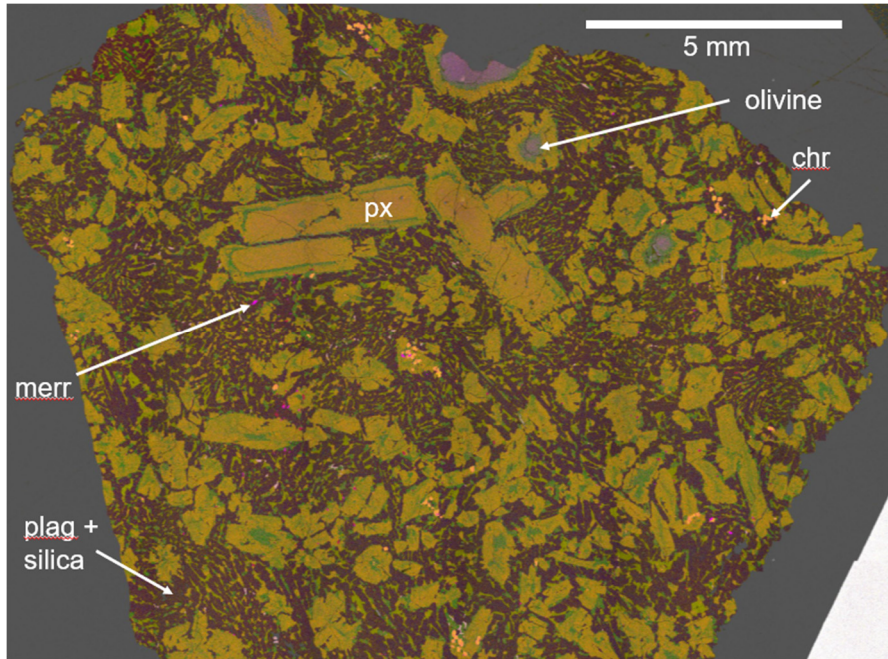


Fig 3.2-1: Backscattered electron image overlaid with energy dispersive spectroscopy composed as a multi-field phase coloured map of Erg Chech 002 polished mount used for the SIMS analyses. Large pyroxene megacrysts and rounded olivine crystals are surrounded by groundmass of sodic plagioclase, pigeonite and accessory chromite, merrillite, and silica polymorphs.

In situ and solution ^{26}Al - ^{26}Mg chronometry and ^{53}Mn - ^{53}Cr chronometry suggest that EC 002 formed within ~ 0.7 to 2.2 Ma after the formation of Ca-Al-rich inclusions (CAIs), making it the oldest known sample of igneous crust in the Solar System. We obtained the U-corrected Pb-Pb age and ^{26}Al - ^{26}Mg age obtained by MC-ICPMS solution analysis of the same mineral separate samples of EC 002. In addition, six merrillite grains were analysed by *in situ* SIMS to determine their Pb-Pb individual ages.

The U isotope composition of EC 002 exhibits internal heterogeneities between leached pyroxene ($^{238}\text{U}/^{235}\text{U} = 137.766 \pm 0.027$) and the bulk rock ($^{238}\text{U}/^{235}\text{U} = 137.8190 \pm 0.0074$). The Pb isotope composition of progressively leached pyroxenes are characterised by radiogenic $^{206}\text{Pb}/^{204}\text{Pb}$ ratios (ranging from 41 to 23487). Using the U isotope composition of the leached pyroxenes, the resulting age of the $^{207}\text{Pb}/^{206}\text{Pb}$ - $^{204}\text{Pb}/^{206}\text{Pb}$ isochron is 4565.87 ± 0.30 Ma (2σ). The weighted mean of the Pb-Pb ages of seven SIMS analyses of merrillites are 4564.3 ± 5.2 Ma (2σ). These similar ages (within uncertainty) indicate rapid cooling and the absence of significant thermal events after ~ 4559 Ma on the parent body of EC 002. The ^{26}Al - ^{26}Mg isochron through a bulk rock, pyroxene, fine-grained and four plagioclase fractions defines an initial $^{26}\text{Al}/^{27}\text{Al}$ ratio of $[8.89 \pm 0.79] \times 10^{-6}$ corresponding to a formation age of 1.83 ± 0.12 Ma after CAIs. The initial ^{26}Al abundance is consistent with previous MC-ICP-MS ^{26}Al - ^{26}Mg reported systematics for EC 002, but 0.46 ± 0.13 Myr older than the *in situ* SIMS ^{26}Al - ^{26}Mg age previously reported (Fig. 3.2-2). When anchored to the absolute Pb-Pb age of CV3 CAIs

(4567.30 ± 0.16 Ma), the Al-Mg model age of EC 002 is 4565.47 ± 0.20 Ma, slightly younger than its U-corrected Pb-Pb age.

The concordance of the Pb-Pb and ^{26}Al - ^{26}Mg ages of ungrouped CC achondrites when anchored to EC 002 suggest that ^{26}Al was homogeneously distributed between the NC and CC reservoirs at the time of their parent body accretion. Given its old age, precise ^{26}Al - ^{26}Mg and U-corrected Pb-Pb ages and straightforward thermal history, EC 002 shows promise to be used as an anchor to date other objects with short-lived chronometers. Furthermore, the presence of internal U isotope heterogeneities found between mineral and whole-rock samples of EC 002 supports the need of U isotope analysis of meteoritic samples dated using the Pb-Pb chronometer.

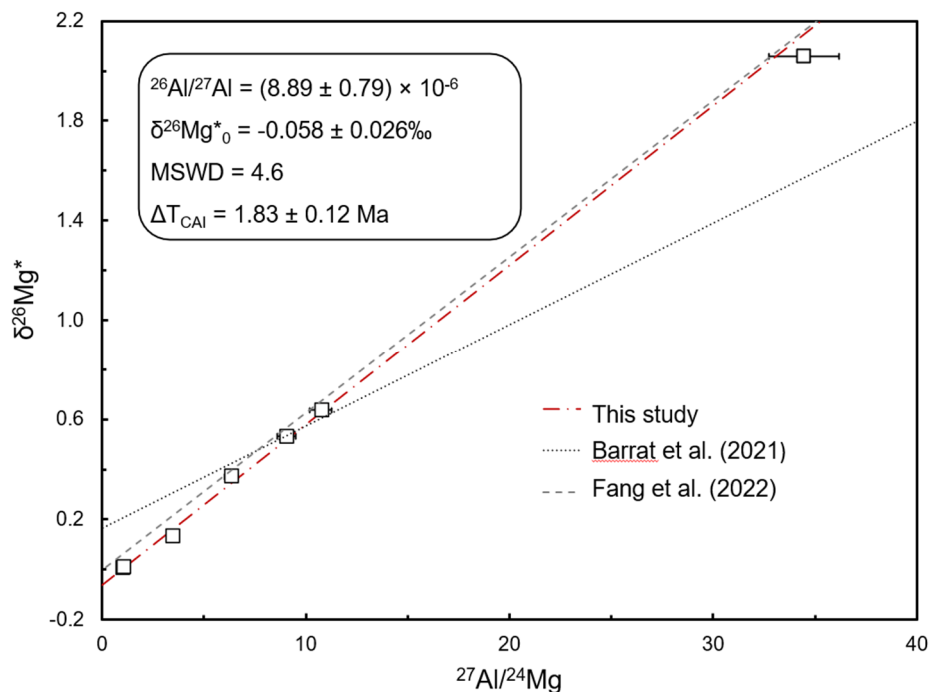


Fig. 3.2-2: Comparison of initial $^{26}\text{Al}/^{27}\text{Al}$ ratios obtained between this study and literature data. Error envelopes of isochrons have been omitted for clarity (Barrat *et al.*, 2021, PNAS 118, e2026129118; Fang *et al.*, 2022, PNAS 119, e2120933119).

b. Sulphide inventory in the meteorite Ksar El Goraane (H5): A window on the formation conditions of ordinary chondrites (S. Arif and H. Chennaoui Aoudjehane/Casablanca, A. Bouvier)

The meteorite Ksar El Goraane was recovered after the report of a fireball event observed in the south-east of Morocco on October 28th 2018. This meteorite (~ 4 kg in total) is an ordinary chondrite petrologic type H5, with an estimated shock stage S3. Preliminary analyses during the meteorite classification indicated the presence of several sulphur phases and abundant FeNi metal. The primary goal of this study is to decipher the origin of the sulphur associated with metal and the thermal history that led to the formation of sulphides present in this ordinary

chondrite. Additionally, we selected 7 other meteorites that were prepared in polished sections. These meteorites are petrological types 4, 5 and 6 of H, L and LL ordinary chondrites that are observed fall meteorites in Morocco and Mauritania.

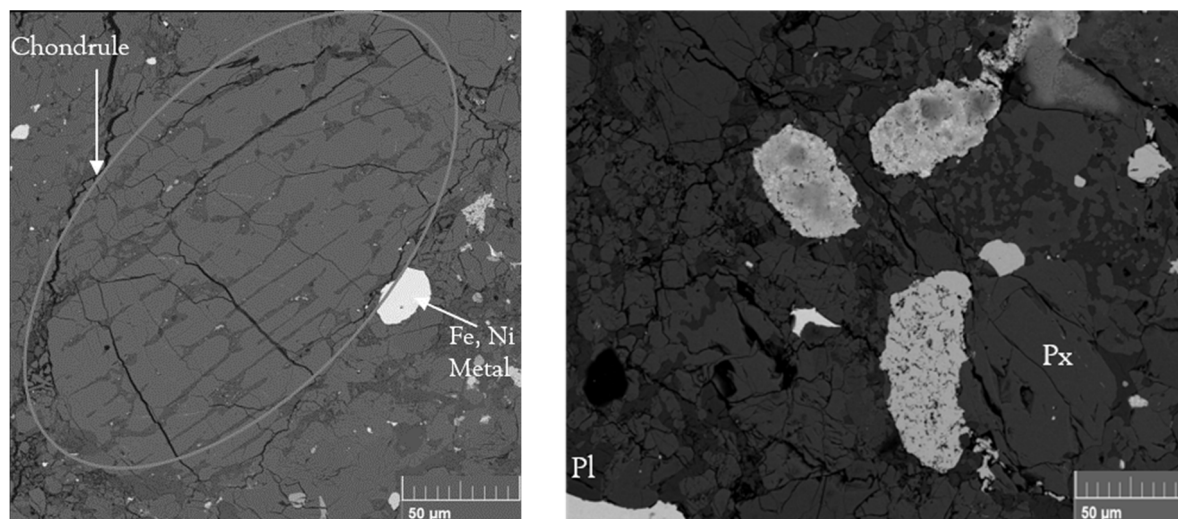


Fig. 3.2-3: Backscattered electron images of Ksar El Goraane. Pl: Plagioclase, Px: Pyroxene.

Backscattered electron images of Ksar El Goraane show the presence of porphyritic chondrules embedded in a recrystallized matrix (Fig. 3.2-3 left). There is no evidence found of brecciation. Feldspar grains are present throughout the matrix with olivine and pyroxene. FeNi metal grains are abundant in the sample, with the presence of sulphide grains. Quantitative elemental analysis by EPMA (JEOL JXA-8200) was obtained in mineral phases at BGI, with a particular focus on metals and sulphides. Based on EPMA analysis carried out on five polished sections of Ksar El Goraane, we were able to identify the following sulphide phases: troilite FeS ($n=21$), pyrrhotite Fe_{1-x}S ($n=7$), pentlandite $(\text{Fe,Ni})_9\text{S}_8$ ($n=4$) and pyrite FeS_2 ($n=1$). We note that pyrrhotite was not initially reported in the classification report of the meteorite. Sulphur inclusions are also present in the metal.

We also identified pyrrhotite in Gueltat Zemour (L4, S2), Benguerir (LL6, S3/4) (in which pyrrhotite is the most abundant sulphide phase, with minor troilite), Tinajdad (H5), while no sulphide phase was found in Tamadakht (H5).

Hydrogen sulphide (H_2S) is the dominant S-bearing species in the gas phase and troilite (FeS) is the primary reservoir for S after condensation. Our study reports four sulphide phases present together in Ksar El Goraane, which are not commonly found in other ordinary chondrites. A planned future study of major and trace elemental compositions of sulphide phases will provide additional constraints on the sulphur chemistry during varying oxygen fugacity conditions in the solar system as well as the thermal history of the ordinary chondrite parent bodies.

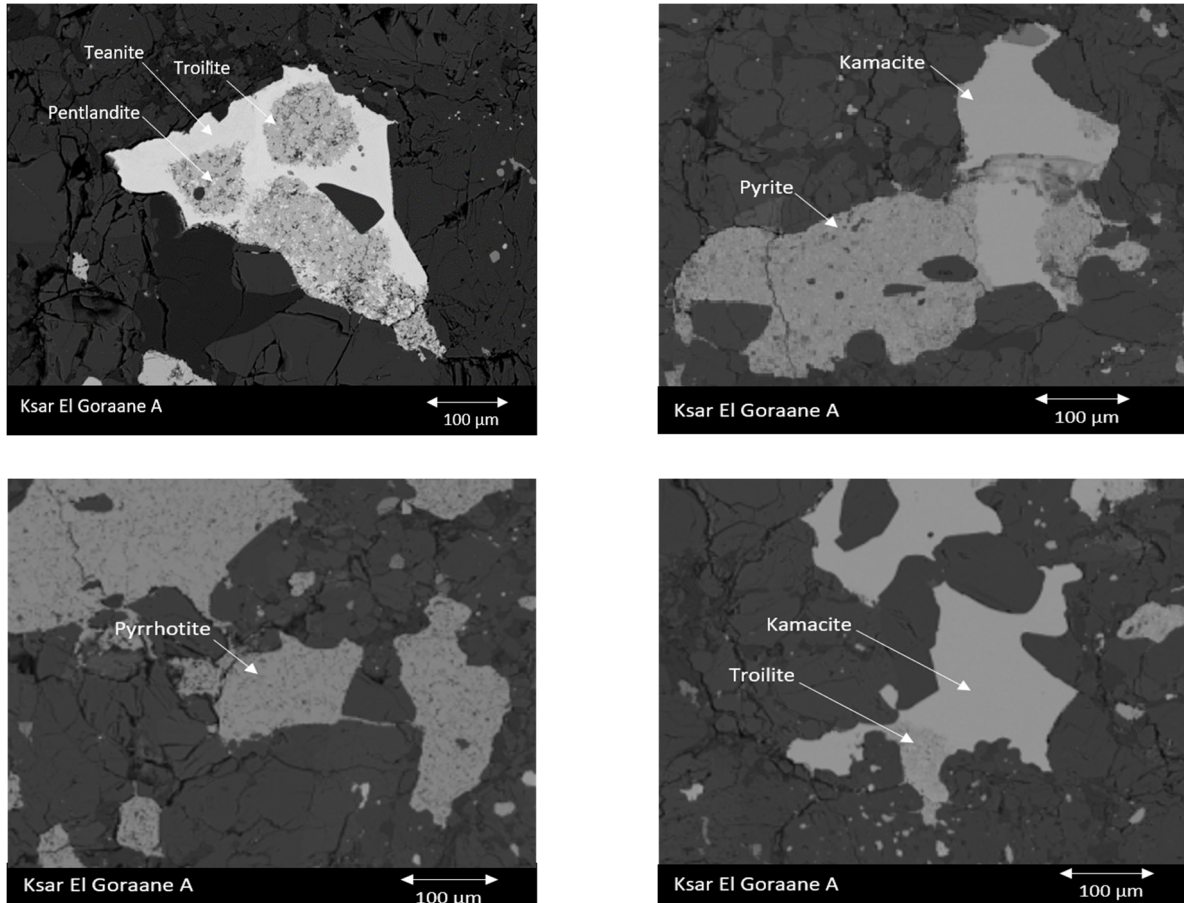


Fig. 3.2-4: Backscattered electron images of sulphide inclusions in metal from Ksar El Goraane.

c. Effect of S on Fe isotopic fractionation between metal and silicate: Preliminary results and implications for Mars' core light element budget (E. Kubik, in collaboration with S. Rabin/Brussels)

The composition of deep Martian chemical reservoirs is a key topic, with implications for understanding differences in planetary formation and the genetic links amongst rocky bodies of the solar system. In particular, Mars' core is thought to contain a large amount of light elements. Sulphur is likely to be a major element in the Martian core, which is supported by analyses of Martian meteorites, cosmochemical arguments as well as geophysical data and metal-silicate partitioning results. This conclusion is also in line with seismic measurements recently made as part of the InSight mission. A S-rich Martian core would contribute to explain the oxygen fugacity of Mars' mantle, estimated to be one log unit below the iron wüstite buffer, *i.e.*, $\Delta IW - 1$.

Experimental metal-silicate Fe isotopic fractionation studies have reported a significant effect of the S content of the metal at 1 GPa. This effect of S on the Fe isotopic fractionation factor

can be used to constrain an upper limit to the S content of the core, in order to maintain the near-chondritic Fe isotopic composition measured in the silicate Mars. However, the effect of S on the Fe isotopic fractionation has never been investigated above 2 GPa. Experiments performed at the pressure conditions of Mars core formation (15-20 GPa) are needed to ensure that possible pressure effects are considered.

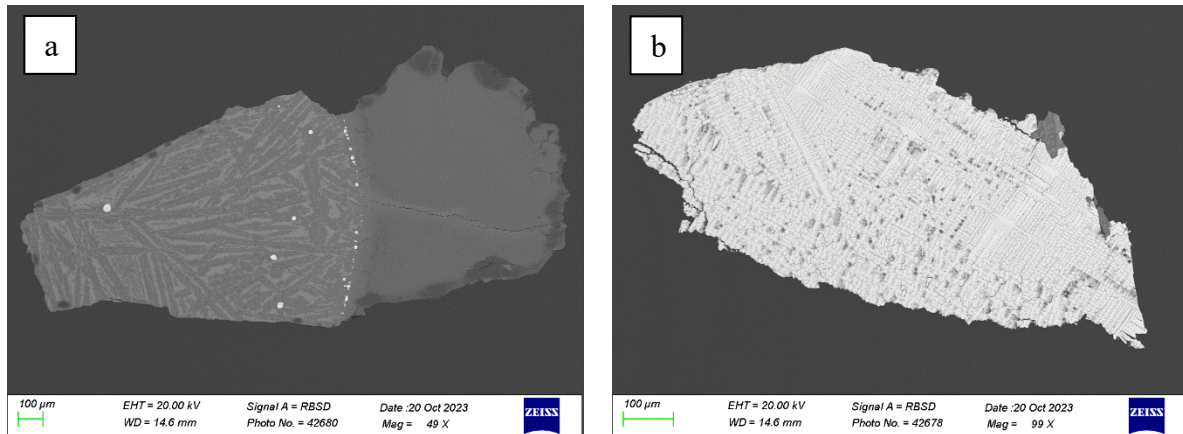


Fig. 3.2-5: Back-scattered electron images from multi-anvil run products. (a) Image of the silicate phase with attached single-crystal MgO capsule showing a typical texture with dendritic olivine crystals and interstitial pyroxenite glass (brighter grey). (b) Image of the metal phase showing dendritic quench texture.

We performed two preliminary experiments at 8 GPa and 2200 K using the 5000-ton multi-anvil press. The experiments were left 3 and 7 minutes at the target temperature to equilibrate. We used custom box-furnace 25/15 assemblies with LaCrO_3 heaters, which allows for the large sample volume necessary for isotopic analysis, while also achieving the high-temperature superliquidus conditions. The starting material was composed of natural MORB, pure Fe and FeS such as to obtain ca. 15 wt. % S in the metal. Single-crystal MgO capsules were used to minimize sample-capsule reactions. The Fe isotopic ratios of metal and silicate separates, shown in Figure 3.2-5, from these two experiments were measured at Ghent University, using a Neptune MC-ICPMS. The Fe isotopic fractionation factor $\Delta^{56}\text{Fe}_{\text{metal-silicate}}$ was found to be insignificant for both experiments, indicating identical Fe isotopic signatures in the metal and the silicate. Our data suggest that the S effect previously observed at low pressure does not exist at 8 GPa due either (1) to differences in the structures of the silicate melt and molten alloy affecting the Fe bonding environment or (2) to the temperature of our experiments being too high to result in significant Fe isotopic fractionation. However, we estimate that the $\Delta^{56}\text{Fe}_{\text{metal-silicate}}$ measured at low pressure and 1923 K in the literature would correspond to a factor of 0.20 ‰ at our experimental temperature of 2200 K, which is a significantly larger fractionation than the factor of 0.03 ± 0.04 ‰ measured at 8 GPa in our study. More high-pressure experiments are needed to fully characterise the effect of S on Fe isotopic fractionation during core formation in terrestrial planets of the size of Mars and Vesta.

d. Evolution of the experimental metal-silicate iron isotopic fractionation with pressure: Implications for core formation on large terrestrial planets (E. Kubik and A. Bouvier, P.A. Sossi/Zurich)

The origin of the significant variability of iron isotopic signatures amongst inner solar system differentiated planetary bodies remains a debated topic. In particular, there is no consensus regarding the process(es) producing isotopically heavy silicate Earth and Moon compared to the chondrite meteorite-like signatures measured in Mars and Vesta. As a large-scale mass transfer process occurring on terrestrial planets, core formation could contribute to establishing these signatures. However, existing experiments investigating Fe isotopic fractionation between molten metal and silicate have been performed at pressures (< 7.7 GPa) that are lower than those expected for core formation on large terrestrial planets such as Mars and Earth. Indeed, the evolution of the metallic and silicate liquid structures as pressure increases may cause changes in isotopic fractionation factors between the involved phases. For instance, a liquid-liquid Fe phase transition at 5.2 GPa is reported to have a strong effect on the partitioning behaviour of siderophile elements. These structural changes modify the bonding environment of Fe, which is the main driver of equilibrium isotopic fractionation, and therefore have the potential to influence the distribution of Fe isotopes between metal and silicate. However, these processes are very poorly understood due to a lack of experimental isotopic fractionation data at high pressure.

Non-traditional stable isotopic measurements of experimental phases require a large sample volume, which becomes a challenge above 3 GPa. However, the combined use of the 5000-ton press and custom-made assemblies (box furnace design of 18M and 25M multianvil assemblies) were used to successfully impart pressures up to 20 GPa and temperatures up to 3000 K onto a large sample charge.

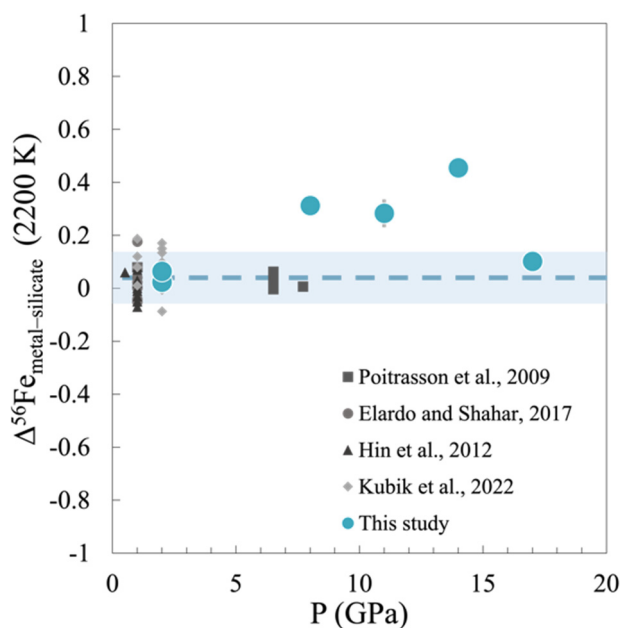


Fig. 3.2-6: Experimental $\Delta^{56}\text{Fe}_{\text{metal-silicate}}$ of experiments from this study ranging from 2 to 17 GPa and recalculated to 2200 K compared to literature data (grey symbols; Poitrasson *et al.*, 2009, EPSL; Elardo & Shahar, 2017, Nat. Geo.; Hin *et al.*, 2012, GCA; Kubik *et al.*, 2022, GCA). The error bars represent 2 standard deviations derived from repeated isotopic measurements of both metal and silicate phases.

In this study, the Fe isotopic fractionation between liquid metal and liquid silicate was measured from 2 to 17 GPa and from 1800 to 2473 K. We observe a significant variation of Fe isotopic fractionation with pressure (Fig. 3.2-6). The positive fractionation factor obtained between 8 and 14 GPa translates into a heavy Fe isotope enrichment in the metallic alloy. However, the data suggests an absence of Fe fractionation at 17 GPa and 2473 K, which is within the range of possible core formation conditions for Mars. This data set yields two main conclusions. (1) The experimental Fe isotopic fractionation between metal and silicate at high pressure (17 GPa) is in good agreement with the chondritic iron isotopic signature measured in the Martian mantle. (2) The observed variations of Fe isotopic fractionation factor with pressure across a 15 GPa range suggest that pressure can have a strong effect on the isotopic fractionation of siderophile elements during core formation. More experiments at high pressure are therefore needed to understand the origin of siderophile element isotopic signatures in large terrestrial planetary mantles.

e. Testing the feasibility of ^{40}K as a heat producing element in planetary cores based on K metal-silicate partitioning experiments (J. Sikdar and E. Kubik)

Potassium (K) is a lithophile and highly incompatible element. As such, K is preferentially incorporated into the silicate mantle of planets during core–mantle differentiation. However, an increasing body of evidence based on laboratory experiments and theoretical calculations suggests that the electronic structure of K changes at high-temperature (~ 2300 K) and -pressure (20-30 GPa) conditions, wherein K starts behaving as a transition metal, thereby increasing its solubility in liquid metal alloy. If true, the presence of K in Earth's core could provide an alternative explanation for the significant depletion of K in the silicate Earth relative to CI-Chondrite (the primary explanation being attributed to loss of moderately volatile K during nebular/planetary volatilization). Earlier studies indicated that a considerable amount of K (~ 35 -200 ppm) could be present in the core and radioactive decay of ^{40}K could serve as a significant heat source that sustains the geo-dynamo.

Nevertheless, the metal–silicate partition coefficient for K ($D=X_{\text{metal}}^{\text{K}}/X_{\text{silicate}}^{\text{K}}$) is generally low (0.0026 at 1450 °C and 1.5 GPa) and the effect of individual parameters (pressure, temperature, oxygen fugacity, silicate melt and metal composition) that can influence the metal–silicate partition coefficient (D) of K is not well constrained. Additionally, there were several issues with the previous experimental studies on K partitioning that complicate the interpretation of the data, such as the high C content, ~ 5 wt. %, of the metallic phase due to the use of graphite capsules.

Therefore, the extent to which K might reside in planetary cores and its feasibility as a major heat producing element remains debated. The lack of K isotope data in high-temperature experimental samples further hinders the accurate interpretation of potassium's fate during

core–mantle differentiation. In this study, we performed preliminary melting experiments at 2 GPa and 1900 K using an end-loaded piston cylinder with durations varying from 10 to 30 minutes. Single-crystal MgO capsules were used, which were loaded with a mixture of powdered MORB (as analogue of silicate melt composition), FeS alloy, and pure K₂O powder. The capsules were contained in ½" talc-pyrex assemblies equipped with a straight graphite furnace. The temperature of the system was monitored by a D-type thermocouple inserted axially above the sample chamber. The quenched run products were found to consist of a metal sphere of up to ~ 1.4 mm surrounded by silicate. The major element abundances of the metal and silicate run products (separated under magnifying glass) were quantified using Electron Dispersive X-ray spectroscopy.

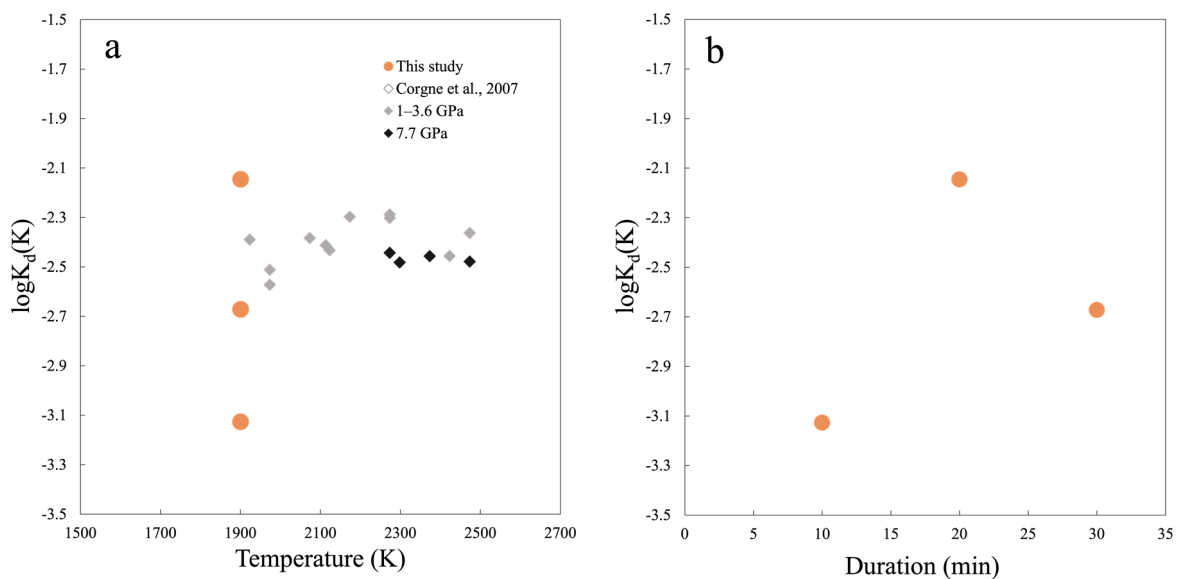


Fig. 3.2-7: Partitioning of K, expressed as logK_d(K), as a function of (a) experimental temperature and (b) run duration of the samples analysed in this study compared with that of published data (Corgne *et al.*, 2007, EPSL).

The K-Fe distribution coefficient, K_d, between metal and silicate calculated from the equilibrium $2K + FeO = K_2O + Fe$, ranges from approximately -3.1 to -2.1 (Fig. 3.2-7a). Although the 20 and 30 min runs indicate values that overlap with literature data, the 10 min experiment has a significantly lower K_d, which could be attributed to incomplete equilibration (Fig. 3.2-7b). Further experiments are required with longer run times to ensure complete equilibration so that the K elemental behaviour during core formation in planetary bodies can be better constrained. Being a moderately volatile element, the potential of K loss during runs and possibly during analysis also needs to be carefully evaluated. Furthermore, future experiments providing high precision K isotope data between metal and silicate at high-pressure and high-temperature conditions will be beneficial to understand the metal–silicate fractionation signatures measured in terrestrial planetary bodies.

f. Tracing the origin of volatile elements with core formation experiments and sulphur isotopes (L.M. Calvo/Paris, E. Kubik, J. Labidi/Paris and J. Siebert/Paris)

Volatile elements, such as H, C, N and S, play multiple and significant roles in planetary evolution. However, the mechanism and timing of their arrival on Earth remains unclear. It has been suggested that the current sulphur isotopic signature of the mantle cannot be explained solely by admixture of extraterrestrial material, raising the question of whether core–mantle equilibration may have played a role for setting the mantle's isotopic composition. It is unclear whether this scenario is viable, given that the sulphur isotope signature of Earth's basalts is lighter than primitive meteorites by $\sim 1.3\%$.

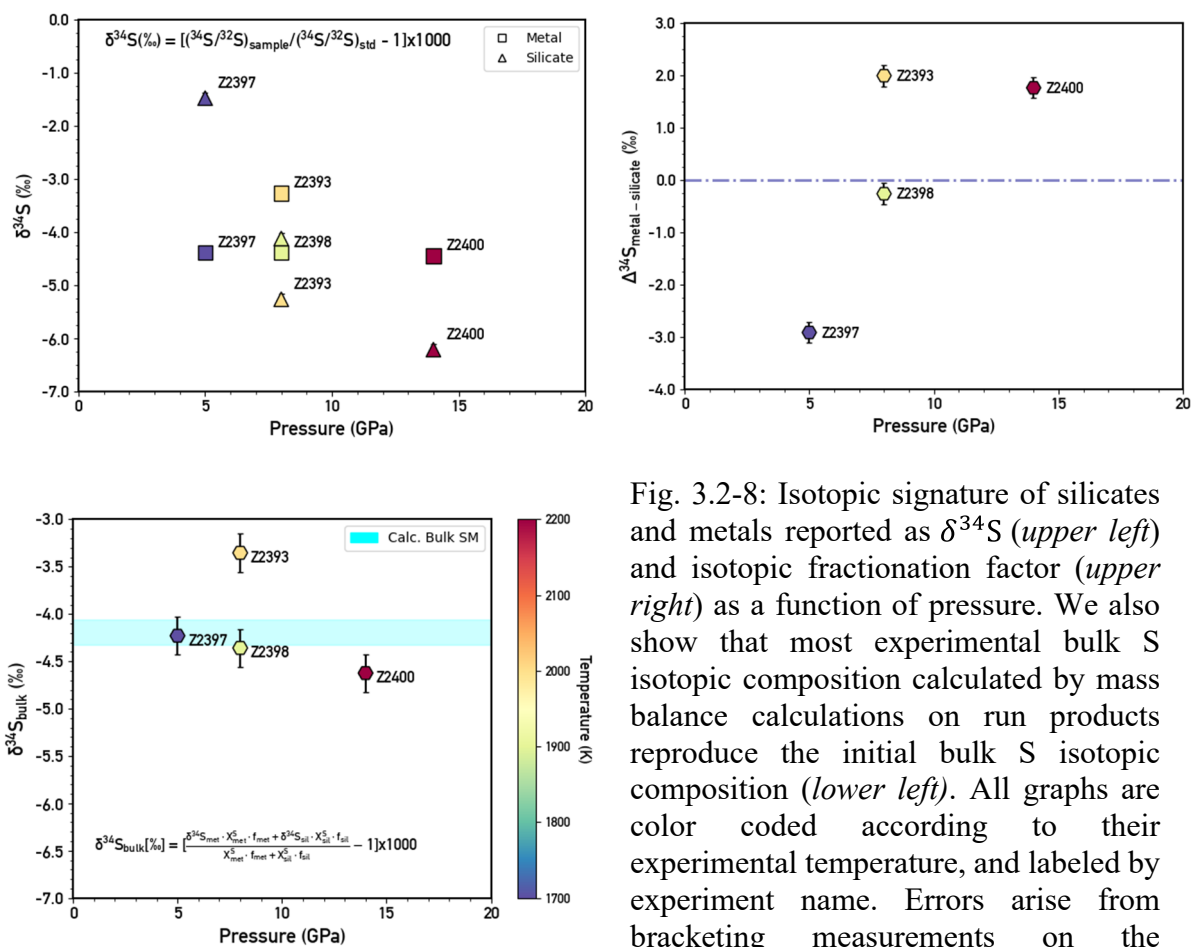


Fig. 3.2-8: Isotopic signature of silicates and metals reported as $\delta^{34}\text{S}$ (upper left) and isotopic fractionation factor (upper right) as a function of pressure. We also show that most experimental bulk S isotopic composition calculated by mass balance calculations on run products reproduce the initial bulk S isotopic composition (lower left). All graphs are color coded according to their experimental temperature, and labeled by experiment name. Errors arise from bracketing measurements on the international standard IAEA S-1.

In order to address this question, we experimentally determined the metal–silicate isotope fractionation of sulphur at high temperature and high pressure. We mixed a natural MORB composition at a 70:30 weight ratio with metallic Fe, S and Si (the latter at a weight ratio of 72.5:20:7.5). Starting materials were heated and compressed using the Zwick 5000 tonne multianvil apparatus at 5–14 GPa and 1700–2200 K in MgO capsules and using a "box-furnace"

assembly. These conditions allowed to equilibrate a molten metal and silicate phase in relatively large experimental charges, such that enough material can be retrieved for isotopic analyses of the experimental runs to be performed, despite the high pressures. Elemental and isotopic analyses were conducted at the Institut de Physique du Globe de Paris (IPGP). Variable fractionation (reported as $\Delta^{34}S_{met-sil}[\text{‰}] = \delta^{34}S_{met} - \delta^{34}S_{sil}$) has been observed among the experiments (Fig. 3.2-8). The different isotopic fractionation factors observed between the experiments at 8 GPa as well as the evolution of the isotopic behaviour with increasing pressure and temperature could be interpreted as disequilibrium in at least one experiment, due to either (1) the short duration of experiments (in the order of minutes) or (2) significant S loss during the experiment. While recent piston cylinder experiments only containing natural MORB (1.5 GPa, 1673 K) seem to prove that MgO capsules do not fractionate S by loss (MORB: -0.72‰, after 6 h: - 0.57‰ in $\delta^{34}S$), more experiments with different time durations are needed to fully characterise the isotopic behaviour of sulphur during core formation at these experimental conditions.

g. Fluxes and reservoirs in the deep Earth oxygen cycle (M.M. Hirschmann)

The deep Earth oxygen cycle describes the long-term storage and exchange of redox-sensitive species between Earth's interior and surface reservoirs. Over geologic time, this cycle has created and maintained the inventory of oxidized material in the exosphere (crust and fluid envelopes) that fosters the planet's atmosphere, climate, and biogeochemical cycles. Return fluxes of these components to the interior are responsible for unique geochemical and petrologic features associated with convergent margins and potentially have contributed to oxidized domains circulating in the deeper mantle and sampled at oceanic islands. Yet, characterisation and quantification of the oxidative power of the interior and surface reservoirs and of the fluxes between them have received comparatively little attention.

To examine and quantify mass balances and fluxes of the deep Earth oxygen cycle, we adopt the Redox Budget (*RB*) formalism proposed first by Evans (Earth-Science Reviews 113, 11-32, 2012), where the *RB* is given in moles of electrons required to bring a mass back to the reference state:

$$RB = \sum_i n_i v_i \quad , \quad (1)$$

where n_i is the number of moles of a species i in a reservoir and v_i is the number of electrons required to take one atom of species i to its reference state. The reference states for redox-sensitive elements are taken to be the predominant valences of elements in the mantle: Fe^{2+} , C^0 , Cr^{3+} , and S^{-2} . *RB*, is positive for materials more oxidized than the reference state and negative for those more reduced, is an extensive quantity, applicable to reservoirs and fluxes.

The *RB* of the exosphere totals $4.2 \pm 0.5 \times 10^{22}$ moles and is dominated by carbonate (71.4 %), ferric iron (24.6 %), and sulphur (sulphate and FeS_2) (3.6 %). Atmospheric dioxygen

contributes only 0.4 % of the total. The *RB* of the mantle is equal to $19 \pm 5 \times 10^{22}$ moles and consists chiefly of Fe_2O_3 (95.7 %), which we take based on the assumption that the average $\text{Fe}^{3+}/\text{Fe}^{\text{T}}$ of the mantle is 0.04 ± 0.01 . Oxysulphide liquid, Cr^{2+} , and carbonate contribute small adjustments to the total mantle *RB*. Therefore, 82 ± 4 % of the *RB* of the bulk silicate Earth (BSE) is in the mantle.

RB outfluxes over the last 200 Ma, calculated with the aid of the GPlates tectonic reconstructions (Wong *et al.*, *Frontiers Earth Sci.* 7, 263, 2019), total $38 \pm 7 \times 10^{12}$ mol/yr, occur at ridges (61 %), oceanic islands (18 %), and intracontinental rifts (21 %), and consist chiefly of magmatic Fe_2O_3 (34 %) and CO_2 degassing (65.7 %). The return flux via subduction over the last 200 Ma is $49 \pm 13 \times 10^{12}$ mol/yr, taken from Evans (2012) and modified with the GPlates reconstruction to adjust for temporal changes in the delivery of sedimentary carbonate and in the net rate of plate convergence. Subducting *RB* fluxes are mostly in the form of Fe_2O_3 (44 %) and CO_2 (24 %).

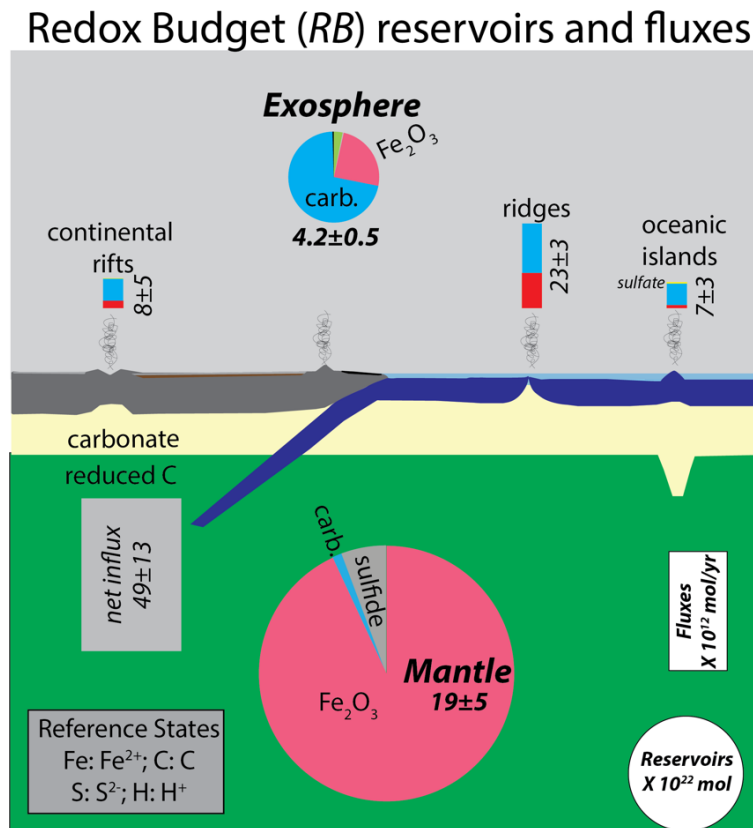
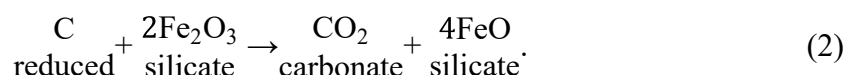


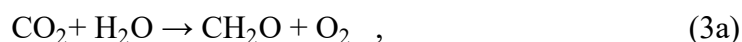
Fig. 3.2-9: Redox budget (*RB*) reservoirs and fluxes for the recent (~ 200 Ma) deep Earth oxygen cycle. Values are in moles of electrons relative to the reference oxidation states of the elements (see text and Evans, 2012, *Earth-Science Reviews*, 113, 11-32). The net influx at subduction zones is the sum of fluxes into the mantle after taking into account the return of oxidants to the surface environment from volcanic and non-volcanic arc fluxes. Reservoirs and outfluxes are color-coded by chemical species, but minor contributions (*e.g.*, atmospheric O_2 , pyrite, sulphate, CrO) are not necessarily illustrated or labeled.

Based on these fluxes and mass balances, the modern outflux is sufficient to supply the entire exosphere *RB* oxidative reservoir in 1.1 ± 0.2 Ga, far less than the age of the Earth. As is the case for C, which has a similarly brief replenishment time, this brief characteristic time indicates that deep Earth oxygen is a dynamic cycle, with large fractions of the whole-Earth oxidative power exchanging between the mantle and surface multiple times over the course of Earth's 4.6 Ga history.

At present, *RB* influxes and outfluxes are approximately in balance, though further refinements could feasibly indicate that the mantle is currently receiving a net influx of oxidizing power. However, outfluxes are dominated by CO_2 , whereas the main influx species is Fe_2O_3 . This suggests a cycle in which a significant fraction of the cycling redox power is transferred from iron to carbon in the mantle and from carbon back to iron on the surface. As a generalization, this relationship can be thought of as two conjugate reactions (Fig. 3.2-10), the first of which occurs as carbonate is created from Fe_2O_3 in upwelling upper mantle



The second reaction occurs in two stages: Initially CO_2 is converted to organic carbon via photosynthesis



and then free oxygen is consumed by oxidative weathering, producing Fe_2O_3



Mantle redox is generally considered in terms of oxygen fugacity, $f\text{O}_2$, a measure of chemical potential, instead of mass balance metrics such as the *RB*. Temporal and spatial variations in mantle oxygen fugacity are subject to intensive study and vigorous debate and oxidized fluxes from the surface are a potential source of redox variations in the mantle, at least locally. The influence of *RB* inputs on variations in mantle $f\text{O}_2$ can be parameterized with a suitable conversion between the *RB* content of peridotite and the $f\text{O}_2$. Taking into account Fe_2O_3 partitioning between phases in lherzolite and applying spinel peridotite and garnet peridotite oxybarometers gives an approximate relationship between the fraction of ferric iron in bulk peridotite, $(\text{Fe}^{3+}/\text{Fe}^{\text{T}})$ and $f\text{O}_2$,

$$\Delta \log f\text{O}_2 = \frac{1}{4} \Delta \log (\text{Fe}^{3+}/\text{Fe}^{\text{T}}). \quad (4)$$

The effects of mantle-surface exchange of oxidants can be evaluated by application of Eqn. 4. For example, if the oxidized surface reservoir is assumed to have accumulated over geologic time from mantle outfluxes, without open-system fluxes to space or the core, then (without adjusting for the effects of secular cooling on mantle $f\text{O}_2$) the mantle would have become commensurately more reduced with time. If the oxidants came uniformly from the entire

mantle, or from the depleted MORB (mid-ocean ridge basalt) source (80 % of the mantle) this decrease would have amounted to reduction equal to $\Delta \log fO_2$ of -0.4 or -0.5, respectively. These relatively small differences may not be resolved easily from the rock record, however surveys of secular changes of mantle oxygen fugacity have concluded either that fO_2 has not changed or has become more oxidized with time.

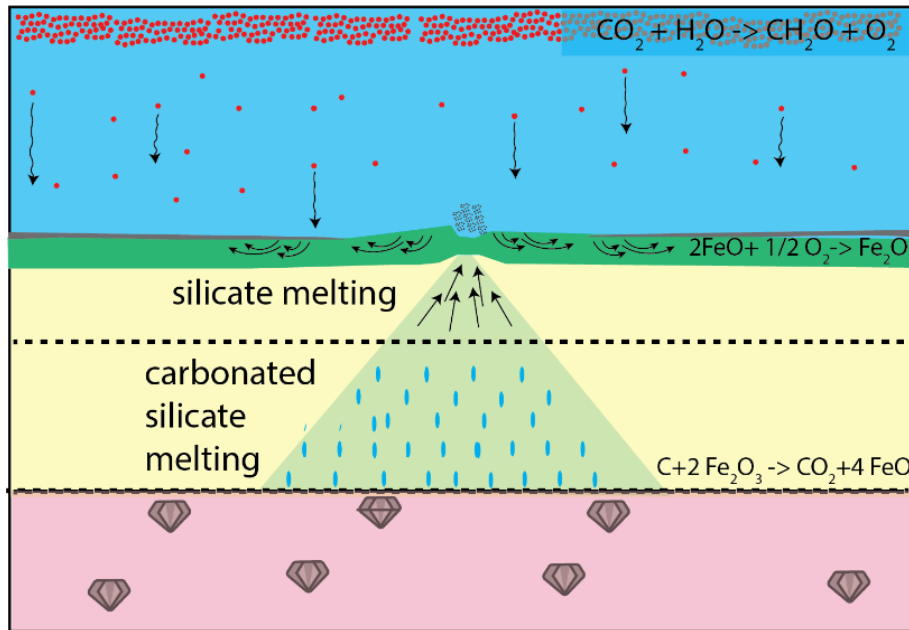


Fig. 3.2-10: Cartoon illustrating the principal reactions influencing redox influxes and outfluxes in the modern Earth. The oxidized outfluxes are dominated by outgassing of CO_2 , which originates from conversion of mantle Fe_2O_3 to FeO in the deep upper mantle, as reduced carbon (diamond) is converted to carbonate (Eqn. 2). The oxidized influxes are dominated by Fe_2O_3 in subducting lithosphere, which is created by a combination of formation of organic matter (converting CO_2 to CH_2O and producing O_2 , Eqn. 3a) and oxidative weathering of the oceanic crust (binding O_2 to FeO to form Fe_2O_3 , Eqn. 3b).

Recycling of surface materials has produced oxidized domains in the mantle, including especially those associated with subduction. Evidence of deeper cycling of oxidants is potentially shown in the source regions of oceanic island basalts, which have enhanced Fe^{3+}/Fe^T but more significantly, are also enriched in CO_2 . In combination, these suggest that OIB source regions have RB enhanced by a factor of 1.5-3 as compared to depleted upper mantle. If the lower mantle reservoir of OIB source regions comprises 20 % of the entire mantle (Arevalo *et al.*, EPSL 278, 361-369, 2009) and if this enhanced RB derives entirely from recycling, then the recycled RB residing in the deep mantle would have to comprise between 0.4 and 1.6 of the present-day exosphere RB . Such massive net influx of RB may be unlikely, and may imply that some portion of the enhanced RB residing in OIB source regions derives from a primordial source. For example, oxidized lower mantle originating from iron disproportionation forced by bridgmanite crystallization.

It is well-established that compared to cosmochemical (metal-saturated) source materials, Earth's mantle became oxidized during its early differentiation. Recently, it has been argued that secular evolution of the mantle between the early Archaean and mid Proterozoic raised mantle fO_2 by a further 1.5 log units. This evidence, based chiefly on V partitioning, is controversial, but if accurate requires that the RB of the mantle has more than doubled over this time interval, from > 0.02 to its present value (0.04 ± 0.01). There are few tenable processes that could potentially account for such a large shift, though gradual mantle mixing of a deep primordial oxidized layer should be considered.

h. *An experimental investigation of the role of NiS in controlling the O content of sulphide melts in the Earth's upper mantle (M.I. Hamadi, S. Abeykoon, A. Néri and D.J. Frost)*

Iron-nickel sulphide minerals are the most common inclusions in diamonds and act as an important reservoir for siderophile and chalcophile elements in the upper mantle. It is plausible that these inclusions were initially trapped as sulphide melts. This is supported by the fact that at least some of these inclusions have reported oxygen contents, whereas oxygen is hardly soluble in sulphide minerals. If these sulphides were initially trapped as melts, then their oxygen contents may help to reveal their formation conditions. Previous experiments have shown that sulphide melt oxygen contents are dependent mainly on the temperature and the FeO contents of coexisting silicates. The presence of Ni also seems to reduce the oxygen content. However, experiments involving Ni have also resulted in a decrease in the sulphur/metal ratio of the melts, creating uncertainty about the individual effect of Ni alone.

To examine whether and how Ni influences the oxygen content of sulphide melts, we performed high-pressure and -temperature experiments using a multianvil, employing iron sulphide samples with various nickel sulphide mole fractions, $X_{NiS} = 0.5, 0.75,$ and 1.0 , coexisting with olivine and orthopyroxene assemblages. We performed the experiments at temperatures and pressures ranging from 1300 to 1400 °C and $5-7$ GPa, respectively, in graphite capsules. The recovered samples were polished and analysed for their chemical composition using an Electron Probe Micro Analyser (EPMA).

Our results show that the presence of NiS does have an influence on the oxygen content of the sulphide melt. We observed a relatively small decrease in the O content in the sulphide melt with increasing NiS content up to $X_{NiS} = 0.75$ (Fig. 3.2-11). When X_{NiS} exceeds 0.75 , there is a very slight increase in the O content, but this is within the analytical uncertainties. Also plotted in Figure 3.2-11 are oxygen analyses of sulphide inclusions found in natural diamonds. As shown, some of these Ni-rich inclusions have very high O contents, which cannot be explained as an effect of Ni on the O content of the melt. It is possible that some of these natural samples became oxidized or that oxide-rich phases fractionally crystallized from the melt and became over abundant compared to the initial melt. Further analyses of diamond sulphide inclusions would be required to understand the origin of these high oxygen contents.

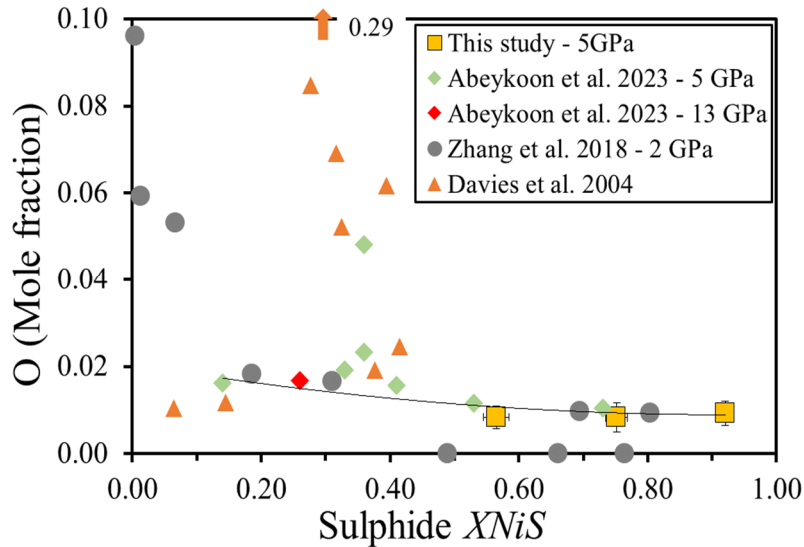


Fig. 3.2-11: Relationship between oxygen mole fraction in sulphide melts with NiS mole fraction in this study compared to previous experimental studies (Zhang *et al.*, 2018, Contrib to Mineral Petrol 173, 19; Abeykoon *et al.*, 2023, Contrib to Mineral Petrol 178, 13) and natural diamond samples (Davies *et al.*, 2004, Lithos 77, 39-55). The trend line is derived from this study and previous studies. Each symbol represents a different study and the arrow points to an exceptionally high O mole fraction (0.29) observed in a natural diamond sample.

i. Peridotite–carbonatite reaction experiments: Testing the validity of chemical fingerprinting of mantle metasomatism (C. Shaw/Fredericton)

Metasomatic enrichment of lithospheric mantle by percolating melts or fluids is a significant contributor to element fluxing in subduction zones, intra-plate volcanic settings and rifts. Studies of peridotite xenoliths from these tectonic settings attempt to characterise the history of the lithospheric mantle and the nature of the metasomatic agent or agents by examining the texture, mineral assemblages and mineral compositions of the xenoliths. Most recent studies indicate that either silicate or carbonatitic magmas are the main agents involved in reactions in the lithospheric mantle. Since the composition of these two magma types is very different, several chemical parameters have been suggested in the literature to allow petrologists to differentiate between them. In particular, the Ca/Al, La/Yb and Ti/Eu ratios in clinopyroxene have been suggested to be reliable indicators of the nature of the metasomatic agent, with Ca/Al > 5 and Ti/Eu < 1500 being indicative of carbonatite metasomatism and vice versa for silicate melt induced metasomatism.

This study examines the reaction of spinel peridotite and single crystals of olivine, clinopyroxene and orthopyroxene with a model carbonatite melt at 1 GPa and 1000-1100 °C using the piston cylinder apparatus. There are two preliminary observations: 1) Both peridotite–silicate melt and peridotite–carbonate melt interaction experiments result in secondary

clinopyroxene that is depleted in aluminium and the resulting Ca/Al ratios are > 5 , indicating that this parameter is not a reliable indicator of the composition of the agent of metasomatism. 2) Peridotite–carbonatite reaction experiments produce all of the secondary minerals observed in natural peridotite xenoliths, *i.e.*, phlogopite, amphibole, and clinopyroxene as well as a CO₂-rich glass. The next phase of the study will examine the trace element content of the secondary minerals to determine if the commonly used fingerprints of carbonatite metasomatism are in fact reliable.

j. *The effect of phengite and apatite on the mobility of trace elements in subduction zones (G. Rustioni, A. Audétat and H. Keppler)*

Eclogites often contain some accessory minerals that may strongly concentrate certain trace elements and affect their behaviour during melting and fluid extraction. It is well established that the presence of rutile helps to retain high field strength elements such as Nb, Ta, and Zr in the solid residues. Sometimes, a similar role is attributed to phengite in retaining large ion lithophile elements such as Rb, Cs, Sr, or Ba while apatite may perhaps control the behaviour of light rare earth elements. For these reasons, it is sometimes believed that simple model compositions that do not include these accessory phases may not be representative for the behaviour of trace elements during melting or fluid release in subducted slabs.

We have tested the effect of phengite and apatite on the behaviour of trace elements in a subduction environment by carrying out piston cylinder experiments with a K- and P-doped MORB starting material at 4 GPa and 800 °C in the presence of an excess hydrous fluid phase. During the experiments, an eclogitic assemblage with omphacite, garnet, and traces of rutile was formed, plus accessory phengite and apatite. The compositions of the coexisting minerals were measured by electron microprobe for major elements and by laser-ablation ICP-MS for trace elements. From the data obtained, the partition coefficients of trace elements between various solid minerals were calculated.

Figure 3.2-12 shows results for the phengite/omphacite partition coefficients of the alkali and heavy alkaline earth elements. As expected, phengite does indeed concentrate Rb, Cs, Sr, and Ba relative to omphacite. However, the partition coefficients range only from close to 10 to less than 100. On the other hand, natural MORB contains on average only 0.16 wt. % K₂O, which is required to form phengite. This translates into at most about 1 wt. % phengite in the eclogitic assemblage – in reality, it will be considerably less since K is also appreciably soluble in omphacite. A simple mass balance then shows that at a phengite/omphacite partition coefficient between 10 and 100, most of Rb, Cs, Sr, and Ba is still contained in the major minerals of the eclogite, in particular in omphacite. This means that the behaviour of these elements during melting and fluid extraction will not change fundamentally in the presence of phengite. Changes in the abundance of elements such as Cs or Ba in arc volcanics with increasing depths of the

subducted slab should therefore not be attributed to the decomposition of phengite, as it was sometimes suggested.

For apatite and the light rare earth elements, the conclusions are similar. Apatite does indeed concentrate La and Ce relative to omphacite, but again, the partition coefficients are not high enough to make apatite the primary host of these elements in eclogite.

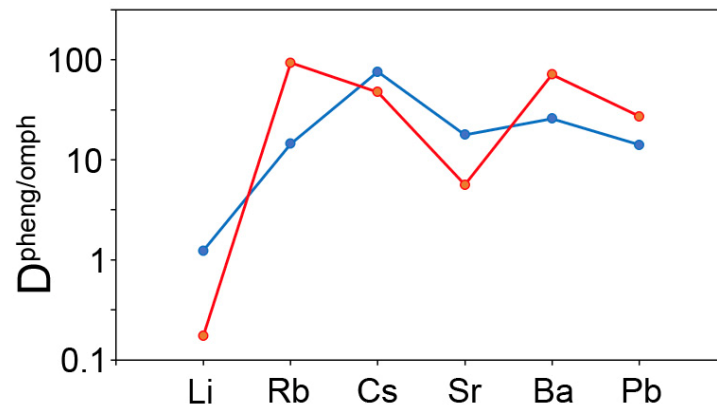


Fig. 3.2-12: Phengite/omphacite partition coefficients of alkali and alkaline earth elements as determined in two experiments at 4 GPa and 800 °C.

k. *The gold content of mafic to felsic potassic magmas (J. Chang and A. Audétat, in collaboration with T. Pettke/Bern)*

About 40 % of the largest Au-rich epithermal and porphyry deposits on Earth are related to potassic igneous rocks, which comprise only 5-10 vol. % of arc igneous rocks. Therefore, potassic magmas are commonly assumed to have been exceptionally Au-rich or to have contained high Au/Cu ratios. However, these hypotheses remain poorly tested. Available evidence is largely based on whole-rock analysis of mafic to felsic potassic porphyry dikes or terrestrial volcanic lavas. Since these rocks cooled relatively slowly after magma emplacement, significant loss of Au may have occurred during magma degassing. The Au content of whole rocks can get modified also by hydrothermal alteration or by magmatic assimilation of Au-rich crustal materials. Melt inclusions, which are tiny parcels of silicate melt trapped in crystallizing minerals, provide a way to circumvent these issues. Nevertheless, melt inclusion studies are rare, mostly because it is challenging to analyse Au concentrations at parts per billion levels in samples weighing only a few tenths of a microgram.

In this study, we report Au concentrations and Au/Cu ratios in melt inclusions from more than a dozen mafic to felsic potassic igneous rocks worldwide, analysed by state-of-the-art laser-ablation inductively-coupled-plasma mass-spectrometry. To independently quantify the Au and Cu contents of variously evolved potassic magmas using numerical models, we also performed

piston cylinder experiments to constrain the behaviour of sulphides during mantle partial melting and subsequent magma crystallization. Measured Au concentrations in olivine-hosted melt inclusions suggest that mafic potassic magmas contain only 2-7 ng/g Au (Fig. 3.2-13a), whose values agree with the Au content of 1-10 ng/g estimated for primitive potassic melts based on mantle partial melting models. Both the absolute Au contents and Au/Cu ratios of potassic magmas are comparable to those of mafic calc-alkaline magmas (Fig. 3.2-13), and they vary little during magma differentiation because magmatic sulphide precipitation is strongly dominated by monosulphide solid solution (Fig. 3.2-14). We thus suggest that the close association of Au-rich deposits with potassic magmas reflects selective Au precipitation at the hydrothermal stage and/or selective fluid–melt partitioning rather than Au enrichment in the magma.

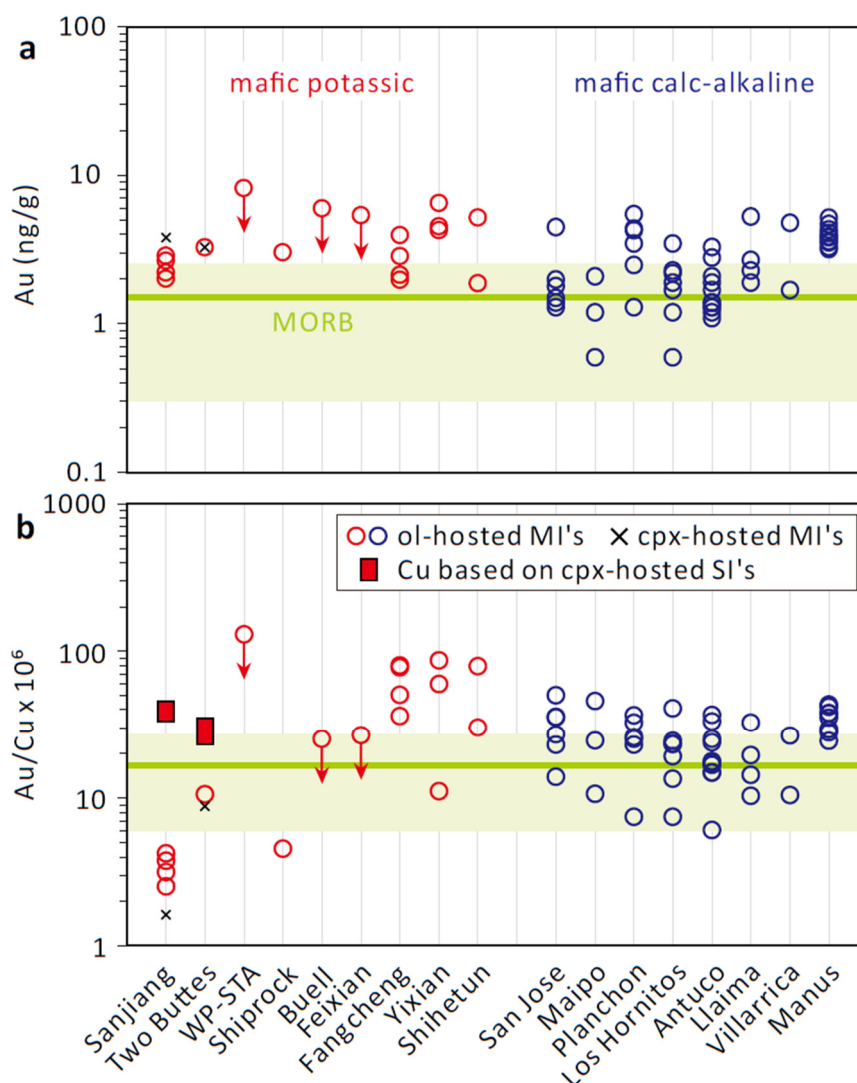


Fig. 3.2-13: Gold content and Au/Cu ratio of mafic potassic versus mafic calc-alkaline magmas. The data of calc-alkaline basalts and mid-ocean ridge basalts (MORB) are taken from literature. Abbreviations: ol, olivine; cpx, clinopyroxene; MIs, melt inclusions; SIs, sulphide inclusions.

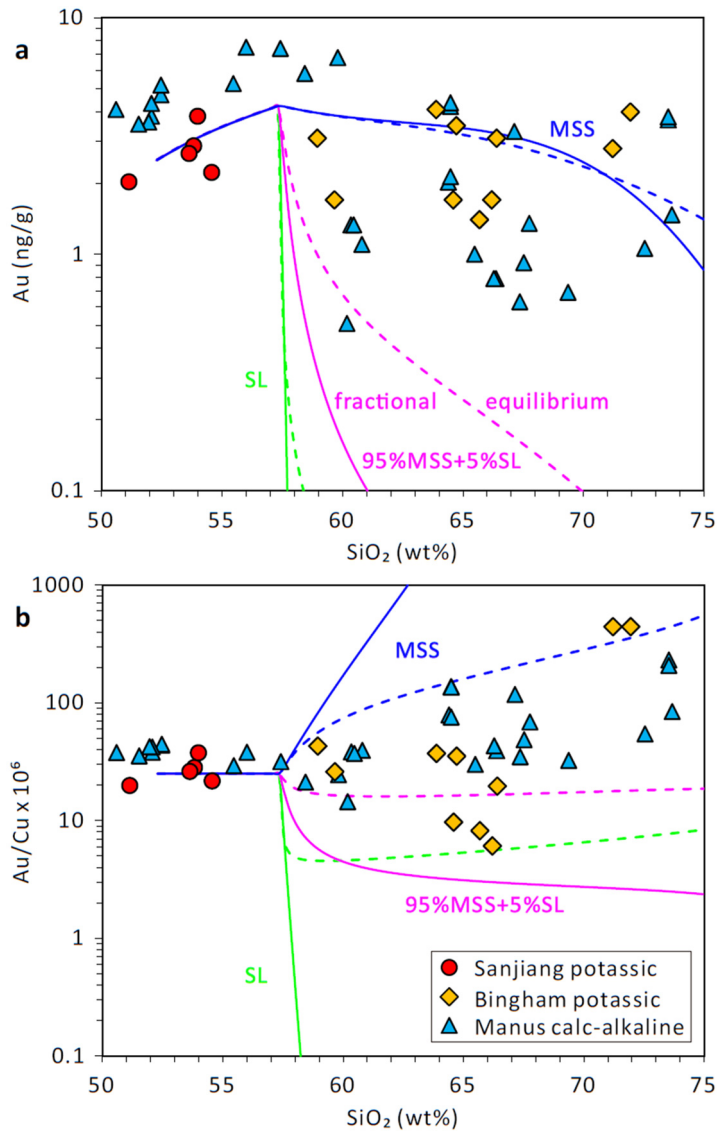


Fig. 3.2-14: Gold contents and Au/Cu ratios of variously evolved potassic versus calc-alkaline melts. The data of Bingham potassic magmas and Manus calc-alkaline magmas are taken from the literature. The curves show quantitative modelling results based on crystallization experiments of a Sanjiang mafic potassic magma and experimentally constrained $D^{MSS/SM}$ and $D^{SL/SM}$ of Cu and Au, with solid lines reflecting pure fractional behaviour of the sulphides, and dashed lines pure equilibrium behaviour. MSS, mono-sulphide solid solution; SL, sulphide liquid.

I. Common anhydrite saturation in Laramide-age arc magmas in southwestern USA (A. Audétat and J. Chang)

Magmatic anhydrite has previously been reported from twelve arc volcanoes and twelve intrusive centres, with the latter also being arc-related and in most cases being genetically related to porphyry Cu mineralization.

Due to instability of anhydrite in (near-) surface environments, phenocrystic magmatic anhydrite can be found only in very fresh volcanic rocks or in deep drill holes. Anhydrite present in fresh volcanic rocks shows a strong spatial association with apatite, with most anhydrite phenocrysts being intergrown with apatite crystals, and apatite microphenocrysts commonly containing inclusions of anhydrite. During alteration and weathering, anhydrite phenocrysts get dissolved, leaving behind either lath-shaped voids, or cavities that have subsequently been filled with secondary minerals such as microcrystalline silica (Fig. 3.2-15a)

or calcite (Fig. 3.2-15b). The occurrence of lath-shaped cavities that show a strong spatial association with apatite microphenocrysts in otherwise fresh or only little-altered rocks (*i.e.*, feldspar and mafic minerals being still intact) is thus a clear indication of the presence of former anhydrite phenocrysts.

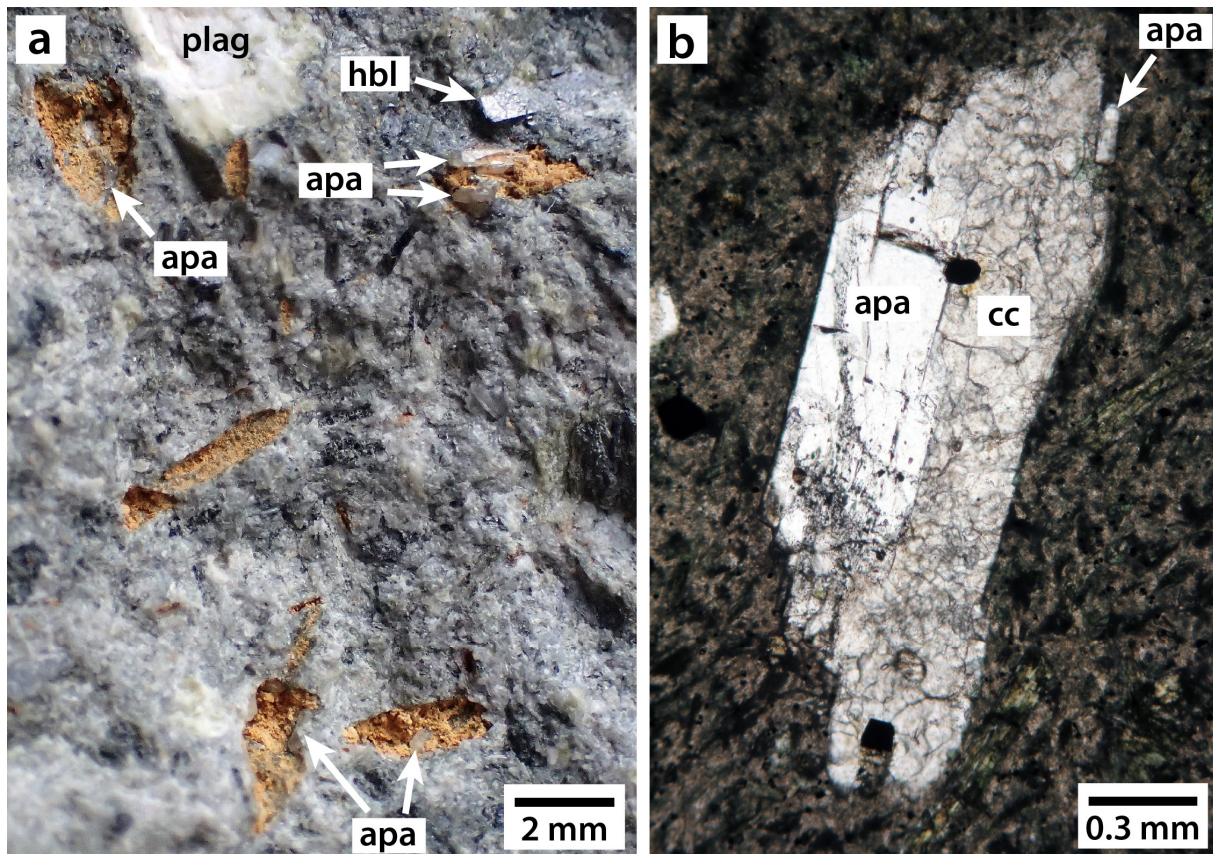


Fig. 3.2-15: (a) Photograph of a hand specimen of a porphyry dike at Santa Rita, showing five former anhydrite phenocrysts that were replaced by orange-colored, microcrystalline silica. Notice the strong spatial association with apatite microphenocrysts and the good preservation state of hornblende and plagioclase phenocrysts. (b) Transmitted-light image of a thick section of another porphyry dike nearby, in which the anhydrite was replaced by polycrystalline calcite. Notice again the spatial association with apatite microphenocrysts. Apa – apatite; cc – calcite; hbl – hornblende; plag – plagioclase.

During a recent field trip to Arizona and New Mexico, more than 300 samples were collected from 16 Laramide-age magma systems (Santa Rita–Hanover Fierro, Tyrone, Morenci, Safford, San Manuel, Christmas, Chilito, Ray, Globe-Miami, Pine Flat, Copper Basin, Bagdad, Ajo, Crown King, Diamond Joe Peak, Granite Peak). Out of these 16 magma systems, 14 produced porphyry Cu mineralization. At all but two locations (Bagdad and Morenci, where most of the collected samples are highly altered), samples containing lath-shaped cavities associated with apatite microphenocrysts were found, suggesting that the magmas were anhydrite-bearing.

However, it is unclear whether magmatic anhydrite is a distinctive feature of porphyry Cu-mineralizing magmas, as also the two sampled barren magma systems (Crown King and Diamond Joe Peak) show evidence for the former presence of anhydrite phenocrysts, and because the features described above are easily missed if one does not specifically look for them. Hence, it is possible that also other non-mineralizing, intermediate to felsic arc magmas were saturated in anhydrite, and that this is a common feature of arc magmas in general.

m. *An experimental study on the partitioning of gallium in felsic magmatic systems (M. Hlede and H. Keppler)*

Gallium is a critical element in various technological semiconductor applications ranging from aerospace and telecommunication industry to medical equipment. As such, the already extensive use of gallium is only expected to increase in the future. However, gallium is currently exclusively produced as a byproduct from sphalerite and bauxite ores. In order to better understand the enrichment processes of gallium that may perhaps lead to minable deposits, the general geochemistry of gallium needs to be better understood. Here, we investigate whether the crystallization of a granitic magma could lead to an enrichment in gallium. In addition, we inspected the behaviour of indium in the same system.

Three types of experiments were performed. For the solubility experiments, cold-seal pressure vessels (CSPV) and piston cylinder presses (PC) were used. Here, a haplogranitic glass was loaded into Pt capsules together with water and Ga₂O₃. A series of mineral–melt (CSPV and PC) and fluid–melt partition experiments were also performed. In the fluid–melt runs, the same haplogranitic glass was used with the addition of Ga₂O₃, In₂O₃ and Na/KCl–H₂O solution, whereas in mineral–melt runs, a glass of realistic granite composition (containing Ga₂O₃ and In₂O₃) was produced and loaded into Au capsules together with water. The run products were investigated using SEM, XRD powder analysis, EMPA and LA-ICP-MS.

In the solubility experiments, we observed white patches of powder inside the quenched glass, representing some Ga₂O₃ (Fig. 3.2-16a) that was not dissolved in the melt. Ga₂O₃ solubility in haplogranitic melt is significant (on the order of several wt. %) and strongly increases with temperature, corresponding to an enthalpy of the dissolution reaction of $\Delta H = 24$ kJ/mol. Mineral–melt partitioning experiments yielded rather small crystals of quartz, plagioclase, orthoclase, biotite, hornblende, and ilmenite, immersed in a glass phase (Fig. 3.2-16b). In general, we note that Ga partitions strongly into biotite ($D^{\text{biotite/melt}}$ ranges from 1.1 to 2.8), possibly substituting Al. It is moderately compatible in both feldspars ($D^{\text{orthoclase/melt}}$ ranges from 0.9 to 1.6, $D^{\text{plagioclase/melt}}$ ranges from 1.5 to 2) and does not readily enter hornblende, quartz, and ilmenite. Indium on the other hand, seems to strongly partition into hornblende and moderately in orthoclase, while being mostly incompatible with the other minerals. Fluid–melt experiments proved to be difficult, leaving only one sample suitable for analysis. We found that both Ga and In partition preferentially into the melt. Our results suggest that the crystallization of a granitic

magma is unlikely to produce residual melts with high Ga enrichment, and strong Ga partitioning into a fluid is likely possible only at very high fluid salinities. These observations suggest that magmatic enrichment of Ga to economic grades will hardly occur in granitic systems.

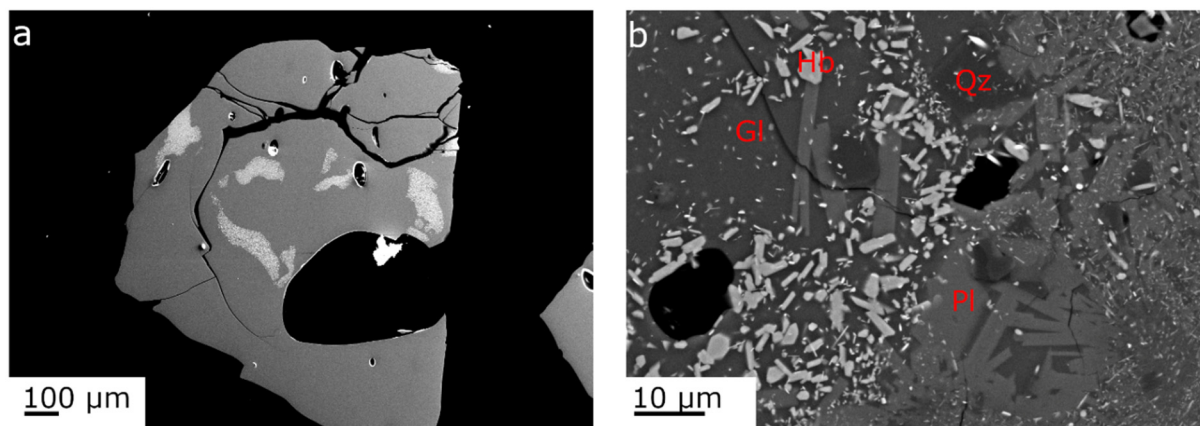


Fig. 3.2-16: SEM images of representative samples from experiments on Ga_2O_3 solubility in melts and on Ga mineral–melt partitioning. a) Solubility experiment: White patches represent undissolved Ga_2O_3 powder inside the glass phase. b) Mineral–melt partitioning experiment: Gl – glass, Qz – quartz, Hb – hornblende, Pl – plagioclase.

n. *Experimental investigation of the stability of calcite in rhyolitic melts (C. Timoner and A. Audétat)*

Calcite has been found as an inclusion in magmatic quartz phenocrysts of granodiorite porphyry dikes related to the porphyry Cu deposit at Santa Rita, New Mexico, USA (Fig. 3.2-17A and B). These granodiorite porphyry dikes represent mechanical mixtures of rhyolitic and mafic magmas, with the quartz phenocrysts belonging to the rhyolitic member. The latter magma was also saturated in magmatic anhydrite. A previous thermodynamic study suggested that the stability of calcite in rhyolitic silicate melts is governed by the position of the reaction quartz + calcite = wollastonite + fluid relative to the granite solidus curve, and that the formation of calcite requires minimum pressures of 3.5-4.0 kbar at temperatures of 650-750 °C. However, thermobarometric data obtained from the naturally occurring calcite-bearing phenocrysts (zircon saturation temperatures of melt inclusions, in combination with Ti-in-quartz thermobarometry of the quartz host) suggest entrapment pressures of only 2.0-2.7 kbar at 725 °C (Fig. 3.2-17C and D).

To test the reliability of these thermobarometric data, and to better understand the controls on calcite stability in rhyolitic melts, we performed piston-cylinder and rapid-quench hydrothermal equilibrium experiments at 705-740 °C and various pressures and water and Cl contents in the rhyolite. The starting material, a well-characterised, natural rhyolitic glass, was mixed with small amounts of calcite, anhydrite, NaCl, and water to mimic the components of the naturally occurring melt inclusions. The run durations ranged from 4.5 to 6 days. The run

products consisted mostly of glass, feldspar, quartz and fluid bubbles composed of H₂O-CO₂ or H₂O-CO₂-NaCl fluids; with minor anhydrite, titanite, diopside-hedenbergite, garnet, wollastonite, and calcite. When present, calcite appeared as rounded crystals of 5 μm diameter, which is considerably bigger than ≤ 3 μm grain size of the starting CaCO₃ powder and thus clearly demonstrates that calcite was stable. The different mineral phases were identified by optical microscopy (Fig. 3.2-18A) SEM-EDS, and Raman spectroscopy (Fig. 3.2-18B). The CO₂ content of the fluid phase was calculated based on the filling ratios of fluid inclusions observed by optical microscopy, and by mass balance as calcite was the only CO₂ source. Moreover, glass and mineral EPMA analyses were performed for the most representative runs. For experiments performed without NaCl, calcite was present only at pressures above 4 kbar. For NaCl-bearing experiments, on the other hand, calcite appeared in runs at pressures as low as 2.5 kbar. However, the experiments are poorly reproducible due to complex interplays between the amounts of added H₂O and CaCO₃, the extent of magma crystallization, and the H₂O/CO₂ ratio developing in the excess fluid phase.

The experimental results suggest that the presence of NaCl (which made up 5 wt. % of the CO₂-free starting fluid composition) was the key to lower the pressure of the reaction quartz + calcite = wollastonite + fluid (Fig. 3.2-19). Although the specific mechanisms of this interaction remain unsolved, a similar effect has been experimentally demonstrated for the reaction Cc + Qtz = Tit + CO₂, and in thermodynamic calculations related to skarn formation.

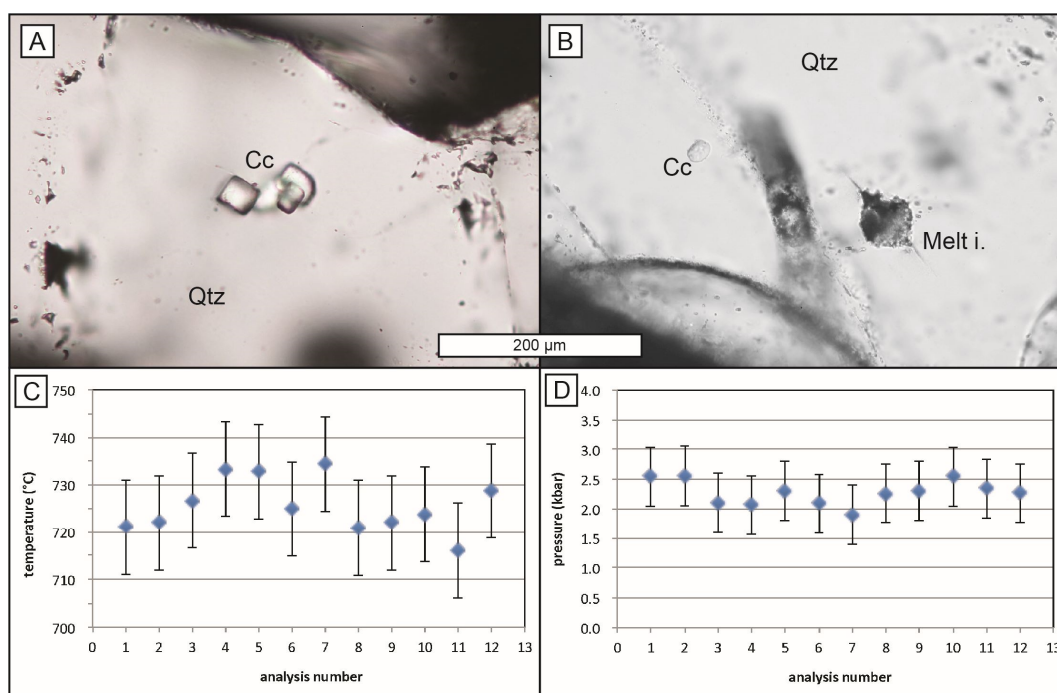


Fig. 3.2-17: Optical microscope images of quartz phenocrysts from Santa Rita. A: Fission-free calcite inclusion aggregate entrapped in quartz. B: Small calcite inclusion (left-side) trapped in the same quartz phenocrysts as a melt inclusion (right side). C, D: Thermobarometric data obtained from the same quartz phenocrysts. Cc – calcite; Qtz – quartz.

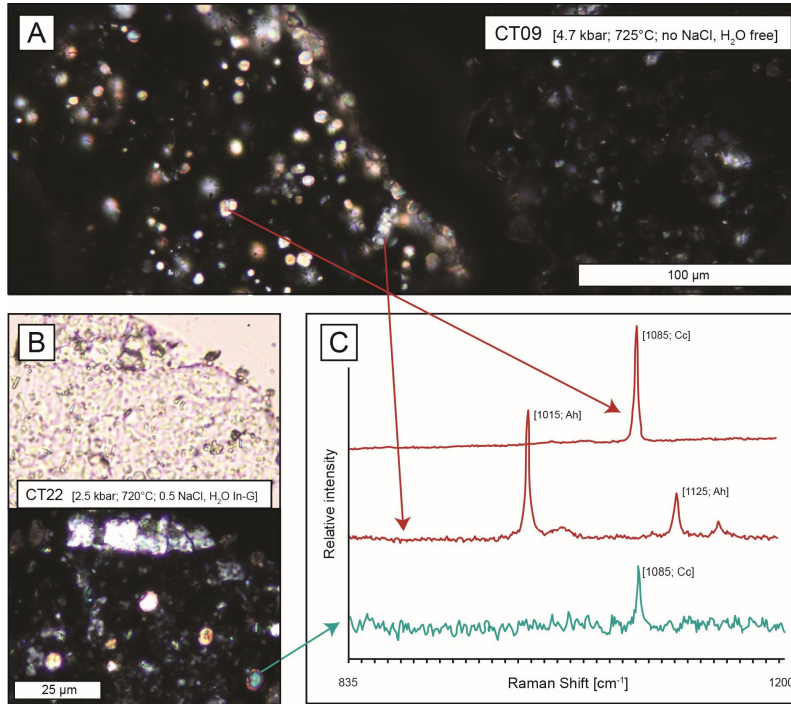


Fig. 3.2-18: Optical microscope images and Raman spectra of magmatic calcite and anhydrite. A: Cross-polarised transmitted-light image of two glass pieces recovered from an experiment conducted at 4.7 kbar, 725 °C. B: Non-crossed and crossed-polarised transmitted-light image of a glass piece recovered from an experiment conducted at 2.5 kbar, 720 °C. C: Raman spectra obtained from individual calcite and anhydrite crystals in these two runs.

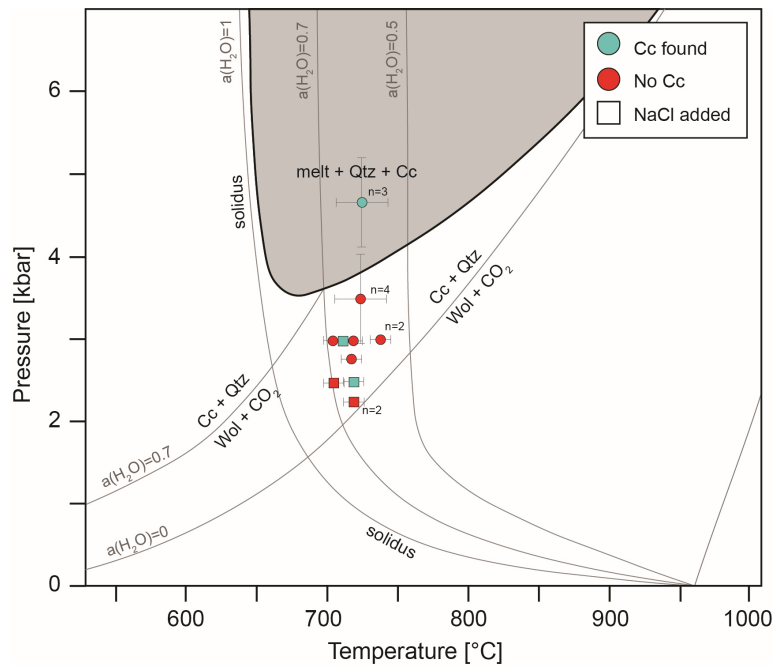


Fig. 3.2-19: Phase diagram showing the thermodynamically predicted stability of magmatic calcite in a previous study (grey field), versus the experimentally observed stability of magmatic calcite in the present study.

o. *Sn isotope fractionation of cassiterite during magmatic-hydrothermal processes (J. Wu and H. Li/Changsha, R. Mathur/Huntingdon, A. Bouvier, W. Powell/Brooklyn, K. Yonezu/Fukuoka and D. Zhu)*

Tin is a crucial metal for numerous high-tech industries. It also has the highest number of stable isotopes and varying valences between fluids and minerals within the Earth's crust. To date, Sn stable isotopes have served as powerful tracers in archaeology, cosmochemistry, and magmatic processes. Recent research shows that Sn isotopes in planetary and terrestrial samples exhibit significant differences and potentially have higher isotope fractionation than previously thought. As the primary Sn-enriched mineral, cassiterite (SnO_2) appears in various geological settings linked to evolved magmatic-hydrothermal processes. The geochemical changes within cassiterite make it a novel indicator for physicochemical conditions. However, the variations in Sn isotopic compositions and the fractionation mechanisms of cassiterite remain to be fully understood. The Xianghualing Sn-polymetallic deposit in South China was chosen as the research subject due to its highly evolved magmatic-hydrothermal system enriched with critical metals. The study aimed to investigate the Sn isotopic compositions of different generations of cassiterite.

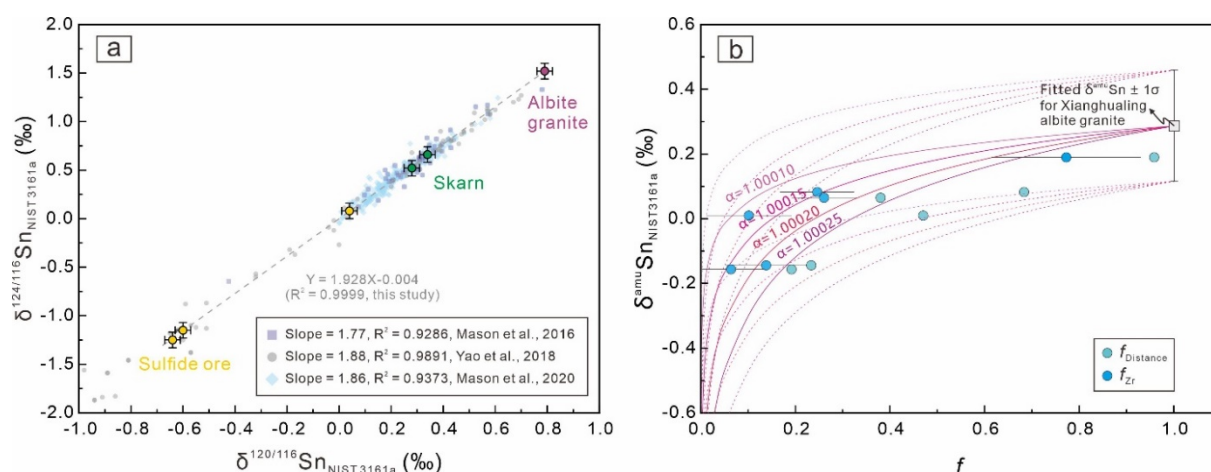


Fig. 3.2-20: (a) Sn isotopic signatures of the cassiterite samples from the Xianghualing deposit ($\delta^{124}\text{Sn} = 1.928 \cdot \delta^{120}\text{Sn} - 0.004$, $R^2 = 0.9999$). Mass-dependent fractionation slope is expected to be 2. (b) Rayleigh modelling results of the Xianghualing cassiterite Sn isotope fractionation.

Based on distinct morphologies and mineral paragenesis, three generations of Xianghualing cassiterites are identified: (1) Cst1 occurs in albite granite and greisen; (2) Cst2 occurs in skarn; and (3) Cst3 is present in sulphide ore. The Sn stable isotopic compositions in the Xianghualing cassiterite samples are notably fractionated among these three groups, with $\delta^{\text{amu}}\text{Sn}$ values (relative to standard NIST 3161a) of $0.19\text{‰} \pm 0.01\text{‰}$ from albite granite and greisen, $0.08 \pm 0.01\text{‰}$ from skarn, and $-0.10 \pm 0.08\text{‰}$ from sulphide ores, respectively (Fig. 3.2-20a).

Equilibrium fractionation can be excluded because of the slope of the fractionation between cassiterite and stannite during the magmatic-hydrothermal stages. The deviations in $\delta^{124}\text{Sn}$ values measured in the Xianghualing deposit are compared with those reported for other hydrothermal deposits. Together, these Sn isotopic data suggest that kinetic disequilibrium fractionation is the primary factor influencing cassiterite Sn isotope fractionation. A Rayleigh fractionation model generates fractionation factors of 1.00010-1.00025 (Fig. 3.2-20b), which align with fractionation factors predicted (1.00013 to 1.00037) for cassiterite that precipitated at 300-700 °C by first-principles calculations. Thus, the progressive precipitation of Sn-enriched minerals due to changes in physicochemical conditions during magmatic-hydrothermal processes results in lighter Sn isotopic compositions in the residual melt/fluid. Additionally, the elemental abundances of Zr, Hf, Nb, and Ta are identified as temperature indicators, while the changes in redox states can be traced by the concentrations and interelement ratios of Sb, Fe, V, and U. The determination of fractionation factors between Sn minerals and hydrothermal fluid under realistic physicochemical conditions by high T - P experiments will be important to better interpret the signatures obtained in cassiterites formed in various ore types.

3.3 Mineralogy, Crystal Chemistry and Phase Transformations

Minerals adjust to changes in their geological environments by changing their chemical compositions and, in extreme cases, their crystalline structures. The mineral chemistry and crystallographic features of both natural and experimental samples therefore reflect the physical-chemical conditions at which the mineral sample formed. Reading this record requires both a detailed study of natural samples and the experimental calibration of how certain conditions of pressure, temperature, oxygen fugacity, and other factors leave their imprint in the mineral record. This section highlights research projects in which we characterise mineral samples from natural high-pressure rocks or use high-pressure experiments with the aim of interpreting the information captured in minerals into models for deep-earth processes.

The first contributions in this section focus on the crystal chemistry of oxide minerals and the post-spinel phase transformation. The study of mantle xenoliths provides valuable links with the Earth's interior. Beltrame *et al.* are investigating mineral reactions involving spinel to develop a new geobarometer for spinel peridotite xenoliths. Natural diamonds and their mineral inclusions open a window into the deeper mantle. The amounts of trivalent elements, such as aluminium and chromium, in oxide phases, such as ferropericlase and magnetite, may contain information about the temperature and depth of formation of the host–inclusion pair. Man *et al.* report alumina solubility in periclase to understand the formation conditions of sublithospheric diamonds, which may act as tracers for carbon-bearing fluids or melts in Earth's mantle.

High-pressure Mg-Fe-oxides with stoichiometries of M_4O_5 and M_5O_6 may form inclusions in diamonds but decompose upon pressure release into mixtures of spinel and other phases. The iron end members Fe_4O_5 and Fe_5O_6 host iron cations in two valence states and may contribute to the mineralogy of the mantle as accessory phases. Schumann *et al.* found that the Fe_4O_5 -structured phase $Fe^{2+}_2(Fe^{3+},Cr)_2O_5$ can incorporate more chromium than the Fe_5O_6 -structured phase. The Fe_4O_5 phase is therefore more likely to be stabilized in rocks with typical Cr-contents of the mantle. The Mg-bearing counterpart of this system was studied by Woodland *et al.* with a similar result that chromium stabilizes the M_4O_5 phase at the expense of the M_5O_6 phase. Magnetite is a common phase among diamond inclusions. The effect of aluminium on the stability of magnetite and related phases at high pressures, however, is not well understood. Uenver-Thiele *et al.* experimentally mapped the phase relations for Al-bearing magnetite compositions. The resulting phase diagram may help explain the microstructures observed in magnetite-bearing diamond inclusions.

At a depth of 660 km, the seismic wave velocities in Earth's mantle change substantially over a very short depth interval. This discontinuity in seismic wave speeds is often explained by the post-spinel phase transformation, *i.e.*, the dissociation of spinel-structured ringwoodite into the lower-mantle minerals bridgmanite and ferropericlase. The exact depth of the discontinuity, however, varies with geographic location, presumably in response to the temperature of the mantle. Chanyshv *et al.* determined the Clapeyron slope of the post-spinel phase

transformation with high precision by using advanced high-pressure *in situ* synchrotron X-ray diffraction techniques. They found the slope for the FeO-MgO-SiO₂ system to be significantly steeper than for the Fe-free MgO-SiO₂ system. As a result, the depth variations of the seismic discontinuity at 660 km depth may indeed be explained by variations in mantle temperature.

The stability of certain key minerals may have implications for the geochemical cycles of volatile elements such as carbon by indicating a specific composition of coexisting fluids or by hosting volatile elements in their crystal structure. The organic mineral whewellite, for example, might indicate the presence of abiotic organic molecules in subduction zone fluids. Czekay & Keppler studied the dissolution and crystallisation of whewellite in water at high pressures to place constraints on the conditions at which whewellite may precipitate from subduction zone fluids. In its oxidised form, carbon may be bound in carbonate minerals, many of which may remain stable at pressures and temperatures of Earth's deep mantle. While the crystal structures of common low-pressure carbonate minerals are based on planar CO₃²⁻ groups, Dubrovinsky *et al.* report the synthesis and crystal structure of a magnesium carbonate phase, Mg₂CO₄, with tetrahedral CO₄⁴⁻ groups. Observed in diamond anvil cell experiments at pressures above 100 GPa, this Mg-rich tetracarbonate phase may host carbon at pressures equivalent to those in Earth's lower mantle.

In Earth's mantle, the oxidation state of carbon and hence the stability of C-bearing minerals depends critically on the prevailing oxygen fugacity. Xenoliths in kimberlites provide unique samples of Earth's mantle that may help to constrain the oxygen fugacity during their formation at depth. Marras *et al.* analysed the crystal chemistry of garnets and clinopyroxenes in xenolithic eclogites. Based on measurements of Fe³⁺/ΣFe ratios, they infer unusually high oxygen fugacities, which are consistent with the absence of diamonds in the xenoliths and highlight the variability of oxygen fugacity in the mantle. Much deeper in the mantle, most ferric iron is believed to be incorporated into the mineral bridgmanite. Wang *et al.* investigated the effect of pressure on the amount of ferric iron in bridgmanite and found that other factors, such as oxygen fugacity, temperature, and aluminium content, might have a stronger effect on ferric iron contents in bridgmanite than pressure.

The conditions at which a mineral formed might also be recorded in structures on the nano- and microscale. By comparing X-ray and electron diffraction patterns of omphacite grains from an eclogitic xenolith, Fukushima *et al.* detected evidence for incomplete cation ordering that might reflect the complex thermal history of the host eclogite. Some mineral phases, such as the calcium silicate perovskite davemaoite, are almost impossible to observe at ambient condition due to their rapid amorphization upon decompression. Nevertheless, Miyajima *et al.* succeeded in quenching a davemaoite sample and determined the symmetry and lattice parameters at ambient conditions using transmission electron microscopy. The quenched davemaoite domains retained their cubic symmetry and were probably protected from amorphization by the surrounding amorphous rims and rigid bridgmanite grains.

a. *Exploring the lithospheric mantle beneath central Mongolia: Constraints from spinel-bearing peridotite xenoliths and high-pressure experiments (M. Beltrame/Trieste and C.A. McCammon, in collaboration with L. Ziberna/Trieste, M. Masotta/Pisa and A. De Min/Trieste)*

The study of mantle xenoliths provides clues to understand the structure of Earth's interior, the mechanisms that generate mantle melts as well as the evolution of the lithosphere beneath regions where no samples have been exposed by tectonic activity. Xenolith composition, mineralogy, and texture provide clues to temperature, pressure, stress conditions, and melting or contamination events before or during entrapment in the host magma. This project focuses on spinel peridotite xenoliths from the magmatic province of Mandak-Mandal-Gobi, Central Mongolia that was active during the late Mesozoic to early Cenozoic (Fig. 3.3-1). By combining new data with those from xenoliths of nearby provinces in Central Asia, we aim to gain insight into links between lithospheric structure, thermal state, metasomatism and geodynamic evolution of this region. In particular, accurate estimates of pressure and temperature for these xenoliths will help answer the following questions: i) Are xenoliths derived from just below the crust-mantle transition zone or do they instead represent fragments sampled throughout the depth interval where spinel peridotites are stable?; ii) What are the vertical and lateral variations in lithospheric structure and thermal state in a region that underwent collisional processes followed by extensive anorogenic-type magmatism?

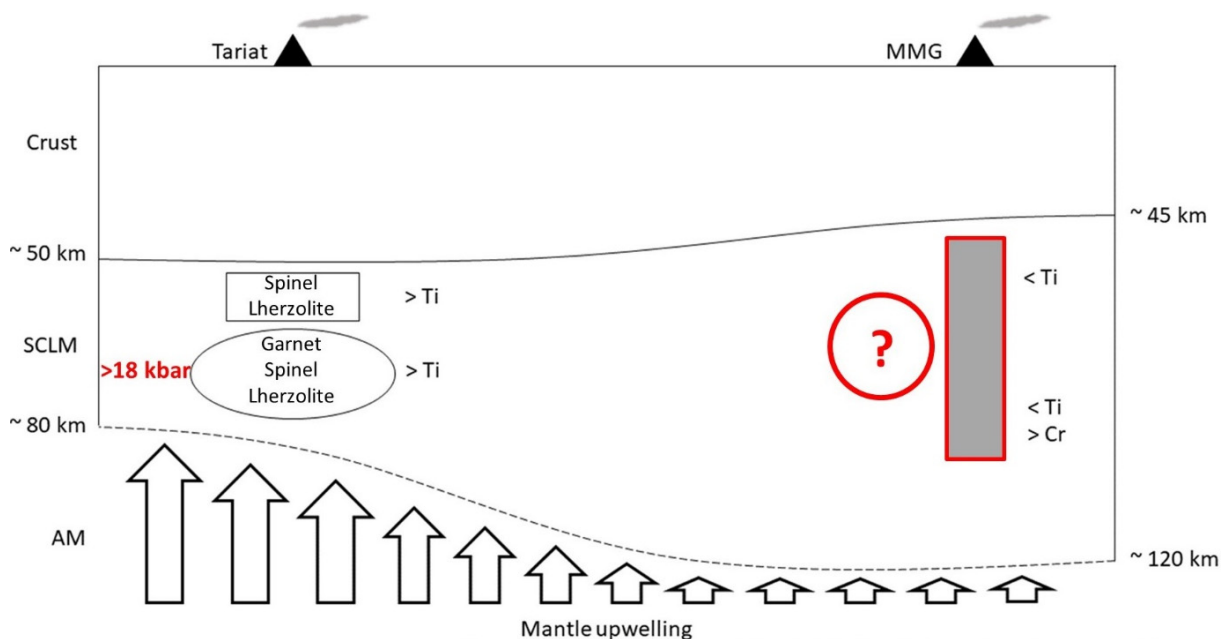


Fig. 3.3-1: Schematic model of the Mongolian lithosphere. The region studied in the present project is indicated by Mandak-Mandal-Gobi (MMG) and the Tariat area was already studied by a different group. Comparisons between the two zones are important to understand lateral variations of the lithospheric mantle.

One of the major obstacles in mantle petrology is the lack of a precise, accurate and well tested geobarometer for spinel peridotites. To address this deficiency, we performed a suite of experiments to test the performance of available geobarometers (*e.g.*, Ca in olivine) and explore other reactions to more precisely determine phase equilibrium pressures and temperatures of natural samples. Experiments were conducted with piston cylinder presses in a pressure-temperature window from 5 to 25 kbar and 1000 to 1200 °C. We used two starting compositions: 1) A mixture of synthetic oxides, reflecting the mineral chemistry of one natural sample (simplified in the system $\text{SiO}_2\text{-Al}_2\text{O}_3\text{-Cr}_2\text{O}_3\text{-MgO-FeO-Fe}_2\text{O}_3\text{-CaO-Na}_2\text{O}$); 2) Powdered hand-picked minerals of the same natural sample. Both starting compositions were placed in each experiment in two separate capsules. Au capsules were used for 1000 °C experiments and for 1100 °C runs with pressures above 15 kbar. For other experiments, Au-Pd capsules were used. The duration of runs was 36 h, 96 h and 312 h for 1200, 1100 and 1000 °C experiments, respectively. Typical run products are shown in Figure 3.3-2.

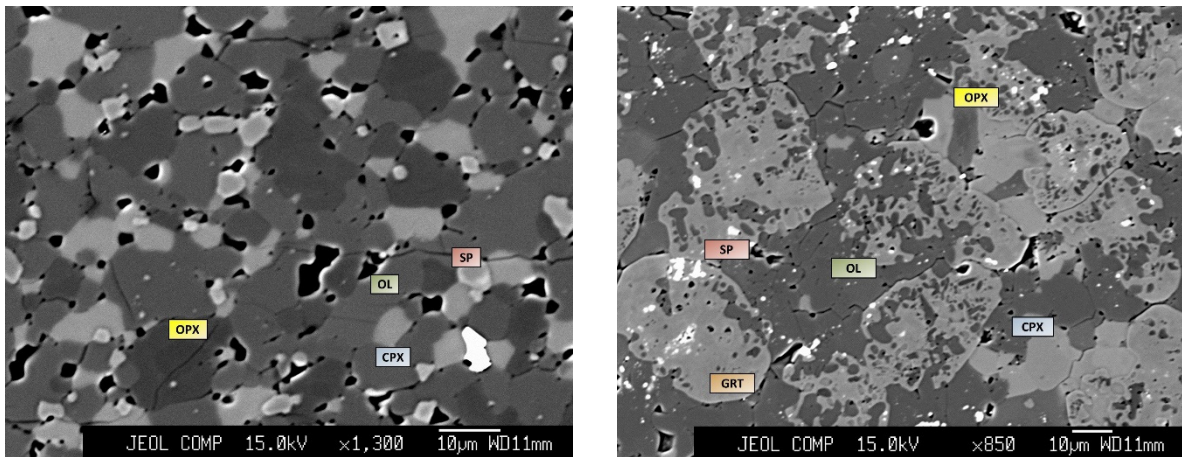


Fig. 3.3-2: Back-scattered electron micrographs of run products. (left) Sample equilibrated at 1100 °C, 15 kbar with natural starting composition. All four phases (olivine, clinopyroxene, orthopyroxene, spinel) are visible. (right) Sample equilibrated at 1000 °C, 20 kbar with synthetic starting composition showing visible garnet, clinopyroxene and olivine. Orthopyroxene and spinel are present but with lower abundances.

At 5 kbar, we observed pockets of liquid with plagioclase-like composition, suggesting that the pressure of the plagioclase-spinel transition falls between 5 and 10 kbar. The spinel-garnet transition is clearly observed in run products from both starting materials, at 20 kbar for low-temperature samples, and at 25 kbar for high-temperature samples. We noted that different starting compositions behaved differently in terms of diffusion of elements. In samples with natural starting composition diffusion appeared to be limited, showing minimal variation with temperature. In synthetic samples, on the other hand, different trends were observed with regard to temperature and pressure. We plan to construct specific chemical maps of run products from

both types of experiments to better understand differences in element diffusion depending on starting composition. In addition, precise Ca analyses will be carried out on olivine to test and possibly recalibrate the existing geobarometer for spinel peridotite and explore new reactions that better represent mineral phase equilibria at low temperatures where natural samples are inferred to have equilibrated. These results will provide important insight to answer our research questions.

b. Alumina solubility in periclase determined to lower mantle conditions and implications for ferropericlase inclusions in diamonds (L. Man, H. Fei, E.J. Kim, A. Néri, L. Xie and D.J. Frost)

Determining the formation conditions of sublithospheric diamonds is important as they provide evidence for the mobility of carbon-bearing fluids or melts in the Earth's deep convecting interior. The inclusions captured inside diamonds can potentially provide information on these formation conditions and possibly on the nature of the mobile carbon-bearing medium from which they formed. Ferropericlase is the most common type of inclusion found in proposed sublithospheric diamonds and is often used to identify them as originating from the lower mantle. In addition to FeO and MgO, substantial amounts of Al₂O₃ can be incorporated into the structure of ferropericlase at high temperature. This suggests the possibility to determine the pressure, temperature, or Al₂O₃ activity at which the inclusions were formed by measuring the Al₂O₃ content in the ferropericlase diamond inclusions, provided that the mixing behaviour of Al₂O₃ in ferropericlase under high-pressure and high-temperature conditions is well-understood. In this study, we conducted a series of high-pressure multianvil experiments in the MgO-Al₂O₃ system between 15 and 50 GPa and at temperatures up to 2623 K, to determine the solubility of Al₂O₃ in periclase in the stability fields of coexisting spinel (Sp), corundum (Cor), the Mg₂Al₂O₅ modified ludwigite (Ldw) phase, MgAl₂O₄ calcium ferrite (CF) phase, and the MgAl₂O₄ calcium titanate (CT) phase. The results show that the Al₂O₃ solubility in periclase is strongly temperature-dependent over the conditions investigated, being, for example, < 0.5 mol. % at 1923 K but up to 6.8 mol. % at 2623 K at 23 GPa (see Fig. 3.3-3). Conversely, periclase Al₂O₃ solubility decreases with increasing pressure. Additional experiments show that the Al₂O₃ solubility is not affected by FeO, as nearly identical solubilities are found for wüstite at high pressures and temperatures.

Based on these experimental results, we built a thermodynamic model to describe periclase Al₂O₃ solubility in the MgO-Al₂O₃ and MgO-SiO₂-Al₂O₃ system up to 40 GPa. This model is used to investigate the Al₂O₃ contents of ferropericlase inclusions observed in natural diamonds, which range up to 0.35 mol. %. Pressure-temperature curves along which particular inclusions formed can be produced if equilibrium can be assumed with Al-bearing minerals found in the same diamond. Alternatively, the maximum possible Al₂O₃ content in ferropericlase can be determined for a certain pressure-temperature profile and inclusions with Al₂O₃ contents that exceed this curve can be excluded from those conditions. To obtain such solubility curves,

calculations are performed for periclase coexisting with the Al-rich phases spinel, garnet, and bridgmanite (Fig. 3.3-4). The calculations indicate that ferropericlase Al_2O_3 -contents cannot be

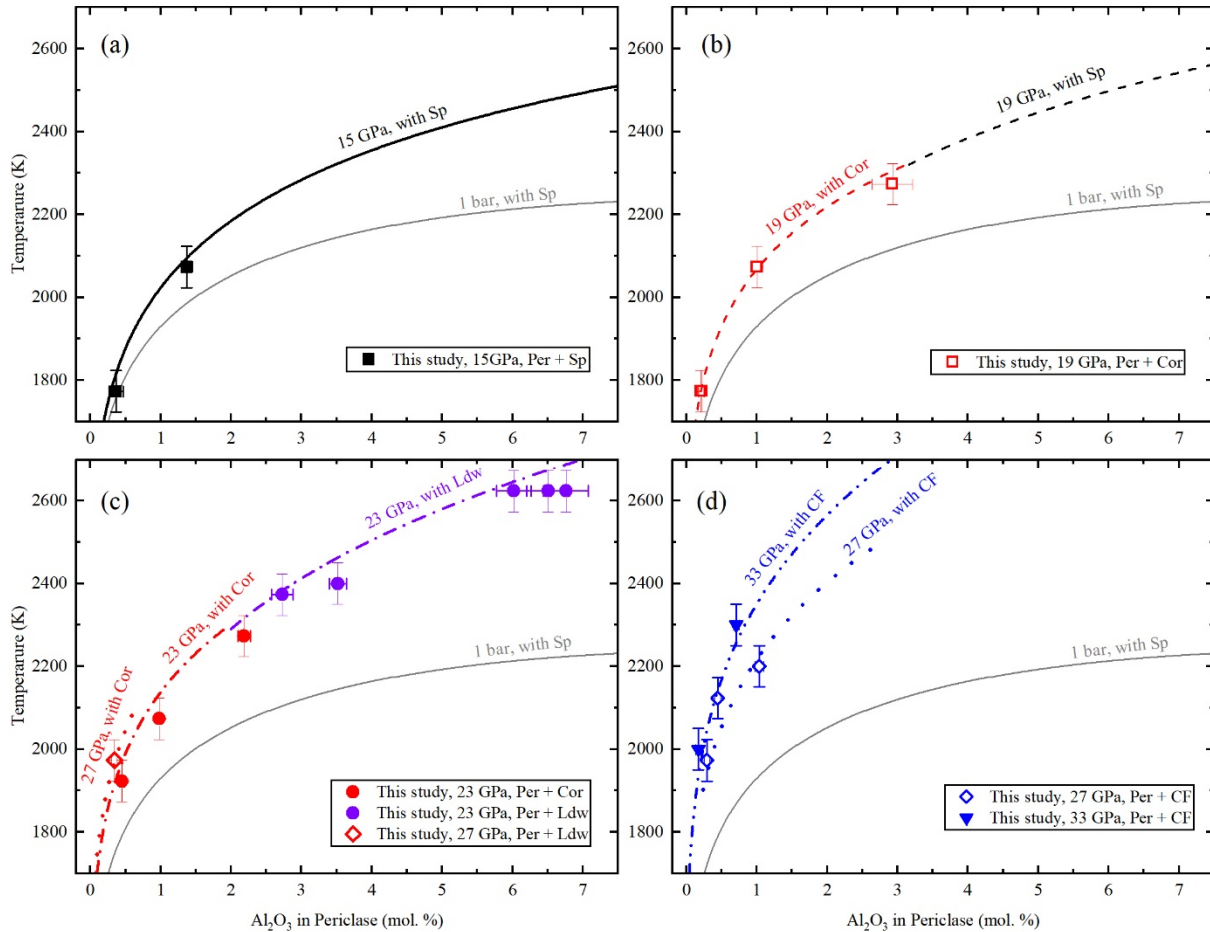


Fig. 3.3-3: Solubility of Al_2O_3 in periclase as a function of pressure and temperature. Experimental results at 15 GPa (a), 19 GPa (b), 23 to 27 GPa (c), and 27 to 33 GPa are compared with the thermodynamic model established in this study. All curves are calculated considering the indicated coexisting phases at the denoted pressures using the thermodynamic model derived in this study.

greater than 0.5 mol. % under present day adiabatic mantle temperatures and go through a minimum at mantle transition zone conditions. This excludes a number of Al-rich ferropericlase inclusions found in natural diamonds from being formed in the transition zone, unless temperatures were super-adiabatic. This subset of inclusions likely formed either at the base of the upper mantle or the top of the lower mantle but must have formed at near adiabatic temperatures. The majority of ferropericlase inclusions have Al_2O_3 contents that are consistent with formation in the transition zone at near slab temperatures but could still have been formed at higher temperatures if Al_2O_3 activities were low.

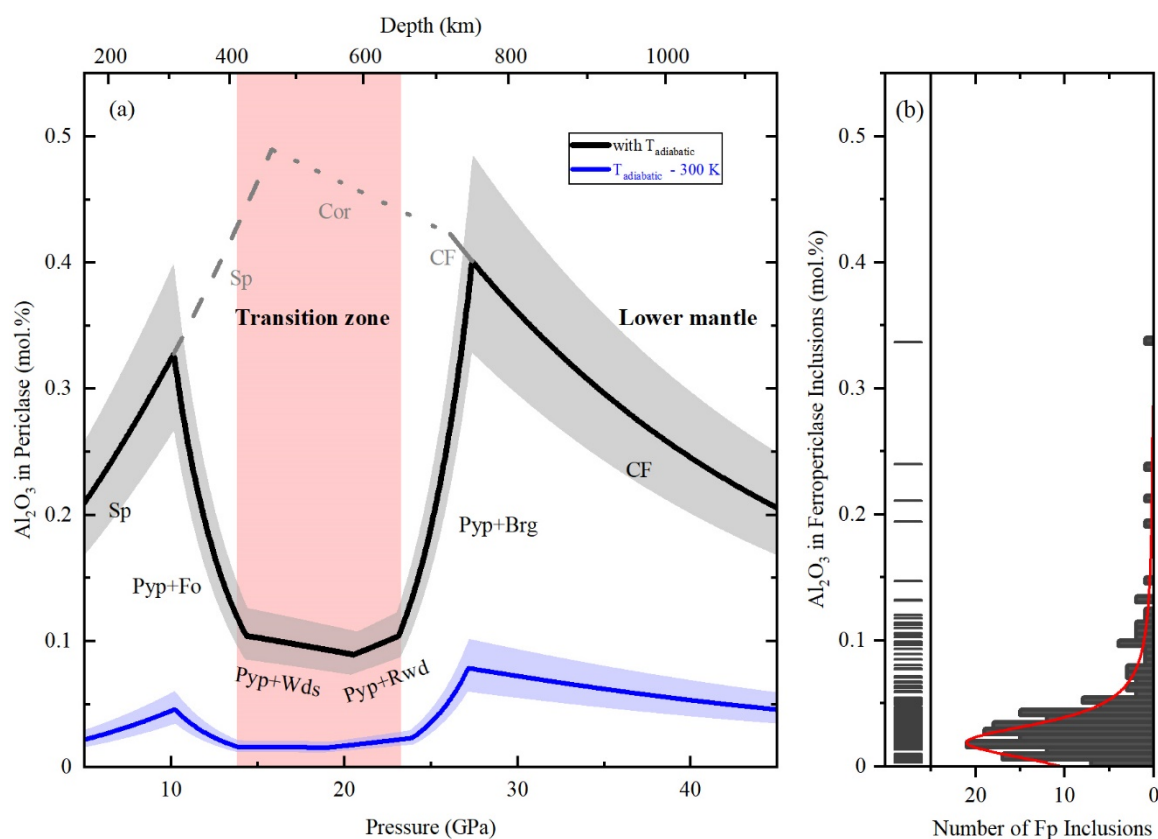


Fig. 3.3-4: (a) Al_2O_3 solubility in periclase in the $\text{MgO-SiO}_2\text{-Al}_2\text{O}_3$ and $\text{MgO-Al}_2\text{O}_3$ systems calculated from the thermodynamic model. The black solid curve shows the calculated periclase Al_2O_3 concentration in the $\text{MgO-SiO}_2\text{-Al}_2\text{O}_3$ system coexisting with Al-bearing minerals stable in the mantle at different depths, *i.e.*, spinel (Sp), pyrope (Pyp), or MgAl_2O_4 CF phase, along a typical adiabatic mantle temperature. (b) The distribution of Al_2O_3 contents in naturally formed ferropericlase inclusions found in diamonds.

c. Cr incorporation in post-spinel $\text{Fe}^{2+}\text{-Fe}^{3+}$ oxides (K. Schumann, L. Uenver-Thiele and A.B. Woodland/Frankfurt a. M.; C. Melai and T. Boffa Ballaran)

Over the past decade since the initial synthesis of Fe_4O_5 under high pressure was documented, a number of studies have demonstrated that a variety of Fe-oxides with distinct stoichiometries and crystal structures (*e.g.*, orthorhombic $\text{Fe}_3^{2+}\text{Fe}_2^{3+}\text{O}_6$, monoclinic-structured phases $\text{Fe}_3^{2+}\text{Fe}_4^{3+}\text{O}_9$ or $\text{Fe}_5^{2+}\text{Fe}_4^{3+}\text{O}_{11}$) can also be stabilized at pressures and temperatures exceeding the stability field of spinel-structured phases. Given that Fe_4O_5 and Fe_5O_6 lie compositionally between wüstite and magnetite with respect to their $\text{Fe}^{3+}/\Sigma\text{Fe}$, they should also be considered as potential accessory phases within the deep Earth. In fact, studies on natural samples have reported micro-textures within magnetite or chromite in deep-mantle and high-pressure metamorphosed samples, which are interpreted as relics of precursor phases like Fe_4O_5 or Fe_5O_6 . Nevertheless, to date only data concerning the stability of the endmembers $\text{Fe}_2^{2+}\text{Fe}_3^{3+}\text{O}_5$ and $\text{Fe}_2\text{Cr}_2\text{O}_5$ are available, while Fe^{3+} -Cr-bearing solid solutions in the M_4O_5 and M_5O_6 stoichiometries remain unknown. Consequently, this study was undertaken to i) test for

the stability of Cr-bearing O₆-phases at high pressures (*P*) and temperatures (*T*) and ii) investigate the crystal structural behaviour of Fe₄O₅-Fe²⁺₂Fe³⁺₂O₅ solid solutions.

Multianvil experiments were conducted in the *P-T* range of 12-20 GPa and 1200-1500 °C using mixtures of Fe²⁺₃Cr₂O₆ or Fe²⁺₃(Cr,Fe³⁺)₂O₆ stoichiometries. After the experiment, run products were analysed by electron probe micro analysis and powder X-ray diffraction (XRD). The analyses demonstrate that solid solution across the binary join Fe₃Cr₂O₆-Fe₃Fe₂O₆ is restricted to Fe³⁺-rich compositions, accommodating only up to 5.5 mol. % Fe₃Cr₂O₆ component. Over a wide *P-T* range, a phase assemblage of Fe₂(Fe,Cr)₂O₅ + wüstite (± hp-Fe(Fe,Cr)₂O₄) was synthesised instead. Despite the fact that the endmembers Fe₂Cr₂O₅ and Fe₂Fe₂O₅ have distinct crystal structures, a complete solid solution along the binary join has been experimentally verified. The transition between the CaFe₃O₅-type structured Fe²⁺₂Fe³⁺₂O₅ (*Cmcm*) and the modified ludwigite-type structured Fe₂Cr₂O₅ (*Pbam*) occurs approximately at a composition of 50 mol. % Fe₂Fe₂O₅ and 50 mol. % Fe₂Cr₂O₅ (Fig. 3.3-5). Powder XRD data demonstrate decreasing molar volumes with increasing Cr content. This can be attributed to the significant shortening of the ~ 9.7 Å lattice parameter in the structure (*b* in *Cmcm* and *a* in *Pbam*) due to substitution of the smaller Cr³⁺ cations for larger Fe³⁺. The shortest lattice parameter (*a* in *Cmcm* and *c* in *Pbam*) remains essentially the same across the solid solution, as its length is controlled predominantly by the height of the prismatic site, which is occupied almost exclusively by Fe²⁺. Based on the very restricted solubility of Cr, an O₆-phase cannot serve as a major carrier of Cr. Instead, Fe₂(Fe,Cr)₂O₅ is more likely to be found in Cr-rich natural samples, and might therefore serve as an indicator for the *P-T* conditions experienced by the host sample.

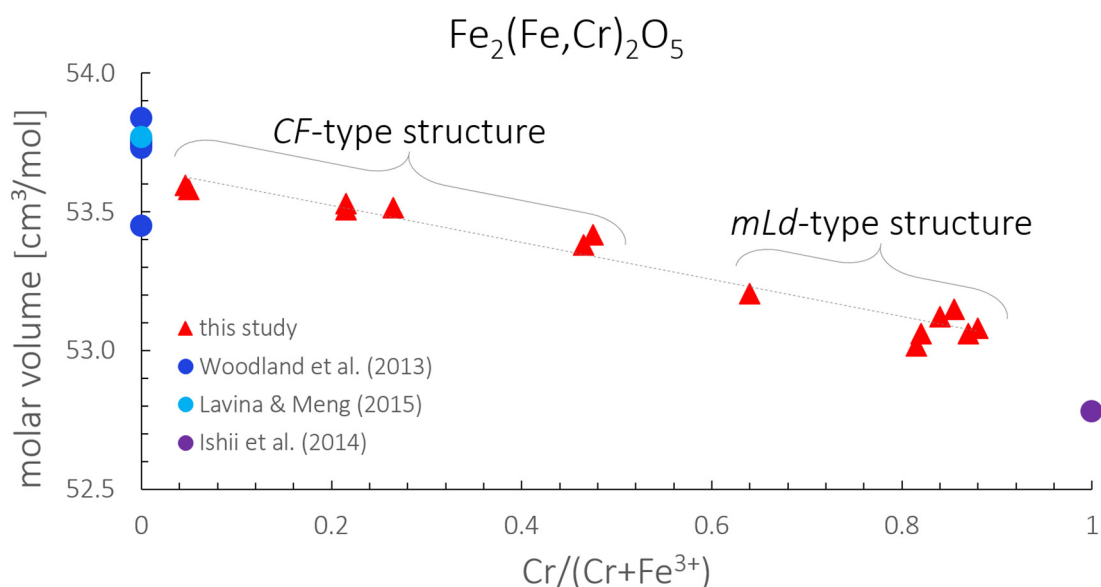


Fig. 3.3-5: Variation in molar volume as a function of the molar fraction of the Fe₂Cr₂O₅ component. The transition from a Ca₂Fe₂O₅-type (CF-type) structure to the modified ludwigite-type (mLd-type) structure occurs approximately at 50 mol. % Fe²⁺₂Fe³⁺₂O₅ and 50 mol. % Fe₂Cr₂O₅. The references referred to in the figure legend are: Ishii *et al.*, 2014, *Am Mineral*, 99, 1788-1797; Lavina and Meng, 2015, *Sci Advances*, 1(5), e1400260; Woodland *et al.*, 2013, *Contrib Mineral Petrol*, 166, 1677-1686.

d. Cr incorporation in post-spinel Mg-Fe³⁺ oxides (A.B. Woodland, L. Uenver-Thiele and K. Rosbach/Frankfurt a. M.; C. Melai and T. Boffa Ballaran)

The presence of Mg-Fe³⁺-Cr-oxides in both terrestrial and extraterrestrial samples, such as inclusions in diamond or meteorites, suggests that these phases can serve as petrogenetic markers. For instance, the experimentally determined phase relations of magnesiochromite (MgCr₂O₄) at high pressures and temperatures have proven valuable in constraining the conditions of a shock event that a host sample might have experienced. While high-pressure Mg-Fe³⁺-Cr-oxides like Mg₂Cr₂O₅ and the high-pressure polymorph (hp-MgCr₂O₄) with a Cationate-type (CT-type) structure have been reported in the literature, the stability of a Mg₃Cr₂O₆ phase in Mg-rich bulk compositions remains unknown. Additionally, the crystal chemistry and stability of Mg-bearing Cr³⁺-Fe³⁺ solid solutions of the "post-spinel" phases need to be determined. Therefore, the focus of this study was to i) experimentally investigate the stability of Mg₃Cr₂O₆ and ii) ascertain the existence of solid solutions involving Fe³⁺ cations. Furthermore, the stability of Mg₂(Fe³⁺,Cr)₂O₅ solid solutions was also of interest, since the Mg₂Cr₂O₅ and Mg₂Fe³⁺₂O₅ endmembers are known to have different space groups: *Pbam* (#55) and *Cmcm* (#63), respectively.

Therefore, multianvil experiments were performed at pressures of 14 to 20 GPa and temperatures of 1100 to 1500 °C. Stoichiometric mixtures of i) pre-synthesised MgCr₂O₄ + MgO or ii) MgCr₂O₄ + MgO + Fe₂O₃ were used to produce different Mg₃(Cr,Fe³⁺)₂O₆ starting compositions with varying Fe³⁺/Cr ratios. In most experiments, PtO₂ was added to the starting material to keep Fe in its trivalent state. Either Ag or Pt capsules were employed. After the experiment, the run products were analysed by electron probe micro analysis and powder X-ray diffraction.

Although experiments covered much of the known stability range of Fe₅O₆, the synthesis of a Cr-bearing O₆-phase could not be achieved, suggesting that Cr might not be compatible with the M₅O₆ structure. Instead, in the absence of iron, the run products are generally composed of Mg₂Cr₂O₅ + MgO ± (MgCr₂O₄ or hp-MgCr₂O₄). These phase stabilities are broadly consistent with literature data for an MgCr₂O₄ bulk composition, even though our bulk composition contains much more MgO. Even with the addition of Fe³⁺, no phase with M₅O₆ stoichiometry was produced. The stable assemblages are similar to those found in the analogous Fe³⁺-Fe²⁺-Cr system. Unlike the O₆-structure, complete solid solution is apparent across the Mg₂Fe³⁺₂O₅ – Mg₂Cr₂O₅ join. Notably, unit-cell volumes appear to behave roughly linearly (Fig. 3.3-6) even though the two endmembers have different crystal structures. The structural transition likely occurs around 50 mol. % Mg₂Fe₂O₅ – 50 mol. % Mg₂Cr₂O₅. The decreasing cell volume with increasing Cr content can be attributed to the smaller ionic radius of Cr compared to Fe³⁺. This is evident in the shortening of both the ~ 9.7 Å and ~ 12.5 Å lattice parameters. The shortest lattice parameter (*a* in *Cmcm* and *c* in *Pbam*) remains relatively constant across the join since its length is predominantly controlled by the height of the prismatic site which is almost exclusively occupied by Mg.

Based on the insights from this study, assemblages containing $\text{Mg}_2(\text{Fe}^{3+},\text{Cr})_2\text{O}_5$, which are stable across wide ranges in Cr content, pressure, and temperature, suggest that an O_5 -phase is more likely to occur in Cr-rich deep mantle environments than an O_6 -phase.

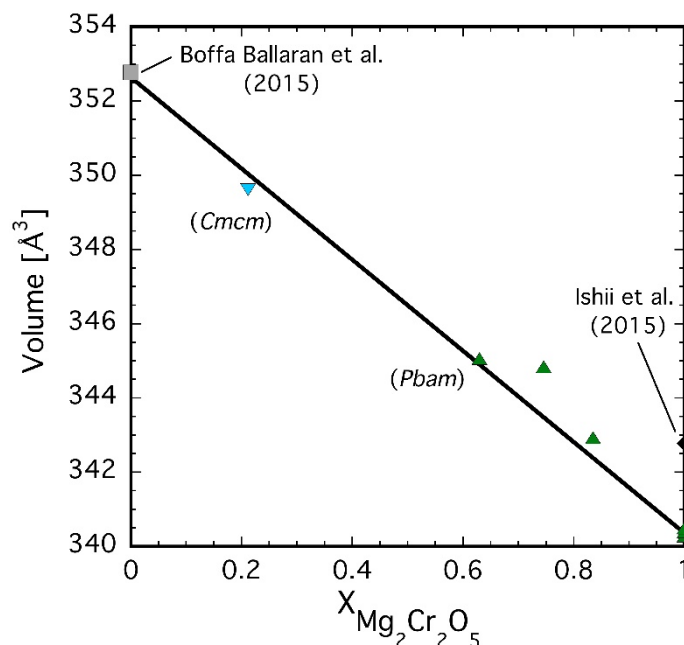


Fig. 3.3-6: Variation in the unit-cell volumes of $\text{Mg}_2\text{Cr}_2\text{O}_5$ - $\text{Mg}_2\text{Fe}_2\text{O}_5$ solid solutions. Literature data on the pure endmembers are also presented for comparison (Boffa Ballaran *et al.*, 2015, *Am. Mineral.*, 100, 628; Ishii *et al.*, 2015, *Am. Mineral.*, 100, 59).

e. High-pressure phase relations of Al-bearing magnetite (L. Uenver-Thiele and A.B. Woodland/Frankfurt a. M.; N. Miyajima and T. Boffa Ballaran)

In the past decade, iron oxide spinels and their respective post-spinel phases have garnered increasing attention since their presence as inclusions in diamonds or in extraterrestrial samples can offer insights into their original depth of formation or the pressure-temperature (P - T) conditions during a shock event. For example, magnetite has been identified as a non-ultramafic inclusion in diamond, either as discrete grains or associated with other phases such as wüstite, metallic Fe, hematite, or pyrrhotite. Since such magnetites typically have almost pure end-member compositions, they must have either crystallized at pressures less than 10 GPa or, if particular microstructures are evident, they may have originated as breakdown products from a high-pressure precursor phase like Fe_4O_5 or Fe_5O_6 . However, up to now the high- P - T phase relations of such phases are mostly known for only end-member compositions. Consequently, the interpretation of natural samples that form complex solid solutions is often hampered by uncertainties in the actual phase relations. It is noteworthy that certain magnetites are reported to contain substantial amounts of Al, which could influence the actual high- P - T stability of this phase.

To address this knowledge gap, we experimentally investigated the phase relations of Al-bearing magnetite ($\text{Fe}^{2+}(\text{Fe}^{3+},\text{Al})_2\text{O}_4$) in the P - T range of 8-22 GPa and 1000-1600 °C using a multianvil press. Analysis of run products reveal that the spinel-structured phase remains stable only up to ~ 10 GPa at 1100-1400 °C, regardless of the amount of hercynite (FeAl_2O_4) component in the starting composition (20, 40 or 60 mol. %). Beyond this pressure, the assemblage $\text{Fe}_2(\text{Fe},\text{Al})_2\text{O}_5 + (\text{Al},\text{Fe})_2\text{O}_3$ becomes stable in the P - T range of 11-20 GPa and 1200-1550 °C (Fig. 3.3-7). Here, X-ray diffraction data indicate that the M_4O_5 phase adopts the CaFe_3O_5 -type structure with the $Cmcm$ space group. Depending on temperature, the assemblage of the monoclinic structured $\text{Fe}_3(\text{Fe},\text{Al})_4\text{O}_9$ ($C2/m$) + $(\text{Al},\text{Fe})_2\text{O}_3$ or a hp- $\text{Fe}(\text{Fe},\text{Al})_2\text{O}_4$ polymorph becomes stable at pressures exceeding 18 GPa (Fig. 3.3-7). Both $\text{Fe}_2(\text{Fe},\text{Al})_2\text{O}_5$ and $\text{Fe}_3(\text{Fe},\text{Al})_4\text{O}_9$ are recoverable from experiments. On the other hand, the hp- O_4 polymorph is unquenchable and yields a defect-rich spinel-phase characterised by abundant twin lamellae parallel to $\{100\}$ or $\{113\}$ planes and a considerably lower Al content than the initial composition. Despite the existence of a complete solid solution between magnetite and hercynite at low pressures, all post-spinel phases demonstrate restricted Al solubility with only up to ~ 0.1 cpfu Al in hp- O_4 , ~ 0.3 cpfu in $\text{Fe}_2(\text{Fe},\text{Al})_2\text{O}_5$ and ~ 0.4 cpfu in $\text{Fe}_3(\text{Fe},\text{Al})_4\text{O}_9$. Excess Al stabilizes an additional $(\text{Al},\text{Fe})_2\text{O}_3$ phase. The phase relations remain essentially the same in Al-richer bulk compositions, where varying proportions of $(\text{Al},\text{Fe})_2\text{O}_3$ complement the assemblage. The co-existence of both hematite- and corundum-rich solid solutions in several experiments suggests that the miscibility gap across the rhombohedral oxide join defined at low pressures (≤ 4 GPa) persists up to at least 20 GPa.

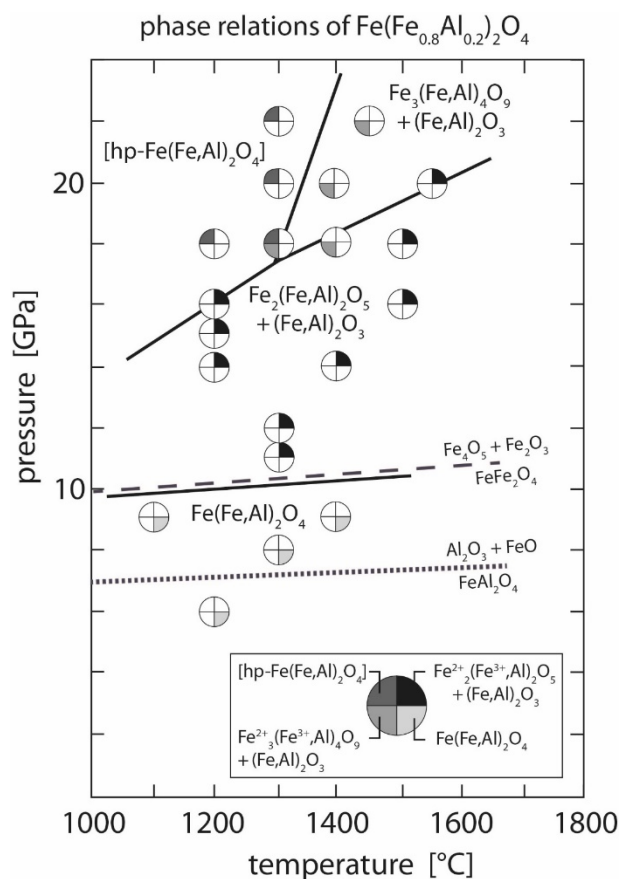


Fig. 3.3-7: Phase stabilities for the bulk composition $\text{Fe}^{2+}(\text{Al}_{0.2}\text{Fe}^{3+}_{0.8})_2\text{O}_4$. The boundaries between the phase stability fields are marked by solid lines. The dashed and dotted lines are plotted for the breakdown reaction of magnetite and the breakdown reaction for hercynite, respectively, as reported in the literature. Uncertainties in pressures and temperatures are roughly the size of the symbols.

f. *Post-spinel phase transition in Mg_2SiO_4 - Fe_2SiO_4 system (A. Chanyshv, F. Wang, N. Martirosyan, K. Han, R. Farla/Hamburg and T. Katsura)*

Seismic wave velocities increase abruptly at a depth of 660 km almost everywhere in the Earth's mantle, which is referred to as the 660-km discontinuity (D660). As the D660 is thus a ubiquitous feature of the mantle, it should provide fundamental information about the Earth's interior. The D660 is usually attributed to the dissociation of $(Mg,Fe)_2SiO_4$ ringwoodite (Rwd) into $(Mg,Fe)SiO_3$ bridgmanite (Bdm) and $(Mg,Fe)O$ ferropericlae (fPc), which is named post-spinel phase (PSP) transition. The D660 is not flat but undulating. It is elevated up to 17 km in hot regions and depressed down to 90 km in cold regions of the mantle. These observations imply that the pressure of the PSP transition should increase/decrease with decreasing/increasing pressure, respectively, *i.e.*, the dissociation of Rw should have a negative Clapeyron slope. However, the experimental results in Mg_2SiO_4 obtained using high-precision multianvil experiments showed a very gentle or almost zero slope (-0.1 ~ 0.9 MPa/K). Such a gentle slope does not account for the topography of the D660. Our previous study interpreted the depression as being caused not by the Rw dissociation but by the akimotoite (Aki)-Brg transition in cold regions. However, as the transition pressure of the Akm-Brg transition is far below the pressure of the D660 (23.4 GPa) in hot regions, Akm-Brg cannot account for the elevation of the D660. Therefore, we need an alternative interpretation for it.

The experiments were performed at the beamline P61B at DESY (Hamburg, Germany) using a multianvil press with *in situ* X-ray diffraction. We used the following strategy to determine transition parameters: (1) the phase stability was determined by the change in the proportions of already coexisting Rw and Brg+fPc. (2) Two diffraction patterns of the sample were collected at a fixed press load and temperature to observe the growth of a stable phase without a sudden pressure change associated with temperature change. (3) In order to avoid the disappearance of either phase and keep the two-phase coexistence, the experimental conditions were kept close to the phase boundary.

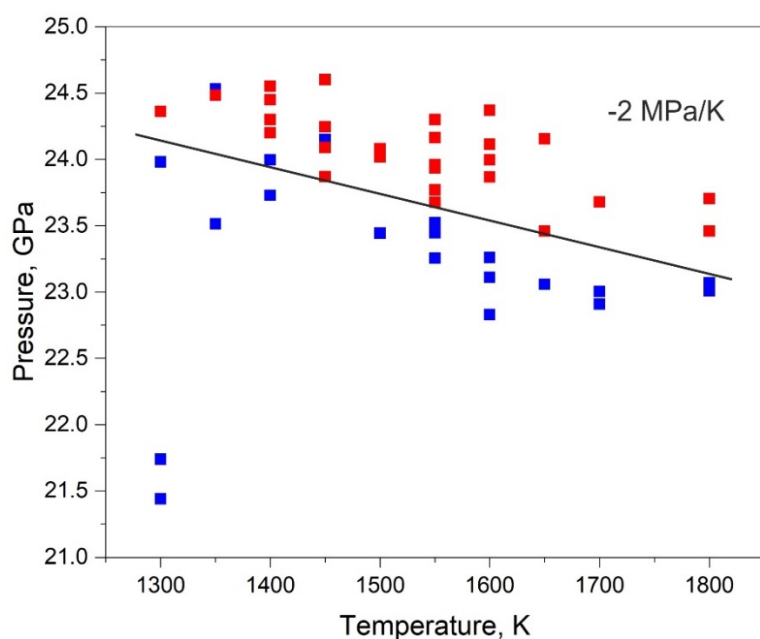


Fig. 3.3-8: Phase diagram for $(Mg,Fe)_2SiO_4$ ringwoodite with $Mg/(Mg+Fe) = 0.9$ at 21-25 GPa. The red and blue squares indicate the pressures and temperatures where the ratio of bridgmanite + ferropericlae to ringwoodite increased or decreased, respectively. The solid black line indicates the most reliable boundary of the post spinel phase transition.

The PSP transition was determined for Rwd with $Mg/(Mg+Fe) = 0.9$ in the temperature range of 1300-1800 K, and the transition pressures were found at 23.2-24.3 GPa (Fig. 3.3-8). This transition has a negative Clapeyron slope (-2 MPa/K). The determined slope is steeper than that defined for the MgO-SiO₂ system; therefore, the PSP transition likely controls the elevation of the D660 in hot regions of the mantle. Moreover, steep phase boundaries produce large buoyancy forces which affect mantle convection. A positive Clapeyron slope of a phase transition enhances mantle convection whereas a negative slope impedes it. Therefore, the PSP transition should impede plume convection in the mantle.

g. Experiments on the stability of whewellite, an organic mineral, in subduction zone fluids (L. Czekay and H. Keppler)

Recent theoretical studies have suggested that organic anions may be abundant in high-pressure subduction zone fluids. Moreover, whewellite CaC₂O₄·H₂O, an organic mineral, was described as inclusions in zircon from subduction-related high-pressure metamorphic rocks. These findings support the idea that abiotic organic molecules may be present in subduction zone fluids and that organic compounds may form by abiotic processes at elevated pressures and temperatures. The presence of organic compounds in subduction zone fluids may have important implications for the properties of these fluids for the deep carbon cycle. We test these hypotheses by performing both *ex situ* piston-cylinder experiments and *in situ* Raman spectroscopic experiments in the externally heated diamond anvil cell at temperatures up to 600 °C and pressures up to 5 GPa.

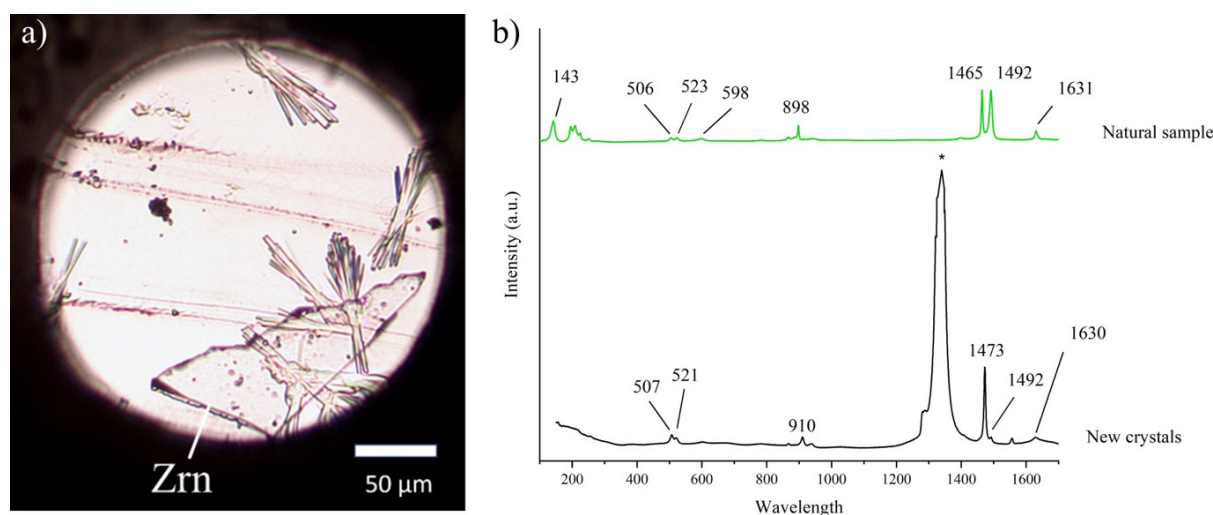


Fig. 3.3-9: a) Sample chamber at 1 GPa filled with fluid, zircon, and newly grown needle-like crystals of whewellite after heating to 300 °C. b) Representative Raman spectrum of natural whewellite starting material and of the newly formed crystals indicated in a. The Raman band of the diamond is marked with a star.

In diamond anvil cell experiments, we first observed that upon heating and pressurisation to 300 °C and 1.5 GPa the whewellite crystals dissolved in water and then recrystallised upon slow cooling. During the cooling process, needle-like crystals formed, which can be clearly seen in Figure 3.3-9a. In this representative example, the newly formed crystals nucleated on the zircon crystal used for pressure measurements and on irregularities within the pressure chamber of the diamond anvil cell. Raman measurements confirmed that the newly formed crystals were whewellite (Fig. 3.3-9b). This implies that whewellite may indeed be a stable phase to 300 °C and 1.5 GPa. Figure 3.3-9b compares the Raman spectrum of a natural whewellite sample before the experiments with the Raman spectrum of the newly formed crystals in the diamond anvil cell. However, the Raman spectra also indicated the presence of some graphitic carbon in the sample chamber, which must have formed by partial decomposition of whewellite, indicating that the conditions of the experiments were already close to the stability limit of whewellite.

h. *Synthesis of magnesium (II) orthocarbonate, Mg₂CO₄, from different precursors (L.S. Dubrovinsky, T. Fedotenko/Hamburg, S. Khandarkhaeva, A. Aslandukov, A. Aslandukova, Y. Yin/Bayreuth, K. Glazyrin/Hamburg, D. Laniel/Edinburgh and N.A. Dubrovinskaia/Bayreuth)*

The source and quantity of carbon in our planet is uncertain, but there is general consensus that the total amount of carbon in the atmosphere, oceans, and other near-surface reservoirs is negligible compared to that stored in the Earth's mantle and core. Deep-mantle diamonds, carbon-rich mantle-derived magmas, carbonate rocks in subduction zones, even carbonates and carbide inclusions in diamonds from the transition zone provide numerous lines of evidence for the early and continuing long-term exchange of substantial carbon between Earth's surface and its interior.

Within the last couple of decades, theoretical and a few experimental studies demonstrated that all major carbonate compounds, such as CaCO₃, MgCO₃, FeCO₃, and CaMg(CO₃)₂ may survive at the pressure-temperature conditions of certain parts of the Earth's mantle, while displaying a variety of different polymorphs. However, due to different possible redox processes, carbonates were proposed to be altered, forming, depending on the stage of reduction, metal carbides, CO₂, or diamond. Nevertheless, carbonate inclusions from deep mantle originating diamonds are direct evidence for oxidized carbon in the form of carbonates and their presence in at least some regions in the mantle. Cold oxidized subducting slabs with low reaction kinetics are believed to provide adequate conditions for hosting carbonates even at depths of the lower mantle.

A recent remarkable experimental discovery was the confirmation of the formation of so called tetracarboxylates, in which *sp*³-hybridization leads to the formation of CO₄⁴⁻ tetrahedrons instead of triangular *sp*²-hybridized CO₃²⁻ groups.

In our experiments, we used large opening BX-90 type diamond anvil cells (DAC) equipped with Boehler-Almax type diamonds. To reach pressures above 100 GPa, diamonds with culet

diameters of 120 and 80 μm were inserted in WC seats. To form a sample cavity, we indented rhenium gaskets with an initial thickness of 200 μm down to 20 μm and laser-drilled holes at the centre of the indentations with diameters equal to half the diameters of the anvil culets.

MgO powder was annealed at 1000 K for 12 hours in order to eliminate possible moisture contamination. In some experimental runs, the MgO powder was compressed between diamond anvils to form thin plates with approximate thickness of 5 μm . The plates were mounted on both sides of the DACs to laterally cover most of the sample cavity. The DACs were cryogenically loaded with oxygen, which served as a chemical reactant, pressure-transmitting medium, and absorber of NIR laser radiation at high pressures. In another experiment, a 50-50 wt. % mixture of MgO and MgCO_3 powders was prepared and loaded into the sample chamber of the DAC along with a piece of platinum. The Raman shift of the diamond band was used to control pressure during compression of the DACs to the target pressure. At the synchrotron facility, pressure was determined by means of X-ray diffraction using the equation of state (EOS) of MgO and Pt. The X-ray diffraction experiment was performed at the material science beamline ID 11 ($\lambda = 0.2845 \text{ \AA}$, Dectris Eiger2 X CdTe 4M detector, X-ray spot size $0.75 \times 0.75 \mu\text{m}^2$) at the European Synchrotron Radiation Facility (ESRF, Grenoble, France).

In all our experiments, we observed a new monoclinic phase with the space group symmetry $P2_1/c$. At $\sim 120 \text{ GPa}$, for example, it had the unit cell parameters $a = 4.0855(7) \text{ \AA}$, $b = 5.63150(9) \text{ \AA}$, $c = 7.6391(4) \text{ \AA}$, $\beta = 108.27(7)^\circ$. High-quality single-crystal diffraction data allowed to solve and refine the crystal structure (Fig. 3.3-10) and determine the chemical composition of the phase as magnesium (II) orthocarbonate, Mg_2CO_4 . Notably, we were not able to find a structural analog of the new orthocarbonate phase among orthosilicates.

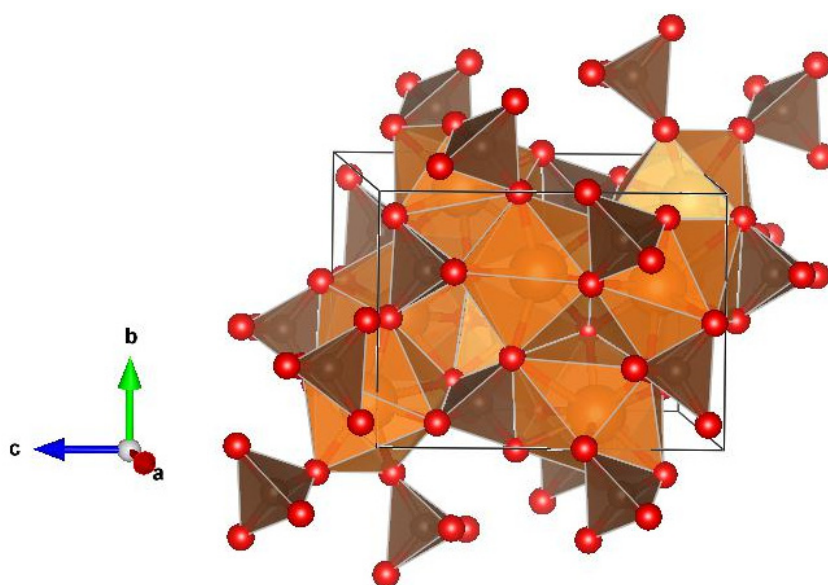


Fig. 3.3-10: Crystal structure of magnesium (II) orthocarbonate, Mg_2CO_4 . Carbon atoms form isolated CO_4 tetrahedra (brown). The Mg atoms (orange) are located in two different sites and form MgO_7 and MgO_9 polyhedra. Oxygen atoms are shown in red.

The monoclinic crystal structure of Mg_2CO_4 is composed of three types of coordination polyhedra: CO_4 , MgO_7 , and MgO_9 . At 120 GPa, the CO_4 group forms distorted tetrahedra isolated from each other while sharing corners and edges with both MgO_7 and MgO_9 polyhedra. The CO_4 tetrahedron has four C–O bonds with lengths varying from ~ 1.30 to ~ 1.36 Å; the angles between C–O bonds vary in the range from 104.32° to 111.93° with an average value of 109.45° , as expected for carbon in sp^3 hybridization state.

Thus, we demonstrate that MgCO_3 and MgO react with formation of a novel magnesium (II) orthocarbonate. In a pyrolitic mantle dominated by Mg-rich oxide (ferropericlase) and bridgmanite, not MgCO_3 -II but Mg_2CO_4 (or its Fe-bearing analog) will be the major host of carbon.

i. Fe oxidation state of garnet and clinopyroxene in grospydite xenoliths from the Zagadochnaya pipe (Yakutia, Russia) (G. Marras/Rome, V. Stagno/Rome, C.A. McCammon and D. Mikhailenko)

The study of kimberlite-borne eclogite provides the opportunity to investigate the chemical, mineralogical, and redox state evolution of their subducted mafic protoliths derived from Archean basalts and gabbros. Grospydites represent a rare variety of grossular–pyroxene–kyanite bearing eclogitic rocks, often associated with coesite and sanidine. Grospydites are sampled in a few localities such as the Zagadochnaya pipe (Yakutia, Siberia) and the Robert Victor kimberlite (South Africa). Knowledge of the redox conditions of mantle-equilibrated grospydites could provide insights into the general lack of diamonds in these xenoliths through the investigation of the Fe oxidation state in coexisting garnets and clinopyroxenes.

In this study, we determined the chemical composition and $\text{Fe}^{3+}/\Sigma\text{Fe}$ of garnet and clinopyroxene fragments extracted from four diamond-free grospydite xenoliths from the Zagadochnaya pipe located at a distance of 30 km from the diamondiferous Udachnaya pipe (Siberia).

The $\text{Fe}^{3+}/\Sigma\text{Fe}$ ratio was measured by milliprobe Mössbauer spectroscopy at the Bayerisches Geoinstitut. Data were acquired at room temperature and in transmission mode on a constant acceleration spectrometer, using a nominal 370 MBq ^{57}Co point source. The collected spectra were fitted by a full transmission integral with a normalized pseudo-Voigt line-shape using the MossA software package. The fitting model consisted of one doublet for Fe^{3+} and one doublet for Fe^{2+} in garnet and one doublet for Fe^{3+} and two doublets for Fe^{2+} in clinopyroxene.

The garnets in the grospydite samples are solid solutions of grossular (23-51 mol. %), pyrope (23-44 mol. %), and almandine (24-34 mol. %) while clinopyroxenes have 5.1-10 wt. % of MgO , 2-3.7 wt. % of FeO , and 5.5-7.7 wt. % of Na_2O . The $\text{Fe}^{3+}/\Sigma\text{Fe}$ ranges between 0.07 and 0.21 (± 0.01) in garnet and between 0.21 and 0.53 (± 0.02 -0.03) in clinopyroxene. These values

are higher than what has been reported in the literature for Udachnaya diamondiferous eclogites, for instance, but are consistent with those observed in diamond-free eclogites from V. Grib pipe (Arkhangelsk Diamond Province; Fig. 3.3-11a). Preliminary estimates for pressure, temperature, and oxygen fugacity indicate that the selected grosspydites equilibrated at 3.6 to 4.6 GPa (± 0.4 GPa) and 830 to 1000 °C (± 60 °C) and record oxygen fugacities between -0.31 and +1.5 (± 0.6) log units relative to the fayalite-magnetite-quartz (FMQ) buffer (Fig. 3.3-11b). These xenoliths are among the most oxidized eclogitic samples studied to date (Fig. 3.3-11b). The high inferred oxygen fugacities may explain the absence of graphite/diamond within the rock matrix. On the other hand, the presence of garnets with high Ca and low Mg contents are unique within the eclogite rocks and might require an accurate test of the existing oxy-thermobarometric models used to determine the pressure, temperature, and oxygen fugacity from the chemical composition of the rock-forming minerals.

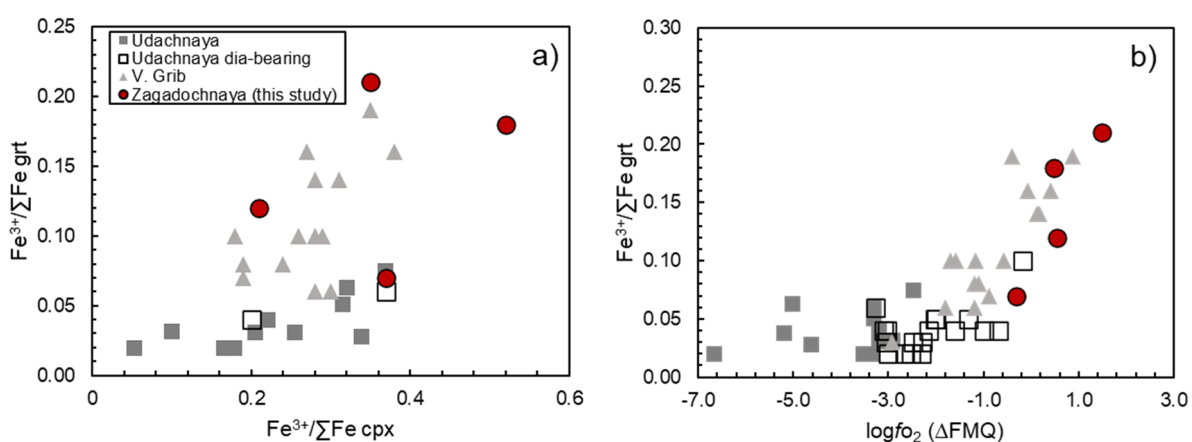


Fig. 3.3-11: (a) $\text{Fe}^{3+}/\Sigma\text{Fe}$ of garnet versus that of clinopyroxene; (b) $\text{Fe}^{3+}/\Sigma\text{Fe}$ of garnet plotted as a function of the calculated oxygen fugacity (expressed as $\log f\text{O}_2$ relative to FMQ). Literature data for eclogites of the Udachnaya pipe (Mikhailenko *et al.*, 2020, *Contrib. Mineral. Petrol.*, 175, 107; Aulbach *et al.*, 2022, *J. Petrol.*, 63, egac076) and the V. Grib pipe (Marras *et al.*, under review) are reported for comparison.

j. *Pressure dependence of $\text{Fe}^{3+}/\Sigma\text{Fe}$ in bridgmanite (F. Wang, L. Wang, H. Fei, N. Miyajima, C.A. McCammon, D.J. Frost and T. Katsura)*

Bridgmanite is the most abundant mineral in the lower mantle. It can contain a large amount of ferric iron even under very reducing conditions. The amount of Fe^{3+} in bridgmanite is important for understanding the oxygen fugacity of the lower mantle and the deep-earth oxygen cycle. Previous studies have shown that $\text{Fe}^{3+}/\Sigma\text{Fe}$ in bridgmanite varies as a function of aluminium content, oxygen fugacity, and temperature. However, there have been few studies on the pressure dependence of $\text{Fe}^{3+}/\Sigma\text{Fe}$, and most of the previous studies did not account for the oxygen fugacity. Therefore, this work was undertaken to quantify $\text{Fe}^{3+}/\Sigma\text{Fe}$ in bridgmanite as a function of pressure.

Two pyroxene samples with chemical formulae of $\text{Mg}_{0.89}\text{Al}_{0.11}\text{Fe}_{0.11}\text{Si}_{0.89}\text{O}_3$ (Fe11Al11) and $\text{Mg}_{0.91}\text{Al}_{0.07}\text{Fe}_{0.11}\text{Si}_{0.91}\text{O}_3$ (Fe11Al7) were each mixed with 5 wt. % $(\text{Mg}_{0.9}\text{Fe}_{0.1})\text{O}$ ferropericlasite and 5 wt. % Ir metal, and the mixtures were used as starting materials. The mixtures were loaded into Pt capsules, which were then loaded into 5.7/1.5 cell assemblies. High-pressure experiments were conducted at 2300 K and 33–50 GPa in a 1500-ton Kawai-type multianvil press with the Osugi-type guide block system. The oxygen fugacity ($f\text{O}_2$) was determined from the composition of an Ir-Fe alloy to be around +1.5 ΔIW . The $\text{Fe}^{3+}/\Sigma\text{Fe}$ ratio in recovered bridgmanite was determined by Mössbauer spectroscopy. The results of our experiments at four different pressures show that the $\text{Fe}^{3+}/\Sigma\text{Fe}$ in both of the two different bridgmanite compositions did not change with pressure (Fig. 3.3-12).

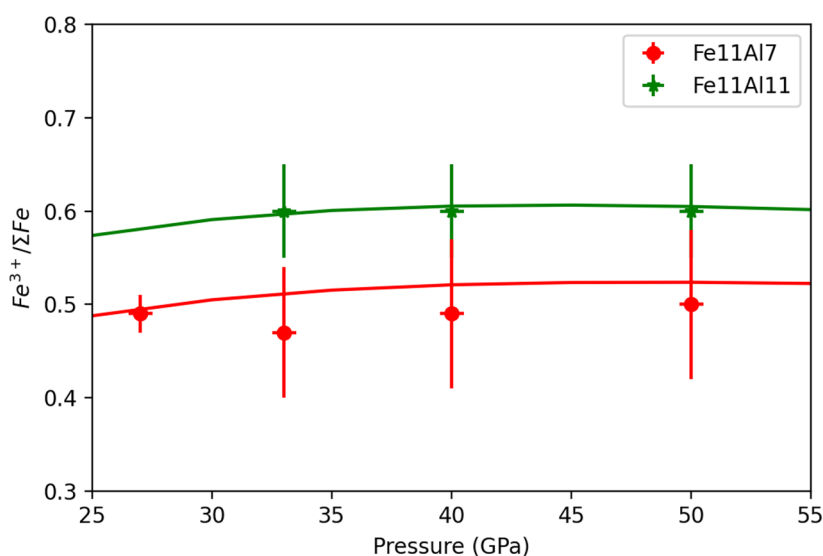


Fig. 3.3-12: $\text{Fe}^{3+}/\Sigma\text{Fe}$ ratio in two distinct (Al, Fe)-bearing bridgmanite compositions as a function of pressure. The solid lines were calculated from a thermodynamic model using the same compositions as given in the text.

k. *Crystallographic features of omphacite in lawsonite-eclogite xenolith from Colorado Plateau* (R. Fukushima and T. Tsujimori/Sendai, N. Miyajima, T. Boffa Ballaran, G. Criniti and C.A. McCammon)

Lawsonite-eclogite xenoliths from the Navajo volcanic field, central Colorado Plateau, are of considerable importance as fragments of the subducted Farallon plate. One can therefore expect that mineralogical/geochemical analyses of its constituting minerals are useful to examine the prograde eclogitization process and dynamics of the diatreme emplacement.

To this end, we have investigated the crystallographic features of omphacite in the lawsonite-eclogite xenolith. The omphacite grains are slightly enriched in Fe^{3+} ($\sim \text{aug}_{35-45} \text{jd}_{40-50} \text{aeg}_{15-20}$) and characterised by local compositional heterogeneities. Although the peak metamorphic temperature (~ 620 °C) is below the critical temperature of its order-disorder transition (~ 865

°C), our X-ray diffraction analysis of representative crystals demonstrated the absence of any super-lattice diffraction peaks belonging to the ordered phase. However, our observation of the omphacite from the same eclogite with transmission electron microscopy revealed the presence of diffuse scattering related to the ordered structure (Fig. 3.3-13).

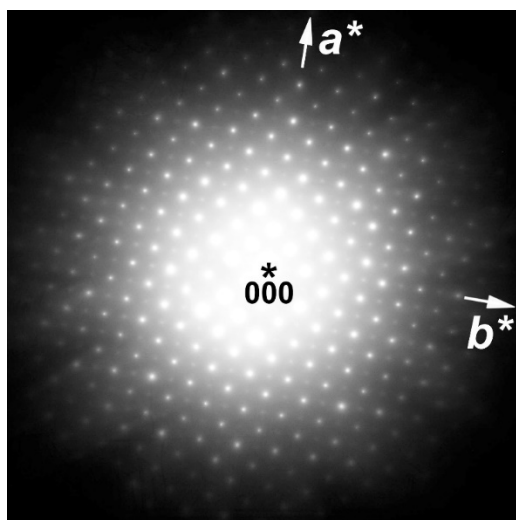


Fig. 3.3-13: Selected area electron diffraction pattern of an omphacite grain in the lawsonite-eclogite xenolith. Odd reflection spots are visible along the b^* direction in the $[001]$ zone axis.

Even if such incomplete ordering is due to their compositional deviations from the ideal omphacite composition ($\text{Ca}_{0.5}\text{Na}_{0.5}\text{Mg}_{0.5}\text{Al}_{0.5}\text{Si}_2\text{O}_6$), we should consider why short-range order remains in the omphacite specimens. This is because a previous study has suggested a Cenozoic thermal pulse ($> \sim 800$ °C) that lasted for $< \sim 1700$ years, which may have caused some extent of disordering. Was the heating temperature/duration too low/short for complete disordering, or is this merely a result of reordering during the cooling process? How can the degree of order change due to the later-stage metasomatism? If we consider the sluggish ordering kinetics of omphacite, as a first approximation, we may explain the short-range order by incomplete heating just before the diatreme emplacement. Nevertheless, we still require additional constraints to fully answer these questions, especially with respect to the potentially short-lasting temperature fluctuation and compositional modification. These peculiar omphacites highlight the difficulty in constraining the detailed thermochemical history of the subducted, metamorphosed, and fragmented slab, based only on the petro-mineralogical information preserved in a given eclogite xenolith.

1. The electron diffraction pattern of quenched davemaoite and the unit cell volume at ambient pressure (N. Miyajima, L. Wang and T. Katsura)

The precise volumes of high-pressure minerals at ambient pressure (V_0) are very important for quantitative discussions in mineral physics. The recovered high-pressure samples are used for the further physical and chemical measurements, even though they are metastable at ambient conditions. Calcium-rich perovskite, davemaoite (Dvm), is often unquenchable to ambient

conditions. However, as reported in the literature, a small amount of Dvm was identified by X-ray diffraction and nuclear magnetic resonance (NMR) spectroscopy in samples recovered from 15 GPa and 1500 °C. In the recovered Dvm, the existence of the reflections could not be indexed with the cubic unit cell, indicating that the symmetry of the Dvm is lower than cubic. To clarify the symmetry and preservation mechanism of Dvm at ambient conditions, we investigated quenched Dvm and its symmetry at the sub-micrometre scale by using conventional transmission electron microscopy (TEM). We present for the first time a selected area electron diffraction (SAED) pattern of Dvm coexisting with Al-Fe-bearing bridgmanite (Bdm).

A high-pressure assemblage of Dvm and Bdm phases was synthesised at 40 GPa and 2000 °C for 24 hrs by using a Kawai-type multianvil apparatus. A thin TEM foil of the recovered sample was prepared with a focused ion milling machine. In bright-field TEM images, submicrometric-sized crystalline Dvm domains are located within amorphized domains that formed from a precursor Dvm grain (Fig. 3.3-14). From the SAED pattern of Dvm, we have confirmed consistency with the space group (S.G.) $Pm\bar{3}m$ and evaluated the cubic lattice parameter as a (cubic) = 0.356 nm ($V_0 = 45.12 \text{ \AA}^3$). The obtained lattice parameter of Dvm is comparable with literature data for the lattice parameter at 0 GPa that were estimated as $a = 0.3572 \text{ nm}$ ($V_0 = 45.576 \text{ \AA}^3$) (Wang *et al.*, *J. Geophys. Res. Solid Earth*, 101, 661, 1996) and 0.358 nm ($V_0 = 45.88 \text{ \AA}^3$) (Tschauner *et al.*, *Science*, 374, 891, 2021). The lattice parameter of Dvm in the present study (0.356 nm) is larger than 0.351 nm, half the length of c (orthorhombic) = 0.702 nm in the coexisting Bdm (S.G. $Pbnm$). This comparison is motivated by the relation that $1/2 c$ (orthorhombic) = a (cubic) in the orthorhombic perovskite structure.

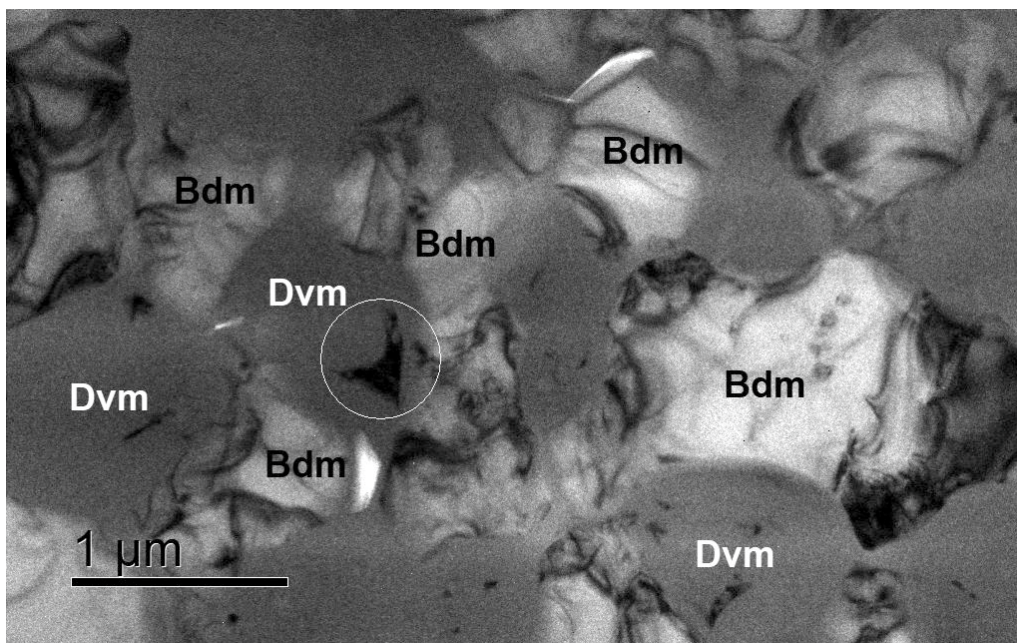


Fig. 3.3-14: Bright-field TEM image of quenched davemaoite domains (Dvm, a black domain indicated by a white circle) surrounded by amorphous domains (grey domains). The surrounding amorphous domains and the coexisting bridgmanite grains (Bdm, white domains) retain an internal pressure preventing the complete amorphization of Dvm.

The mechanisms preventing the complete amorphization of Dvm upon decompression may be explained from the microtextures displaying a remaining crystalline domain of Dvm at the centre surrounded by an amorphous rim. The significant volume expansion due to the amorphization of Dvm induces static stress which prevents the complete amorphization. The same mechanism has been proposed to explain the presence of bridgmanite in shocked meteorites.

3.4 Physical properties of Minerals

The physical properties of minerals influence a wide range of processes that we observe in the Earth and in extra-terrestrial systems, from how elements can be transported in the deep interior to how resistant to stress rocks can be and how fast seismic waves can travel through a planet. The contributions in this section describe the behaviour of minerals present on Earth, as well as on Mars and achondritic meteorites.

In the first contribution the dihedral angles present in the olivine-fluid system have been studied as a function of pressure, temperature and fluid composition to better constrain the pore fluid geometry in mantle wedges. The proportion of faceted interfaces in the olivine-fluid system appears to be independent of the P - T -fluid composition conditions and increases the dihedral angle with consequent increase of the critical fluid fraction for percolation.

The next two contributions are aimed at characterising the high-pressure behaviour of phases which may act as hosts of volatiles in the Earth's mantle. In contribution **b.**, high-pressure experiments were conducted to investigate nitrogen incorporation in antigorite. The resulting product consisted of a mixture of olivine, enstatite, and an N-bearing phase which appears to be part of a solid solution between talc and tobelite. This phase has a smaller bulk modulus and larger elastic anisotropy than talc. In contribution **c.** the acoustic wave velocity of Mg-sursassite, which may form directly after chlorite destabilisation within subducted oceanic plates, has been measured by means of Brillouin scattering for a single-crystal oriented along [001] showing a significant anisotropy of the longitudinal wave velocity at room pressure.

In order to extract information about the composition and temperature variations in the Earth's lower mantle from seismic observations, accurate constraints on the high-pressure behaviour of candidate minerals are needed. The fourth contribution of this section describes the compressibility of sodium-rich aluminous silicate minerals with Ca-ferrite type structure, which may be the major phase in subducted metabasalts from the top through to the middle of the lower mantle. The study shows that Mg and Fe content increase the isothermal bulk modulus with respect the NaAlSiO₄ end-member, and that above 25 GPa a spin crossover occurs in Fe-bearing samples. In the fifth contribution, single-crystals of Fe²⁺-rich bridgmanite have been studied by means of X-ray diffraction at simultaneous high pressure and high temperature conditions to determine the thermal equation of state of this major component of the Earth's lower mantle.

The history of Earth is strictly correlated to that of the other planets and asteroids in our solar system, therefore efforts have been made not only on constraining the properties of terrestrial material but also on understanding the composition and formation of extraterrestrial objects. In the last two contributions experimental studies have been performed in order to give insight into the composition of Mars' interior and into the formation of enigmatic textures in the Fe-rich phases present in achondrites. In contribution **f.** single-crystals of a synthetic Fe-rich ringwoodite with a composition expected in the martian mantle have been studied by means of

Brillouin scattering coupled with a CO₂ laser heating system in order to reach the temperature expected in Mars' interior. The measured acoustic wave velocities can be used to obtain the seismic signature of this material to compare with the seismic data sent from the seismometer installed in the NASA Insight lander. In the last contribution, the texture produced in a simplified analog system (olivine, troilite and gold) equilibrated at high temperature and high pressure have been compared with those occurring in Fe-rich phases of primitive achondrite. This shows that such textures do not reflect high-temperature equilibration, but instead record annealing processes during the slow cooling history of the achondrites' parent bodies.

a. *The effect of faceting on olivine wetting properties (Y. Huang/Guangzhou, T. Nakatani and S. Sawa/Sendai, G. Wu/Guangzhou and Beijing, M. Nakamura/Sendai and C.A. McCammon)*

Grain-scale pore geometry primarily controls the fluid distribution in rocks, affecting material transport and geophysical response. The dihedral angle (θ) in the olivine–fluid system is a key parameter determining the pore fluid geometry in mantle wedges. Both curved and faceted olivine–fluid interfaces define θ in the system, generating faceted–faceted (FF), faceted–curved (FC), and curved–curved (CC) angles (Fig. 3.4-1a). However, the effect of faceting on θ under various pressure and temperature (P – T) conditions and fluid compositions have not been constrained, and its mineralogical understanding is unresolved. This study evaluates the facet-bearing θ and their proportions in olivine–multicomponent aqueous fluid systems. Our results show that 1/3 of olivine–fluid θ are facet-bearing angles, regardless of the P – T conditions and fluid compositions. Faceting produces larger dihedral angles than CC angles (Fig. 3.4-1b).

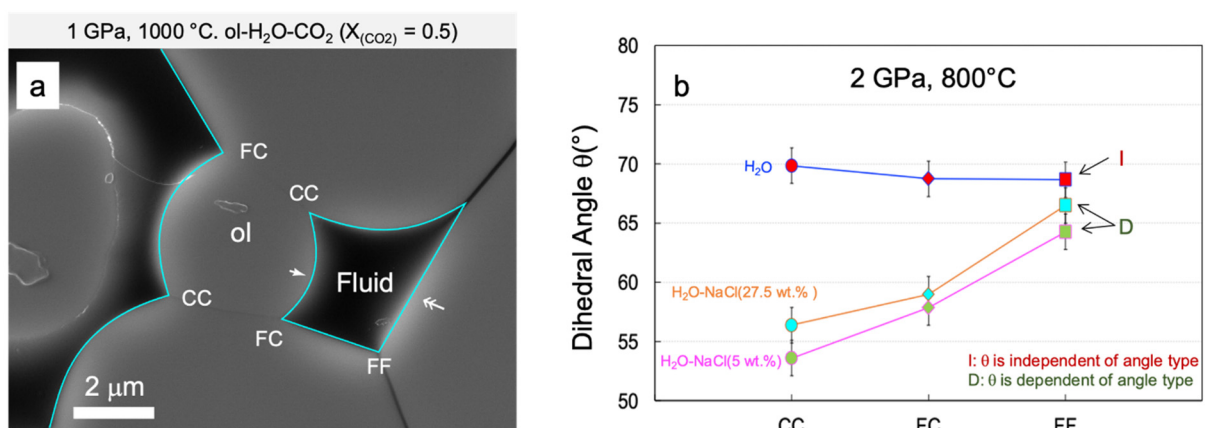


Fig. 3.4-1: **(a)** High-magnification secondary electron image of the typical apparent θ in the H₂O–CO₂ system ($X_{\text{CO}_2} = 0.5$) at 1000 °C and 1 GPa for 211 h. The run products are composed of mineral grains and epoxy resin-filled pores previously filled with aqueous fluid during the experiment. The white single and double arrows represent the curved and faceted interfaces, respectively. For the CC, FC, and FF angles, the interfaces are highlighted by cyan curves. **(b)** Faceting dependence of the median dihedral angles (θ) in the olivine–fluid system at 2 GPa and 800 °C.

The grain boundary plane (GBP) distribution reveals that the GBPs of faceted interfaces at triple junctions were subjected to low Miller Index faces ($\{100\}$, $\{010\}$, and $\{101\}$) (Fig. 3.4-2). The misorientation angle/axis distributions of adjacent grain pairs are in accord with the theoretical distribution of a random olivine aggregate. Moreover, the calculation of the FF angles for

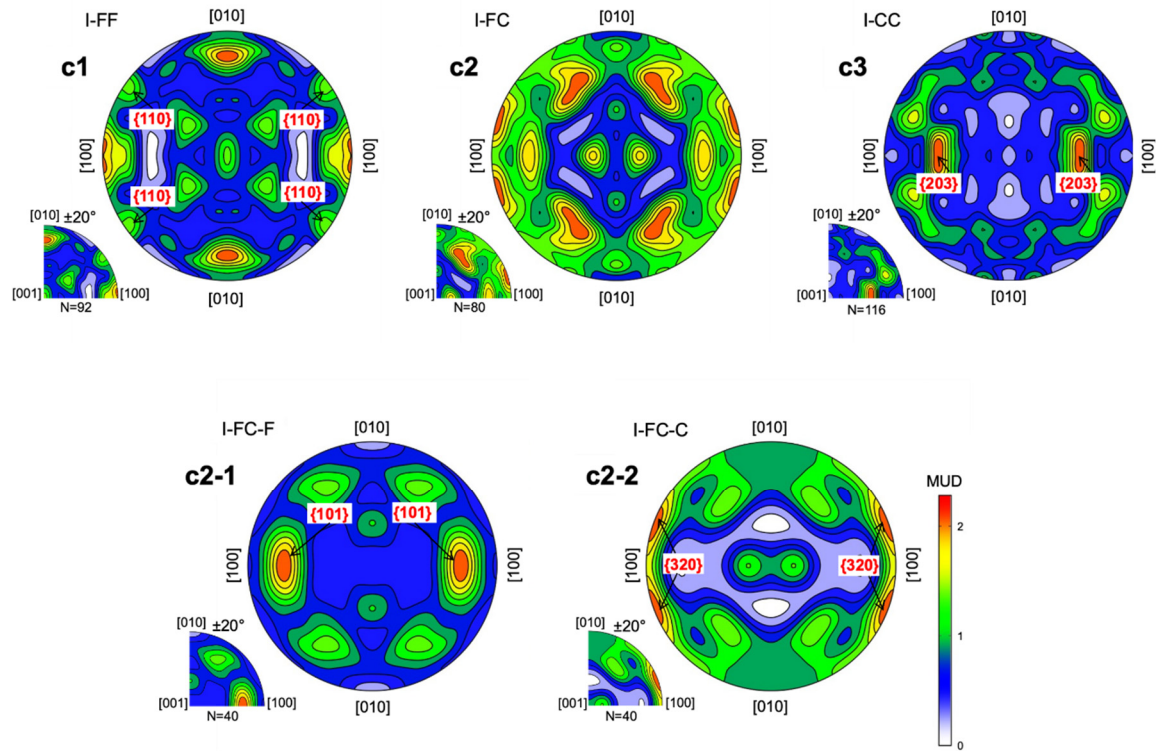


Fig. 3.4-2: (**c1–c3**) Pole figure of grain boundary plane distribution in the **I** group (*i.e.*, the systems where the θ values are independent of the angle–type). Pole figure of grain boundary plane distributions of faceted (**c2–1**) and curved (**c2–2**) sides at the FC triple junction for the **I** group. The equivalent olivine orientations obtained in the analysis were rearranged into the first quadrant to make the results more evident. Subsequently, by assuming that the grain boundary planes were equally distributed in each quadrant, the orientations in the first quadrant were copied in the other quadrants to obtain the pole figure. The analysed number (N) in the first quadrant is shown at the lower left in each pole figure. MUD is the multiples of uniform density, shown by the color bar's intensities. The Miller Indexes were marked around the high MUD. Abbreviations: FF = faceted–faceted angle, FC = faceted–curved angle, CC = curved–curved angle, I = angle–type independent group, D = angle–type dependent group.

adjacent grain pairs with low Miller index GBPs reproduces very well the measured angle values based on the olivine crystal habit. Therefore, our study suggests that the FF angle is strongly affected by olivine crystallography. The presence of faceting increases θ and the critical fluid fraction for percolation, thus decreasing the permeability. In the mantle wedge, where olivine crystallographic preferred orientation (CPO) is expected due to corner flow,

increasing the FF angle proportion with associated changes in fluid pore morphology will lead to permeability anisotropy, controlling the direction of fluid flow and resulting in geophysical anomalies such as seismic wave attenuation and high electrical conductivity.

b. Compressibility of N-bearing talc and insights into the deep nitrogen cycle (A. Minchenkova, D.J. Frost, T. Boffa Ballaran, A. Kurnosov, G. Criniti and C. Melai, in collaboration with W. Zhou and M. Hanfland/Grenoble)

Nitrogen concentrations in mantle xenoliths are typically below one part per million (ppm) but rocks related to subduction zones can show higher values ranging up to nearly 100 ppm. This is likely related to the presence of nitrogen in organic matter in subducting sediments which is the main route through which nitrogen is recycled into the interior. Despite the potential for nitrogen to be returned to the interior in this way, there remains a limited understanding of how nitrogen is partitioned among different phases once it enters the mantle.

To address this knowledge gap, high-pressure experiments were conducted to investigate nitrogen incorporation in typical subduction related mantle minerals. The starting materials employed were antigorite $(\text{Mg, Fe, Al})_{48}(\text{Si, Al})_{34}\text{O}_{85}(\text{OH})_{62}$ and glycine $\text{C}_2\text{H}_5\text{NO}_2$. Glycine, although more nitrogen rich, is used as a proxy for organic material in subducted sediments. It breaks down at the experimental conditions to produce graphite and a NH_3 - and N_2 -bearing H_2O -rich fluid. The experiments were conducted at 2.5 and 5 GPa and temperatures ranging from 500 to 700°C in a multianvil apparatus. Scanning electron microscope observations and X-ray powder diffraction analyses revealed that, in addition to unreacted serpentinite, the recovered products were mainly composed of olivine and enstatite in addition to a nitrogen-bearing mineral with a chemical composition resembling that of talc (Fig. 3.4-3c). This phase has the approximate chemical formula $(\text{NH}_4)_{0.97}\text{Mg}_{5.2}\text{Fe}_{0.31}\text{Si}_{7.6}\text{Al}_{0.1}\text{O}_{20}(\text{OH})_4$, determined with energy dispersive X-ray analysis. Relatively large ($\sim 80 \mu\text{m}$), platy single crystals of this phase could be recovered. Due to the very similar crystal structures (Fig. 3.4-3a, b), the recovered phase appears to be part of a solid solution that includes both talc and the mineral tobelite, $(\text{NH}_4, \text{K})_2\text{Al}_4(\text{Si}_3\text{Al})_2\text{O}_{20}(\text{OH})_4$.

Raman spectroscopic measurements confirmed that nitrogen was indeed incorporated as NH_4^+ ions between the T-M-T layers, where T indicates tetrahedral, and M octahedral sites. These layers are vacant in the talc structure (Fig. 3.4-3a), but in the tobelite structure they contain NH_4^+ and K (Fig. 3.4-3b). The lattice parameters for monoclinic 1M polytype tobelite with space group $C2/m$ are typically $a = 5.219 \text{ \AA}$, $b = 8.986 \text{ \AA}$, $c = 10.447 \text{ \AA}$, with a β angle = 101.31°. In contrast, pseudo-monoclinic 1A polytype talc (space group $C\bar{1}$) has a more compact lattice due to the shorter c axis, with parameters: $a = 5.29 \text{ \AA}$, $b = 9.173 \text{ \AA}$, $c = 9.46 \text{ \AA}$, and β angle = 98.68°. The recovered crystals showed monoclinic symmetry, and the incorporation of NH_4^+ resulted in a larger c -axis compared to talc, with $a = 5.282 \text{ \AA}$, $b = 9.148 \text{ \AA}$, $c = 10.325 \text{ \AA}$, and β angle = 99.778° (Fig. 3.4-3d). The crystals also displayed strong diffuse scattering, which is currently under evaluation.

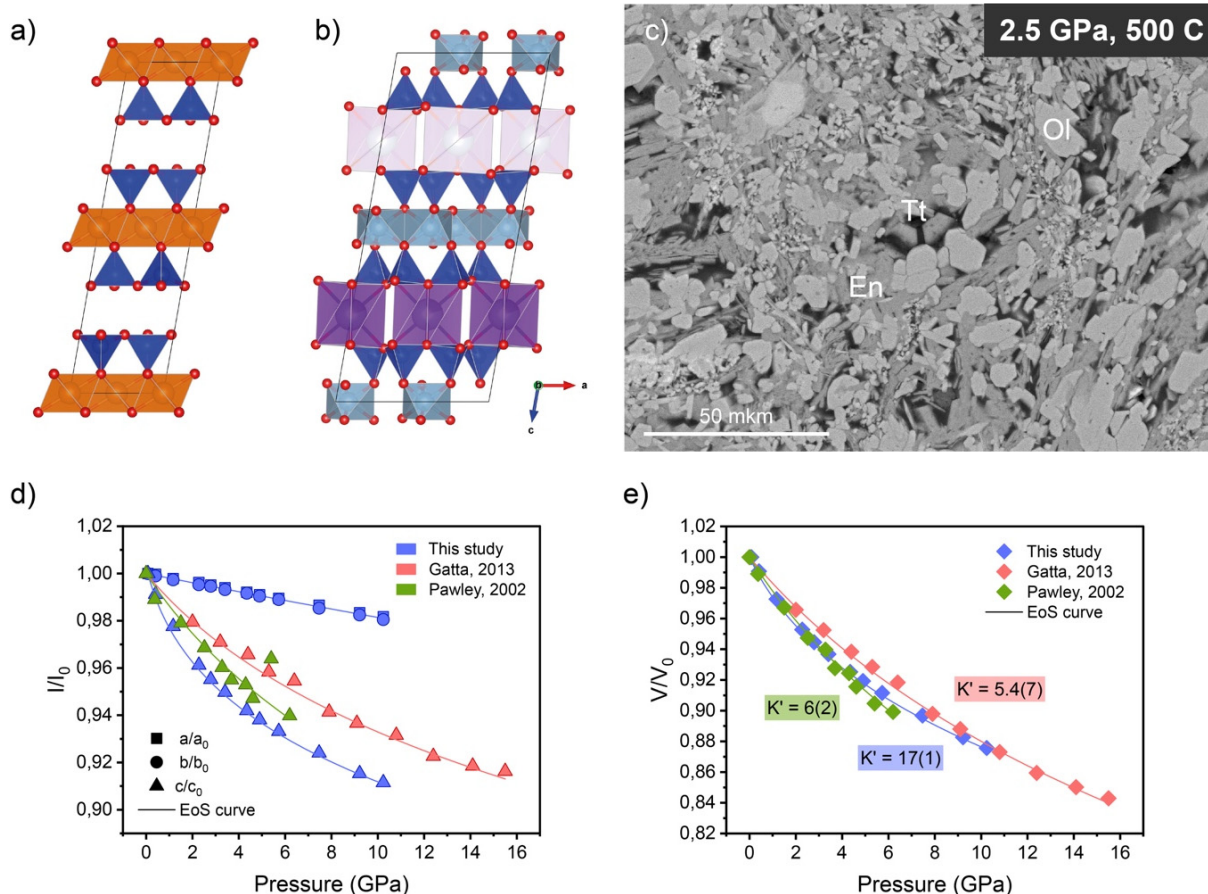


Fig. 3.4-3: **(a)** talc and **(b)** tobelite crystal structures along the b-axis. Oxygen (O) atoms are denoted by red dots, silicon (Si) tetrahedra are depicted in deep blue, aluminium (Al) octahedra in turquoise blue, magnesium (Mg) octahedra in orange, and the site containing potassium (K) / ammonium (NH_4^+) ions is shown in violet; **(c)** SEM-image of sample V1276-2 containing olivine and enstatite crystals and in the centre hexagon-shaped mica-like crystals of talc-tobelite; **(d)** normalized parameters (I/I_0), where I is either the a, b or c axis as indicated and **(e)** volume (V) as a function of pressure (P) for talc-tobelite samples (blue) within a pressure range of 0.08 to 10.24 GPa. For comparison, data for triclinic talc from Gatta *et al.*, 2013, *Phys Chem Minerals*, 40, 145-156 (red) and monoclinic talc from Pawley *et al.*, 2002, *Am Mineral*, 87, 1172-1182 are also given. The curves indicate the calculated equations of state.

To further investigate the impact of NH_4^+ incorporation on the compressibility of talc, single-crystal X-ray diffraction experiments were conducted. The talc-tobelite crystals were carefully broken into pieces of 60 and 30 μm and loaded into a diamond anvil cell (DAC) with helium as the pressure-transmitting medium. The pressure was determined using a ruby chip. Single-crystal X-ray diffraction measurements were performed at pressures up to 10.24 GPa at the ESRF ID15B beamline. The results indicate a highly anisotropic axial compressibility (Fig. 3.4-3e), a common feature in phyllosilicate minerals. The c-axis, perpendicular to the layers, exhibited the highest compressibility. Interestingly, the N-bearing talc structure demonstrated greater compressibility than talc. However, a notable finding was the smaller bulk modulus

($K_0 = 31(4)$) and its large first derivative ($K' = 17(1)$) in comparison with previous monoclinic data from Pawley (2002) $K_0 = 41(1), K' = 6(2)$ or Gatta (2013) $K_0 = 56(3), K' = 5.4(7)$, indicating that the small amount of NH_4^+ present in the interlayer sites significantly influences the response of the talc structure to increasing pressure. This suggests a nuanced and intricate interplay between nitrogen incorporation and the compressibility behaviour of talc under high-pressure conditions.

c. The elastic behaviour of Mg-sursassite (B. Chrappan and M. Merlini/Milan, in collaboration with G. Criniti, T. Boffa Ballaran and A. Kurnosov)

Experimental studies have shown that the pressure- and temperature-induced destabilization of chlorite within subducted oceanic plates does not automatically result in a complete release of water and that a wide range of new hydrous phases may exist even beyond the chlorite stability field. In the past thirty years, some previously unknown phases have been identified (*e.g.*, Mg-sursassite, 11.5 Å phase, Hyso phase, *etc.*) in both the MSH ($\text{MgO-SiO}_2\text{-H}_2\text{O}$) and the MASH ($\text{MgO-Al}_2\text{O}_3\text{-SiO}_2\text{-H}_2\text{O}$) systems, which can be ascribed to the group of so-called "dense hydrous magnesium silicates" (DHMS). As water can significantly affect the physical properties of silicates, several experimental and computational studies have tried to assess whether the presence of these phases in hydrous peridotitic systems could produce a seismologically detectable "water signature" within subducted slabs and if the alleged "water signature" could help tracing the cycling of water from the subducting plate to the overlying mantle wedge and/or toward the mantle transition zone. Among these phases, Mg-sursassite $\text{Mg}_5\text{Al}_5\text{Si}_6\text{O}_{21}(\text{OH})_7$ is one of the best candidates to form directly after chlorite destabilization in chlorite-rich peridotites. It was shown to be stable from 6 to 7 GPa at 973 K in the MASH system, before being replaced by the 11.5 Å phase at higher pressure.

Here, we report the first experimental data on the sound velocities of single-crystal Mg-sursassite by means of single-crystal X-ray diffraction and Brillouin spectroscopy. Large single crystals of Mg-sursassite were synthesised in a multianvil apparatus at 10 GPa and 1273 K for 288 hours at the Department of Earth Sciences, University of Milan. Three high-quality single crystals of approximately $120 \mu\text{m} \times 110 \mu\text{m} \times 70 \mu\text{m}$ were selected and oriented along the three principal directions (*i.e.*, [001], [010], [100]) using a single-crystal X-ray diffractometer at the Bayerisches Geoinstitut, University of Bayreuth. Once oriented, the crystals were polished on both sides to obtain 17 μm -thick slides and subsequently cut with a focused ion beam device to remove cracked or inclusion-bearing portions from each slide. Preliminary data collected on the (001) platelet are reported in Figure 3.4-4, showing a significant anisotropy of approximately 1500 m/s in the compressional velocity (v_P) as a function of the rotation angle χ of the diffractometer. Future measurements on the remaining two platelets will be needed for the complete elastic tensor to be obtained from the inversion of experimentally measured velocities and density. Additional work will also be devoted to measuring the sound velocities

of Mg-sursassite at high pressure in the diamond anvil cell to determine its anisotropic and aggregate elastic properties at the pressure conditions of its stability field in the Earth's upper mantle.

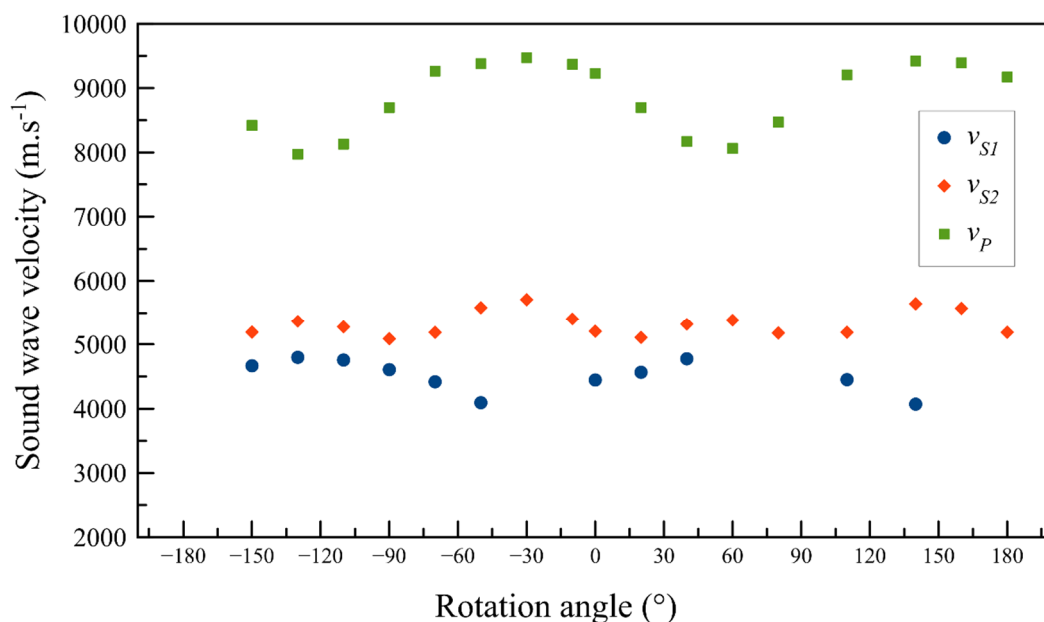


Fig. 3.4-4: Preliminary results on the sound wave velocities of Mg-sursassite measured by Brillouin scattering on the (001) platelet at ambient conditions.

d. *Effect of chemistry on the compressibility and structural evolution of CaFe₂O₄-type aluminous phases (G. Criniti, T. Boffa Ballaran, A. Kurnosov and D.J. Frost, in collaboration with T. Ishii/Misasa, K. Glazyrin/Hamburg and T. Fedotenko/Hamburg)*

The interpretation of seismic observations of the Earth's lower mantle is only possible if the physical and chemical properties of candidate lower mantle minerals are tightly constrained. For instance, the presence of recycled oceanic materials in the top- and mid-lower mantle was highlighted from seismic scattering and tomographic models and mineral physical models of subducted mafic and ultramafic rocks. At these pressure and temperature conditions, one of the major mineral phases of a subducted metabasalt is a sodium-rich aluminous silicate with CaFe₂O₄-type structure, also known as CF-type phase. The crystal chemistry of the CF-type phase is rather complex, with the most abundant component being NaAlSiO₄, followed by MgAl₂O₄, Mg₂SiO₄, Fe²⁺Al₂O₄ and Fe²⁺Fe³⁺₂O₄. Understanding the link between the possible cation substitutions in the CF phase and changes in its physical properties is therefore critical to refine existing models of depth-dependent density and seismic velocities of subducted metabasalt and solve potential trade-offs arising from variation in its bulk chemistry and temperature.

In this study, we have determined the equation of state of high-quality CF-type single crystals synthesised in a multianvil press in the NaAlSiO_4 , $\text{NaAlSiO}_4\text{-MgAl}_2\text{O}_4$, and $\text{NaAlSiO}_4\text{-MgAl}_2\text{O}_4\text{-Fe}_3\text{O}_4$ systems and analysed at high pressure using diamond anvil cells and synchrotron X-ray diffraction in several experimental runs. We found that the isothermal bulk modulus (K_{T0}) of the CF phase increases with increasing Mg and Fe content (Fig. 3.4-5), which was difficult to infer from previous studies which showed contrasting results for the NaAlSiO_4 end member. Above 25 GPa, a subtle change in the compression mechanism of the Fe,Mg-bearing sample (Fig. 3.4-5, right) was observed, suggesting the onset of a high-spin to low-spin crossover of octahedrally coordinated Fe^{3+} , as indicated in previous studies. Structural refinements were also obtained from the single-crystal X-ray diffraction data and helped us understand the individual effects of chemical substitutions in the different crystallographic sites of the CF crystals. The main factor contributing to the stiffening of the CF structure as a function of composition seems to be the substitution of Na by Mg and Fe^{2+} in 8-fold coordinated A-site. Conversely, the effect of Si replacement by Al and Fe^{3+} appears less straightforward, as the pressure-induced spin crossover of Fe^{3+} also affects the polyhedral compression behaviour. Data determined in this study on the bulk and site compressibility of CF-type phases will help model the elastic properties of relevant end-members, which can then be used to both extrapolate phase equilibria and calculate the seismic properties of metabasaltic rocks.

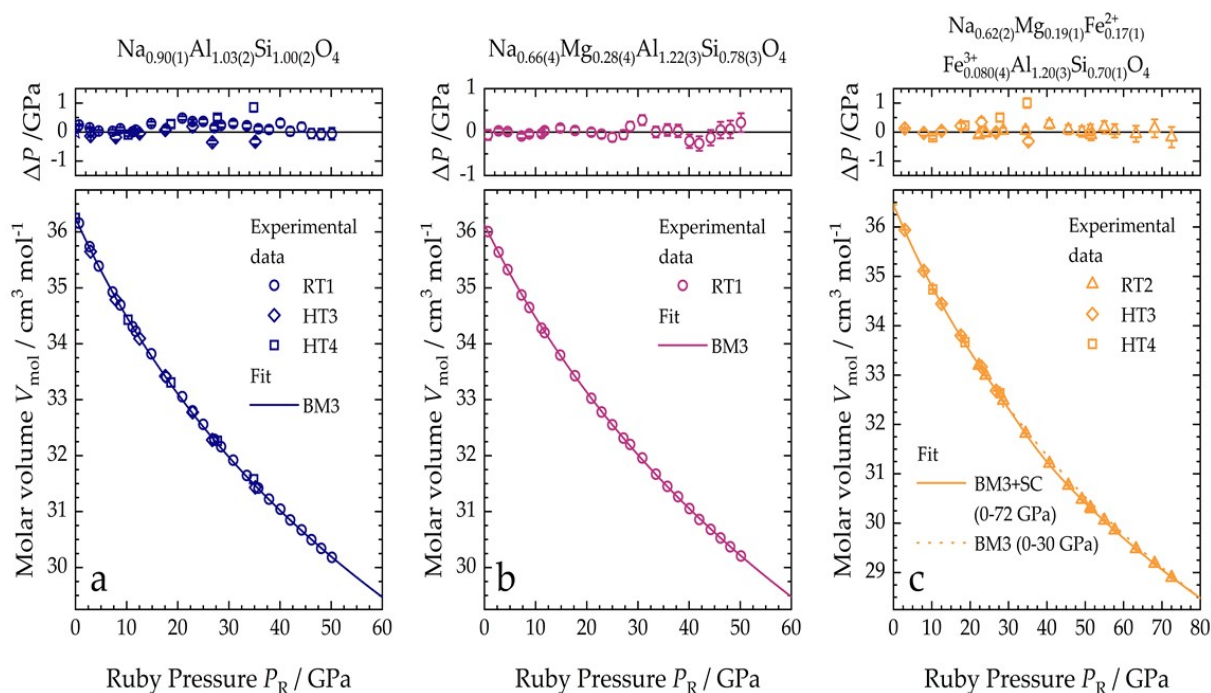


Fig. 3.4-5: Pressure-volume relations of CF-type phases investigated in this study and their respective 3rd-order Birch Murnaghan (BM3) or spin-crossover (BM3+SC) equations of state. Residuals calculated from the observed ruby pressures and calculated pressures from the equations of state are shown above each graph.

e. *Thermal equation of state of an Fe²⁺-rich aluminous bridgmanite (G. Criniti, T. Boffa Ballaran, A. Kurnosov and D.J. Frost, in collaboration with T. Ishii/Misasa and K. Glazyrin/Hamburg)*

Bridgmanite, (Mg,Fe²⁺,Fe³⁺,Al)(Si,Al,Fe³⁺)O₃ with a distorted perovskite-type structure, is the most abundant mineral in Earth's lower mantle. In the topmost region of the lower mantle, bridgmanite can accommodate relatively large amounts of ferric iron (Fe³⁺/ΣFe ~ 0.7) in both its crystallographic sites even at low oxygen fugacity conditions due to the charge disproportionation reaction 3Fe²⁺ = 2Fe³⁺ + Fe⁰. As pressure increases, this equilibrium is expected to progressively shift to the reactants side, hindering the incorporation of Fe³⁺ in bridgmanite. Fe²⁺-rich bridgmanite is therefore likely to become relevant in deeper regions of the lower mantle. Synthesising suitable bridgmanite samples to investigate the compressibility and elastic properties of Fe²⁺-rich mantle bridgmanite is experimentally challenging at topmost lower mantle pressures. Even in Al-free systems, where iron is mostly ferrous, some amounts of ferric iron have been consistently reported in both the pseudo-dodecahedral and the octahedral sites. This is problematic as increasing pressure induces a spin crossover of octahedrally coordinated Fe³⁺ which is unlikely to take place in the deep lower mantle and challenging to deconvolute from the effect of Fe²⁺ incorporation in the pseudo-dodecahedral site.

This problem can be circumvented if synthesis experiments are conducted at higher pressure, where the disproportionation reaction is inhibited. For this purpose, we performed a multianvil synthesis experiment employing tapered anvils made of hard WC alloys to achieve a pressure of 45 GPa at 2000 K. The composition of the recovered bridgmanite sample, determined by electron microprobe analyses and Mössbauer spectroscopy, is (Mg_{0.856(19)}Fe²⁺_{0.075(5)}Fe³⁺_{0.019(5)}Al_{0.044(13)})(Al_{0.050(11)}Si_{0.950(11)})O₃, with all Fe in the Mg site and most of it being ferrous. The sample was then polished to an 8 μm thick slide and gently crushed to produce grains with a grain size of the order of 5 μm. The crushed grains were tested at the Extreme Conditions Beamline P02.2 of the PETRA-III synchrotron (Hamburg, Germany) to select suitable single crystals to be used in high-pressure/-temperature single-crystal X-ray diffraction experiments. Diamond anvil cells equipped with Pt-wire external resistive heaters were used to generate simultaneous high-pressure and high-temperature conditions up to approximately 66 GPa and 960 K (Fig. 3.4-6). Helium or neon were used as pressure-transmitting media and nanocrystalline gold was used as a pressure standard. Third-order Birch-Murnaghan and Mie-Gruneisen-Debye equations of state were used to model the bridgmanite sample behaviour at room and high temperature, respectively, providing a good fit to the experimental data points. Once included in appropriate mineral physical models, the equation of state parameters of Fe²⁺-rich aluminous bridgmanite determined here will allow for more accurate estimates of the elastic and thermodynamic properties of the lower mantle phase assemblage to be made and compared to seismic observations.

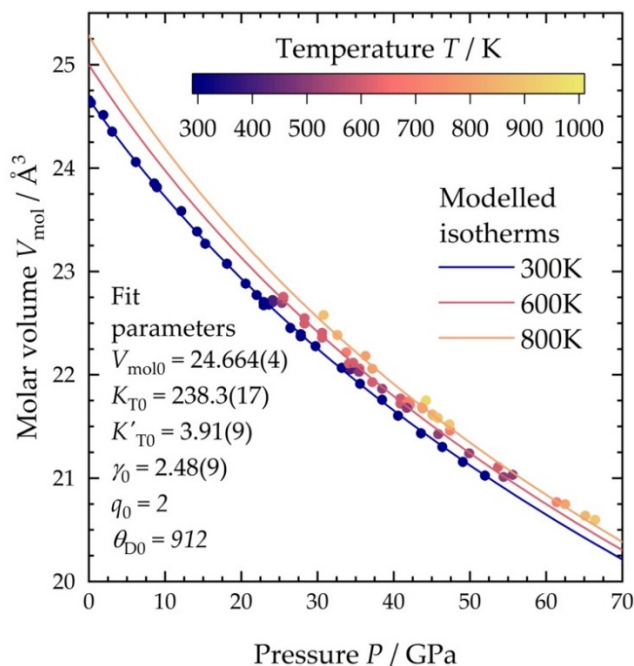


Fig. 3.4-6: Pressure-volume-temperature relations of Fe²⁺-rich aluminous bridgmanite determined in the present study. Experimental temperatures are expressed through colour coding and equation of state fit parameters are reported on the left-hand side of the figure, with numbers in italics being fixed during the fit. Solid lines are isotherms at selected temperatures calculated using the fit parameters reported in the figure.

f. Elasticity of Martian ringwoodite (*A. Kurnosov, T. Boffa Ballaran, G. Criniti and D.J. Frost*)

Ringwoodite (Rw) (Mg,Fe)₂SiO₄, a high-pressure polymorph of olivine having the spinel structure, is a major rock-forming mineral both in the Earth's transition zone and in the Martian mantle. Knowledge of the elastic behaviour of this mineral, therefore, is essential for modelling plausible compositions and temperature gradients in both Earth and Mars interior. The major difference between the terrestrial and the Martian ringwoodite resides in the larger Fe content of the latter. There are, however, conflicting experimental results reported in the literature on the effect of iron on the room-temperature elastic properties of Rw, making any estimate based on velocity modelling subject to significant uncertainties. Moreover, there is only one experimental study reporting the elastic behaviour of ringwoodite having a terrestrial composition at temperature up to 700 K, so that the temperature dependence of elastic properties is practically unconstrained. For this reason, we have decided to determine the variation with pressure and temperature of the full elastic tensor of an Fe-rich Rw (Mg_{0.7}Fe_{0.3})₂SiO₄, Rw70.

Single-crystals of Rw70 (see annual report 2021) have been measured using simultaneous high-pressure X-ray diffraction and Brillouin scattering up to 21 GPa at room temperature. In this way the effect of iron on the aggregate wave velocity of Rw has been accurately determined up to the pressures at which this mineral is stable in the Martian mantle. Substitution of Fe into the ringwoodite structure gives rise to a major decrease in both aggregate shear, v_S , and longitudinal, v_P , wave velocities (Fig. 3.4-7). Rw70 appears elastically anisotropic at room pressure with a variation of v_S and v_P of ~ 400 m/s between minima and maxima. Such variation, however, decreases rapidly with increasing pressure and the anisotropy of Rw70 is negligible above 16 GPa.

High-pressure and high-temperature Brillouin scattering measurements have been performed using the CO₂ laser heating system installed at BGI. An articulated arm (AA), which has been developed for surgical use, allows us to use the CO₂ laser in a completely closed environment. Mirrors are mounted in each junction of the AA to direct the laser to the exit point. The final junction of the AA contains already a 50 mm focusing distance lens and therefore it is sufficient to mount this junction on a X, Y and Z translation stage close to the diamond anvil cell (DAC) and to focus the laser on the sample inside the DAC. For these measurements, three crystals of Rw70 oriented along the [100] direction, double-side polished down to a thickness of 15 μm, and cut into circular disks of 40 to 60 μm in diameter using a focused ion beam (FIB) instrument, were loaded together between two KBr disks used as thermal insulation from the heat-conductive diamond anvils. An Sm-doped Y₃Al₅O₁₂ garnet (Sm:YAG) crystal inserted close to the diamond has been used for determining pressure at high temperature, since its fluorescence signal does not depend on temperature, in contrast to the fluorescence of ruby. Several loadings were necessary, due to the fact that Brillouin scattering collection at high temperature, although faster than at room temperature, still takes almost an hour, causing damage of the crystal surface after a few measurements. Since the anisotropy of Rw70 may change with temperature, Brillouin scattering spectra were collected for different orientations in order to constrain the full elastic tensor of Rw70 at each temperature. So far, the aggregate wave velocities v_s and v_p have been constrained between 17 and 21 GPa at 1600 K (Fig. 3.4-7). Moreover, several measurements have been already performed at temperatures as high as 1950 K (Fig. 3.4-8).

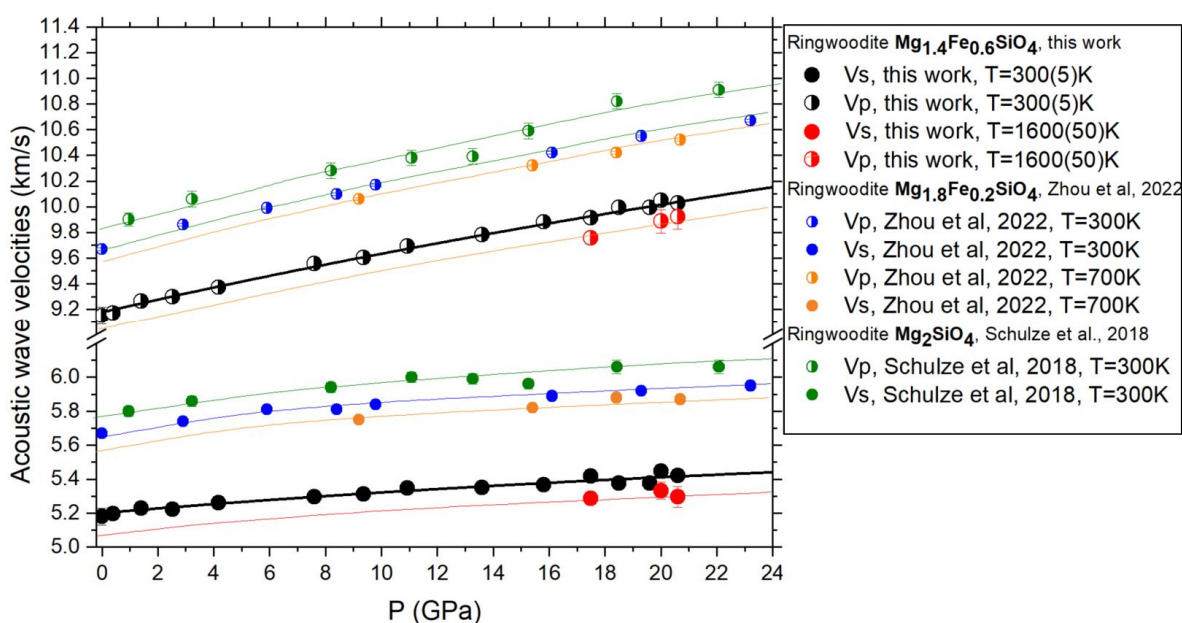


Fig. 3.4-7: Acoustic wave velocities of Martian composition ringwoodite at pressures up to 20.6 GPa at room temperature and some preliminary HP-HT data measured *in situ* in laser heated diamond anvil cell. Literature data for Rw100 and Rw90 are shown for comparison. The references referred to in the figure legend are: Schulze *et al.*, 2018, Earth Planet Sci Letters, 498, 9-16; Zhou *et al.*, 2022, Earth Planet Sci Letters, 579, 117359.

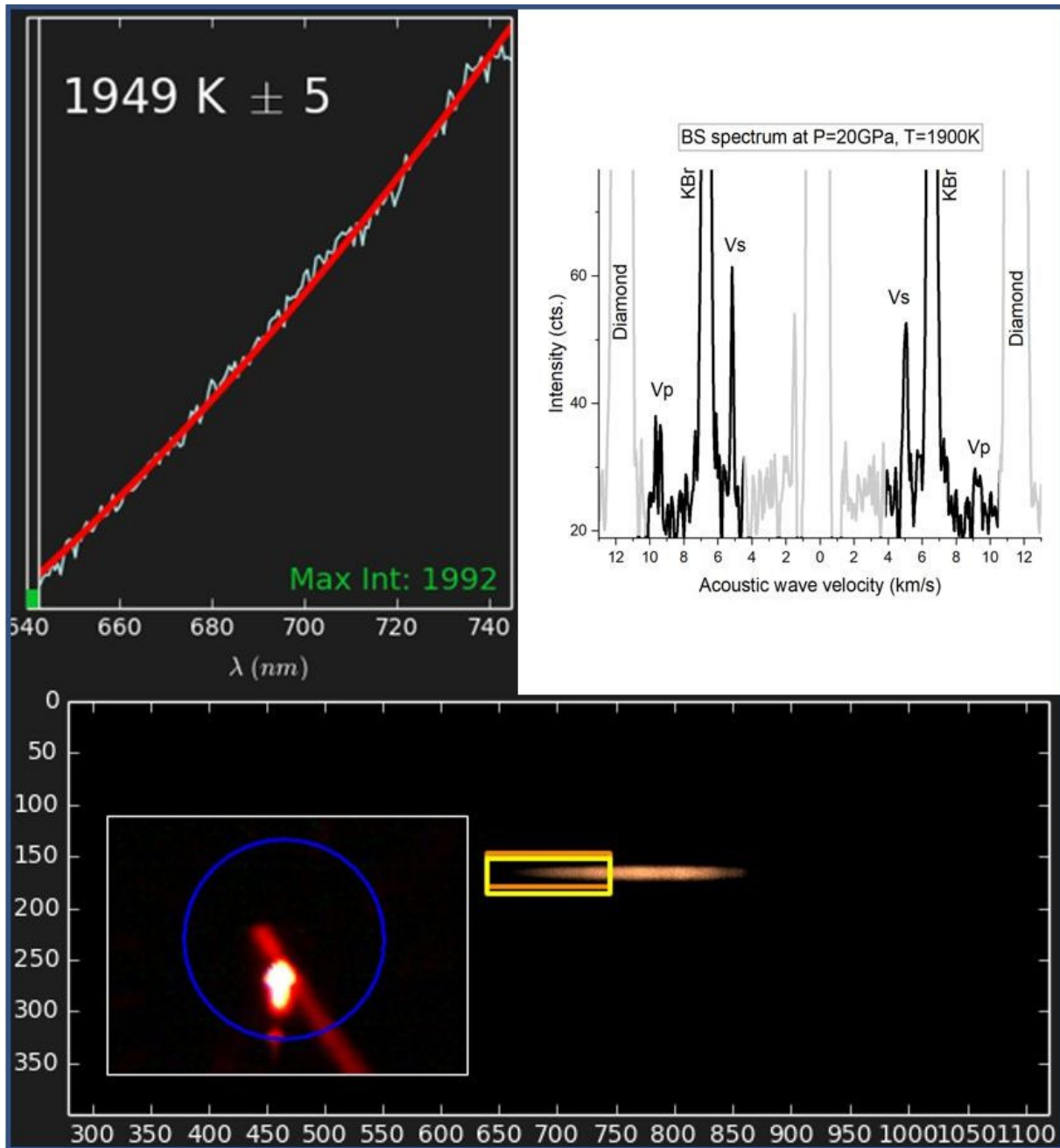


Fig. 3.4-8: Thermal radiation image of the Rw70 sample at 20 GPa and 1950 K determined using a W-wire calibration and the corresponding Brillouin scattering spectrum collected for 40 minutes.

g. *Reproducing iron-rich phase textures in primitive achondrites: Overcoming surface tension in solids* (A. Néri, E. Kubik, G.J. Golabek and A. Bouvier, in collaboration with N.P. Walte/Garching)

Primitive achondrites, like acapulcoites and lodranites, are partially differentiated meteorites which originate from parent bodies that accreted at around 1.3 Myr after CAIs, limiting their

heating potential, due to limited amount of ^{26}Al . Despite limited melting and maximum temperatures, these samples show a high degree of textural equilibration based on silicate phases, while textural features of iron-rich phases indicate otherwise. Based on the minimization of interfacial energies, the iron-rich phases are expected to distribute in a specific way above the Fe-Ni-S solidus, where the Fe-Ni residues (high surface energy phase) are surrounded by the sulphide melt (lower surface energy phase). This minimum energy configuration is not observed in sections of acapulcoites and lodranites (Fig. 3.4-9A), where kamacite-taenite (Fe-Ni) and troilite (FeS) are equally contacting the silicate phases and both of these phases are spatially separated.

To understand these features and their formation, a series of experiments was conducted. A simplified analog system (olivine, troilite and gold) was enclosed in graphite capsules and compressed to 2.5 GPa, using a 25/17 (octahedron edge length to truncation edge length) standard BGI multianvil assembly. In this simplified system, gold acts as the high interfacial energy phase, and troilite as the low energy one.

When equilibrated at 1300 °C, and regardless of experimental duration (3 hours to 1 week), the recovered textures correspond to the expected energy minimum, with the gold pools fully surrounded by troilite melt (Fig. 3.4-9B). Although our conception of the system thus proved correct, this experiment also hinted that high-temperature equilibration above the metal solidi may not be the only process at play to produce the textural features observed in natural samples. Thus, additional experiments were conducted, but with a different temperature path, in an attempt to mimic the cooling phase that a planetesimal may have experienced. Samples were also equilibrated for 3 h at 1300 °C, but the temperature was rapidly (within ≈ 2 min) decreased to 1000 °C and held constant for timescales ranging from one week to one month. From the recovered samples, it is visually striking that troilite and gold were spatially separated during the annealing phase at 1000 °C (Fig. 3.4-9C). The extent of this separation increases with extended experimental time.

From the recovered samples, the evolution of the contact length between different phases was investigated to track the evolution of interfaces with high (Au-Ol on Fig. 3.4-9D) and low energy (Au-FeS on Fig. 3.4-9D). Interestingly, and very counterintuitively, the contact lengths with high energy costs increase at the expense of those of low energy cost, which seems to violate the principle of minimization of interfacial energies during annealing.

This evolution allowed us to implicate grain growth of solid phases as the process counteracting small-scale geometry changes due to surface tension. Indeed, in the solid state, metallic phases have high viscosities and diffusion is sluggish, meaning that the timescale required to maintain the local low surface energy configuration is greater than that for geometrical changes induced by migrating silicate grain boundaries. In summary, the textures of iron-rich phases in primitive achondrites do not reflect high-temperature equilibration, but instead recorded annealing processes during the slow cooling history of their parent body. This process can also explain

previous observations of decreasing Fe-Ni–troilite phase boundary lengths with increasing metamorphic grade of ordinary chondrites (H3 – H6).

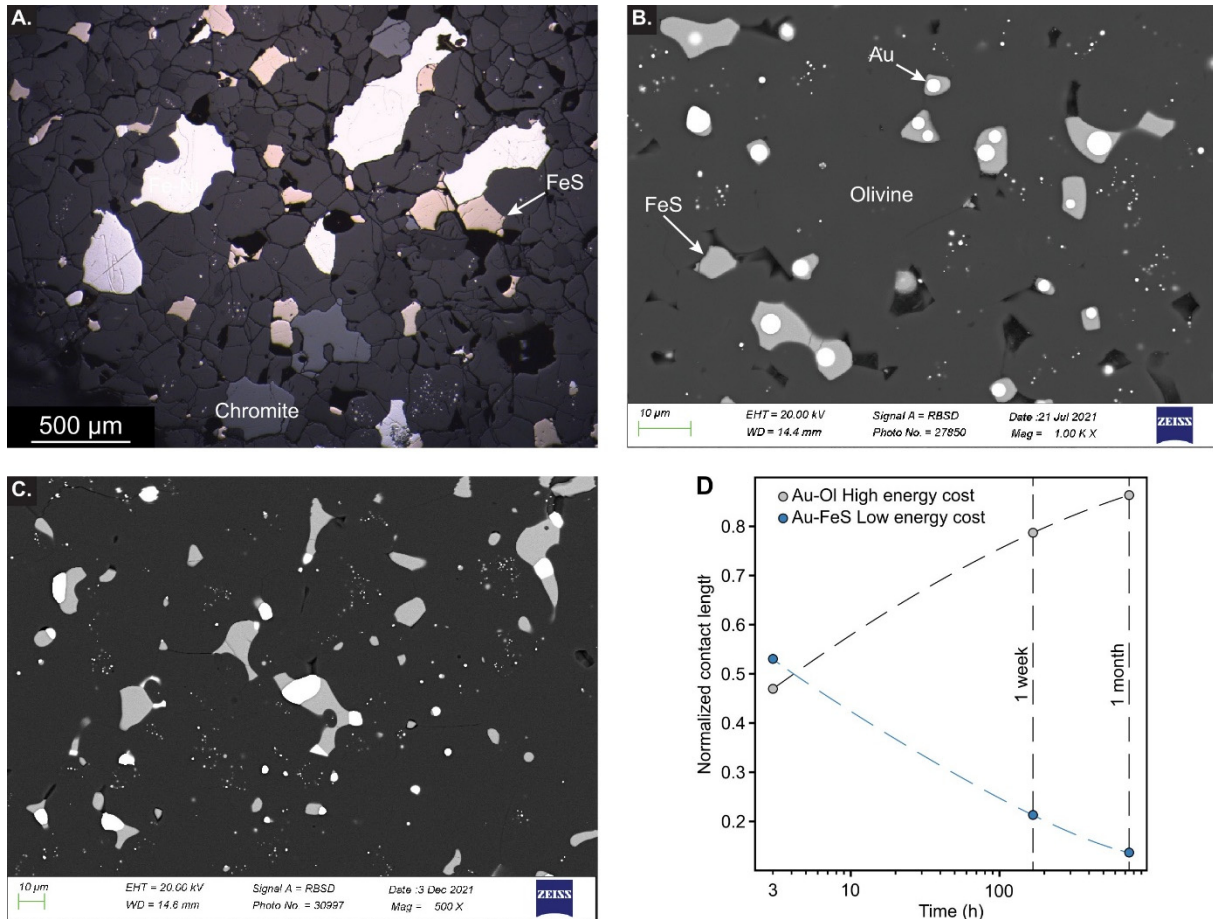


Fig. 3.4-9: (A) Optical image of a section from the meteorite Acapulco. (B) and (C) Scanning Electron Microscopy (SEM) images of recovered samples. (B) After equilibration at 1300 °C and 2.5 GPa for 3 h. (C) After equilibration at 1300 °C and 2.5 GPa for 3 h and then subsequent re-equilibration at 1000 °C lasting for one month. (D) Evolution of the contact length between gold and olivine, and gold and troilite, as a function of annealing time.

3.5 Fluids, melts and their interaction with minerals

Air mainly consists of nitrogen (78 % N₂) and for a long time, the atmosphere was believed to be the main nitrogen reservoir on our planet. Overall, this would imply that compared to other volatiles, such as hydrogen or carbon, the Earth is anomalously depleted in nitrogen. However, research at the Bayerisches Geoinstitut in recent years has shown that very likely, the deep mantle is a major nitrogen reservoir. It is the poor sampling of this reservoir which may convey the impression of a selective depletion of nitrogen on Earth, which in reality may not exist. The first contribution in this chapter provides additional evidence for this idea. In a project that was originally designed to study nitrogen solubility in aluminous bridgmanite, the main phase of the lower mantle, some Fe-rich magnesiowüstite (Fe,Mg)O was also formed. Chemical analyses revealed spectacularly high nitrogen contents in this phase, sometimes exceeding 10 wt. %. Apparently, under the high-pressure conditions of these experiments, there is an extended solid solution between (Fe,Mg)O and FeN. In early Earth history, this effect may have produced an extreme enrichment of nitrogen just above the core mantle boundary. The zones of ultra-low seismic velocities (ULVZs) which can be detected at this location are believed to be regions strongly enriched in Fe-rich magnesiowüstite, which precipitated upon crystallization of a deep magma ocean. This would therefore be a mechanism to concentrate most of the nitrogen on Earth in a thin layer just above the core.

In addition to the mantle, the core may also be an important reservoir of volatile elements in Earth's deep interior. However, studying the behaviour of volatiles under the pressure and temperature conditions of the core by laboratory experiments is extremely challenging. In order to overcome these problems, the following contribution in this chapter used molecular dynamics simulations with neural network interatomic potentials to estimate the partitioning of hydrogen between the solid inner core and the liquid outer core. The data show that H is only mildly enriched in the liquid by about a factor of two. Hydrogen could therefore significantly contribute to the known density deficit in both the outer and inner core.

In the Earth's mantle, "water" is mostly present as OH defects in minerals. Although these defects occur only in rather low concentrations, they constitute a major water reservoir in our planet and they may have an important effect on the physical properties of the mantle. Two contributions therefore look at OH defects in mantle minerals. Olivine, the most abundant mineral of the upper mantle, often shows very complex infrared spectra indicating the presence of several types of OH group at different places in the structure. The "group II bands" between 3250 and 3400 cm⁻¹ have often been attributed to OH defects associated with Fe³⁺. This interpretation is, however, problematic, as these bands are also seen in samples equilibrated at very reducing conditions, where Fe³⁺ should be negligible. By looking at infrared spectra of olivines produced with different trace element doping, it is now demonstrated here that in reality, the "group II bands" are due to OH groups associated with Cr³⁺. Another study investigates water solubility in Al-free stishovite and concludes that this phase contributes only little to water transport in deeply subducted slabs.

Dehydration of hydrous minerals in subducting slabs releases free aqueous fluids that move upward and cause melting in the mantle wedge. The mechanism and speed of this fluid flow is, however, poorly constrained. Two studies provide some experimental constraints on this problem. Multianvil experiments were designed such that there is a fluid source on one side of a sample capsule and a sink on the other side. Permeability data from such experiments suggest that the flow of water along the grain boundaries of a polycrystalline olivine aggregate is very slow, with a movement of only about 1 meter over one million years at 700 °C. Very likely, some kind of channelized flow is required to enhance fluid movement in nature. Preliminary experimental results indicate, however, that at more reducing conditions, H₂ would move much faster than water.

While the (anhydrous) melting temperature of the upper mantle is well constrained, phase relations in the mid-mantle are still much more uncertain. A new study using advanced multianvil technology, such as zero-gradient assemblies, suggests that solidus temperatures are 45-60 °C higher than previously thought. The last two contributions in this chapter of the annual report describe improved data and models for silicate melt viscosities. The presence of nano-scale crystals of Fe-Ti oxides may have affected previous measurements of the viscosity of andesite melts. Available models for the viscosity of natural melts suffer from the fact that there is a gap in the range of viscosities that are readily accessible by laboratory measurements. By combining a synthetic data approach with an artificial neural network, this limitation can be overcome and physically meaningful viscosity data can be predicted in a data space that is inaccessible for measurements.

a. *A major nitrogen reservoir near the core mantle boundary (G. Rustioni, M. Wiedenbeck/Potsdam, N. Miyajima, A. Chanyshv and H. Keppler)*

Bridgmanite and ferropericlase (or magnesiowüstite) are the main minerals of the lower mantle. However, their capability to store nitrogen in their crystal structure is only poorly known. We therefore carried out a series of multianvil experiments at 24-33 GPa and 1600-1800 °C in order to measure nitrogen solubility in these lower mantle phases. Starting materials were oxide-hydroxide mixtures together with isotopically labelled ¹⁵NH₄¹⁵NO₃ as a source of nitrogen. All runs were buffered close to the iron wüstite buffer by adding Fe metal to the charge. Nitrogen contents in the run products were measured by SIMS (secondary ion mass spectrometry) at GFZ Potsdam.

A typical run product showing the coexistence of magnesiowüstite with bridgmanite, Fe-rich metal, and minor stishovite is shown in Figure 3.5-1. Most of the magnesiowüstite formed by oxidation of the Fe-metal during the experiment, such that the compositions of this phase in the run products can be very Fe-rich. SIMS analyses of the ferropericlase-magnesiowüstite solid solution are shown in Figure 3.5-2. They show a striking, orders-of-magnitude increase in the solubility of nitrogen in this phase with increasing Fe/Mg ratio, from a few tens of ppm to more than 10 wt. %. The SIMS data were confirmed by independent analyses by electron microprobe,

which yielded results overlapping with the SIMS data, although they suffered from some N degassing during the measurements.

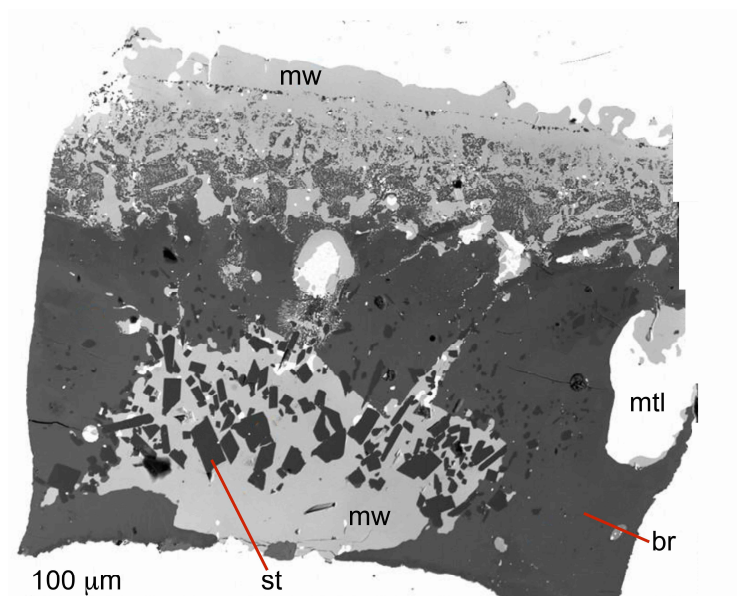


Fig. 3.5-1: Backscatter electron image of a run product from a multianvil experiment at 24 GPa and 1700 °C in the presence of a N-rich fluid phase. mw = magnesiowüstite, br = bridgmanite, st = stishovite, mtl = Fe-rich metal

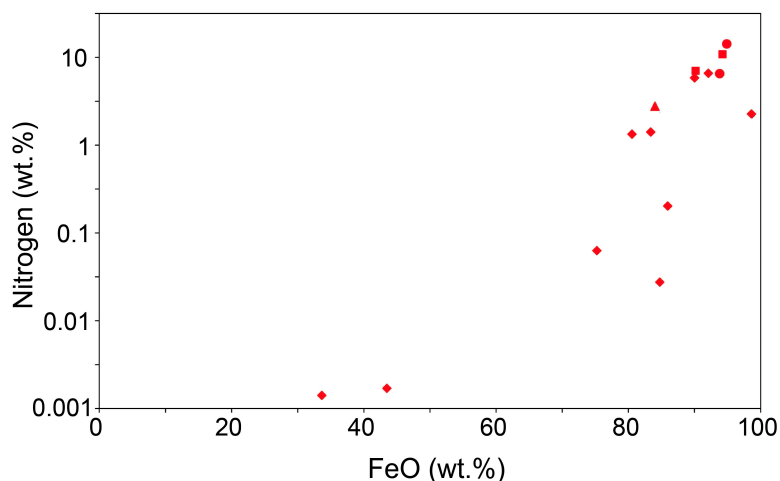


Fig. 3.5-2: Nitrogen solubility in magnesiowüstite-ferropericlase solid solution as a function of FeO content. Shown are data from single point SIMS analyses.

In order to constrain the dissolution mechanism of nitrogen in the magnesiowüstite, some N-rich samples were investigated by Raman spectroscopy and by transmission electron microscopy (TEM). Raman spectra did not show any evidence for N-H stretching vibrations, such that the incorporation of N as ammonium ions (NH_4^+) or other N-H species can be

excluded. Electron diffraction patterns (Fig. 3.5-3) show that the high nitrogen contents come from regions of single-crystal magnesiowüstite without phase impurities. N- and O-K edge ELNES (energy loss near edge structure) spectra of these regions further suggest that N and O in these crystals are in similar chemical or structural environments. Therefore, very likely, the high nitrogen solubilities are due to some solid solution between (Fe,Mg)O and NiAs-structured FeN. This is plausible, since the rock salt structure of (Fe,Mg)O and the NiAs structure of FeN only differ by the stacking sequence of densely packed anion layers. Indeed, extensive solid solutions between oxide and nitride phases are known from the materials science literature.

The experimental results obtained here may imply that most of Earth's nitrogen resides in the lowermost mantle, just above the core. There, zones of ultra-low seismic velocities (ULVZs) exist, which are believed to consist mostly of Fe-rich magnesiowüstite. They may be the result of the fractional crystallization of a deep remnant of the magma ocean, which caused magnesiowüstite to precipitate and to sediment on top of the core-mantle boundary. Mass balance calculations suggest that if Earth's primordial nitrogen content was similar to that of enstatite chondrites (about 600 ppm by weight), the ULVZs may have sequestered eight times more nitrogen than what currently resides in the atmosphere. This would mean that nitrogen is not anomalously depleted relative to other volatile elements on Earth. Rather, this apparent depletion results from the sequestration of N into a deep reservoir that is very poorly sampled.

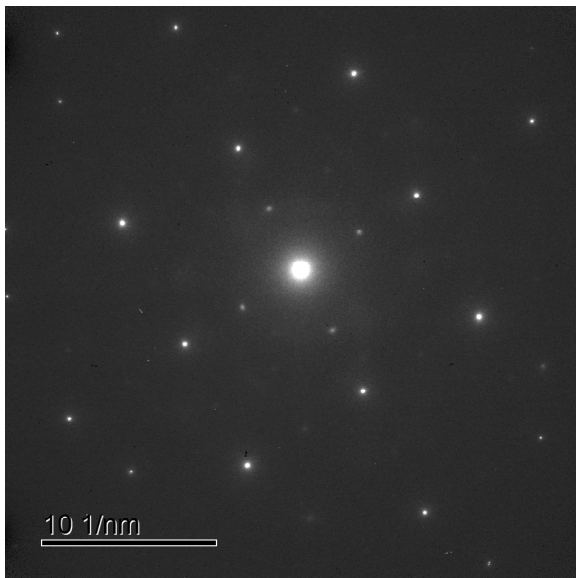


Fig. 3.5-3: Electron diffraction pattern of nitrogen-rich magnesiowüstite, demonstrating that the sample is a single crystal without phase impurities.

b. Hydrogen distribution between the Earth's inner and outer core (L. Yuan and G. Steinle-Neumann)

Explaining the physical state of Earth's core requires that in addition to iron, it also contains a significant amount of light elements. Among many candidates proposed, hydrogen attracts special attention as it is the most abundant element in the universe. Moreover, a substantial amount of H might have been sequestered into the core during planetary accretion, as

experiments and calculations show that it partitions into the metallic phase at high pressure. Distinguishing the behaviour of H in liquid and solid Fe is a prerequisite to developing and testing self-consistent chemical models for the entire core: If H disproportionately favors one phase – like oxygen that partitions strongly into the liquid – inner core crystallization will selectively enrich the inner or outer core in H. In experiments at high pressure, H enrichment in liquid FeH_x over solid FeH_x has been inferred in a semi-quantitative manner. Here, we tested this inference by performing molecular dynamics (MD) simulations to constrain the H partition coefficient, $D^{s/l}$, the ratio of mass fractions of H in solid and liquid iron at inner core boundary (ICB) conditions and to estimate the H content of the inner and outer core self-consistently.

To bypass the computational cost of determining the potential energy surface of FeH_x at density functional theory level, we constructed a neural network interatomic potential (NNP) that uses relative atomic coordinates to compute atomic energies and forces for large-scale MD simulations. We generated the NNP with a training dataset consisting of a total of 114,667 configurations selected by an active learning scheme using the DeePMD-kit. With the NNP, we performed MD simulations over a temperature range of 5000-7200 K and a pressure range of 300-330 GPa.

We used the solid–liquid coexisting method to study H partitioning between the hcp and liquid phases at temperatures between the solidus and liquidus of the system (Fig. 3.5-4). As H diffuses readily between coexisting solid and liquid in our MD simulations, we can quantify $D^{s/l}$ by directly counting the number of H atoms in solid and liquid. This seemingly straightforward approach requires large-scale cells which are only possible using NNP-MD, because in smaller cells with hundreds of atoms, typical for DFT-MD, solid–liquid coexistence cannot easily be controlled. Using the scalability of NNP-MD simulations, we performed a series of trial runs to locate T at which the solid–liquid interface remains stationary. In this way, we sampled two-phase configurations with excellent statistics. To identify how H distributes in the simulation cell, the snapshot was divided into slices of equal thickness parallel to the interface. Particle numbers N for Fe and H were then counted in each slice, resulting in number density profiles (Fig. 3.5-4) with the following characteristics: (i) large-amplitude periodic oscillations of $N(\text{Fe})$ in the solid, and a fairly smooth distribution in the liquid; (ii) the absence of a concentration gradient in the liquid and solid for Fe, and H suggests chemical equilibrium; (iii) the number of H atoms in the liquid region $N(\text{H}^l)$ is larger than that in the solid region $N(\text{H}^s)$, with a jump of $N(\text{H}^l)/N(\text{H}^s) \sim 2$ across the interface. We determined $D^{s/l} = 0.50 \pm 0.03$ – 0.62 ± 0.03 for a bulk H content of 0.13-0.34 wt. % by averaging over 2000 solid–liquid coexisting snapshots.

Our predicted $D^{s/l}$ are comparable to recent experimental estimates (0.70-0.89), an agreement that may be fortuitous, as the experimental results were obtained at $P < 50$ GPa, vastly different from ICB conditions that we consider. Unlike oxygen, which partitions strongly between solid and liquid Fe, a $D^{s/l} = 0.50 \pm 0.03$ – 0.62 ± 0.03 for H ensures an appreciable amount of H in the inner (and outer) core regardless of its crystallization history, which is a prerequisite for using

H-bearing Fe alloys to explain seismic characteristics of the core. An upper bound of ~ 0.3 wt. % combined with our predicted $D^{s/l}$ values and inner core growth to its current size (5 % total core mass) results in a concentration of 0.15-0.19 wt. % H in the inner core, equivalent to one times the mass of H in the ocean (ocean mass: $\sim 1.5 \times 10^{21}$ kg), and in a slightly enriched outer core with 0.31 wt. % H (33 times the mass of H in the ocean).

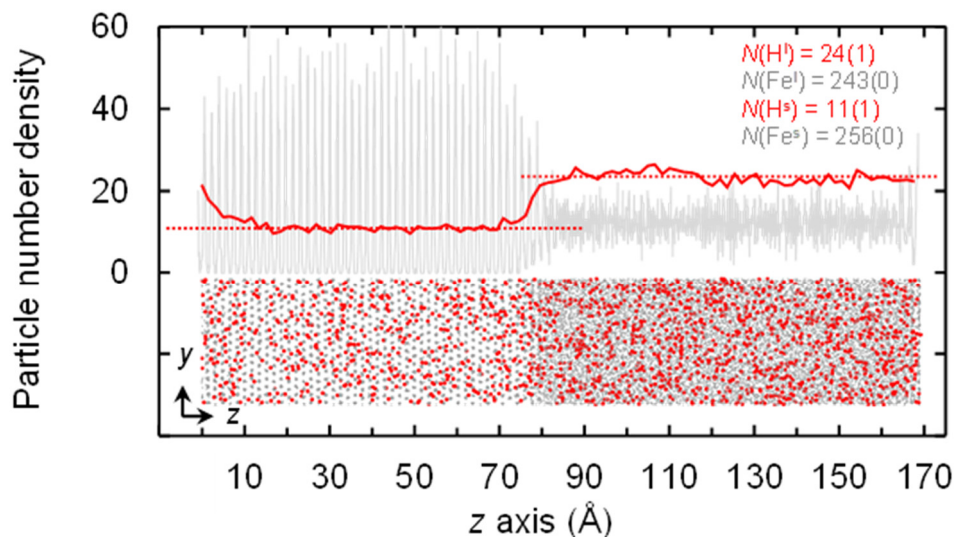


Fig. 3.5-4: Representative two-phase simulation result of hydrogen partitioning between solid and liquid FeH_x ($x = 0.13$ wt. %). We identify the distribution of atoms in the simulation cell by dividing the snapshot into 100 slices of equal thickness parallel to the interface. Particle numbers for Fe, $N(\text{Fe})$ in grey, and H, $N(\text{H})$ in red, are counted in each slice. Superscripts "s" and "l" denote solid and liquid, respectively. The lower panel shows a two-phase configuration with the left half Fe atoms (grey) in the solid state and the other half in the liquid state, while H atoms (red) distribute heterogeneously between the two regions. $N(\text{H})$ and $N(\text{Fe})$ are averaged over 20 snapshots.

c. *Fingerprints for coupled substitutions of H and trivalent elements in olivine from polarised infrared spectroscopy (A.C. Withers)*

Infrared spectroscopic measurements of olivines from mantle xenoliths commonly reveal evidence for the presence of trace amounts of H_2O . The complexity of infrared spectra in the OH-stretching region shows that several competing substitutional mechanisms for H can operate at the same time. Previous work has shown convincingly that peaks appearing in the region between 3250 and 3400 cm^{-1} , the so-called group 2 bands, arise from OH groups that form a defect complex with an M-site vacancy and a trivalent element, such as Fe^{3+} or Al. These group 2 bands are commonly observed in olivines from mantle xenoliths, and are frequently attributed to a coupled substitution that involves Fe^{3+} . However, the positions of the various peaks associated with coupled substitutions with different trivalent elements are similar, so an unambiguous assignment was not previously possible using a spectroscopic fingerprint.

Moreover, a couple of puzzling observations suggest that a coupled substitution with Fe^{3+} may not adequately account for the group 2 bands: (1) Group 2 bands are observed in olivines from xenoliths that appear pristine, and show no additional evidence for oxidation; (2) in previous experimental studies that use natural olivine as starting material to show that the H content of olivines varies systematically with the oxygen fugacity, the group 2 peaks persist even at low $f\text{O}_2$ corresponding to the iron-wüstite buffer. However, at these conditions, concentrations of Fe^{3+} in olivine are likely negligible.

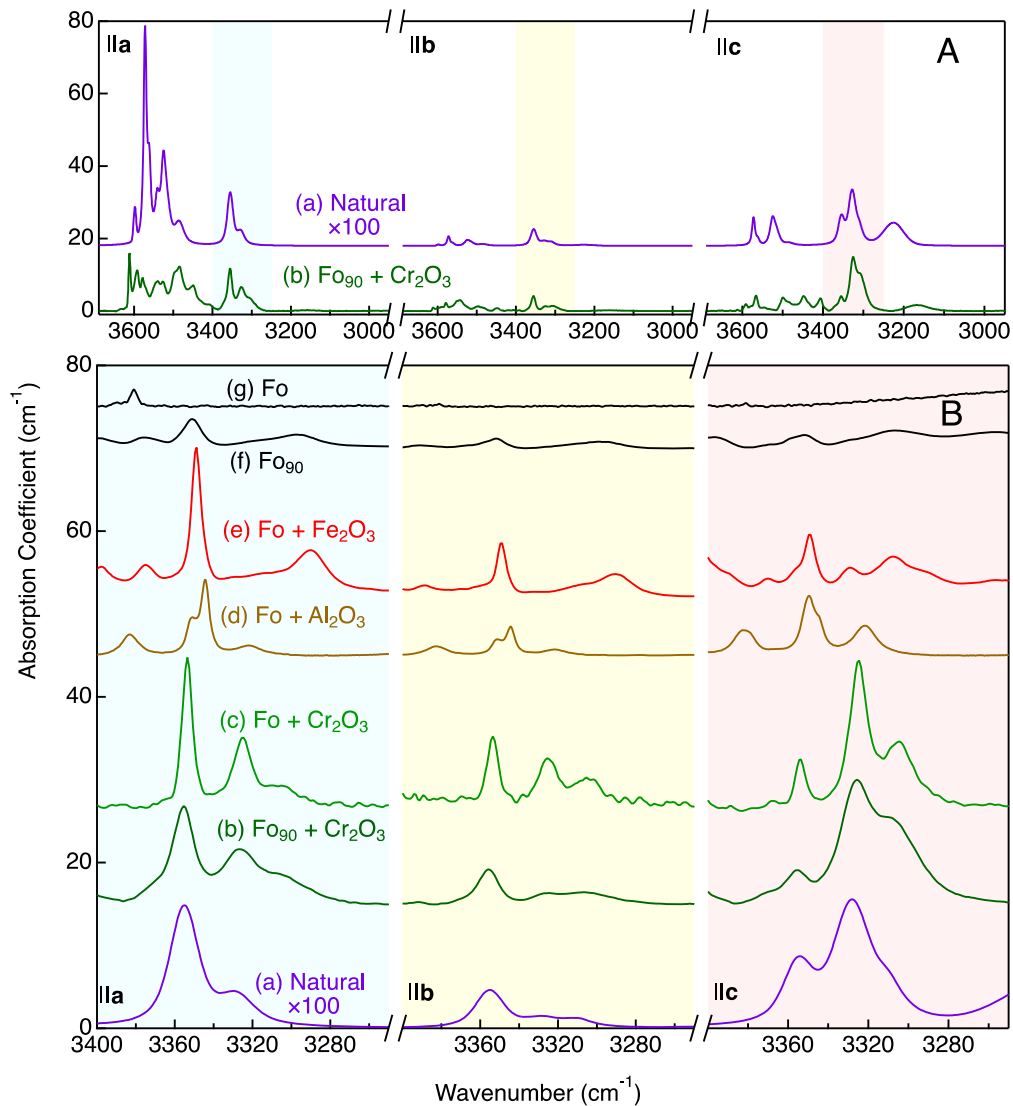


Fig. 3.5-5: (A) Representative polarised infrared spectra of olivine in the region 2950-3700 cm^{-1} . (B) An expansion of the shaded region in (A) to show the OH-stretching peaks associated with Fe^{3+} , Al and Cr. The samples were oriented with the \mathbf{E} -vector of the polarised beam parallel to the crystallographic a, b, and c axes in the left, centre, and right panels, respectively. Samples d, e, and g were synthesised under oxidized conditions with PtO_2 added to the sample capsule. The $f\text{O}_2$ in sample c was buffered by addition of $\text{Re} + \text{ReO}_2$. Synthesis pressure for sample d was 3 GPa and for all other samples was 6 GPa. The absorption coefficient of the natural olivine sample has been multiplied by a factor of 100 and the spectra are vertically offset for clarity.

Here, polarised transmission infrared spectroscopy of olivines synthesised in multianvil experiments is used to fingerprint the different elemental substitutions. Olivines were synthesised in hydrothermal experiments at 6 GPa and 1400 °C, with added Fe₂O₃, Al₂O₃, or Cr₂O₃. Oxidizing conditions were created in experiments with forsterite by the addition of PtO₂ or ReO₂, while experiments with Fe as a major element in olivine were unbuffered. An infrared spectrum of an olivine from a mantle xenolith (spectrum a, olivine from Mount Gambier, Australia) is compared with spectra from olivines synthesised in experiments in Figure 3.5-5. The orientations of OH dipoles for forsterites doped with Cr, Al, and Fe³⁺ (spectra c, d, and e, respectively) are distinct and provide fingerprints for the different possible substitutions. Iron-bearing olivine synthesised without oxygen buffer and without Cr or Al (spectrum f) shows limited group 2 bands, indicating that under these conditions a small proportion of the H in olivine is associated with Fe³⁺. With the addition of Cr₂O₃ to the starting material, on the other hand, a good match for the group 2 bands of natural olivine is obtained (spectrum b).

While minor contributions from coupled substitutions involving Al and Fe³⁺ cannot be ruled out, it is clear that the group 2 bands in natural olivines and in experiments using natural starting materials are dominantly attributable to a coupled substitution that involves Cr³⁺. Without performing polarised analysis of oriented samples, it was not previously possible to differentiate between the infrared fingerprints for different coupled substitutions involving trivalent elements. Group 2 bands were sometimes, but not always, observed in previous experimental studies, where natural olivines were used as starting materials. This inter-study variation is likely owing to variations in Cr concentrations in the starting materials. Because Cr is a trace element, the importance of the role of Cr in changing the OH speciation in olivine has not been previously recognized. The OH speciation in olivine is therefore sensitive to the availability of trace concentrations of Cr. The fO_2 dependence of the group 2 bands in olivine observed in previous studies is likely attributable partly to changes in f_{H_2O} and partly to a redox reaction that consumes Cr³⁺ and creates Cr²⁺ with decreasing fO_2 .

d. *The temperature dependence of H₂O solubility in Al-free stishovite (N. Purevjav, H. Fei, T. Ishii, G. Criniti, Y. Lin, H.K. Mao/Beijing and T. Katsura)*

Subduction zones allow water to be transported into the Earth's deep mantle in the form of OH groups in hydrous and nominally anhydrous minerals. Stishovite is the high-pressure polymorph of silica (SiO₂) stable above 10 GPa and constitutes 20 ~ 25 vol. % of the subducted oceanic crust. Stishovite could potentially act as a water carrier into the lower mantle. However, studies on the water storage capacity of stishovite have yielded conflicting results. To constrain the water solubility in Al-free stishovite and the role of stishovite in deep water recycling, we investigated the water solubility in Al-free stishovite as a function of temperature from 1300-2100 °C at 22 GPa. High-quality stishovite single crystals were synthesised under water-saturated conditions using a multianvil press. Each crystal was double-side polished to a thickness of 80-100 µm and analysed by unpolarised Fourier transform infrared spectroscopy. Two to three crystals from each run were measured using a Bruker IFS 120 high-resolution spectrometer coupled with a Bruker IR microscope. The water contents were calculated by the

earthquakes. The passage of H₂O-rich fluids released from subducting lithosphere into the sub-arc mantle wedge, for example, is considered to be responsible for the high degrees of partial melting, the raised concentrations of H₂O-soluble trace elements and the generally higher volatile contents of arc magmas, compared to mid ocean ridge melts. The time required for this fluid transport is important, however, because slow rates would tend to trap fluids within the subducting lithosphere. Whether fluid flows in a pervasive or channelized manner is also important as it determines the extent to which other components, such as carbonates, may be mobilised by transiting fluids. In this study, experiments are being performed to determine the mechanisms and time scales of fluid transport within subducting slabs, by examining the rate of fluid flow through hot pressed mantle minerals.

We have developed an experimental set-up, that allows us to determine the permeability of mantle mineral assemblages to water at high pressure and temperature. A hot-pressed, polycrystalline core of olivine, pyroxene, or mixtures of the two is sandwiched between a fluid source of either serpentinite or Al(OH)₃ and a fluid sink of MgO. Upon dehydration within the source, an overpressure is created, which leads to fluid flow through the polycrystalline core. The fluid is captured by the sink on the other side of the core through the formation of brucite, Mg(OH)₂. The experiments are performed in a multianvil apparatus at temperatures between 500 and 900 °C and pressures of 2.5 to 8 GPa. Furthermore, we have started to vary the grain size of the hot-pressed cores to evaluate its effect on permeability. The permeability is calculated using Darcy's law,

$$q = -(k/\eta) \Delta P/x,$$

where the fluid flux q across a distance x , is related to the permeability k , the fluid viscosity η and the pressure difference ΔP . We calculate the overpressure of serpentinite and Al(OH)₃ dehydration to be approximately 0.3 and 2 GPa, respectively, and assume that the pressure of the fluid sink remains that corresponding to the applied load. This might be an over simplification as the overpressure will likely relax due to deformation and the fluid flow itself, but there are indications that this may be a reasonable approximation. We have also performed experiments where a diamond powder layer is placed at the boundary between the sample and the fluid sink. Due to the strength of the diamond grains, the pressure within the pores in this layer is expected to be near room pressure, significantly increasing the ΔP of the experiment, until the pores fill with fluid.

Identical experiments run for different periods of time indicate that the calculated permeability decreases with time, likely due to a decrease in overpressure as fluid migrates from the hydrous layer through the hot-pressed core. This effect is not yet accounted for in the calculations, but appears to be relatively small and less than one log unit. As shown in Figure 3.5-7, the main factor affecting permeability is the grain size of the assemblage, due to larger grain sizes having a smaller proportion of grain boundaries along which fluid can migrate. Evidence for transport along grain boundaries can be seen in the top image in Figure 3.5-8, which shows growth of

brucite crystals at the boundary between olivine grains. Preliminary results indicate that the presence of a saline fluid increases the permeability, while the presence of carbonate seems to decrease it.

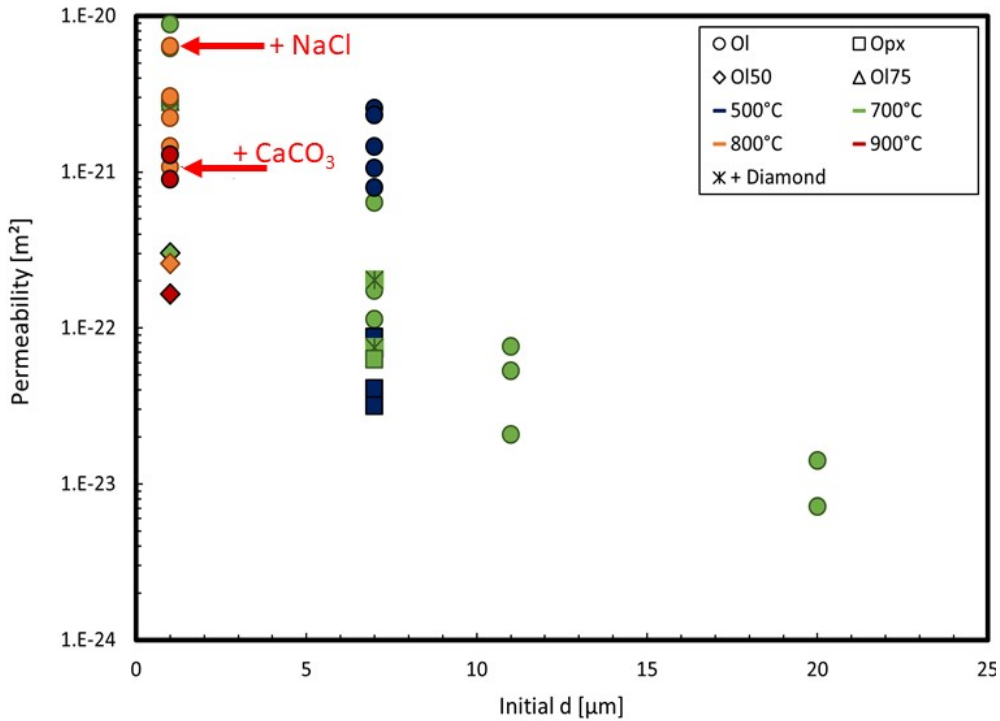


Fig. 3.5-7: Calculated permeability as a function of grain size for different mineral assemblages, temperatures and fluid sources from experiments performed at 2.5 GPa. Symbols show different minerals: Circles – olivine (Ol), squares – orthopyroxene (Opx), diamonds – Ol/Opx(1:1) mixtures, triangles – Ol/Opx (3:1) mixtures. Colours vary with temperature: blue – 500 °C, green – 700 °C, orange – 800 °C, red – 900 °C. The 500 °C experiments (blue) were performed with an Al(OH)₃ fluid source, whereas all other experiments were performed with a serpentinite fluid source. Stars in the symbols mark experiments in which a layer of diamond was added between the core and the fluid sink to increase the pressure gradient. NaCl (2 %) and CaCO₃ (10 %) were mixed with the serpentinite for one experiment each at 800 °C to see possible effects on the permeability.

The higher overpressure of the Al(OH)₃ source appears to increase the permeability of olivine, implying that there may be another faster migration mechanism operating at these overpressures. The permeability of opx is lower than that of olivine when using the Al(OH)₃ source, but this seems to be due to the formation of a thin, less permeable layer of chlorite at the boundary between the opx and the source. As can be seen in Figure 3.5-7, an almost identical permeability for opx is calculated in diamond layer experiments, compared to other serpentine source experiments, where such a layer is not included. Although the fluid flux is faster in the diamond layer experiments, the pressure gradient is assumed to extend to room pressure, resulting in the same calculated permeability, which supports the validity of the pressure gradient assumptions.

The results indicate that at 700 °C, H₂O-fluid would permeate in one million years through only 1.1 meters of olivine. This is far too slow to allow water to be transported via pervasive flow from a subducting slab to the overlying mantle wedge, given a typical rate of subduction. This implies that a different migration mechanism must exist under certain conditions. In the experiments, there is some evidence of channelized flow in the diamond-layer experiments and those involving Al(OH)₃ as the fluid source, but this does not seem to raise the permeability significantly. The bottom image of Figure 3.5-8, however, shows an experiment performed using an opx core at 900 °C. Half of the lower portion of the original opx core has reacted with the MgO sink and formed olivine. Pockets of fluid in the remaining opx portion indicate that fluid has wet the opx grain boundaries and can migrate freely due to a lowering of the opx-fluid dihedral angle. No such flow takes place through the transformed olivine layer of the sample, however, resulting in an overall low permeability. Similar behaviour is seen at 800 °C. It is possible, therefore, that rapid fluid migration requires opx-rich heterogeneities in the subducting slab. Experiments are continuing to constrain this behaviour and the timescale required for water to wet grains of opx rich assemblages.

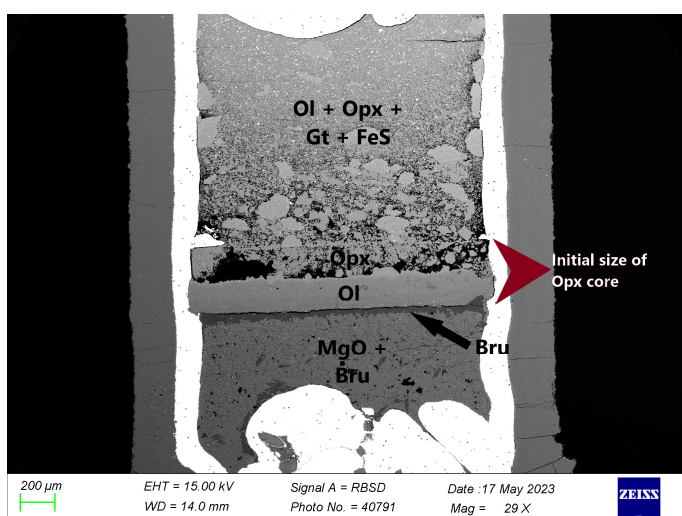
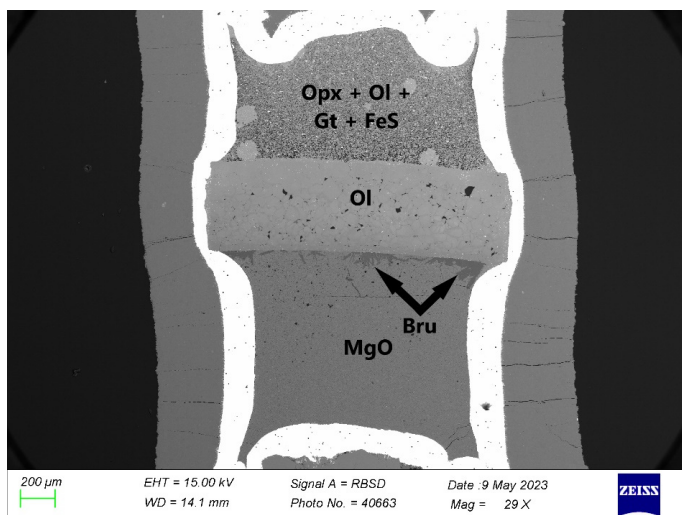


Fig. 3.5-8: Backscattered electron images of the run products of a permeability experiment with an Ol core (top) and an Opx core (bottom) at 2.5 GPa and 900 °C. The serpentinite decomposed into Ol + Opx + garnet + FeS in both experiments. Top: Brucite has formed single crystals along the Ol-MgO boundary, as fluid exits the Ol core. The crystals do not form a continuous layer and in fact appear to grow at Ol grain boundaries. This is a strong indication that fluid has migrated through the core and does not migrate along the capsule wall. Bottom: Half of the initial Opx core has transformed to Ol due to reaction with MgO. The top part of the core contains significant fluid pockets indicating that fluid was able to wet the Opx grain boundaries but not those of Ol.

f. The diffusivity of hydrogen through olivine assemblages at high pressure and temperature (M. Pöppelbaum and D.J. Frost)

The oxygen fugacity within some portions of subducting lithosphere, the subcontinental lithosphere and the deep mantle may be low enough to stabilise hydrogen-rich fluids. If hydrogen is very mobile, however, as some evidence suggests, it may tend to diffuse out of such reduced regions quite rapidly, resulting in it being stored in the Earth mainly as H₂O in more oxidised portions of the mantle. Determining whether this is the case requires measurements of the rate of hydrogen diffusion through different mantle assemblages. In this study, the diffusivity of hydrogen through a polycrystalline olivine assemblage is being investigated at high pressures and temperatures. The method could be similarly applied to examine the suitability of different rock types for subsurface hydrogen storage.

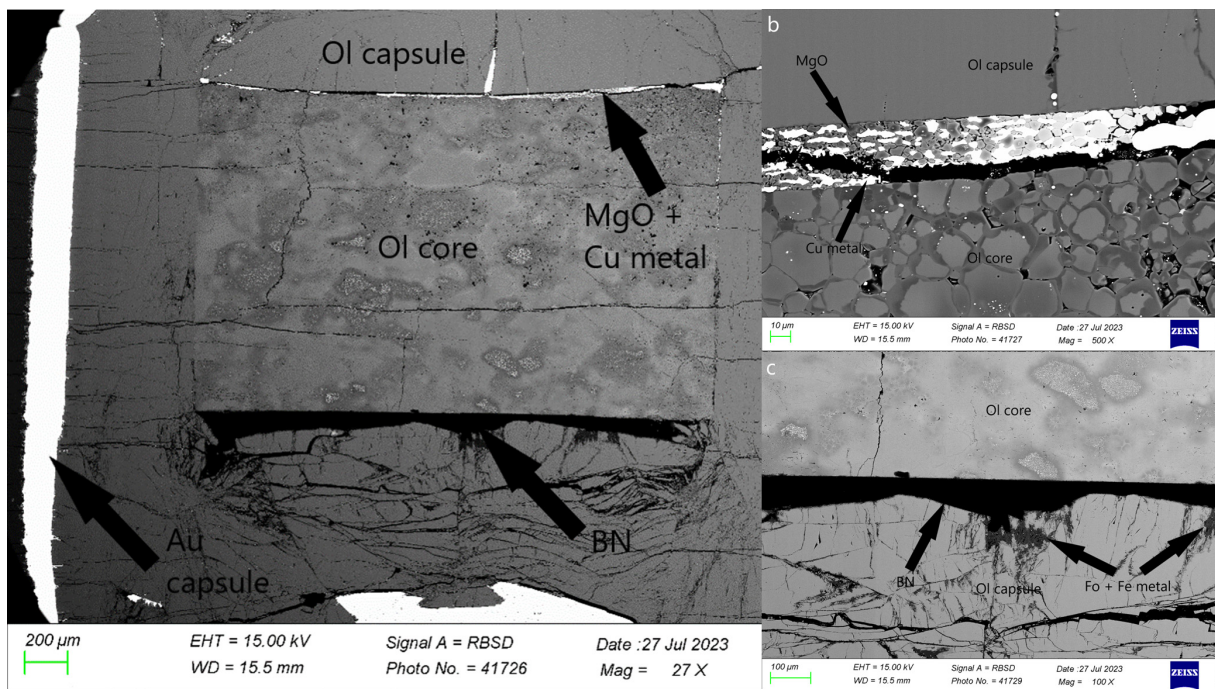


Fig. 3.5-9: Backscattered electron images of a run product from an experiment on H₂ permeability performed at 2.5 GPa and 700 °C for 1 hour on an olivine (Ol) core. a) Overview of the capsule showing the outer Au capsule and inner single crystal olivine liner. Black regions below the sample are the BN residue from the hydrogen source. b) An enlargement of the top right region of the core, indicated by the arrow, showing MgO + Cu metal in the sink. The darker rims around olivine grains result from reduction of FeO by the diffusing H₂ fluid. c) An enlargement of the BN layer. Above is the olivine core and below the single crystal capsule, which appears to be extensively fractured.

The technique uses BH₃NH₃ as a source of hydrogen, which breaks down at a few hundred degrees to produce inert boron nitride (BN) assemblage plus H₂ fluid. The fluid can then pass

through a hot-pressed olivine core and is locked down in a sink on the other side of the core comprised of a mixture of CuO and MgO. If H₂ reaches the sink it reduces CuO to Cu metal and the resulting H₂O should react with the MgO to form brucite. The source, core, and sink are placed inside an olivine single crystal capsule to avoid loss of hydrogen through the wall of a metal capsule. The single crystal capsule is placed inside a welded gold capsule. So far, the shortest time duration experiment was performed for 1 hour at 2.5 GPa and 700 °C in a multianvil apparatus.

The run product from the 1-hour experiment is shown in Figure 3.5-9. The hydrogen migrated through the olivine core during the experiment, resulting in the complete reduction of CuO to Cu metal. No brucite was formed, most likely because the concentration of H₂ that passed through the sample was so high that the activity of H₂O was not significant. Furthermore, hydrogen reduced iron oxide in olivine both in the capsule and in the core. This produces dark, iron-poor rims on the olivine grains and white Fe metal grains throughout the core (Fig. 3.5-9b) and similar features in the capsule (Fig. 3.5-9c). The path of H₂ through the core can be traced by this reduction. From this experiment, we can calculate only that the diffusivity of hydrogen must be faster than 6×10^{-10} m²/s. Shorter experiments are necessary in order to find the time scale at which hydrogen does not diffuse through the sample or only partial CuO reduction occurs. Nevertheless, this is still at least one order of magnitude faster than the diffusivity of water through a similar olivine assemblage with the same grain size.

g. *Melting of primitive peridotite under mid-mantle conditions (N.S. Martirosyan, A.D. Chanyshv, H. Fei and T. Katsura)*

The melting relations of peridotite under lower-mantle conditions are essential for modelling the early chemical evolution of the mantle in the primordial Earth. The early history of the Earth's mantle involved extensive melting, forming what is known as a magma ocean. This phenomenon may have been triggered by giant impacts during planetary accretion, radiogenic heating from short-lived radioisotopes, and the process of core formation. The fractional crystallization and gravitational differentiation in a magma ocean may have produced an early stratification of the mantle. The present-day composition of the mantle is thought to result from the chemical evolution of this stratified structure.

While there have been comprehensive studies on the melting of peridotite under deep-mantle conditions using multianvil presses and diamond anvil cells (DACs), the phase relations under lower mantle conditions are not well-established. Discrepancies in solidus and liquidus temperatures across various studies may be due to steep temperature gradients in experiments, causing instantaneous melt segregation to the highest-temperature region of the sample chamber. This segregation leads to a misinterpretation of the melting sequence.

This project focuses on conducting peridotite melting experiments in multianvil presses at pressures resembling mid-mantle conditions. A novel multianvil zero-gradient assembly design

was used to minimize the thermal gradient within the cell. In this design, heater rods placed at both ends of a short cylindrical heater eliminate axial heat flow. To achieve high temperatures, a boron-doped diamond heater capable of reaching temperatures up to 4000 K was developed.

Experiments were conducted on the peridotite "KLB-1" composition at 12-33 GPa. While the liquidus temperature is reasonably consistent with previous phase diagrams, the solidus is elevated by 40-60 °C depending on pressure. Accordingly, the temperature interval between the liquidus and solidus may be smaller than previously thought. These initial results underscore the uncertainty in the melting relations of primitive peridotite, emphasizing the need for further experimental endeavors.

h. *The pure melt viscosity of andesitic magmas: Understanding the effect of nanocrystallization and iron oxidation in the laboratory (P. Valdivia Munoz, A. Zandonà and J. Löschmann/Clausthal, C. McCammon, A. Kurnosov, T. Boffa Ballaran, D. Di Fiore and C. Romano/Rome, J. Deubener/Clausthal and D. Di Genova/Rome)*

Viscosity is a critical physical property governing both magma transport and eruptive styles. Magma viscosity is intricately linked to melt composition and temperature, with secondary influences stemming from crystal and bubble content. Recent studies have shown that iron oxidation and the nano-crystallization of Fe-Ti-oxides can take place during viscosity measurements. These processes induce substantial chemical and structural changes in the melt, causing eventually an overestimation of the so-called pure-melt viscosity. Furthermore, previous studies have illustrated that iron oxidation is also associated with an increase in melt viscosity. These factors collectively pose challenges to the precise determination of the pure melt viscosity for iron-titanium-bearing melts.

In this work, we constrain the viscosity of four anhydrous andesitic melts and one Fe-Ti-free analogue as a function of temperature and iron oxidation. Viscosity values were obtained through direct viscometry techniques, specifically concentric cylinder and micropenetration methods. Additionally, to further expand the dataset, indirect derivations were conducted using conventional and flash differential calorimetry. To assess potential sample modifications during measurements (*i.e.*, crystallization and/or iron oxidation), we measured Raman and Mössbauer spectra before and after experiments.

Our viscosity data (Fig. 3.5-10) show that the viscosity of our samples increases as FeO_{tot} and TiO_2 are removed from the melt, and it also increases with increasing $\text{Fe}^{3+}/\sum\text{Fe}_{\text{tot}}$ content. Utilizing exclusively nanocrystal-free viscosity data as indicated by consistent iron oxidation states, we develop novel viscosity models for the studied compositions (Fig. 3.5-10). For this purpose, we employed the Mauro–Yue–Ellison–Gupta–Allan (MYEGA) parametrization to ascertain the fit melt fragility index (m), fixing the glass transition temperature (T_g) to our DSC-derived values.

When comparing our models with previous literature viscosity data, we observe that there are significant disparities. For example, for AND100 composition, our determined m and T_g ($m_{\text{AND100_CC}} = 33 \pm 1$; $T_{g_AND100_CC} = 654 \pm 1$ °C) diverge from the values using the Giordano *et al.* (2008, EPSL 271: 123) model ($m_{\text{GRD_AND100_CC}} = 34.8$; $T_{g_GRD_AND100_CC} = 699.6$ °C), which is overestimating T_g by nearly 45 °C. Similarly, for AND65, the Giordano *et al.* (2008) model estimates a $T_{g_GRD_AND65} = 711$ °C, while we measured $T_{g_AND65} = 696 \pm 0.5$ °C. On the other hand, we notice that the nanolite-free viscosity data reported by Okumura *et al.* (2022, Comm Earth Environ 3: 241), a composition which is closely alike to our AND100 sample, is ~25 times higher than our AND100 parametrization (Fig. 3.5-10). Moreover, we observe that their nanolite-free viscosity data closely aligns with our AND65 viscosity curve, which represents a 35 wt. % depletion of FeO_{tot} and TiO_2 with respect to AND100. Our findings indicate that thermal treatment can trigger processes such as iron oxidation and nanocrystallization, and these changes depend on iron-titanium content, temperature, and experimental time. It is noteworthy that these alterations become more pronounced as temperatures deviate further from the glass transition temperature (T_g), producing a noticeable overestimation of viscosity.

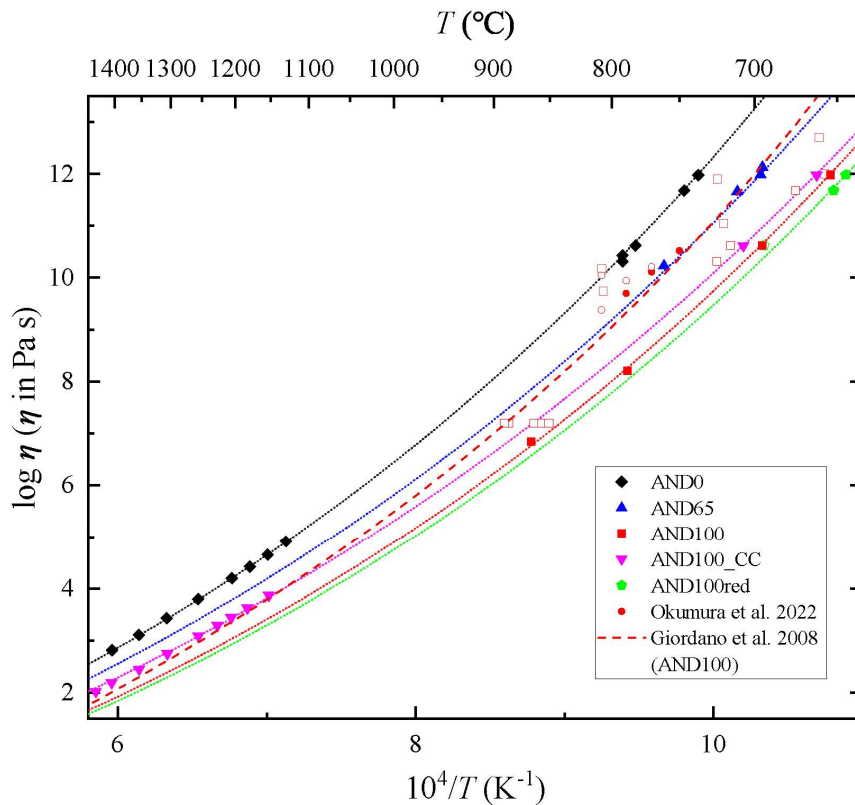


Fig. 3.5-10: Viscosity data and MYEGA parametrizations for various andesitic melts. Every colour represents one chemical composition. Closed symbols representing nanolite-free measurements and open symbols corresponding to nanolite-bearing measurements. Red circles correspond to the viscosity data reported by Okumura *et al.* (2022, Comm Earth Environ, 3, 241) compositionally similar to our AND100. Dotted lines correspond to our proposed viscosity models after Mauro *et al.* (2009, Proc PNAS, 106, 19780) The red dashed line is the predicted viscosity of Giordano *et al.* (2008, EPSL, 271, 123) for AND100 composition.

i. Combining a synthetic data approach with an artificial neural network to determine the viscosity of volcanic melts (D. Langhammer, D. Di Genova/Rome and G. Steinle-Neumann)

The dependence of volcanic melt viscosity η on composition is extremely complex, and due to the interactions of oxide composition and structural factors, no general physical/mathematical model has been found. Current research focuses on modifying fitting parameters of empirical temperature-dependent equations. These modifications are performed in a trial-and-error process, until a model with satisfactory accuracy is found. This introduces a bias in the formulation of the equations that we try to avoid by training an artificial neural network (ANN) using a large data base of experimental measurements of η for a wide range of melt compositions. This ANN was compared to popular literature models, showing better agreement with experimental data within the high and low η intervals in which viscometric measurements can be performed. Since silicate melt η cannot be measured between these intervals, the ANN cannot be reliably trained there which results in unphysical predictions (Fig. 3.5-11). Since characteristic eruptive conditions for volcanoes lie within the data gap, it is important to solve this problem. To rectify this situation, we applied a synthetic data approach. It introduces physical boundaries on the ANN using the MYEGA equation (Mauro *et al.* 2009, PNAS 106: 19780). This T -dependent η model is a simple three parameter fitting equation, derived on a solid physical basis.

The ANN and MYEGA equation were combined in the following two-step process: First, using the ANN, *synthetic data* were generated for a specific composition within the high and low η regimes since, as mentioned before, training data for the ANN is only available there. An important step is the separation of relevant temperature intervals in the high T regime. The calculated synthetic data were then fit using the MYEGA equation. This results in a T -dependent model for a specific composition, which combines the predictive capabilities of the ANN and the physical basis of the MYEGA model. Subsequently, we compared our approach to two popular empirical melt viscosity models and the ANN by Le Losq *et al.* (2021, Chem Geol 346: 57). Our synthetic data approach outperforms both of the empirical models (Fig. 3.5-12). The ANN by Le Losq *et al.* (2021) is limited to the K_2O - Na_2O - Al_2O_3 - SiO_2 system while ours contains 11 oxides and H_2O . Nevertheless, even for compositions in the K_2O - Na_2O - Al_2O_3 - SiO_2 system, our model reaches higher accuracies (with a root mean squared error of 0.29 vs. 0.39).

In summary, we constructed a solution for the unphysical behaviour exhibited by our ANN between the experimentally accessible high and low η regimes. We did so by generating *synthetic data* in both regimes using the ANN, justified by the availability of training data. These *synthetic data* were then fit using the physically motivated MYEGA equation, to ensure the expected T behaviour. The resulting model outperforms well established empirical models and predictions from another ANN based approach.

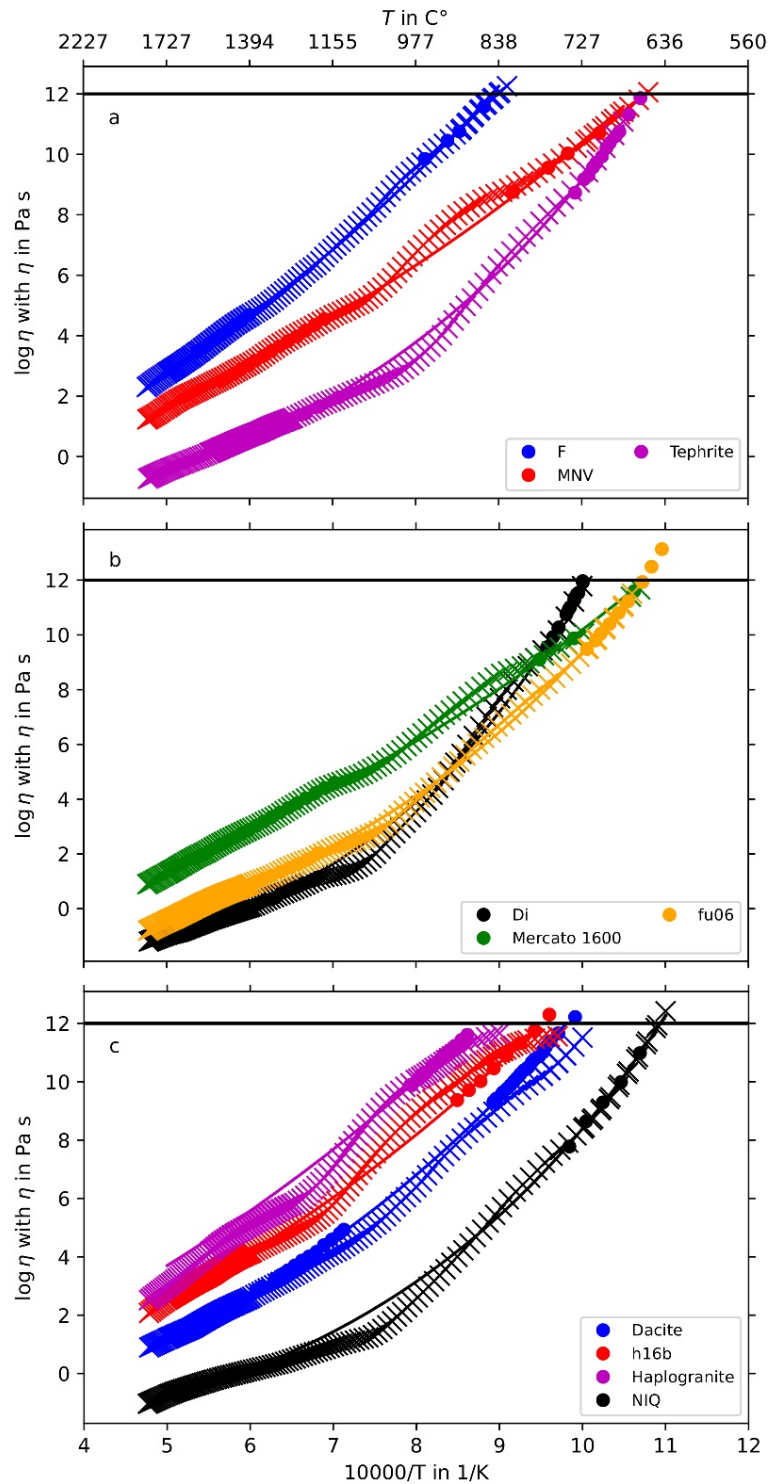


Fig. 3.5-11: Viscosity ($\log \eta$) as a function of inverse temperature ($10000/T$) for some anhydrous volcanic compositions in the database used for training and validation of the ANN (panels a and b), and for testing (panel c). Experimental data are shown by filled circles, viscosity values predicted from the ANN by crosses, where bold crosses indicate the η range for the synthetic data approach. Solid (dashed) lines show MYEGA fits to the experimental (synthetic) data. The horizontal lines indicate 10^{12} Pa s. As experimentally measurable intervals in the low η range differ for different SiO_2 content, we use different $\log \eta$ intervals for synthetic data generation for compositions with ≥ 60 wt. % of SiO_2 .

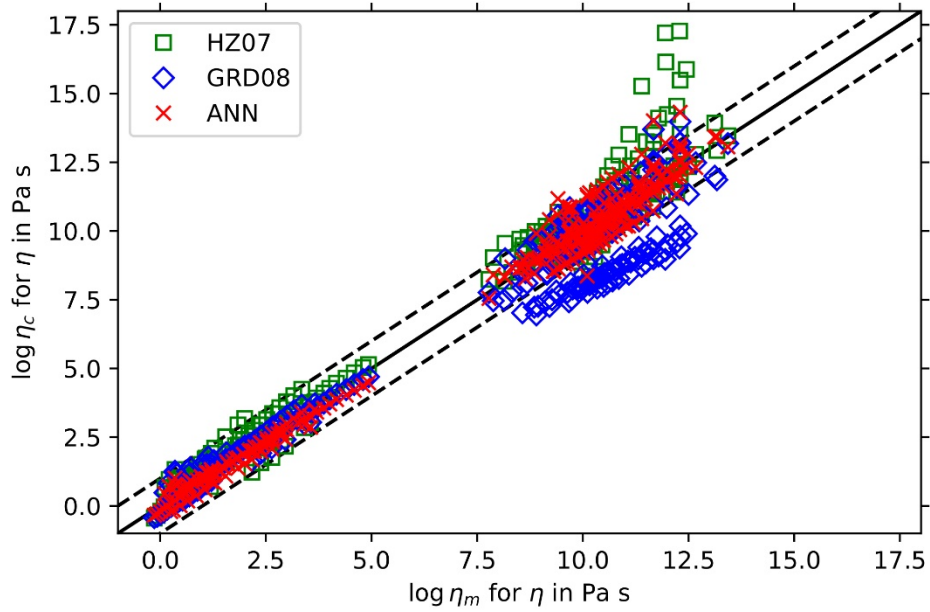


Fig. 3.5-12: Comparison of calculated ($\log \eta_c$) and measured ($\log \eta_m$) viscosities for the synthetic data approach (ANN, red crosses, RMSE = 0.52), with the model by Giordano *et al.* (2008, EPSL, 271, 123) (GRD08, blue diamonds, RMSE = 1.23) and Hui and Zhang (2007, GCA, 71, 403) (HZ07, green squares, RMSE = 0.89) for melts in the test sets. The one-to-one correspondence is shown by the solid black line, dashed lines indicate a ± 1 log-unit deviation from identity.

3.6 Rheology and metamorphism

The rheology of rocks and minerals under the high-temperature and -pressure conditions of the Earth's interior is crucial for the understanding of the dynamic processes inside our planet. The critical rheological parameters stress and strain rate define the flow laws and the viscosity of a material. However, they present an experimental challenge especially at the high pressures of the Earth's deep interior (see also Methodological developments). Therefore, alternative approaches have also been pursued at BGI in the last year such as geodynamical simulations of different types of deformation or the experimental investigation of fundamental mechanisms such as solid state diffusion as rate limiting processes during deformation.

The first three contributions in this chapter employ 1D and 2D computational approaches to model rapid ductile strain localization and thermal runaway in olivine as a possible mechanism causing earthquakes at great depths where temperatures are too high for brittle deformation to occur. The simulations show that it is possible to generate a fault by thermal runaway if a certain strength contrast between perturbed region and host rock can be generated. Also, a large rupture can be generated by the thermal runaway process by aligning a number of small perturbed regions which predominantly deform by dislocation creep whereas the surrounding is dominated by low-temperature plasticity. In the third contribution the potential of a phase transition between olivine and ringwoodite for triggering an earthquake by thermal runaway is evaluated computationally. The simulations show that thermal runaway becomes more likely with high initial stresses, fast transformation times, at higher temperatures and with smaller grain sizes after the phase transition. In the fourth contribution mantle convection has been simulated over the last 4.5 Ga with special regard to the influence of grain size development in upper and lower mantle as well as diffusion creep as the dominating deformation mechanism. Results indicate that grain size has a remarkably small influence on the overall viscosity, temperature and mobility of the convecting mantle at least for long time scales.

The two following contributions present experimental results which have profound consequences for the rheology of the lower mantle. In the fifth contribution the static annealing of the experimentally deformed grain structure of the lower mantle assemblage bridgmanite-magnesiowüstite is investigated in order to determine if bridgmanite or magnesiowüstite are determining the strength of the assemblage. Results indicate that the presumably stronger bridgmanite will form a load-bearing framework and as such determine the viscosity of the lower mantle. The following project presents diffusion experiments of Si in bridgmanite at lower mantle conditions which allow to determine flow laws for this mineral under the assumption that the self-diffusion of Si is the rate limiting factor in high-temperature creep. The resulting diffusivities and derived viscosities for bridgmanite fit well with those derived from geophysical data. The last contribution shows the complexity of the interplay of rock deformation and mineral reactions in a natural example of a high-pressure mylonite from the Sesia zone in the Southern Alps. Very detailed microstructural investigations show that reaction progress in a natural environment is closely linked to plastic deformation which complicates the interpretation of the actual p,T - deformation history of the rock complex.

a. *1D numerical models of rapid ductile strain localization (A. Spang and M. Thielmann, in collaboration with D. Kiss/Mainz)*

Strain localization is a crucial process for lithosphere and mantle deformation as it allows for the formation of faults and shear zones that enable plate tectonics. In the upper crust, strain localization usually occurs via brittle failure (*i.e.*, breaking the rock). The deeper and/or hotter the setting, the less likely brittle failure becomes as the critical stress increases with the increasing overburden pressure while the temperature-dependent rheology of rocks limits the stresses that can be accumulated before being relaxed by slow, viscous flow.

Yet, we do observe fast and localized deformation (*i.e.*, earthquakes) at depths of several hundred kilometres. These deep earthquakes either require local differential stresses of several Gigapascal (GPa) to trigger brittle failure or a different, ductile, failure mechanism that significantly reduces rock strength while at the same time creating highly localized shear zones. Here, we investigate thermal runaway, the feedback loop of temperature- and stress-dependent, visco-elastic deformation and shear heating, to determine whether it can lead to a localized viscosity reduction and allow for fast slip.

We present a 1D numerical code written in the Julia programming language which uses the pseudo-transient approach to model the process of ductile localization and thermal runaway in a simple-shear setting. Our models employ a nonlinear, visco-elastic olivine rheology, including diffusion creep, dislocation creep and low-temperature plasticity. We find that the combination of the aforementioned mechanisms is sufficient for deformation to localize on a small perturbation and cause fast slip events. The models reveal that dislocation creep is the dominant deformation mechanism during thermal runaway.

By nondimensionalizing the energy conservation equation, we are able to identify two non-dimensional scales that govern whether thermal runaway occurs in our models.

$$\frac{\Delta T'}{dt'} = \underbrace{\frac{\kappa}{h^2}}_{\frac{1}{t_d}} \underbrace{f_{\text{an}} \frac{\tau_c}{2\varepsilon_{\text{out}} G}}_{t_r} \frac{\partial^2 \Delta T_{\text{an}}}{\partial x'^2} + \underbrace{\frac{\omega_0 f_{\text{an}} \tau_c^2 L}{\rho C_p T_c h}}_{\frac{1}{U_{\text{th}}}} \underbrace{\frac{G}{U_{\text{el}}}}_{U_{\text{el}}} f_{\text{ND}}$$

t_r/t_d denotes the ratio of the time scale of visco-elastic stress relaxation in the host rock to the time scale of thermal diffusion in the perturbation. $U_{\text{el}}/U_{\text{th}}$ is the ratio of stored elastic energy density to thermal energy density of the system. If t_r/t_d is small (*i.e.*, stress relaxation is faster than thermal diffusion) and $U_{\text{el}}/U_{\text{th}}$ is large (*i.e.*, stored elastic energy density is higher than thermal energy density in the system), thermal runaway occurs, resulting in strong ductile localization and fast slip events comparable to intermediate- and deep-focus earthquakes. We test the validity of this scaling approach and its limits by comparing its predictions to 6000 simulation results with different input parameter combinations. Figure 3.6-1a shows that the

scaling works very well if the host rock is 2 to 10 times stronger than the perturbed region (*i.e.*, strength contrast (ω_0) equals 2-10). For smaller and larger strength contrasts, there are some cases where this simplified relationship does not accurately predict thermal runaway (Fig. 3.6-1b). This limitation is rooted within the strongly nonlinear feedbacks that characterise the interplay between the different temperature-dependent creep mechanisms and shear heating.

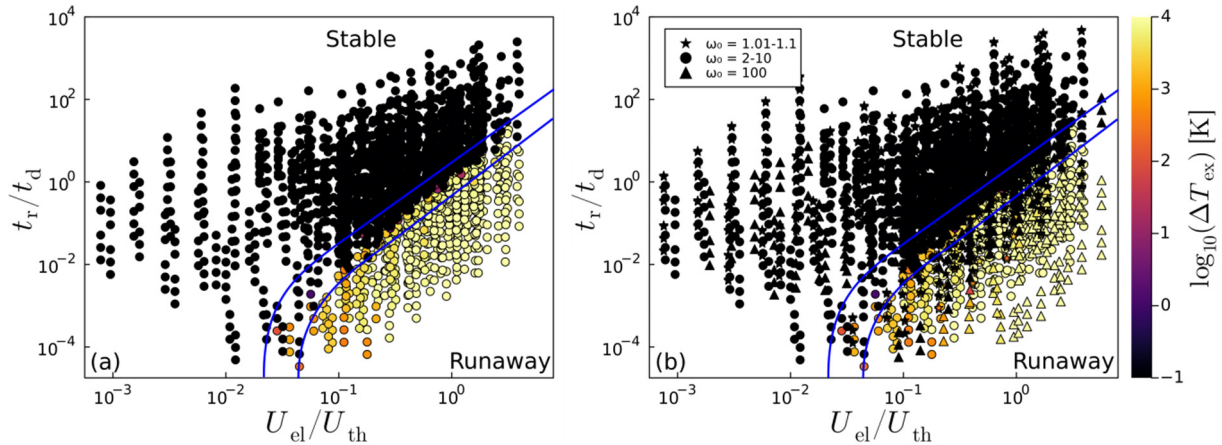


Fig: 3.6-1: Difference between maximum temperature and steady-state temperature as a function of two non-dimensional parameters. t_r/t_d denotes the relation between stress relaxation time scale and heat diffusion time scale. U_{el}/U_{th} denotes the ratio between elastic and thermal energy density. The area between the blue lines denotes the transition from the stable to the runaway regime. (a) Models with $\omega_0 = 2-10$. (b) All models. Note that the transition between stable and runaway regimes is much more clearly defined in (a). The colorbar is truncated at 10^{-1} towards lower values.

b. Modelling nucleation and propagation of ductile ruptures (A. Spang and M. Thielmann)

Thermal runaway is a localization mechanism for viscous deformation that can cause fast slip events in the ductile regime of the lower crust, upper mantle, and mantle transition zone. Here, we present 2D numerical models, written in the Julia language and compatible with graphics processing units (GPU), that investigate ductile rupture propagation in simple shear due to thermal runaway. We employ a temperature- and stress-dependent visco-elastic rheology, encompassing diffusion creep, dislocation creep and low-temperature plasticity.

Our models show ductile rupture propagation, nucleating from single perturbations or linking several nucleation sites to form one large rupture (Fig. 3.6-2a). We identify dislocation creep as the dominant deformation mechanism inside the rupture and low-temperature plasticity in the host rock ahead of the tip (Fig. 3.6-2b). The propagation of the tip represents a transition from low-temperature plasticity to dislocation creep and subsequent stress release of the host rock.

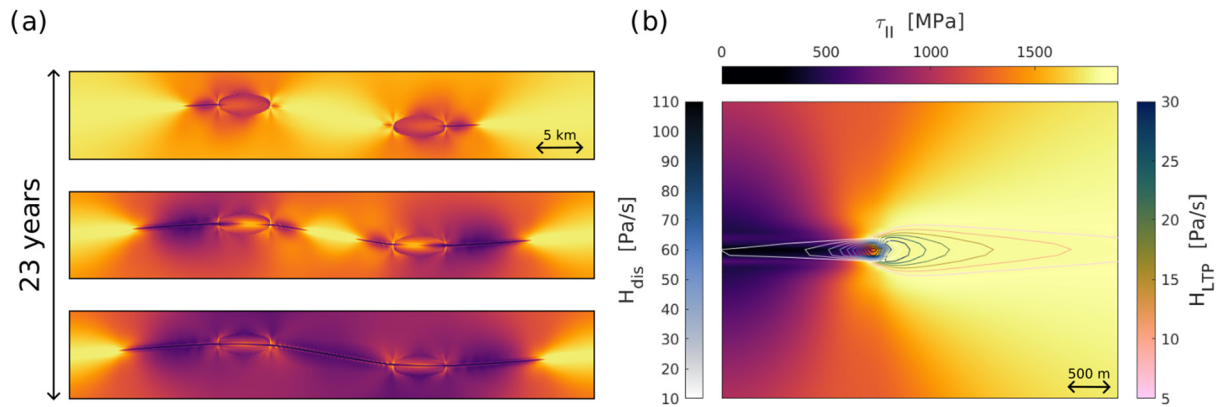


Fig. 3.6-2: Deviatoric stress state. (a) Ductile rupture propagation due to thermal runaway in simple shear. Top: Rupture nucleates at all anomaly tips. Middle: Ruptures propagate outwards, between the perturbations and within the perturbations. Bottom: Ruptures inside and between perturbations have connected and continue to propagate outwards. (b) Zoom in on rupture tip. Two sets of contour lines show the viscous dissipation due to dislocation creep and low-temperature plasticity. Dislocation creep dominates inside the rupture and low-temperature plasticity in the high-stress region ahead of the tip.

c. The dual mechanism of transformational faulting and thermal runaway for deep earthquakes: A numerical study (M.I. Hamadi, A. Spang and M. Thielmann)

Earthquakes occur at various depths below the Earth's surface, extending up to 700 km. Due to the increasing pressures and temperatures at depth, brittle failure becomes increasingly unlikely at depths larger than 70 km. The causes for the observed intermediate-depth (70-300 km depth) and deep focus (300-700 km depth) earthquakes remains a mystery up to this day.

Three possible mechanisms (dehydration embrittlement, transformational faulting, and thermal runaway) have been proposed for both intermediate and deep-focus earthquakes. Dehydration embrittlement is commonly suggested to be the nucleation mechanism for intermediate-depth earthquakes. As slab dehydration is assumed to be completed at ~ 300 km depth, dehydration embrittlement is less likely to occur at larger depths. For deep-focus earthquakes, both transformational faulting and thermal runaway hence remain as potential candidates. Recently, it has been proposed that both mechanisms form a feedback loop where deep earthquakes are nucleated via transformational faulting and the subsequent rupture is governed by thermal runaway.

In this study, we explore this feedback loop by employing 1D numerical models of a 100 m thick olivine slab being deformed in simple shear. The model employs a visco-elastic rheology where viscous deformation is described with a composite rheology. In the central part of the model, a perturbation with a width of 1 m is introduced where the olivine transforms to spinel with a given reaction time scale t_{react} . Using this model, we then investigated the effects of changing the background temperature, background pressure, initial stress and post-transformation grain size on the occurrence of thermal runaway in the model.

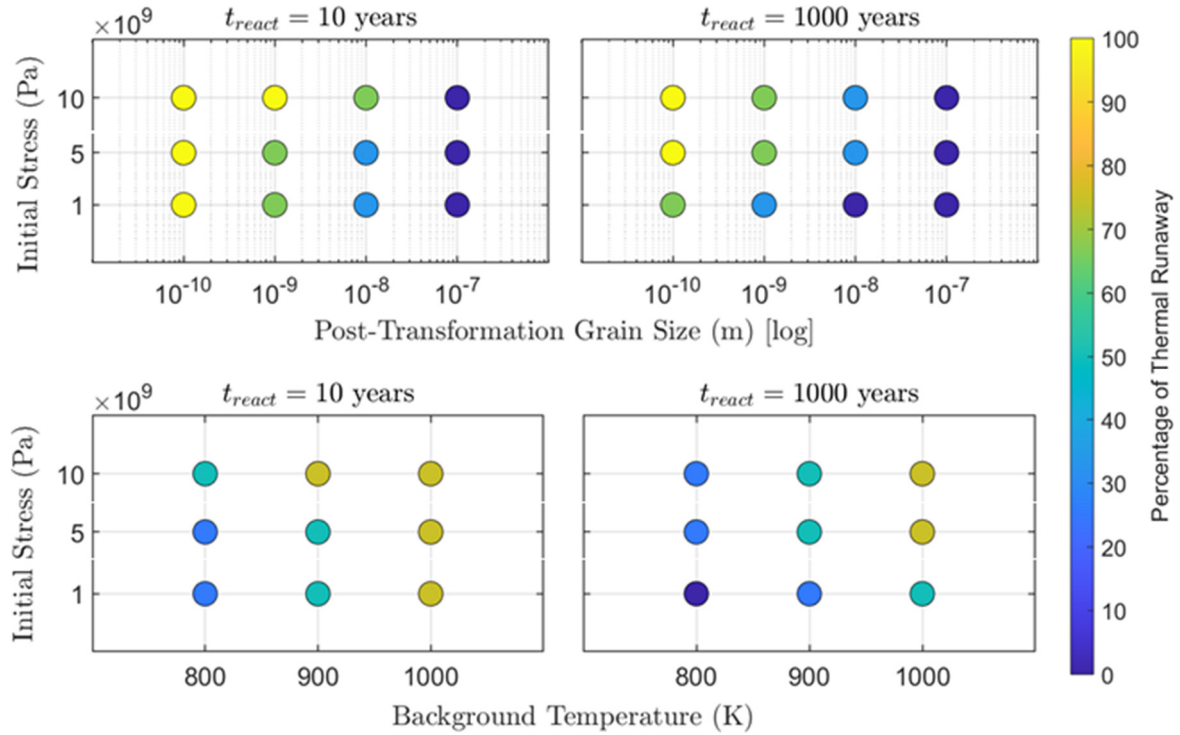


Fig. 3.6-3: Dependence of the occurrence of thermal runaway on modelling parameters initial stress, post-transformation grain size (top row), background temperature (bottom row) and reaction time scale (columns). Circle colors denote the percentage of models exhibiting thermal runaway for otherwise identical parameters.

Our results (Fig. 3.6-3) show that the dual mechanism of phase transformation triggered thermal runaway is capable of generating thermal runaway and thus seismic events (deep earthquakes) in our model. Due to the employed model parameters, large stresses (> 5 GPa) are required to initiate thermal runaway. The regime boundary between the stable (no thermal runaway) and the unstable (thermal runaway) regime is quite sharp. Models exhibiting thermal runaway are characterised by a significant increase in temperature and strain rate together with a strong negative stress gradient. Thermal runaway is furthermore significantly facilitated by a short reaction timescale together with a small post-transformation grain size. This highlights the necessity of understanding and quantifying the transformation process at high pressures and temperatures. Nevertheless, the required stresses in our model are too large to allow thermal runaway at Earth-like conditions. As these stresses strongly depend on the employed rheology in our models, further studies are needed to quantify the rheological impact on critical stresses.

d. *Negligible effect of grain size dependent viscosity in the Earth's lower mantle (J. Paul, G.J. Golabek, T. Katsura, H. Fei/Zhejiang, A. Rozel and P. Tackley/Zürich)*

Grain size has long been speculated about as a pivotal factor influencing mantle viscosity under diffusion creep. Despite expectations of a significant increase in diffusion-creep viscosity with

an order of magnitude rise in grain size, this hypothesis remains untested within self-consistent numerical models incorporating the latest grain growth parameters for the lower mantle's composite rheology. Our study employs grain size evolution parameters for bridgmanite-ferropericlasite assemblage determined at 27 GPa and 1400-2400 K to assess the impact of grain size on viscosity in the lower mantle. Various scenarios, including those without grain size evolution, with faster olivine grain size evolution, and a case with pure diffusion creep, are also explored.

Using the grain-size evolution data, we develop 2D annulus numerical models evolving self-consistently for 4.5 billion years using the finite volume code, StagYY. The models assume the mantle to consist of 60 % olivine and 40 % pyroxene-garnet, namely pyrolitic. The phase-transition depths, temperatures, densities, and Clapeyron slopes are calculated for olivine and pyroxene-garnet phases independently.

The study's primary finding is that grain size has a negligible effect on modifying the average mantle viscosity and dynamics for 4.5 billion years (Fig. 3.6-4). We have calculated both the whole mantle and only lower mantle average viscosity which does not show much difference (Fig. 3.6-4b, f) in different models with. In the initial stage there is a difference between the viscosity of models with and without grain size evolution. With more rigorous convection and mixing, the viscosity tends to converge into similar values in all models (Fig 3.6-4b, f). One of the reasons is grounded in the consideration of the most up-to-date grain size evolution parameters. Bridgmanite-ferropericlasite grains exhibit limited growth in the lower mantle, restricting the impact of grain size-dependent viscosity (Fig. 3.6-4c, g). The slow increment in grain size is overshadowed by temperature-dependent viscosity. Even in scenarios where mantle plumes exhibit the largest grain sizes, their viscosity remains low as hot plumes represent the weakest part of the mantle. Additionally, in instances where the mantle deforms under purely diffusion creep, the slight increase in grain size fails to appreciably alter viscosity (Fig. 3.6-4c, g).

Alternative models with forcing large grain sizes within the lower mantle reaching sizes of the order of 1 mm, do not significantly affect viscosity (Fig. 3.6-4b, c, f, g). This phenomenon is attributed to the presence of composite rheology in the models, mimicking the most realistic conditions within the lower mantle. Due to large grain sizes, the mantle deforms in dislocation creep (Fig. 3.6-4h), rendering viscosity practically independent of grain size. This outcome aligns with experimental results demonstrating that larger grain sizes deform under dislocation creep.

From 15 different models, we find that grain size may have an insignificant effect on mantle viscosity in the long term. It might be important to investigate the effect of grain size in shorter time scale processes, such as earthquake generation.

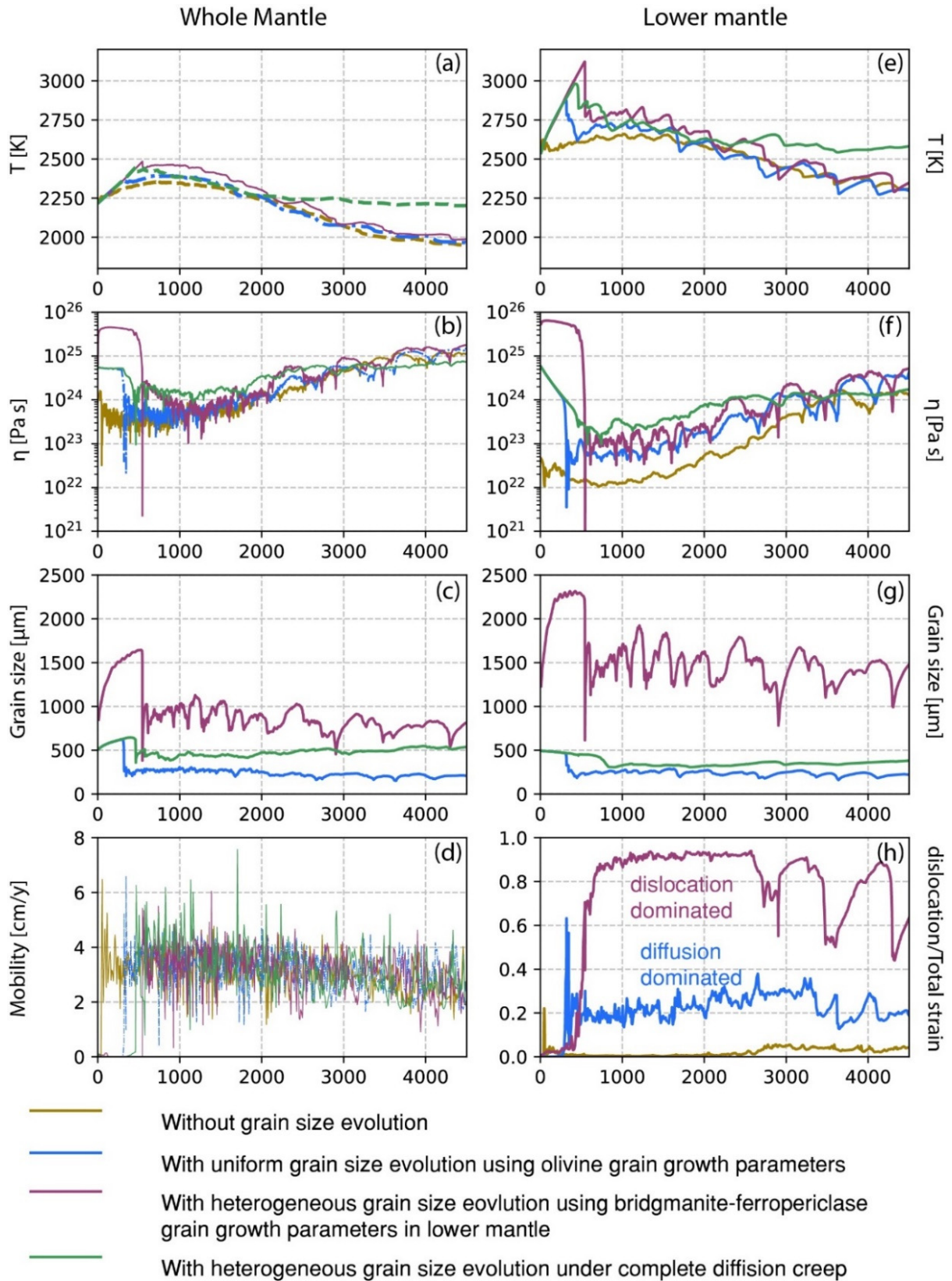


Fig. 3.6-4: (a-d) Time evolution of average temperature, viscosity, grain size and mobility within the whole mantle. (e-h) Time evolution of average temperature, viscosity, grain size and creep regime in lower mantle. Four lines of different colors represent four models, which are briefly described in the lower legend.

e. Investigation of the rheology of the Earth's lower mantle due to ferropericlasite morphology (A. Chakraborti, H. Fei/Zhejiang, Y. Nishihara and W. Wu/Matsuyama, M. Thielmann, A. Chanyshiev, F. Heidelbach, N. Tsujino/Sayo and T. Katsura)

The lower mantle is mainly composed of bridgmanite (80 %) and ferropericlasite (20 %). Thus, bridgmanite should ideally control lower mantle viscosity because of its larger fraction (load bearing framework LBF). However, geological time scales create large total strains that can interconnect ferropericlasite grains (interconnected weak layers IWL) – this would make ferropericlasite morphology the controlling factor. The ferropericlasite morphology should also be affected by the surface energy which would lead to the aspect ratio approaching unity over time. Thus, the aim of the current project is to study morphology of ferropericlasite grains under high-pressure/-temperature-total-strain conditions to settle the question whether the LBF or IWL model is more realistic for lower mantle conditions.

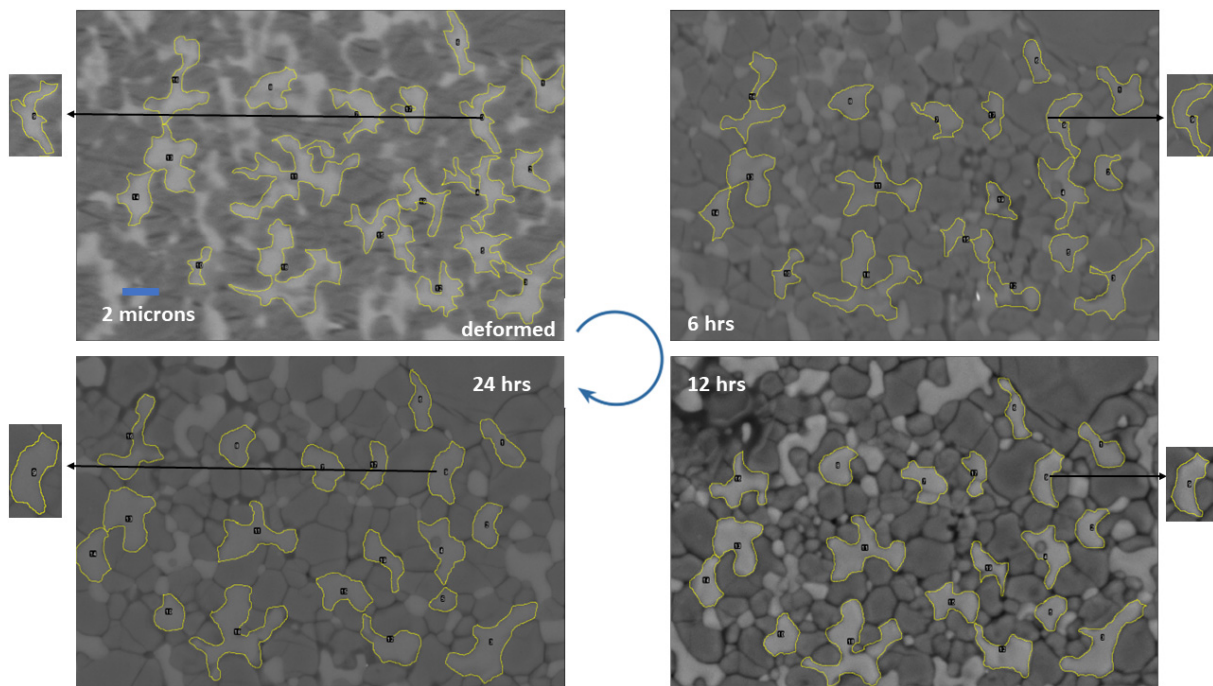


Fig. 3.6-5: Images of run products. The deformed aggregates are annealed over durations of 6, 12 and 24 hours (clockwise from top left) and the ferropericlasite clusters show significant rounding.

The methodology of the project is as follows: Bridgmanite and ferropericlasite aggregates were synthesised at high-pressure and -temperature conditions (27 GPa, 2000 K) from San Carlos olivine at BGI. Next, we put the synthesised aggregates under large strains (over 50 %) in the D111 press in Spring-8, Japan to deform them plastically in axial compression. In a following step the elongated grains are annealed to observe the effects of surface energy on the grain morphology. The observed rounding rate due to the surface energy is being used to establish

LBF or IWL as more realistic for lower mantle. Preliminary results (Fig. 3.6-5) point to a fast rounding rate for ferropiclasite clusters compared to the slow strain rate in the lower mantle, supporting an LBF model and thereby suggesting that bridgmanite controls the viscosity of the lower mantle.

f. *Si self-diffusion in bridgmanite accounts for the viscosity and seismic anisotropy of the mid-mantle (L. Wang, J. Wang/Washington D.C., F. Couffignal/Potsdam, R. Dohmen/Bochum, H. Fei/Zhejiang, M. Wiedenbeck/Potsdam and T. Katsura)*

Global seismic tomography showed that the upper and lower mantle interact mainly via subducting slabs and plumes. Therefore, the rheological properties of the uppermost lower mantle, located at depths of 660-1000 km, play an essential role in global dynamics. The viscosity of this region is estimated at about 10^{21-22} Pa·s and seismic anisotropy is observed near the subducting slabs while other parts are seismically isotropic. To interpret the observed viscosity and spatial distribution of seismic anisotropy, it is indispensable to constrain the rheological properties of the constituent minerals, especially those of bridgmanite, the most dominant mineral in the lower mantle.

The strength of minerals is controlled by the diffusion of the slowest species, usually Si, under mantle conditions. Therefore, we systematically studied the temperature effect on the Si lattice and grain boundary diffusion in bridgmanite. For the determination of lattice diffusivity, a ^{29}Si enriched thin film with a composition of MgSiO_3 was coated on a pre-synthesised MgSiO_3 single crystal bridgmanite using pulsed laser deposition technique. The diffusion experiments were done at 27 GPa and 2100-2600 K and the obtained Si lattice diffusion coefficients can be fitted to an Arrhenius equation,

$$D_{La}(m^2/s) = 10^{-9.59} * \exp\left(-\frac{486 \pm 69 \text{ kJ/mol}}{RT}\right).$$

where R and T are the gas constant and temperature. The current lattice diffusion is nearly 4 orders of magnitude lower than previous studies (Fig. 3.6-6). The apparent long diffusion length in previous studies could be caused by the large surface roughness in previous studies. To determine the Si grain boundary diffusion coefficient, a ^{29}Si enriched thin film with a composition of $(\text{Mg}_{1.8}\text{Fe}_{0.2})\text{SiO}_4$ was coated on a pre-synthesised post-spinel assembly with the same composition, and the diffusion experiments were conducted at 27 GPa and 1300-1700 K and the obtained grain boundary diffusion coefficients can be fitted to

$$\delta D_{Gb}(m^3/s) = 10^{-14.68} * \exp\left(-\frac{376 \pm 20 \text{ kJ/mol}}{RT}\right),$$

where δ is the grain boundary thickness. The Si grain boundary diffusion coefficient is generally the same as previous studies (Fig. 3.6-6).

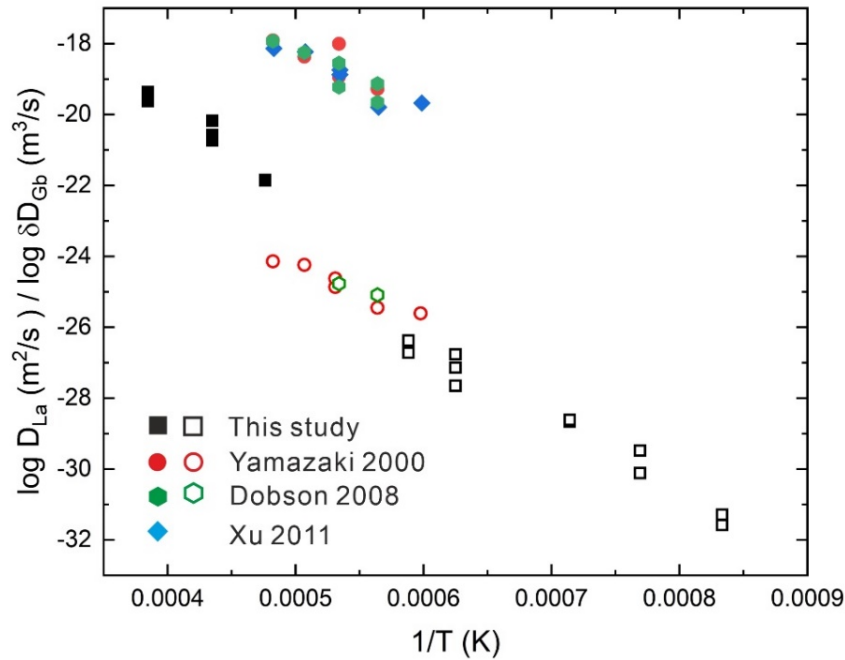


Fig. 3.6-6: Si lattice (solid) and grain boundary (open) data in the current (black) and previous studies. The red ones are from Yamazaki *et al.* (2000, *Phys Earth Planet Inter*, 119 (3-4), 299-309). The green ones are from Dobson *et al.* (2008, *Earth Planet Sci Lett*, 270 (1-2), 125-129). The blue ones are from Xu *et al.* (2011, *J Geophys Res Solid Earth*, 116 (B12), B12205).

The current diffusion coefficient can be used to explain the viscosity of the topmost lower mantle and the spatial distribution of the observed seismic anisotropy. We constructed deformation mechanism maps of bridgmanite at 2000 K and 27 GPa (Fig. 3.6-7) based on the current diffusion data. The grain size of the topmost lower mantle is estimated to be 200-500 μm . The plate motion has a velocity of 1-10 cm/y and assuming that the deformation occurs for the whole mantle (3000 km) or localizes near the slab (300 km) would yield a strain rate for the mantle convection of about 10^{-16} - 10^{-14} s^{-1} . With this grain size and strain rate, the viscosity of the topmost lower mantle is calculated as 7×10^{20} - 1×10^{22} Pa·s, which agrees with the geophysical observations (Fig. 3.6-7A).

Since the deformation of mantle materials may localize near slabs, the region away from slabs should have a low strain rate ($< 10^{-16}$ s^{-1}) while the region close to slabs should have a higher strain rate ($\sim 10^{-14}$ s^{-1}). Based on our calculated deformation map (Fig. 3.6-7B), the deformation of bridgmanite in the region away from slabs is controlled by diffusion creep, resulting in the observed seismic isotropy. In the region near slabs, the deformation mechanism is at the boundary between diffusion creep and dislocation creep assuming the same grain size near and away from slabs. Enrichment of fluid near slabs could enlarge the grain size and make dislocation creep more dominant in this region. The lattice-preferred orientation in bridgmanite produced by dislocation creep may explain the observed seismic anisotropy in the near-slab regions.

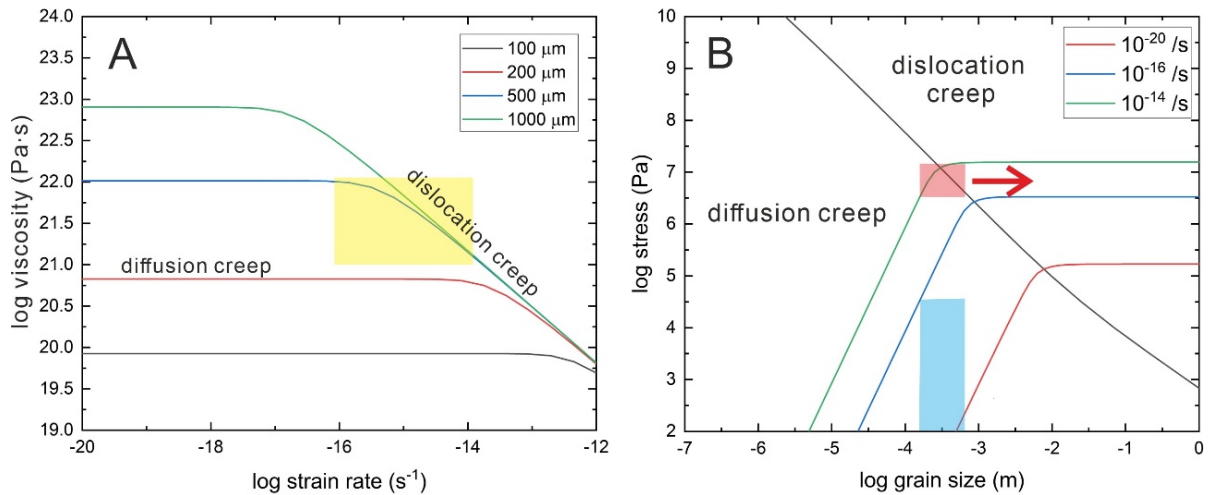


Fig. 3.6-7: Deformation mechanism maps for bridgmanite at 27 GPa and 2000 K constructed by using current diffusion data. (A) Strain rate and viscosity relationship with constant grain size. The yellow region represents the grain size of 200-500 μm and strain rate of 10^{-16} - 10^{-14} s⁻¹. The calculated viscosity is between 7×10^{20} - 1×10^{22} Pa·s, which agrees with the observed mantle viscosity. (B) Stress and grain size relationship with constant strain rates. Black solid line shows boundary between dominant deformation mechanisms of the dislocation creep and the diffusion creep regimes. The blue and red regions denote the region away from and near slabs, respectively. The red arrow indicates that fluid near slabs could enlarge the grain size of bridgmanite in this region, make dislocation creep more dominant.

g. Reaction-enhanced deformability of the eclogite-facies metagranitoids in the Sesia Zone, Western Alps: Revisit with advanced electron microscopy (S. Wen/Oxford and N. Miyajima)

One of the very important problems in the field of geology is the relationship between deformation and metamorphism. In continental collision belts, where crustal thickening occurs by thrusting, rocks are expected to undergo a series of metamorphic reactions when they encounter the pressure and temperature conditions for different metamorphic facies. However, it is often unclear whether metamorphism primarily enhanced the deformation (reaction-enhanced ductility) or whether deformation primarily catalysed the metamorphic reactions (deformation-enhanced metamorphism). Fortunately, the eclogite-facies metagranitoids in the Sesia-Lanzo Zone, Western Alps, can provide insights into this question. This report challenges the previous literature studies of quartz diorite to address the relationship between deformation and metamorphism and to understand the mechanisms of reaction-enhanced deformability at the nanometre scale. The first question is whether jadeite or albite exists in a high-pressure meta quartz diorite collected from Monte Mucrone, Italy, *i.e.*, if the plagioclase was transformed completely into jadeite and quartz under the peak pressure and temperature conditions.

Employing scanning electron microscopy (SEM) we confirmed that the pseudomorphic plagioclase domains exhibit a Si/O ratio of 3:8 instead of 1:3 in the mineral formulae,

suggesting the potential presence of $\text{NaAlSi}_3\text{O}_8$ albite within these domains instead of a complete transformation into jadeite and quartz (Fig. 3.6-8). Albite, Ca- and Fe-bearing jadeite and zoisite coexist with biotite (Bt) in the domains. Surprisingly, our chemical analyses did not reveal any pure $\text{NaAlSi}_2\text{O}_6$ jadeite-like compositions in the samples, which contradicts findings from the previous literature. This discrepancy raises the possibility that composition alone might not be sufficient to differentiate between jadeite and albite. Consequently, further investigation is warranted. Since albite and jadeite possess distinct crystal structures, triclinic and monoclinic symmetries, respectively – they can be discerned through electron diffraction patterns. Therefore, the transmission electron microscopy (TEM) analysis of individual mineral grains in the pseudomorphic plagioclase domains in question is a reasonable approach to determine their crystal structures in the next step. It can provide useful information to understand agent minerals of a reaction-enhanced deformability in the rock transition from quartz diorite to orthogneiss.

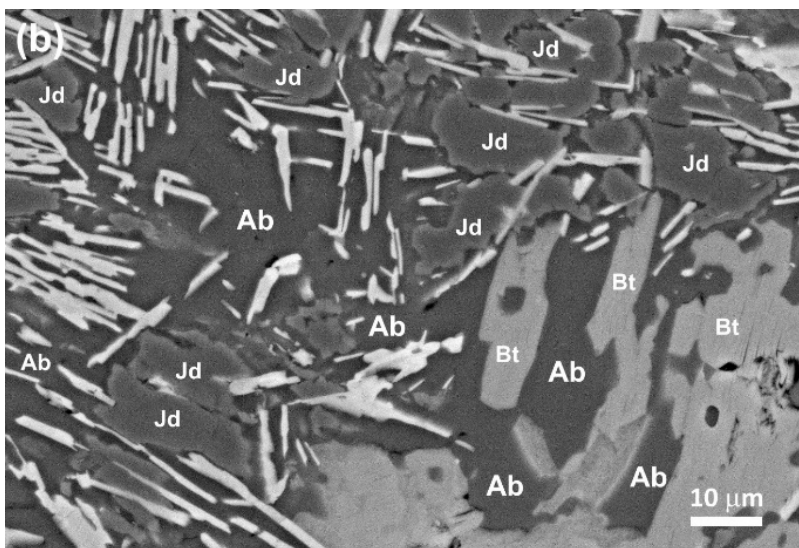
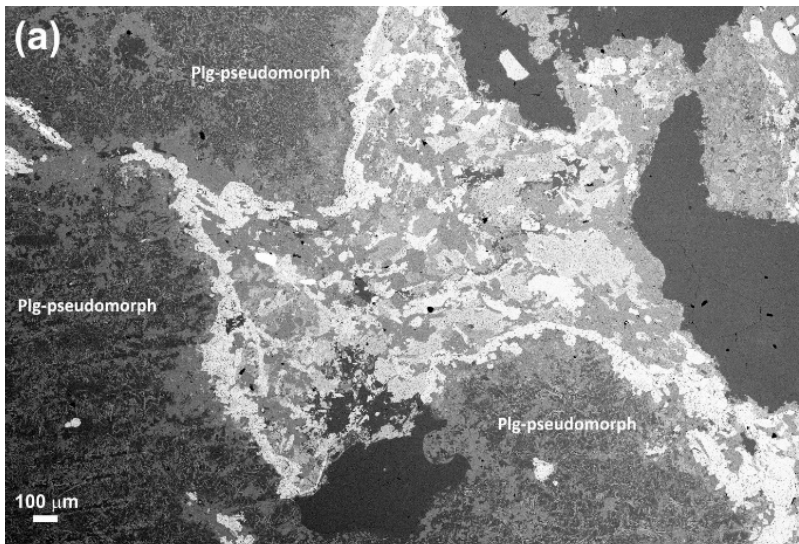


Fig. 3.6-8: Back-scattered electron images of a pseudomorphic plagioclase domain (Plg-pseudomorph) in meta quartz diorite from Monte Mucrone, Western Alps, Italy. (a) at low magnification, (b) at high magnification. Ab: albite, Bt: biotite, Jd: Jadeite.

3.7 Material Science

A unique combination of *in situ* high-pressure technology, advanced facilities for sample characterisation and high scientific expertise, permit sophisticated and challenging research into material physics and chemistry at the Bayerisches Geoinstitut. In this section of the annual report, a number of studies are presented that demonstrate a diversity of novel materials, synthesised under extreme conditions, that show unprecedented changes in chemical behaviour.

The variable valence state of iron cations give rise to a series of iron-oxides, and the first contribution in this section of the annual report explores properties of the mixed-valence iron oxide Fe_4O_5 that holds significant interest from geological, chemical, and physical perspectives. By means of X-ray absorption, the study finds that Fe_4O_5 exhibits semimetal conductivity, combining high charge carrier concentration typical of metals with low electrical conductivity, characteristic of semiconductors. Yttrium bromide oC16-YBr_3 is another semiconductor synthesised at high-pressure and high-temperature conditions. When decompressed, the 3D framework transforms to a layered structure with semiconductor properties and low exfoliation energy. This YBr_3 phase expands the list, and our understanding, of layered trivalent rare-earth metal halides and demonstrates how high pressure can alter structural motifs and physical properties.

Carbides present a class of materials that recur in this section of the annual report, and the third contribution reports on novel high-pressure dysprosium carbides with various stoichiometries and unique carbon arrangements. Synthesised in a diamond anvil cell, these rare-earth metal carbides exhibit diverse structural forms, showcasing different types of chemical bonding, significantly expanding our understanding of carbide chemistry based on rare-earth metals. Although these carbides have not been quenched to room conditions yet, density functional theory calculations suggest their dynamic stability at ambient pressure, which holds the promise of them being recoverable. Although not in the form of carbides, carbon is also an important player in the fourth contribution. Here, high-pressure synthesis facilitates the stabilization of the CN_3^{5-} guanidinate anion, leading to a new class of inorganic ternary metal-carbon-nitrogen compounds: Several isostructural lanthanite (Ln) oxoguanidates $\text{Ln}_3\text{O}_2(\text{CN}_3)$ have been successfully synthesised, and their crystal structures were determined using synchrotron single-crystal X-ray diffraction, supported by X-ray absorption measurements and density functional theory calculations. Further, the CN_3^{5-} guanidinate anion in these compounds can be quenched to ambient conditions. The next contribution on a carbon-based material makes the step to organic chemistry and explores the high-pressure behaviour of C_{14}H_8 anthracene. Here, the molecular herringbone structure is maintained to ~ 42 GPa, above which the absence of a pattern in single-crystal X-ray diffraction suggests amorphization.

Structural transformations in the perovskite-type solid solution $(1-x)\cdot\text{Na}_{0.5}\text{Bi}_{0.5}\text{TiO}_3-x\cdot\text{BaTiO}_3$ (NBT- x BT), as a lead-free ferroelectric of potential industrial interest, occur across a rhombohedral-tetragonal morphotropic phase boundary. These subtle structural changes may

be enhanced at high pressure, and high-pressure experiments may therefore help to shed light on general processes in the transition. In the final contribution, high-pressure X-ray diffraction and Raman spectroscopy data are reported for $x = 0.048$, and reveal significant changes in the compressional mechanism of the NBT- x BT structure.

a. *Electronic properties of Fe_4O_5 (S.V. Ovsyannikov, F. Wilhelm/Grenoble, A. Rogalev/Grenoble and L.S. Dubrovinsky)*

A recently discovered mixed-valence iron oxide with Fe_4O_5 stoichiometry is an important archetypal material, which is of great interest from geological, crystal chemical and fundamental physical perspectives. Its electronic properties are controversially discussed in the literature, for example, whether Fe_4O_5 is a metal or a semiconductor. We experimentally investigated electronic properties of Fe_4O_5 by a number of experimental techniques, including X-ray absorption near edge spectra (XANES) at the Fe K-edge, and determined an effective electronic state of iron in Fe_4O_5 .

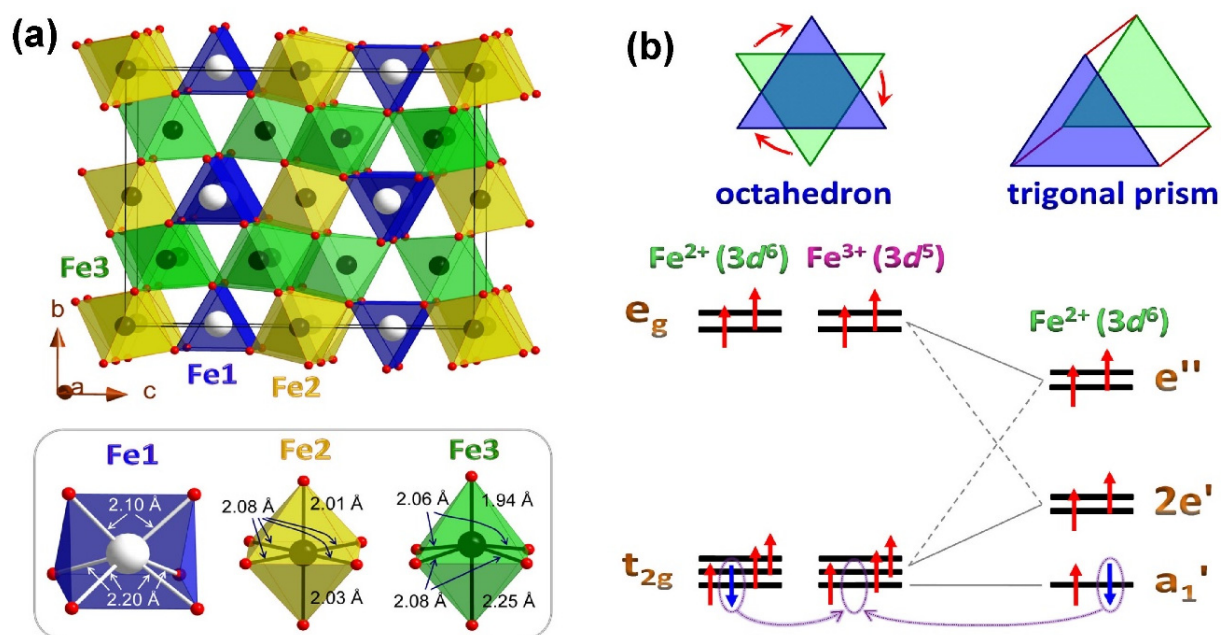


Fig. 3.7-1: Crystal structure of Fe_4O_5 and d -orbital splitting of Fe ions at ambient conditions. (a) Crystal structure of Fe_4O_5 projected along the a axis, along chains of prismatic-ly-coordinated iron. Trigonal-prismatic and octahedral oxygen coordination of Fe1, Fe2, and Fe3 atoms in this structure and Fe-O distances at ambient conditions, are shown at the bottom. (b) Schematic representation of d -orbital splitting of Fe^{2+} ($3d^6$) and Fe^{3+} ($3d^5$) ions in highly-symmetric octahedral and trigonal-prismatic oxygen coordinations. The red arrows in the top panel show how an octahedron can be converted to a trigonal prism by rotating one oxygen plane. The red upward arrows in the d -orbital diagrams are spin-majority electrons, and blue downward arrows spin-minority electrons. The purple arrows at the bottom of the diagram show a possible electron transfer to the unfilled state of Fe^{3+} ions.

The CaFe_3O_5 -type crystal structure of Fe_4O_5 (Fig. 3.7-1a) comprises two types of crystallographic sites for iron: trigonal prisms (Fe1), filled with Fe^{2+} , and mixed valence ($\text{Fe}^{2+}/\text{Fe}^{3+}$) octahedra (Fe2 and Fe3). A typical splitting of d -orbitals for Fe^{2+} ($3d^6$) and Fe^{3+} ($3d^5$) ions in octahedral and trigonal-prismatic oxygen coordinations, is depicted in Figure 3.7-1b. Electrical conductivity in Fe_4O_5 should be related to hopping of charges, from spin-minority states of Fe^{2+} ions to available vacancies of the lowermost t_{2g} electron states of the Fe^{3+} ions. Charge hopping should be accompanied by a local elastic deformation of the crystal lattice due to the difference of $\langle\text{Fe}^{2+}\text{-O}\rangle$ and $\langle\text{Fe}^{3+}\text{-O}\rangle$ bond lengths in the polyhedra. This lattice deformation dramatically increases the effective mass of hopping charges, and hence, decreases their mobility value. This circumstance leads to semimetal conductivity in Fe_4O_5 , combining a high concentration of charge carriers, like in metals, with a low electrical conductivity, like in semiconductors.

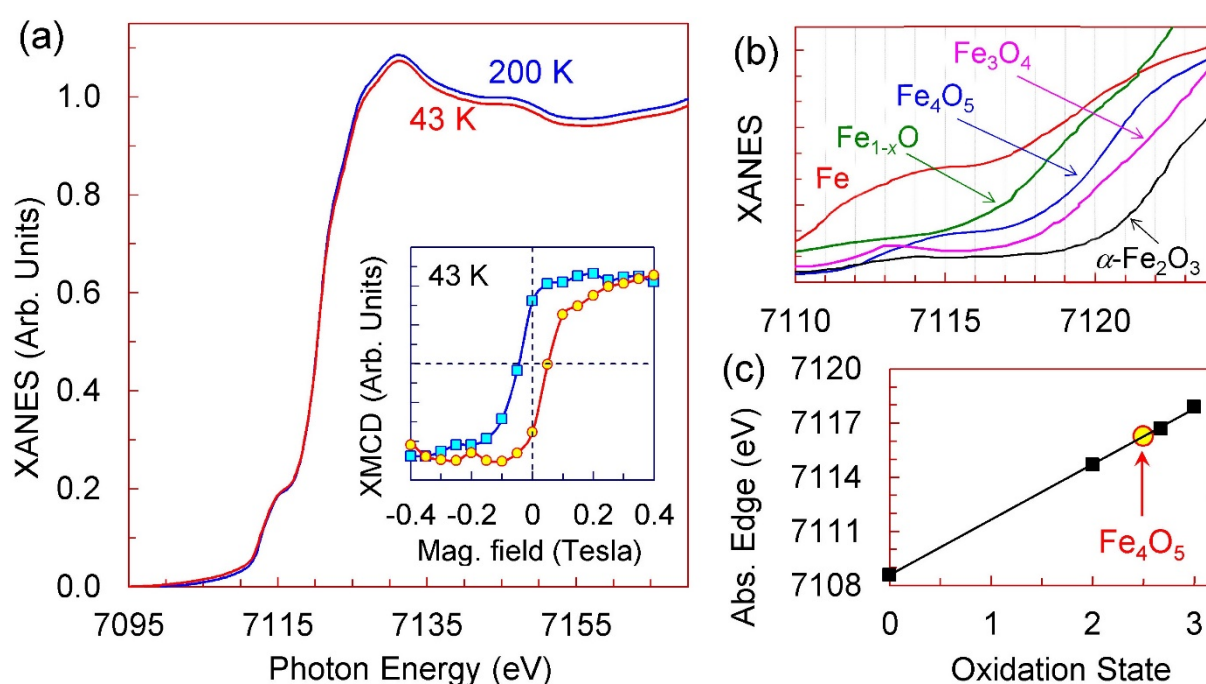


Fig. 3.7-2: X-ray absorption near edge spectra (XANES) of a Fe_4O_5 polycrystal. (a) Normalized XANES spectra at the Fe K-edge of Fe_4O_5 polycrystal, acquired above and below the charge-ordering phase transition at 150 K. The inset depicts a magnetic-field hysteresis of an X-ray magnetic circular dichroism (XMCD) signal at 43 K, suggesting the appearance of magnetic order. (b) Comparison of absorption edges of Fe_4O_5 and iron-oxide calibrants, including a nearly stoichiometric Fe_{1-x}O . (c) Absorption edges of Fe_4O_5 , iron, and of other iron oxides as a function of their nominal oxidation states.

Polycrystals of Fe_4O_5 were synthesised from powders of magnetite and iron at high-pressure (P) high-temperature (T) conditions using multianvil presses at the BGI. Typical conditions of the syntheses were $P=14$ GPa and $T=1100\text{-}1200$ °C over several hours. XANES spectra were acquired on two single-phase polycrystalline samples of Fe_4O_5 at ambient P at the ID12 beamline of the European Synchrotron Radiation Facility (Grenoble, France).

The XANES spectra were acquired both above and below the charge-ordering phase transition at 150 K; no changes in the spectra across the transition were found. The spectra had an apparent pre-edge feature at about 7115 eV, which could not be separated from the main absorption edge (Fig. 3.7-2a). We compared the spectra for Fe₄O₅ with reference spectra for other iron oxides with well-known mean oxidation states of iron, namely, α -Fe₂O₃, Fe₃O₄, and nearly stoichiometric Fe_{1-x}O (Fig. 3.7-2b). The photon energy of the absorption edge for Fe₄O₅ lies between those of Fe_{1-x}O and Fe₃O₄, significantly closer to the latter. This result is consistent with an expected mean oxidation state of Fe^{2.5+} in Fe₄O₅, as absorption edges are primarily related to mean oxidation state. This comparison is illustrated by plotting absorption edge energies of α -Fe, Fe₃O₄, Fe₄O₅ and α -Fe₂O₃ as a function of their nominal oxidation states (Fig. 3.7-2c). If we assume an oxidation state to be close to Fe⁺² for Fe_{1-x}O, its absorption edge energy falls onto the general linear trend established by the other compounds. This linear dependence visually confirms the mean oxidation state of +2.5 for Fe₄O₅.

The magnetic-field dependence of X-ray magnetic circular dichroism signals below the transition point of 150 K demonstrates a distinct hysteresis loop (inset in Fig. 3.7-2a), suggesting the emergence of a net magnetization in the low-*T* phase of Fe₄O₅. This finding is consistent with a canted antiferromagnetism in this phase reported earlier.

b. *High-pressure oC16-YBr₃ polymorph recoverable to ambient conditions: From 3D framework to layered material (A. Aslandukova, A. Aslandukov, F.I. Akbar, L.S. Dubrovinsky, N.A. Dubrovinskaia/Bayreuth; S. Chariton and V. Prakapenka/Chicago; A. Pakhomova and M. Hanfland/Grenoble)*

Rare-earth metal halide materials possess a variety of physical properties that have led to important technological applications, such as scintillating materials for X-ray detection, ionic conductors for energy storage applications, magnetic, and luminescent materials. The low exfoliation of weakly bonded layered metal halides raises the prospect of fabricating promising 2D materials. However, layered halides are less studied than layered nitrides, sulphides, selenides or tellurides, with BN, MoS₂, WSe₂, Bi₂Se₃, and Bi₂Te₃ as examples of the latter. Among metal halides, yttrium trihalides are important as they are often used as crystal matrices for luminescent lanthanides ions.

In this work, a new orthorhombic polymorph of yttrium bromide, *oC16*-YBr₃ was synthesised from yttrium and CBr₄ in a laser-heated diamond anvil cell at 45 GPa and 3000 K. The structure of *oC16*-YBr₃ was refined using *in situ* synchrotron single-crystal X-ray diffraction. At high pressure (*P*) it can be described as a 3D framework of YBr₉ polyhedra. Upon releasing *P*, the Y-Br network changes in such a way that below 25 GPa the structure can be considered as layered. The layers are comprised of edge-sharing YBr₈ polyhedra, weakly bonded by van der Waals and non-covalent Br-Br interactions (Fig. 3.7-3). According to DFT calculations, *oC16*-YBr₃ is a semiconductor with a band gap strongly sensitive to *P*. The layered material can be recovered to ambient conditions and the calculations show that it has a low exfoliation energy

of 0.30 J/m^2 . Our results expand the list of layered trivalent rare-earth metal halides and provide insight into how high P alters their structural motif and physical properties.

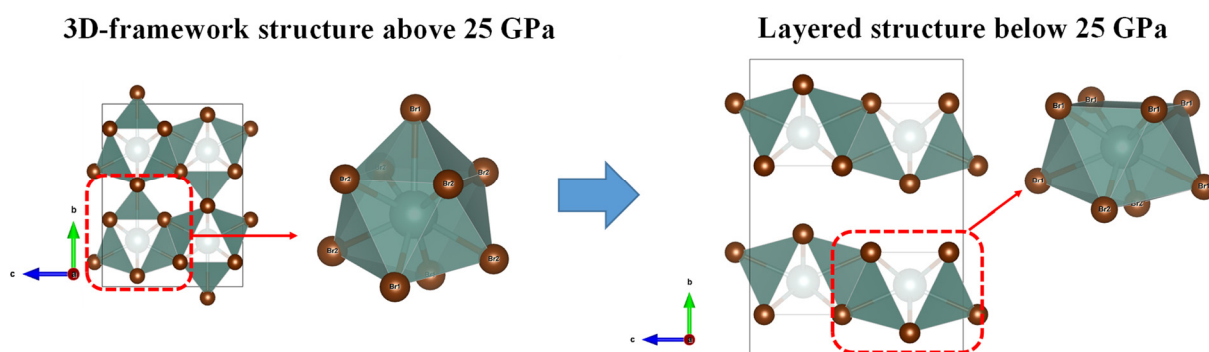


Figure 3.7-3: Illustration of the change in the oC16-YBr₃ structural motif from a 3D framework of Y-Br polyhedra to a layered structure.

c. *Novel high-pressure rare-earth metal carbides with diverse carbon atoms arrangements (F.I. Akbar, A. Aslandukova, A. Aslandukov, N.A. Dubrovinskaia/Bayreuth, L.S. Dubrovinsky, Y. Yin/Linköping, E. Bykova and M. Bykov/Frankfurt a. M., D. Laniel/Edinburgh)*

High-pressure (P) techniques serve as a valuable method for delving into the crystal chemistry of compounds that remain undiscovered at ambient conditions. Such explorations unveil novel forms of chemical bonding and promising properties. For carbides, for example, we can broaden the range of carbide compounds which hold significant relevance in both science and technology. Structural adaptations driven by composition and external factors like P and temperature (T) can give rise to carbides with diverse forms of chemical bonding and, consequently, captivating crystal chemistry.

In this work, dysprosium carbides of varying stoichiometries, Dy₃C₂, Dy₄C₃, γ -Dy₄C₅, Dy₅C₉, and γ -DyC₂ were synthesised in the diamond anvil cell (DAC). We employed the BX90 type DAC equipped with Boehler-Almax type anvils and a rhenium gasket. Flakes of pure Dy were loaded into the P chamber together with dried NaCl (used as thermoinsulator). After compression of the sample to ~ 20 -95 GPa, the dysprosium flakes were heated by a NIR laser (1070 nm wavelength) from both sides to $T \sim 2800$ K. The DAC with the sample was transferred to the Extreme Conditions Beamline (PETRA III, DESY) and ID15b/ID11 Beamlines (ESRF) for *in situ* X-ray diffraction structural studies of reaction products. Interaction of Dy and carbon from the diamond resulted in the formation of dysprosium carbides, Dy₃C₂, Dy₄C₃, γ -Dy₄C₅, Dy₅C₉, and γ -DyC₂ (Fig. 3.7-4), based on single-crystal synchrotron X-ray diffraction.

Dysprosium carbide Dy₃C₂ ($P4/m\bar{3}m$) was discovered at ~ 55 -70 GPa (Fig. 3.7-4a). Its structure contains C-C dumbbells with a C-C distance of $1.49(4) \text{ \AA}$ at 70 GPa. Dy₄C₃ ($I-43d$) synthesised at 19-95 GPa was found to have the anti-Th₃P₄-type structure (Fig. 3.7-4b), which has been

described for scandium carbide, Sc_4C_3 , but not observed in lanthanide or Y carbides. $\gamma\text{-Dy}_4\text{C}_5$ is isostructural to $\gamma\text{-Y}_4\text{C}_5$ ($Cmce$), recently discovered at ~ 50 GPa, and contains carbon dumbbells ($\text{C-C} = 1.38(4)$ Å at 70 GPa) and trimers ($\text{C-C} = 1.428(19)$ Å at 70 GPa) (Fig. 3.7-4c). Dy_5C_9 ($P4/mnc$) was synthesised at 70 GPa (Fig. 3.7-4d); it contains polymeric carbon chains with a C-C distance of $\sim 1.46(2)$ Å at this P . $\gamma\text{-DyC}_2$ ($Immm$) was observed at 70 GPa, for which carbon atoms polymerize to form flat ribbons with C-C distances of 1.47(3) Å and 1.501(10) Å at 70 GPa (Fig. 3.7-4e).

Density functional theory calculations agree with the experimental data and suggest the dynamical stability of $\gamma\text{-DyC}_2$, $\gamma\text{-Dy}_4\text{C}_5$ and Dy_4C_3 at ambient conditions. The identification of polycarbon anions, previously not observed for rare-earth carbide systems, significantly broadens carbides chemistry.

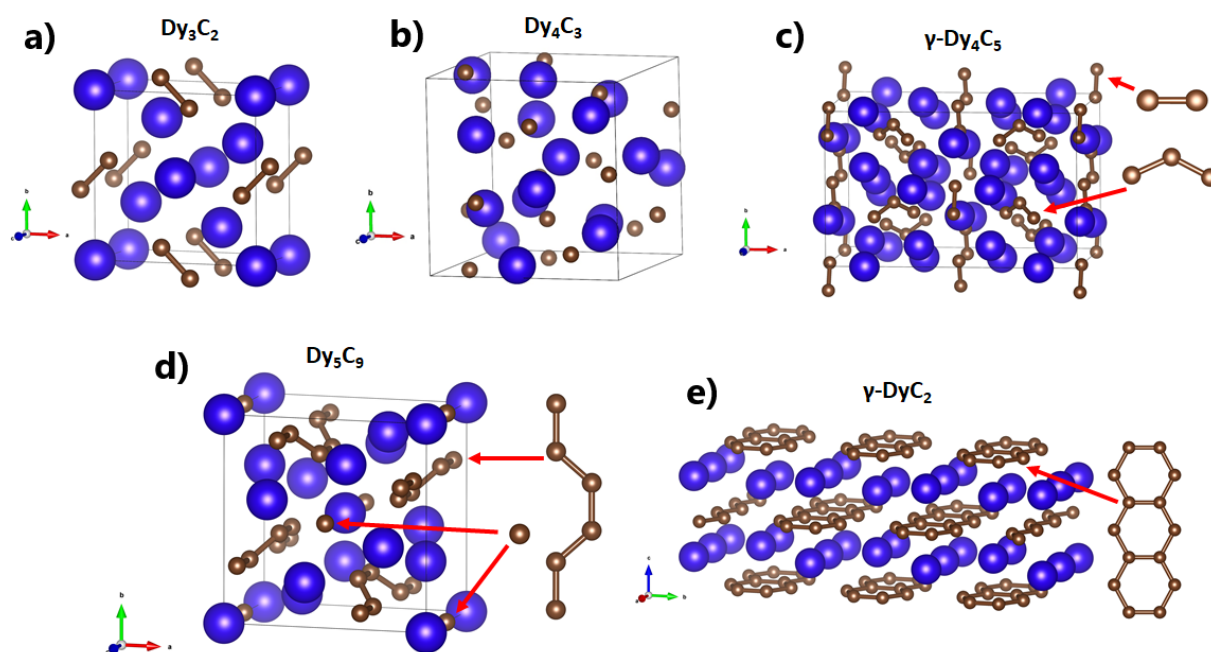


Fig. 3.7-4: Structures of dysprosium carbides synthesised in a laser-heated diamond anvil cell: a) Dy_3C_2 , b) Dy_4C_3 , c) $\gamma\text{-Dy}_4\text{C}_5$, d) Dy_5C_9 , and e) $\gamma\text{-DyC}_2$. The blue and brown spheres represent dysprosium and carbon, respectively.

d. *Stabilization of the CN_3^{5-} anion in recoverable high-pressure $\text{Ln}_3\text{O}_2(\text{CN}_3)$ ($\text{Ln} = \text{La}, \text{Eu}, \text{Gd}, \text{Tb}, \text{Ho}, \text{Yb}$) oxoguanidates (A. Aslandukov, A. Aslandukova, A. Chanyshev, Y. Yin/Bayreuth, F.I. Akbar, S. Khandarkhaeva, N.A. Dubrovinskaia/Bayreuth, L.S. Dubrovinsky, P.L. Jurzick and M. Bykov/Köln, D. Laniel/Edinburgh, T. Fedotenko and K. Glazyrin/Hamburg, S. Chariton and V. Prakapenka/Chicago, F. Wilhelm, A. Rogalev, D. Comboni and M. Hanfland/Grenoble)*

Inorganic ternary metal-C-N compounds with covalently bonded C-N anions encompass important classes of solids. The most investigated classes are cyanides (CN^-) and carbodiimides (NCN^{2-}), which are used in a number of applications. While CN^- and CN_2^{2-} anions are well-

known, the next member of this series, the CN_3^{5-} anion (completely deprotonated guanidine) has been unknown. Despite numerous attempts to synthesise the guanidinate anion by deprotonation of guanidine molecule using strong bases, only partially deprotonated guanidine has been stabilized

Here, we present the successful stabilization of the CN_3^{5-} guanidinate anion using a non-conventional route of solid-state synthesis under extreme conditions, rather than a classic *wet chemistry* approach. A series of isostructural $\text{Ln}_3\text{O}_2(\text{CN}_3)$ ($\text{Ln} = \text{La, Eu, Gd, Tb, Ho, Yb}$) oxoguanidates was synthesised under high-pressure (25-54 GPa) high-temperature (2000-3000 K) conditions in laser-heated diamond anvil cells. The crystal structure of this novel class of compounds was determined *via* synchrotron single-crystal X-ray diffraction as well as corroborated by X-ray absorption near edge structure measurements and density functional theory calculations (Fig. 3.7-5). Decompression experiments show that $\text{Ln}_3\text{O}_2(\text{CN}_3)$ compounds are recoverable to ambient conditions. The synthesis of the CN_3^{5-} guanidinate anion extends the list of carbon-nitrogen inorganic anions and its stabilization at ambient conditions provides new opportunities for inorganic and organic synthetic chemistry.

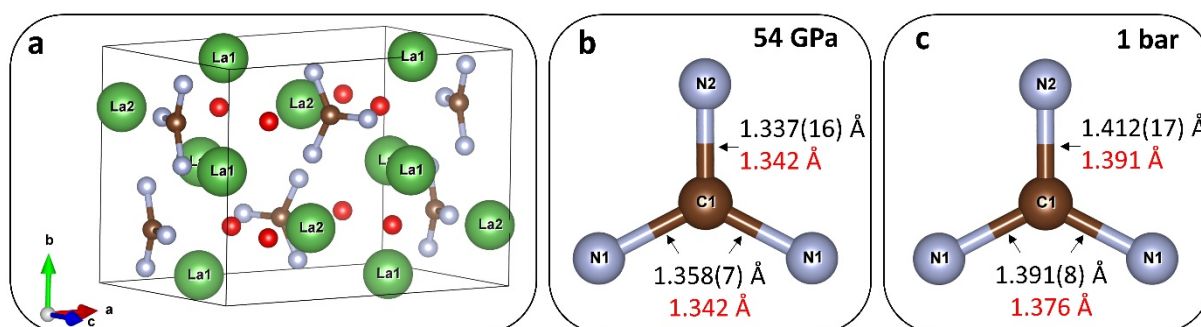


Fig. 3.7-5: (a) General view of $\text{La}_3\text{O}_2(\text{CN}_3)$ crystal structure. The CN_3 unit (b) at 54 GPa and (c) CN_3 unit at 1 bar. La atoms are green, C atoms are brown, N atoms are grey, and O atoms are red. Thin grey lines outline the unit cell. The bond length values obtained from experiments are shown in black, those obtained from the DFT calculations in red.

e. *High-pressure behaviour of anthracene up to 42 GPa (W. Zhou/Bayreuth, L.S. Dubrovinsky, N.A. Dubrovinskaia/Bayreuth and M. Hanfland/Grenoble)*

Polycyclic aromatic hydrocarbons (PAHs) have long attracted interest as potential materials for various optical, optoelectronic and electronic applications. In addition to application-oriented research, much work has been done for understanding the fundamental processes associated with their structure-property relationships. Further, PAHs are one of the most abundant types of carbon-based molecules in the universe, their properties at various thermodynamic conditions are therefore important for understanding the physical and chemical processes that occur in interstellar and planetary environments. Mechanisms of molecular packing and polymerization of organic compounds under compression are yet to be investigated, and high-pressure (P) single-crystal X-ray diffraction (SCXRD) is the best method to do so.

In order to analyse the crystal structure of anthracene ($C_{14}H_8$) at high P , we loaded single crystals into a membrane-type diamond anvil cell (DAC) equipped with diamonds with the culets size of 250 μm and a rhenium gasket with a hole of $\sim 120 \mu\text{m}$ in diameter. Helium (He) was used as a P -transmitting medium. The DAC was gradually pressurized to 50 GPa. The samples were characterised using synchrotron SCXRD at the European Synchrotron Radiation Facility (ESRF) at the ID15B beamline ($\lambda = 0.410 \text{ \AA}$). During the compression process, the sample consistently maintained its good crystallinity. At ambient conditions, anthracene has a monoclinic structure (space group #14, $P2_1/c$) with molecular herringbone pattern (Fig. 3.7-6), and each planar molecule is composed of three fused benzene rings. The planar structure remains intact up to 42.3 GPa, above which the absence of diffraction pattern suggests the amorphization of the sample. The interplanar angle gradually decreases from 51.4° at ambient P to 41.8° at 42.3 GPa (Fig. 3.7-6) and the β angle from 103.58° to 92.14° . Lattice parameters at 42.3 GPa are $a = 7.769(19) \text{ \AA}$, $b = 5.0266(9) \text{ \AA}$, and $c = 6.6325(8) \text{ \AA}$. Using the ambient P volume (V_0) of anthracene, a third-order Birch–Murnaghan equation of state fit to the experimental P - V data leads to parameters for the bulk modulus and its P -derivative at V_0 , $K_0 = 8.4(2) \text{ GPa}$ and $K_0' = 8.0(4)$, respectively.

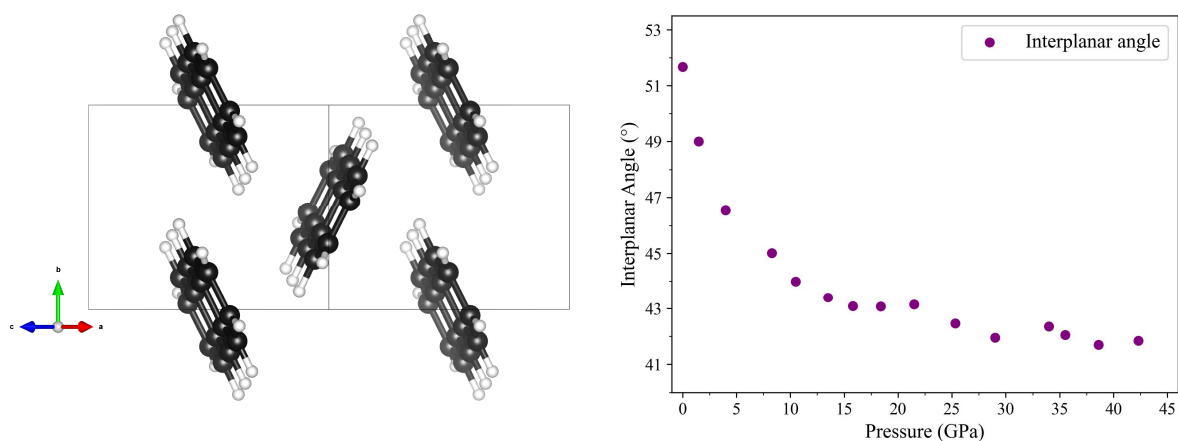


Fig. 3.7-6: Crystal structure of anthracene. a) View along the $[101]$ direction, C and H atoms are shown in black and white colors.; b) Pressure dependence of the interplanar angle.

f. *Pressure-induced structural transformations in $(1-x)\cdot Na_{0.5}Bi_{0.5}TiO_3-x\cdot BaTiO_3$ at the morphotropic phase boundary (C. Rösche/Hamburg, T. Boffa Ballaran and B. Mihailova/Hamburg)*

Ferroelectrics are an important class of technological materials due to their excellent dielectric, piezoelectric, pyroelectric and optoelectric properties that are used for the construction of sensors, actuators, imaging devices and memory chips. At the moment the focus in the scientific community is to find alternatives for the market-dominating lead-based ferroelectric materials like $PbZr_{1-x}Ti_xO_3$ (PZT), since the toxicity of lead poses environmental and health risks during

mining, processing and disposal. The lead-free perovskite-type (ABO_3) solid solution $(1-x)\cdot Na_{0.5}Bi_{0.5}TiO_3-x\cdot BaTiO_3$ (NBT- x BT) is a promising alternative due to its high electric-field-induced strains. For $x = 0.05-0.06$ NBT- x BT exhibits a morphotropic phase boundary, where the symmetry changes from rhombohedral to tetragonal and the relevant material properties are strongly improved. However, for NBT- x BT to make the leap from the research laboratories to industrial application further advances are required. For an effective modification of the material, a better understanding of nanoscale structural features is required. The analysis of structural transformations occurring at non-ambient conditions allow conclusions to be drawn on subtle structural features, which are hardly detectable at ambient pressure (P) and temperature. It is known from high- P analyses of relaxor ferroelectrics that P suppresses polar order in favour of antiferrodistortive order, meaning that polar atomic displacements are reduced, while octahedral tilting is enhanced.

We have performed high- P X-ray diffraction experiments on single crystals of NBT- x BT at the morphotropic phase boundary ($x = 0.048$) at BGI using a four circle Huber Eulerian goniometer coupled with an ultra-high intensity rotating anode X-ray source with Mo $K\alpha$ radiation equipped with a multilayer VaryMaxTM focusing optic and a point detector. Two separate experiments were performed up to 6.1 GPa and 1.6 GPa using two different specimens of $\sim 60\times 60\times 40$ μm dimensions from the same bulk crystal. In the first run, a BX90 diamond anvil cell (DAC) with 500- μm culets was used, while the second run was conducted using a Boehler-Almax DAC with 600- μm culets. Stainless steel gaskets were pre-indented to 70 μm and 96 μm , respectively, and 280- μm holes were generated by laser drilling. The P -transmitting medium was a 16:3:1 methanol-ethanol-water mixture in the first and a 4:1 methanol-ethanol mixture in the second experiment, both solutions ensuring hydrostatic conditions in the probed pressure range. In the first run the fluorescence spectra of ruby measured before and after the X-ray measurements were used for determining pressure, whereas in the second run the unit-cell volume of quartz loaded together with the NBT-0.048BT crystal was used instead, allowing to determine the P with accuracy < 0.01 GPa.

The averaged structure of the NBT-0.048BT crystals appear to be cubic with the unconstrained unit-cell parameters determined with high accuracy (a_1 and a_2) identical up to 4 GPa. Above this P , however, a_1 and a_2 start to differ from each other, and the difference is above the 2σ standard deviation at 5.4 GPa (Fig. 3.7-7a).

Pressure-induced phase transitions as well as changes in compressional mechanism can be better seen if the P -volume (V) data are recalculated in terms of normalized pressure $F = P/3f(1+2f)^{5/2}$ versus Eulerian strain $f = [(V_0/V)^{2/3}-1]/2$. In the P range 0.23-1.68 GPa, the $F(f)$ plot of NBT-0.048BT shows three discontinuities at 0.5, 0.9 and near 2 GPa (Fig. 3.7-7b). The maximum near 0.5 GPa as well as the minimum near 0.9 GPa has been observed for data collected in separate experiments both on compression and decompression and thus likely indicate changes in the elasticity triggered by structural transformations.

A piece from the same bulk crystal was also analysed by high- P Raman spectroscopy up to 8.9 GPa. The P ranges where structural transformations are observed via anomalous behaviour of the Raman modes agree with the XRD data. In addition, the Raman data indicate that the irregularities in elasticity near 0.5 and 0.9 GPa are triggered by rearrangements in the B-cation subsystem and the constant $F(f)$ behaviour above 2 GPa (Fig. 3.7-7b) is due to the enhancement of octahedral tilts that act as a new compression mechanism allowing the structure to better accommodate at larger P .

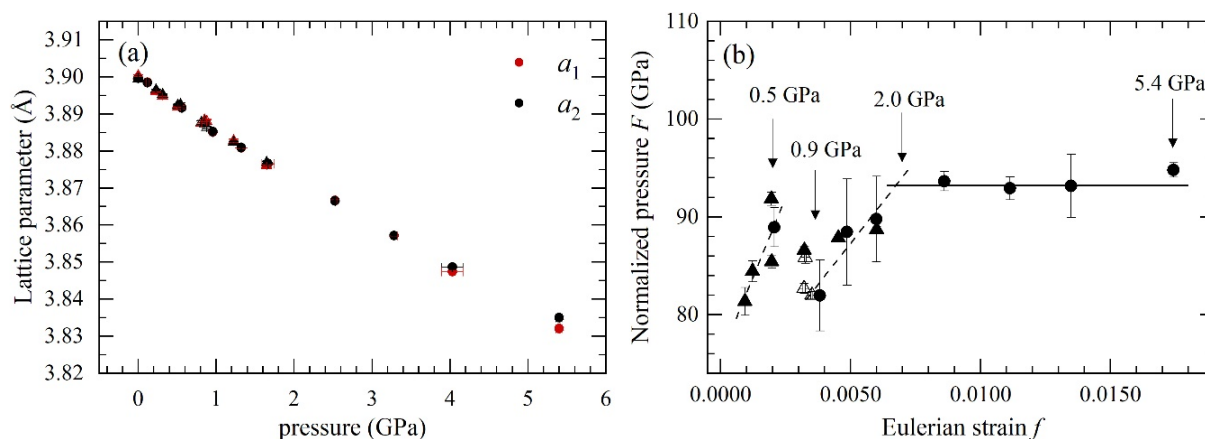


Fig. 3.7-7: (a) Pressure dependence of the two unconstrained unit-cell lattice parameters a_1 and a_2 of the pseudo-cubic NBT-0.048BT crystal which could be determined with high accuracy; (b) Normalized pressure plotted versus the Eulerian strain calculated for the unit-cell volume of the NBT-0.048BT crystal showing that below 2 GPa there are several changes in the compression mechanism of the perovskite structure.

3.8 Methodological Developments

Since its foundation in 1986, the Bayerisches Geoinstitut (BGI) has consistently led the way in the development and enhancement of methodologies for exploring Earth's interior. This includes the invention of novel experimental apparatus and techniques, as well as substantial improvements to existing methodologies. These advancements have had a profound impact on our understanding of the Earth's interior, facilitating the study of Earth materials under extreme conditions that were previously unattainable. This has deepened our understanding of the processes driving plate tectonics, the evolution of the Earth's atmosphere, and the formation of the Earth's core. BGI's unwavering commitment to methodological innovation continues to this day. Its ongoing methodological advancements will continue to significantly enrich our understanding of the Earth's interior. BGI is proud of its legacy of innovation and remains dedicated to continually pushing the boundaries of scientific knowledge in this field.

Over the past year, our efforts have been sustained, culminating in the following contributions. The initial two studies focused on measuring the elasticity of minerals at high pressures using diamond anvil cells. Buchen *et al.* delved into the elastic response of aggregates derived from X-ray diffraction under high pressures that can be directly correlated with an applied stress at seismic frequencies. Heidelbach *et al.* probed the effects of extreme conditions on the orientation and chemical distribution of ringwoodite single crystals demonstrating that Brillouin spectroscopy in the diamond anvil cell can be performed on single crystals at high temperatures. Hirschmann and Zhang's contribution introduced a new calibration for the activity of Fe in solid and molten FePt alloys, commonly used as oxygen fugacity sensors in high-pressure/-temperature experiments. This calibration is applicable to the calculation of oxygen fugacity in an experiment involving a molten FePt alloy equilibrated with an iron-bearing silicate melt under extreme conditions. Whitney *et al.* investigated the role of lawsonite and epidote-group minerals in redox and intraslab mass transfer, with a focus on their composition and stability in subducted crust and sediments. They point out that the orientation may be an important parameter in the XANES analysis of certain minerals for the determination of $\text{Fe}^{3+}/\Sigma\text{Fe}$ ratios and consequently oxygen fugacity.

The subsequent two contributions were geared towards the analysis of run products produced by multianvil presses. Bondar *et al.* explored the relationship between secondary ion mass spectrometry (SIMS) and elastic recoil detection analysis (ERDA) in measuring hydrogen in various silicate glasses, emphasising the pronounced SIMS matrix effect across a broad compositional range. Timoner *et al.* demonstrated the use of low-voltage SEM-EDS for high-resolution chemical analysis of Al-bridgmanite and Fe-bearing minerals, achieving spatial resolution superior to that available on electron microprobes. This technique is particularly beneficial for experimental geoscience research where the small crystal size of high-pressure samples poses a significant analytical challenge. The two following contributions improved the design of high-pressure assemblies in multianvil experiments for different purposes.

The following three studies present advances in the design of high-pressure cells in the multianvil press for specific experiments. Han & Katsura propose a new design for electrical conductivity measurements at lower mantle pressures and temperatures. Kubik *et al.* recalibrated temperatures in box furnace multianvil experiments and could reduce thermal gradients significantly which is particularly important for experiments calibrating chemical reactions. Dolinski *et al.* demonstrate that the use of piezocrystals as stress sensors in the sample assembly yields quantitative results comparable to stress measurements with X-ray diffraction in high-pressure deformation experiments with the six-anvil press. The final contribution by Howard *et al.*, documents the progress in the setup of a high-pressure neutron beamline at the research reactor FRM II in Garching. An advanced array of 2D detector banks has been installed and calibrated in order to collect neutrons in a wide range of scattering angles, which is crucial for optimal use of scattered neutrons.

a. *Cyclic loading experiments of polycrystalline aggregates at high pressures (J. Buchen; B. Wang, N. Satta and V. Trautner/Oxford; G. Criniti; A.S.J. Méndez and H.-P. Liermann/Hamburg and H. Marquardt/Oxford)*

The minerals that form the rocks in the Earth's mantle have different aggregate and anisotropic elastic properties. When a seismic wave passes through a rock, the deformation of individual mineral grains depends on their elastic properties and their orientation with respect to the strain and stress fields imposed on the rock by the seismic wave. Since each grain is surrounded by other grains with different orientations and elastic properties, neighbouring grains may mutually influence each other in terms of their elastic strains. As a result, the distribution of both elastic strain and stress may be non-uniform throughout the rock. For the calculation of the aggregate elastic properties of rocks, however, it is commonly assumed that either the stress (Reuss bound) or the strain (Voigt bound) is uniform throughout the rock in order to average the elastic properties of different minerals and grains with different orientations. While these two assumptions provide useful bounds, they do not capture the actual elastic response of the rock, which may fall somewhere between both bounds and depend on other factors such as temperature and the frequency of seismic waves.

To probe the elastic response of polycrystalline aggregates at high pressures and frequencies that approach those of seismic waves, we performed cyclic loading experiments in combination with time-resolved X-ray diffraction. Powders or sintered polycrystals of oxides and silicates were loaded into diamond anvil cells, which were then coupled to a piezo-electric actuator. By feeding sinusoidal voltage–time paths into the piezo-electric actuator, we imposed oscillating stress and strain fields on the sample inside the DAC. Figure 3.8-1a shows an example of a voltage-time path composed of nine sinusoidal oscillations with a period of 100 s and a steady increase in amplitude. During this cyclic loading procedure, X-ray diffraction patterns were recorded in radial diffraction geometry and at a repetition rate of 1 pattern/second. All experiments were carried out at the Extreme Conditions Beamline (P02.2) at PETRA III of the German Synchrotron Radiation (DESY) in Hamburg.

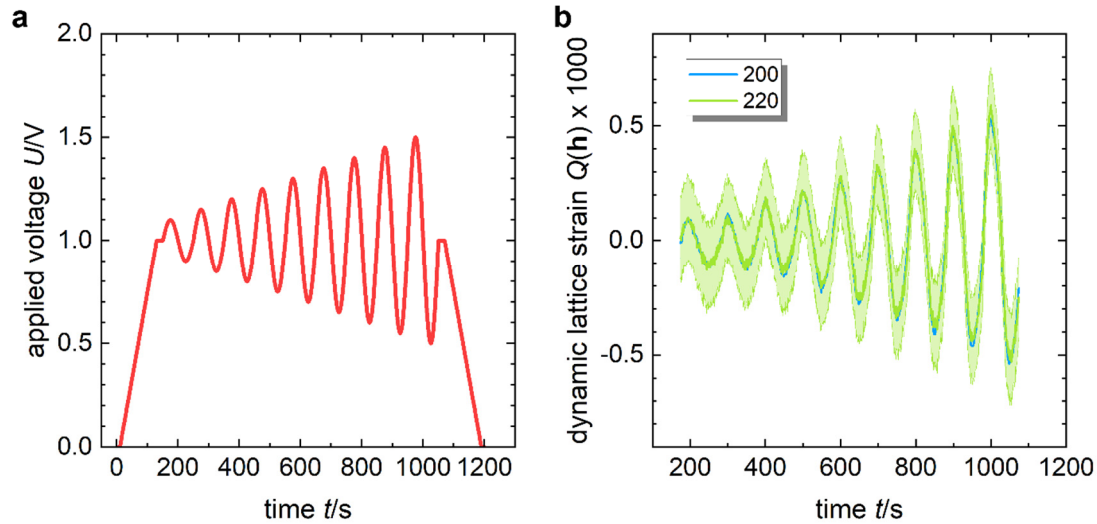


Fig. 3.8-1: a) Voltage–time path for a cyclic loading experiment on MgO powder. b) Dynamic component of the lattice strain Q in MgO derived from the reflections 200 and 220. The pressure during the experiment was around 40 GPa.

The diffraction patterns were analysed to separate compressional and deviatoric contributions to the strain as captured by the d -spacing of the (200) and (220) lattice planes of MgO. In addition, the total strains were decomposed into static and dynamic, *i.e.*, oscillatory, components. As an example, Figure 3.8-1b shows the dynamic component of the lattice strain Q , which corresponds to the deviatoric (or shear) contribution to the oscillating component of the elastic strain. By decomposing the overall strain into different contributions, we can reconstruct the overall strain and stress fields acting on the sample. From a comparison of the strain and stress fields derived from different lattice planes of elastically anisotropic materials, it might be possible to resolve whether the elastic response of a polycrystalline aggregate is closer to one of the bounds or falls somewhere in between. By varying the frequency of the oscillations, it might further be possible to test whether the elastic response varies with frequency and hence shows dispersion.

b. Insights on the orientation and chemical distribution of laser heated ringwoodite single crystals (F. Heidelbach, A. Kurnosov, T. Boffa Ballaran and G. Criniti)

Mineral-physics models are used to infer possible compositions and temperature gradients in the interiors of the Earth and other planets by comparing the wave velocities of candidate minerals with the seismic wave velocity structure measured by seismometers. To this end, the elastic behaviour of such minerals has to be accurately constrained at the relevant pressures and temperatures. The CO₂ laser heating system coupled with Brillouin spectroscopy developed at BGI is very important in this context since it allows determining the full elastic tensor of high-pressure minerals simultaneously at high pressures and high temperatures. A major concern in these experiments is related to whether the single crystals, which are usually oriented along

given direction for the Brillouin experiment, survive heating at temperatures as high as 1900 K for several minutes followed by quenching and re-heating, since each Brillouin scattering measurement can take up to 30 minutes. Crystal mosaicity is especially important because it determines how accurately the elastic tensor can be obtained.

In order to investigate the effect of laser heating, two single-crystal platelets of ringwoodite have been recovered after Brillouin scattering measurements at 17 and 20 GPa and at different temperatures up to 1900 K for 3 and 4 days, respectively. These two crystals were oriented, double-sided polished to a thickness of 15 μm and cut into circular disks of 60 μm diameter using a Focussed Ion Beam (FIB) instrument before the high-pressure/high-temperature experiments.

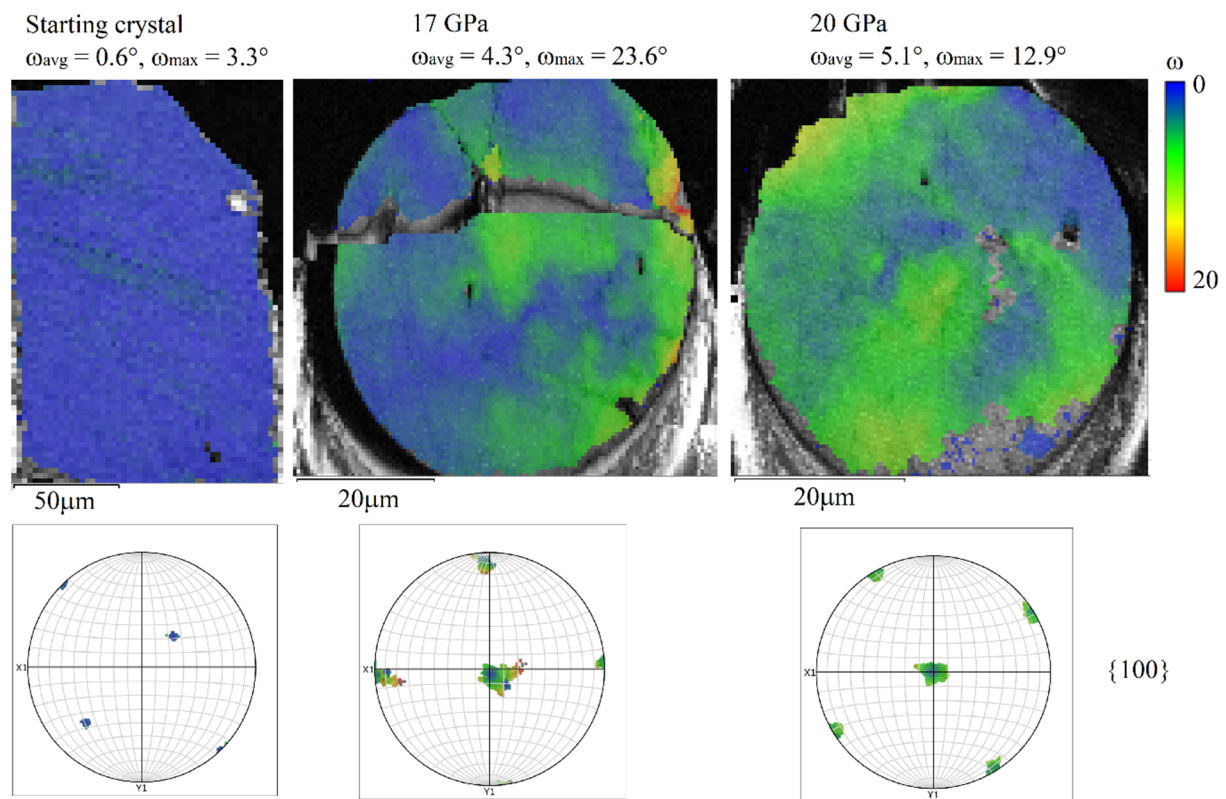


Fig. 3.8-2: SEM-EBSD orientation maps (top row) and corresponding $\{100\}$ pole figures (bottom row) of the three crystals investigated; the rainbow colouring shows the distribution of the misorientation angle ω between the orientation of one pixel and the averaged orientation over all pixels in one grain. Note that ω_{max} values in all three maps are at the edges, whereas the bulk of the material remains at much lower ω as expressed in the ω_{avg} .

The recovered crystals appeared intact and were then mounted in epoxy together with a ringwoodite crystal from the same synthesis batch that had not been subjected to high pressures and temperatures. During standard polishing to prepare the samples for SEM analysis, one of

the two recovered crystals broke into three pieces, whereas the edges of the other one appeared slightly stressed.

The mosaicity of the crystals is mapped as the deviation angle ω of individual orientations (map pixels) from the overall averaged orientation of the complete crystal (Fig. 3.8-2). The starting crystal displays a tight single crystal orientation with an average ω of 0.6° whereas the two crystals that were exposed to high pressure and temperature have an increased ω_{avg} of 4.3° (17 GPa) and 5.1° (20 GPa). Maximum ω values reach 23.6° (17 GPa) and 12.9° (20 GPa) as opposed to 3.3° (starting crystal) but are always restricted to a few points at the rims of the crystals, making it likely that they are due to damage during preparation. The orientation spread in the crystals is rather continuous and only very few subgrain boundaries (misorientations $> 2^\circ$ between pixels) have formed, indicating that no significant recovery took place during the high-temperature phases of the experiments. Chemical mapping by EDS showed a homogeneous chemistry with no apparent Fe gradient or loss. The degree of mosaicity introduced into the ringwoodite crystals during the HP-HT experiments is within the angular resolution of the Brillouin scattering experiment such that the accuracy of the determination of the elastic tensor is not critically affected.

c. Thermodynamic model for the activity of Fe in solid and molten FePt alloys for use as f_{O_2} sensors at extreme temperatures and pressures (M.M. Hirschmann and H.L. Zhang/Beijing)

FePt alloys are commonly employed as oxygen fugacity sensors in high-pressure/high-temperature experiments. To extend their utility to more extreme conditions, including those in which the alloy is molten, we developed a new calibration for the activity of Fe in solid and molten FePt alloys. The f_{O_2} prevailing in these experiments can be constrained from the reaction



provided that the activity of Fe in the alloy may be determined based on its composition and that there are also estimates of the activity of FeO in a silicate or oxide phase present.

The mixing properties of FePt alloy at 100 kPa have been the subject of numerous previous investigations, though significant discrepancies persist, especially for Pt-rich compositions. However, the effects of pressure are less well characterised, and the mixing properties of molten alloys remain poorly defined.

Quantification of the effects of pressure on the thermodynamics of FePt alloys requires evaluation of the excess volumes of mixing. These are generally taken from room temperature measurements, which are complicated by stabilization of ordered FePt intermetallic alloys and by magnetostriction (the "Invar" effect). Consequently, we have evaluated excess volumes of

mixing of FePt alloys by considering only measurements on the disordered fcc phase and by developing a correction for those compositions affected by magnetostriction.

Combining this function for the excess volume of mixing of disordered *fcc* FePt with a regression that considers activity-composition relations at 100 kPa from a wide range of studies including recent data not incorporated into previous models, we arrive at a revised model for the activity coefficient for Fe, γ_{Fe} , in FePt alloy based on an asymmetric Margules formulation:

$$RT \ln \gamma_{Fe} = (W_{FePt} + 2(W_{PtFe} - W_{FePt})X_{Fe})X_{Pt}^2. \quad (2)$$

Here, X_{Fe} and X_{Pt} are mole fractions and the interaction parameters are given by

$$W_{FePt} = -121.5 \pm 2.1 + 1.07 \pm 0.2 P \text{ (kJ/mole)}; W_{PtFe} = -93.3 \pm 4.3 + 1.66 \pm 0.22 P \text{ (kJ/mole)} \quad (3a; 3b)$$

where P is pressure in GPa.

Direct thermodynamic measurements of non-ideal mixing in molten FePt alloys are scarce. However, strong constraints on these mixing properties can be obtained from the fusion relations in the Fe-Pt binary, which are highly sensitive to non-ideality in the liquid. Therefore, given values of the enthalpies of fusion of pure Fe and Pt, both of which are well-known, and assuming the accuracy of the non-ideal model for of solid FePt alloy, described above, mixing parameters for the liquid can be tightly constrained to within ± 2 kJ from experimental determinations of the Fe-Pt melting loop. Resulting coefficients for Eqn. 2 for FePt liquid are

$$W_{FePt} = -124.5 \pm 2 + 1.75 P \text{ (kJ/mole)}; W_{PtFe} = -94 \pm 4 + 1.75 P \text{ (kJ/mole)}. \quad (4a; 4b)$$

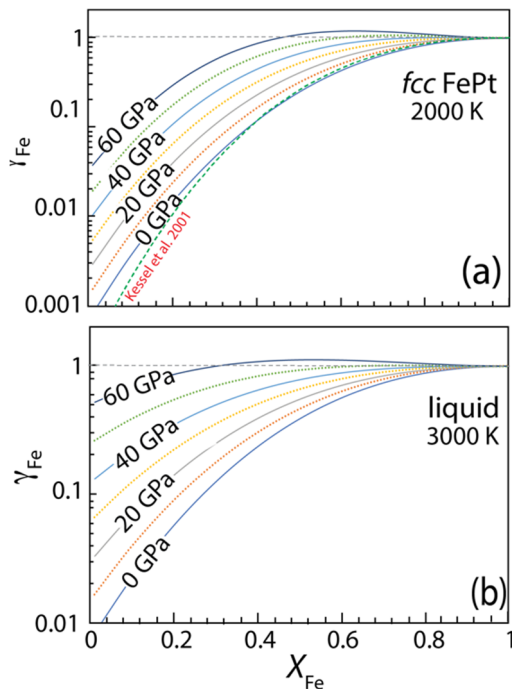


Fig. 3.8-3: Calculated activity coefficient for Fe (γ_{Fe}) as a function of temperature and pressure for (a) fcc solid and (b) molten FePt alloy, based on Equations 2-4. Pt-rich solid and molten alloys are strongly non-ideal at low pressure, but become less non-ideal at very high pressures. Also shown in (a) for comparison is the room pressure model of Kessel *et al.* (2001, *Am. Mineral.*, 86, 1003-1014).

These activity-composition relations (Fig. 3.8-3) are believed to be reliable to at least 60 GPa, although further studies of the equation of state of disordered *fcc* FePt alloy at high pressure are needed to refine these properties. An example of their application is illustrated in Figure 3.8-4, in which molten FePt alloy was equilibrated with iron-bearing silicate melt in a diamond anvil cell at 43 GPa and 3900 K, thereby allowing calculation of the oxygen fugacity in the experiment.

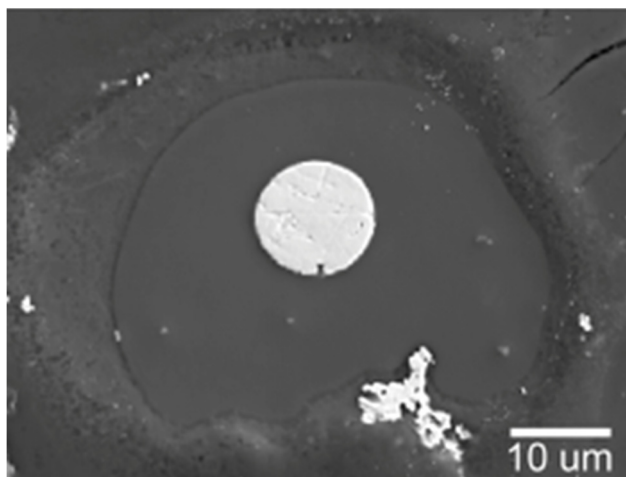


Fig. 3.8-4: Secondary electron image of diamond anvil experiment conducted at 43 GPa, 3800 ± 90 K showing central region of molten FePt alloy equilibrated with surrounding silicate melt. The alloy has the composition of $X_{\text{Fe}} = 0.228$, which, based on Eqns. 2 & 4, translates to an activity of Fe, a_{Fe} , of 0.12. This in turn aids calculation of the oxygen fugacity in the melt as $\Delta\text{IW}=0.46$.

d. *Lawsonite and epidote as novel sensors of redox and intraslab mass transfer (D.L. Whitney/Minneapolis, M. Wilke/Potsdam and F. Heidelbach)*

The stability, abundance, and composition of hydrous minerals in oceanic crust, sediments, and serpentinites strongly influence element cycling via subduction zones. Hydrous minerals record the pathways, extent, and conditions of element transport because their composition reflects fluid-mediated processes, including those that control the redox state of subducted materials and subsequently the mantle and continents.

Lawsonite and epidote-group minerals (EGMs) are hydrous silicates that are important sources and sinks of H_2O and multivalent transition metals (primarily Fe, + Cr, Mn, V) in subducted oceanic crust and sediments. Lawsonite contains ~ 12 wt. % and EGMs ~ 2 wt. % H_2O . Most EGMs contain Fe, and some also contain substantial amounts of Mn (piemontite) \pm REE (allanite). Lawsonite commonly contains Fe, Cr, and Ti, and lawsonite and EGMs are major hosts of trace elements (U, Th, Pb, Sr, REE), which are useful monitors of subduction processes.

The composition of lawsonite and EGMs is influenced by the composition of the protolith bulk composition as well as the composition of fluids derived from other subducted materials (serpentinites, sediments). Furthermore, lawsonite and EGMs are commonly zoned and occur in a range of textural sites (inclusions, matrix, veins), providing information about processes and conditions during changes in pressure-temperature through time.

In metamorphic rocks, lawsonite and EGMs are typically assumed to contain only Fe^{3+} : *e.g.*, as a major component of epidote and a minor one in lawsonite. However, substantial Fe^{2+} in lawsonite and epidote has been detected by XANES in some blueschists (but not others). Variation in $\text{Fe}^{3+}/\Sigma\text{Fe}$ could be related to protolith composition (*e.g.*, extent of pre-subduction alteration of oceanic crust) and/or interaction with fluids from different sources that affect the oxidation state of oceanic crust during subduction. Fe^{2+} in lawsonite and EGMs in subducted oceanic crust may be greater than is currently known, with implications for phase equilibria calculations and understanding of subduction redox conditions and processes.

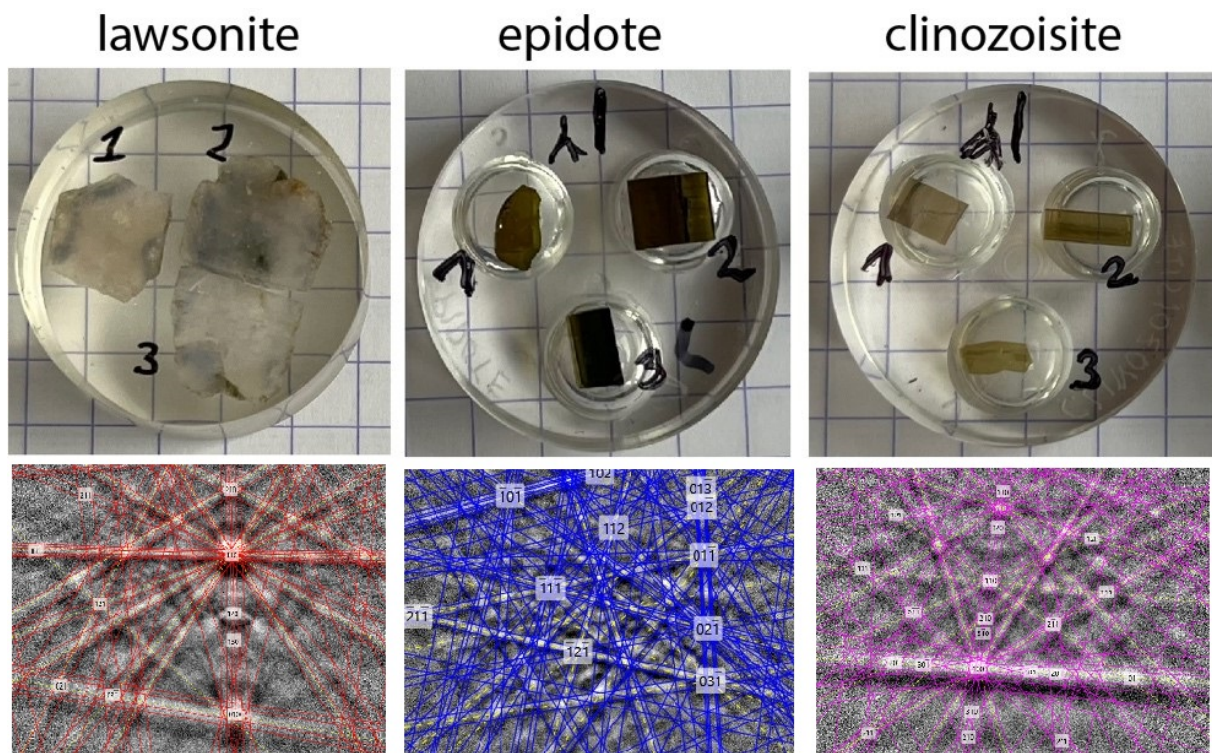


Fig. 3.8-5: Grain mounts of single crystals cut along 3 different planes. The crystallographic orientation of each grain was determined by EBSD (examples for each phase in the lower row). The epidote sample is from the BGI collection.

Lawsonite and EGMs were characterised prior to Fe K-edge μ -XANES synchrotron analysis, including determination of composition and zoning by electron microprobe for major and some minor elements and crystallographic orientation by electron backscattered diffraction. Samples analysed include grain mounts prepared from single crystals cut in distinct orientations (Fig. 3.8-5) as well as thin sections of blueschist and eclogite from two subduction complexes (Fig. 3.8-6).

Preliminary XANES analysis shows a strong orientation effect in epidote-group minerals, making quantitative determination of $\text{Fe}^{3+}/\Sigma\text{Fe}$ difficult. Lawsonite, however, does not appear

to have a strong orientation effect. Ongoing work is investigating the possible causes of variation in $\text{Fe}^{3+}/\Sigma\text{Fe}$ in lawsonite and EGMs, whether Fe^{2+} in these phases is common, and where Fe^{2+} resides in the crystal structure of the phases.

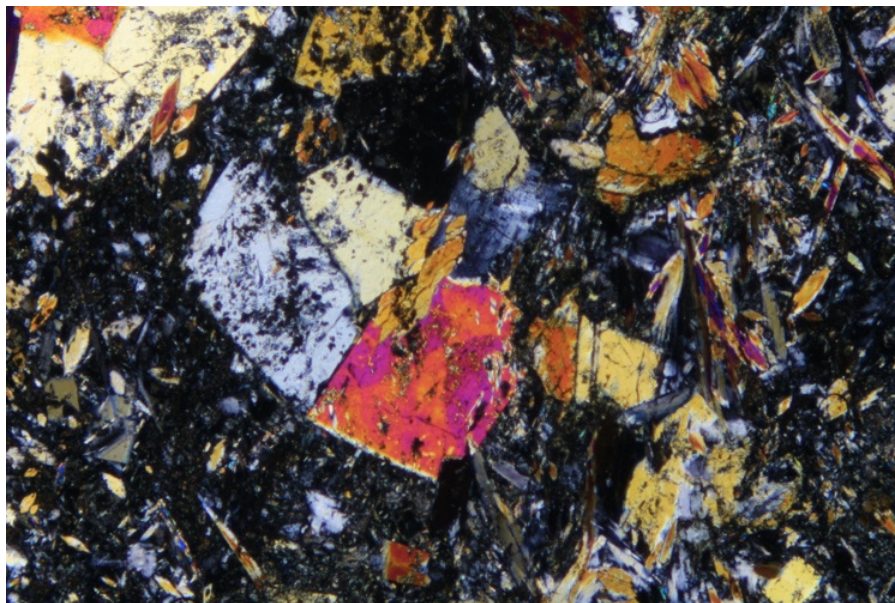


Fig. 3.8-6: Crossed polarised light photomicrograph of lawsonite in blueschist. One of the lawsonite grains displays sector zoning. Field of view ~ 2 mm.

e. Relations between the secondary ion mass spectrometry and elastic recoil detection analyses of hydrogen in various silicate glasses (D. Bondar, A.C. Withers, D. Di Genova, M. Wiedenbeck/Potsdam, H. Bureau/Paris, H. Khodja/Paris-Saclay, F. Couffignal/Potsdam, H. Fei and T. Katsura)

Accurate knowledge of water contents in silicate glasses is crucial for the meaningful interpretation of high-pressure/high-temperature experiments. While most of the available techniques rely on established calibrations, their applicability to novel materials with compositions significantly deviating from calibration standards is limited. This study addresses this challenge by employing elastic recoil detection analyses (ERDA) to directly determine water contents in a set of newly synthesised peridotitic glasses. In addition, we investigated the secondary ion mass spectrometry (SIMS) matrix effect through the analysis of diverse glass sets by SIMS and ERDA, including rhyolitic, basaltic, and peridotitic compositions.

The recent development of the rapid-quench multianvil technique enabled us to synthesise 11 high-pressure peridotitic (KLB-1) glasses with H_2O contents varying from 0 to 5 wt. % at pressure up to 4 GPa for the first time. The synthesised glasses are transparent, optically isotropic, and chemically homogeneous. Raman spectroscopy revealed no long-range atomic ordering.

These peridotitic glasses as well as two sets of rhyolitic and basaltic reference glasses were analysed by SIMS and ERDA. Before the analyses, the glasses and standards were embedded in indium, polished, and coated with a gold layer for SIMS and a 10-nm carbon layer for ERDA. In ERDA samples were analysed by rastering the 2.8 MeV $^4\text{He}^+$ beam over 50×80 to $100 \times 200 \mu\text{m}^2$ areas depending on the available amount of the sample material. Analysis time varied from one hour for relatively water-rich samples to two hours for samples with low water contents. SIMS measurements were performed using 5-10 nA primary Cs^+ beam with an impact energy of 19 keV. Before data acquisition, each spot was pre-sputtered for 90 s using a $35 \times 35 \mu\text{m}$ raster; the total duration of one analysis was approximately 10 minutes.

Figure 3.8-7 shows the relations of the product of the $^{16}\text{O}^1\text{H}/^{30}\text{Si}$ ratio measured using SIMS and SiO_2 content measured using EPMA with the H_2O contents in rhyolitic, basaltic and peridotitic glasses analysed by ERDA. A clear difference in these relations was observed between basaltic, rhyolitic, and peridotitic glasses, namely the quantity $(^{16}\text{O}^1\text{H}/^{30}\text{Si}) \cdot (\text{SiO}_2)$ increases with increasing concentrations of depolymerising species at a given H_2O content.

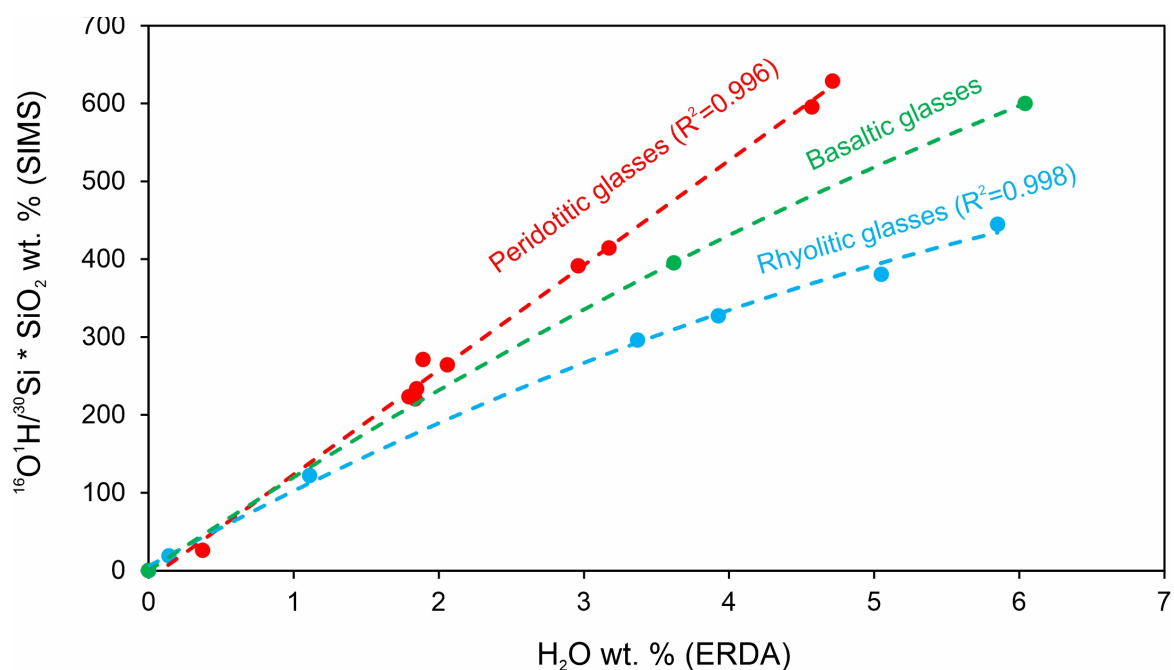


Fig. 3.8-7: ERDA-SIMS relations for rhyolitic, basaltic and peridotitic glasses. Polynomial fitting was used for rhyolitic and basaltic glasses and linear fitting was used for peridotitic glasses. Nominally anhydrous Suprasil glass was used as a blank for all of the calibration lines.

In summary, our study clearly illustrates the pronounced SIMS matrix effect over a broad compositional range, from rhyolitic to peridotitic glasses. This highlights the necessity of employing a set with a composition akin to the analysed materials for precise hydrogen analysis via SIMS. Furthermore, through ERDA analysis, we directly obtained hydrogen concentration

in peridotitic glasses. This enables us to calculate water partitioning coefficients between silicate glasses and mineral phases quenched in high-pressure/-temperature experiments, and also sets the foundation for constructing an ERDA-FTIR calibration, utilising previously gathered FTIR data.

f. Sub-micrometer quantitative high-resolution chemical analysis of Al-bridgmanite and Fe-bearing minerals using low voltage SEM-EDS (C. Timoner and N. Miyajima)

Improvements in the resolution and quality of energy-dispersive X-ray spectroscopy (EDS) chemical analyses are of great importance to developing quantitative analyses of submicrometer-scale samples. The spatial resolution of EDS analyses is fundamentally enhanced by lowering the acceleration voltage. Recent analytical studies show that EDS analyses of 20 nm samples with very low voltages of 5 to 1 kV and Si-drift detectors up to 150 mm² are in the same range of quality as wave-dispersive X-ray spectroscopy (WDS) in electron probe microprobe analyses (EPMA). However, whether this technique is suitable for electron-beam sensitive experimental minerals such as aluminous bridgmanite (Al-Bdm), or accurate enough to quantify oxygen vacancies in iron-bearing samples at low kV is unknown. Here we show the quantitative analysis of Al-Bdm and the Fe L-line peak intensity in Fe-bearing silicate minerals by using 3 to 5 kV and various beam currents with a conventional field-emission (FE) scanning electron microscope (SEM) with a 20 mm² SDD-type EDS detector.

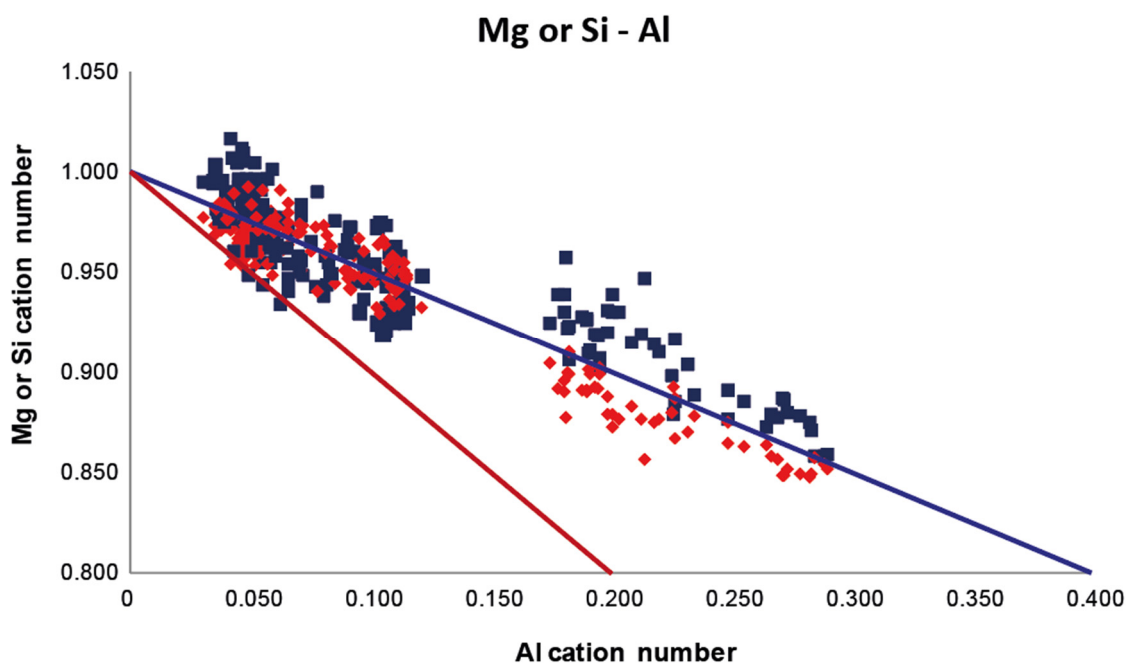


Fig. 3.8-8: Low voltage SEM-EDS analyses of aluminous bridgmanite (Al-Bdm). Si and Mg cation vs Al cation for all the 9 examined samples. Mg = blue; Si = red. The blue line (Al₂O₃) represents the CC stoichiometric substitution for the Si cation number; while the red line (MgAlO_{2.5}) represents the non-stoichiometric OV substitution.

Quantification of Al-substitution oxygen vacancy ($\text{MgAlO}_{2.5}$) and charge-coupled (Al_2O_3) mechanisms in 9 Al-Bdm samples have been carried out using a beam current of 120 pA and with several synthetic and natural standards (Fig. 3.8-8). The spatial resolution obtained is about 400 nm, showing no contamination from nearby phases and precision three times worse than EPMA-WDS (Fig. 3.8-9). Two different electron-beam stable Fe-bearing minerals have been also studied. The quantitative composition of natural orthopyroxene lamellae in clinopyroxene from Moncaup, France was obtained at a resolution of 200 nm using 980 pA-probe current in a line-scan analysis mode. Additionally, a high-pressure Fe-bearing Al-Bdm has been analysed under the same conditions as Moncaup clinopyroxene, giving a spatial resolution of 400 nm with three times better statistics than that of TEM-EDS obtained from the same sample.

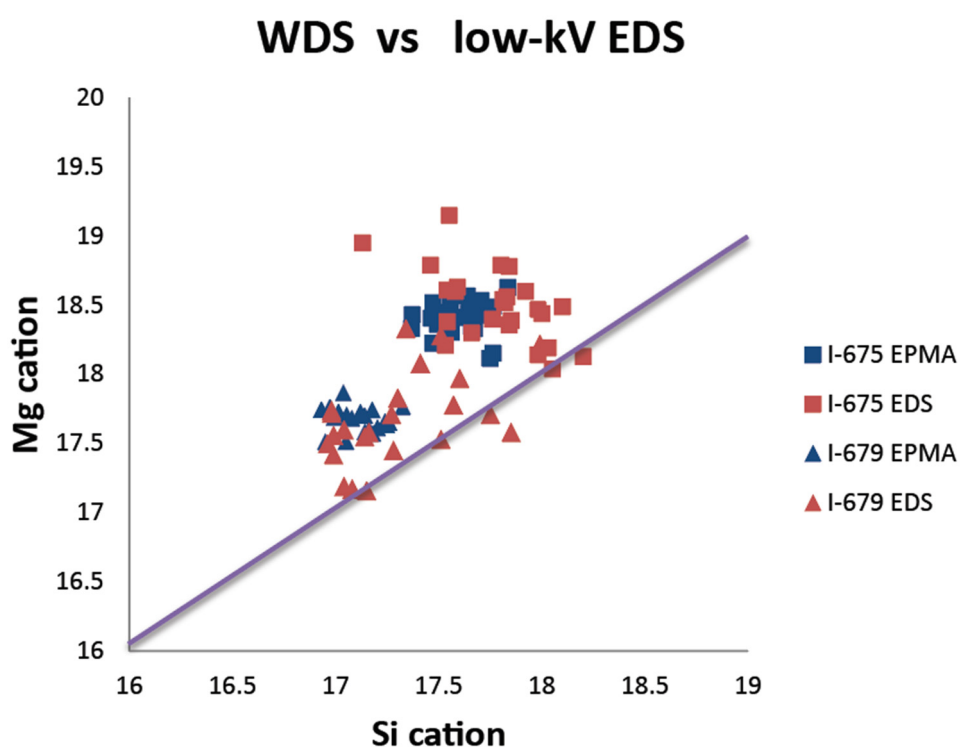


Fig. 3.8-9: Comparison of low-voltage SEM-EDS analyses to EPMA-WDS of Al-Bdm, plotting the Mg cation number vs Si cation number. The data of low-voltage SEM-EDS are more scattered than those of the EPMA-WDS, but the averages of cation ratios of Mg/Si obtained from the different analytical methods are comparable.

The obtained high-resolution analytical results exceed the spatial resolution available on electron microprobes. Further developments of this technique by using better standards and a bigger SDD-type EDS detector could be of great importance to experimental geosciences research, where the small crystal size of high-pressure samples is a critical analytical limitation. Moreover, quantitative EDS analyses at a low voltage in an FE-SEM could become a standard analytical technique for those institutions lacking any electron microprobe equipment with WDS and TEM.

g. *The effect of iron content on the electrical conductivity of Al-bearing bridgmanite (K. Han and T. Katsura)*

Geophysical observations reveal the lateral variation in electrical conductivity in the uppermost lower mantle. Some conductive anomalies could be one order of magnitude higher than the ambient mantle, for example, the uppermost lower mantle beneath western North America. The interpretation of such conductivity profiles could provide a valuable constraint on the composition of the lower mantle.

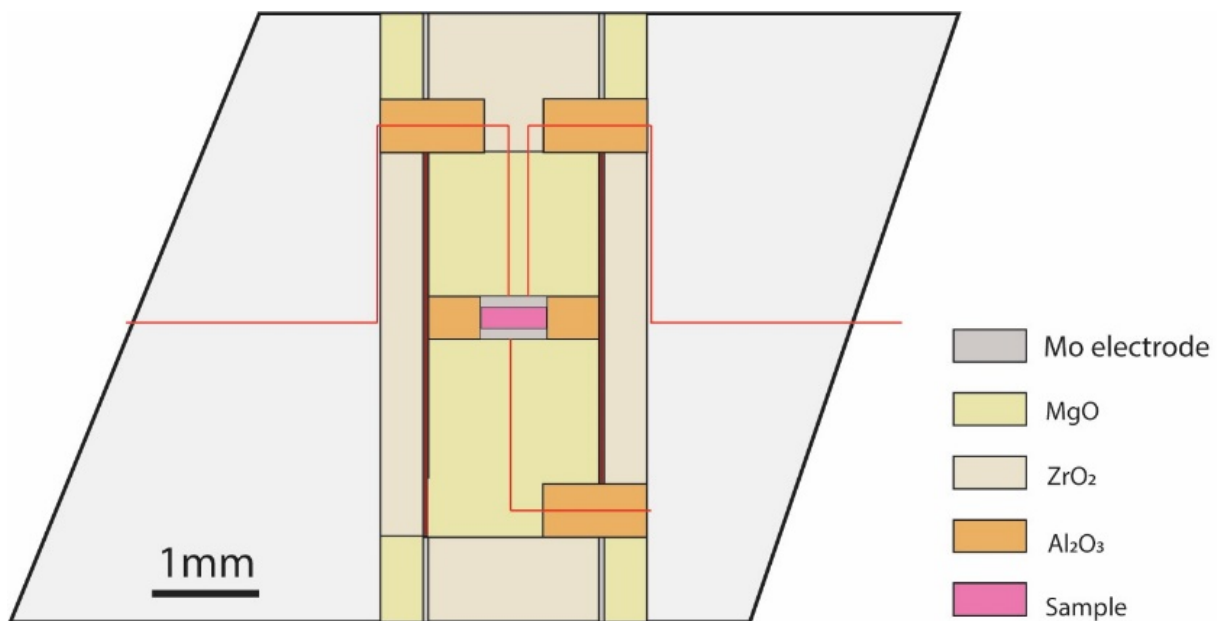


Fig. 3.8-10: Schematic design of a 7/3 assembly for electrical conductivity measurements at 27 GPa in the multianvil press.

Bridgmanite is the most abundant mineral in the lower mantle. The chemical composition of bridgmanite is likely to be heterogeneous due to the subduction of oceanic plates as well as plumes originating from the core-mantle boundary. In pyrolitic mantle composition, the bridgmanite generally contains 10 wt. % of FeO/Fe₂O₃ at the uppermost lower mantle, while in basaltic composition, the total iron content could be as high as 25 wt. %. However, the correlation between iron content and electrical conductivity remains poorly understood. In this study, we prepared bridgmanite with various iron contents in high-pressure/high-temperature experiments. The electrical conductivity of these samples will be measured at 27 GPa and varying temperatures, using the Solartron 1260 Impedance Analyser and a specially developed high-pressure assembly for the the multianvil press (Fig. 3.8-10). The voltage amplitude will be 0.5V with a frequency range from 0.1 to 1 MHz. The results will be interpreted with respect to the distribution of the iron content in the uppermost lower mantle.

h. Thermal gradient measurements in box furnace 25/15 assemblies designed for high-temperature experiments (E. Kubik, A. Néri/Lille and R. Hin/Milan)

Box furnace multianvil assemblies (Fig. 3.8-11a) can present a number of advantages compared to the standard assemblies for certain experimental applications. In the context of experimental metal–silicate isotopic fractionation studies aiming to reproduce the chemical equilibrium occurring during core formation in terrestrial planets (see also contributions 3.2 c, d, and f), we find that box furnace assemblies allow a significant broadening of the possible experimental conditions. First, the efficient thermal insulation due to the use of LaCrO_3 heaters enhances significantly the heating efficiency, thus expanding the maximum temperature generation under stable heating conditions. Using the 25/15 configuration on the 5000-ton press at 9-11 GPa, we were able to reach superliquidus conditions for both MORB and Fe alloy (ca. 2400 K), a feature that remained impossible when using standard assemblies equipped with a LaCrO_3 furnace. Second, the sample volume in this assembly design was increased to contain capsules of 5 mm in diameter and 6 mm in height. This corresponds to a 235 % sample volume increase compared to the standard assembly. Such voluminous samples are useful in a wide range of applications, including isotopic fractionation experiments where several milligrams of crushed run products are necessary to measure isotopic ratios with a multi-collector inductively-coupled plasma mass spectrometer. Third, similarly designed assemblies were reported to produce limited thermal gradients at 4 GPa and 1773 K, estimated to < 2.4 °C/mm.

In the context of our applications where sensitive isotopic tracers are used to study equilibration processes, minimising thermal gradients during the experiments is critical. Although thermal gradients were previously estimated for a 25/15 box furnace assembly hosting a smaller sample, these estimates were produced at lower P,T conditions than those of our experiments (8-11 GPa, 2100-2500 K). We conducted an experiment at 8 GPa and 2473 K to measure thermal gradients using the spinel layer growth kinetics technique. A pile of 7 interposed discs of crushable MgO and Al_2O_3 were loaded in a crushable MgO capsule and directly inserted into the LaCrO_3 furnace. The experiment was left for 30 minutes at the target temperature of 2473 K to induce sufficient spinel growth, and the temperature was measured with a D-type thermocouple inserted vertically in the assembly directly above the experimental capsule, offset from the central axis where the upper molybdenum electrode is located.

The spinel layers that grew at the interface of MgO and Al_2O_3 were observed and measured using the scanning electron microscope (Fig. 3.8-8b-e). The thickness of the spinel layer was 120 μm in the centre of the experiment, 130 μm in the corners and 137 μm in the bottom centre, close to the electrode. These thicknesses can be translated into 2504, 2525 and 2538 K respectively using the empirical relationship of spinel layer growth kinetics, indicating a maximum thermal gradient of 17 degrees/mm. The reported gradients are slightly lower but of the same order of magnitude than gradients measured in standard assemblies. To conclude, these assemblies present the following advantages: (1) enhanced experimental temperature range, (2) sample volume increased by 235 % with respect to the standard assembly, (3) high-pressure application when combined with the 5000-ton multianvil press and (4) limited

temperature gradients with stable heating for significant time durations at very high temperature.

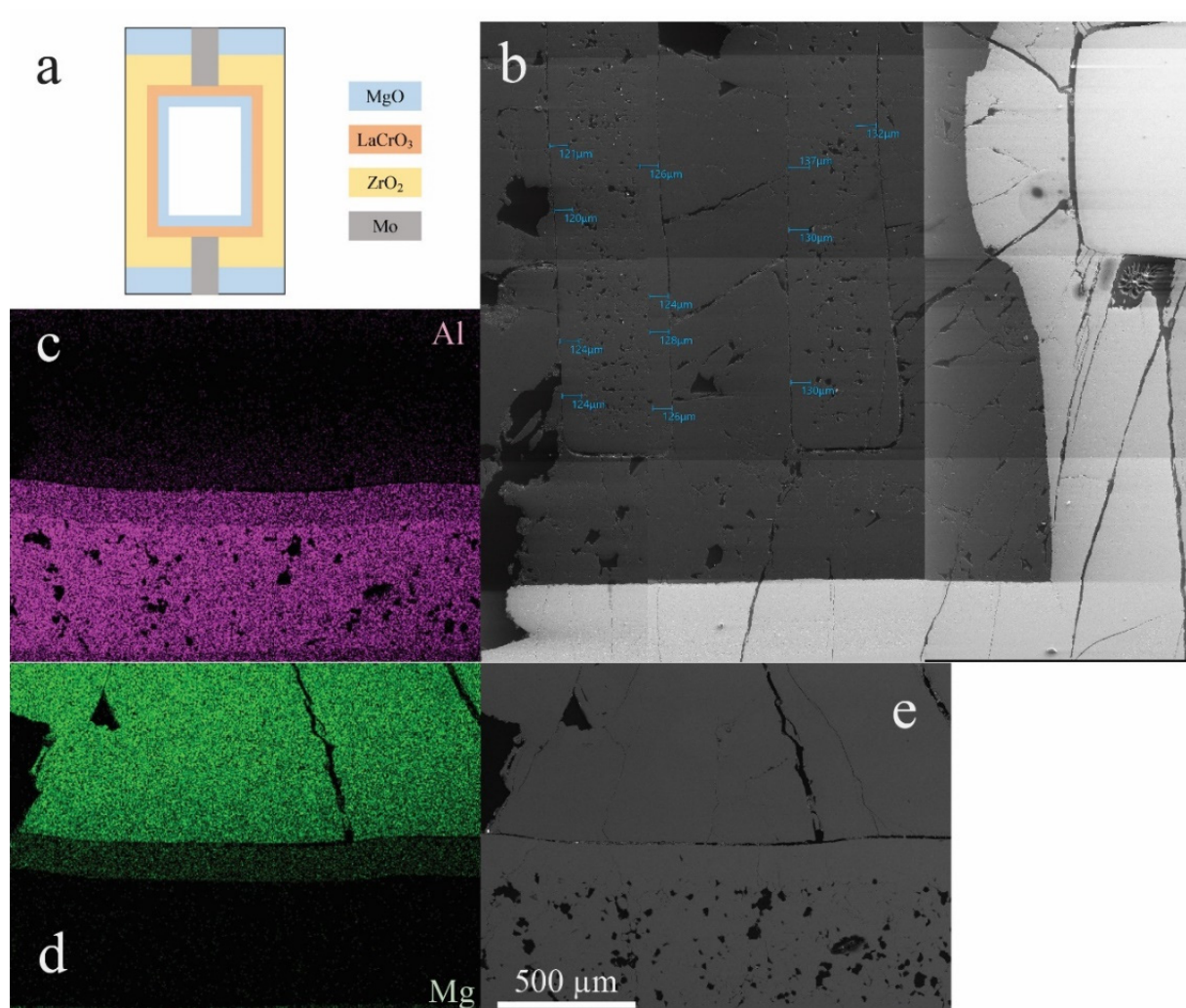


Fig. 3.8-11: Thermal gradient measurements in box furnace assemblies. (a) Schematics of the 25/15 multianvil box furnace design. (b) Back-scattered electron map of a quarter of the polished experiment presenting two disks of Al₂O₃ interspersed with MgO in which spinel layer growth has been measured. The surrounding LaCrO₃ heater is visible as well as the Mo electrode to the right. (c & d) Elemental EDX maps for Al (pink) and Mg (green), respectively. The growth of spinel in the Al₂O₃ disk can be observed. (e) Corresponding back-scattered electron image.

i. *In situ stress measurement of San Carlos olivine at high pressure and temperature using two methods (J.D. Dolinschi, L. Man, A. Chakraborti, L. Wang, R. Farla/Hamburg and D.J. Frost)*

The study of the Earth's interior, particularly the upper mantle and asthenosphere, is pivotal in advancing our understanding of global geodynamics. These deep Earth layers, characterised by

extreme conditions, are the driving forces behind plate tectonics, mantle convection, and associated seismic activities. Measuring *in situ* stresses in these regions is not only critical for assessing the strength and rheological behaviour of materials but also for understanding how these properties influence broader geophysical phenomena such as mantle flow and earthquake genesis. Our research this year has been intensively focused on refining and applying methodologies to accurately simulate and measure the conditions within these deep Earth layers. We have made significant progress in developing a direct method for measuring *in situ* stresses, a technique that has the potential to revolutionize our understanding of the dynamics at play within the Earth's mantle and asthenosphere.

The cornerstone of our approach is an advanced assembly centred around a piezoelectric crystal. This crystal, upon being subjected to mechanical stress, is capable of generating a precise electrical signal, which directly correlates to the magnitude of the stress applied. The latest improvements to our assembly, including the transition to a higher-performance CTGS crystal and the incorporation of a diamond disk for effective heat dissipation, have substantially enhanced its capability to function under the extreme pressures and temperatures that epitomize the upper mantle and asthenosphere. This year's experiments at the Petra III synchrotron have been a significant milestone. We achieved successful *in situ* stress measurements on San Carlos olivine at high temperatures, up to 1200 °C, markedly advancing beyond our previous experiments conducted at room temperature (Fig. 3.8-12). A key achievement in these experiments was the ability to measure stresses in both compression and tension modes

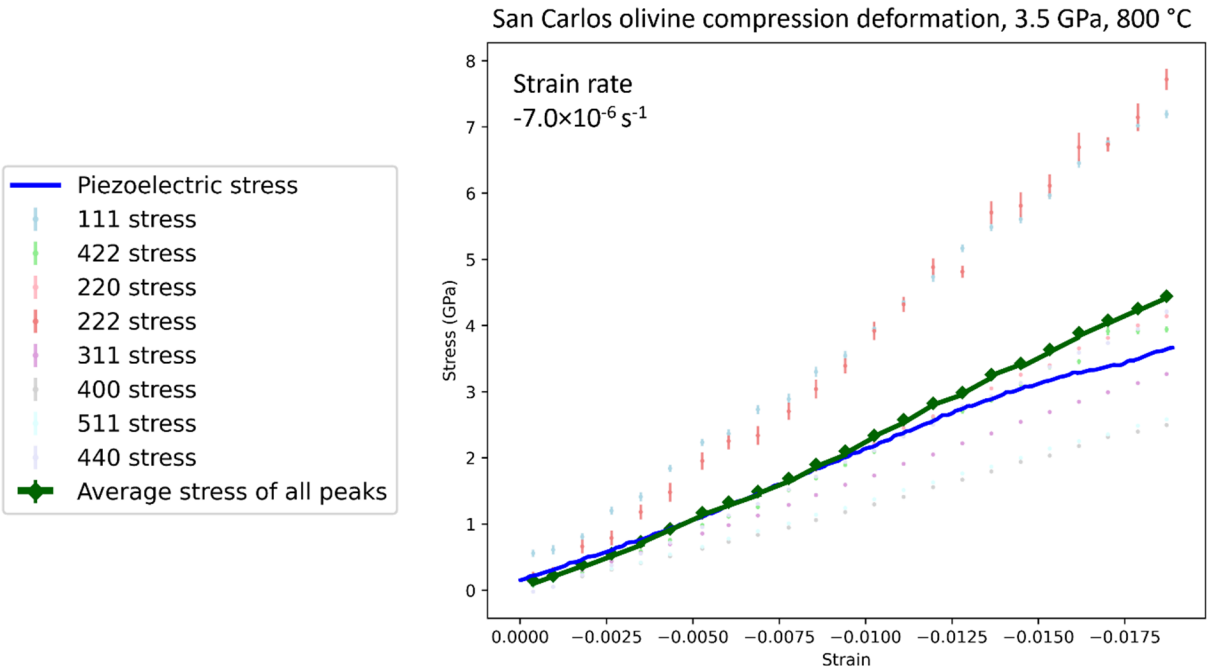


Fig. 3.8-12: Polycrystalline San Carlos olivine sample deformed in compression at the Petra III DESY synchrotron, beamline P61B. The stress, as measured by X-ray diffraction, for each peak fitted is shown separately, and then the final averaged stress from all of them is plotted in green. The stress measured by the piezoelectric crystal is overlain in blue.

accurately. This dual-mode measurement capability is crucial for a comprehensive understanding of the stress responses and strength of geological materials under the multifaceted conditions present within the Earth's upper mantle and asthenosphere.

In a parallel vein, our off-beam experiments conducted at BGI on single crystal forsterite, with a precise orientation of the [100] axis parallel to the deformation, have provided valuable additional insights. These experiments were meticulously designed and executed at various pressures, ranging from 1.5 to 3 GPa, and across a spectrum of temperatures, from 600 °C to 1300 °C. The primary goal was to explore in depth the temperature-dependent stress behaviours and mechanisms in mantle materials. By applying a controlled strain rate of 2.5×10^{-5} per second and reaching strains up to 0.10, we were able to observe distinct stress weakening effects associated with temperature variations (Fig. 3.8-13).

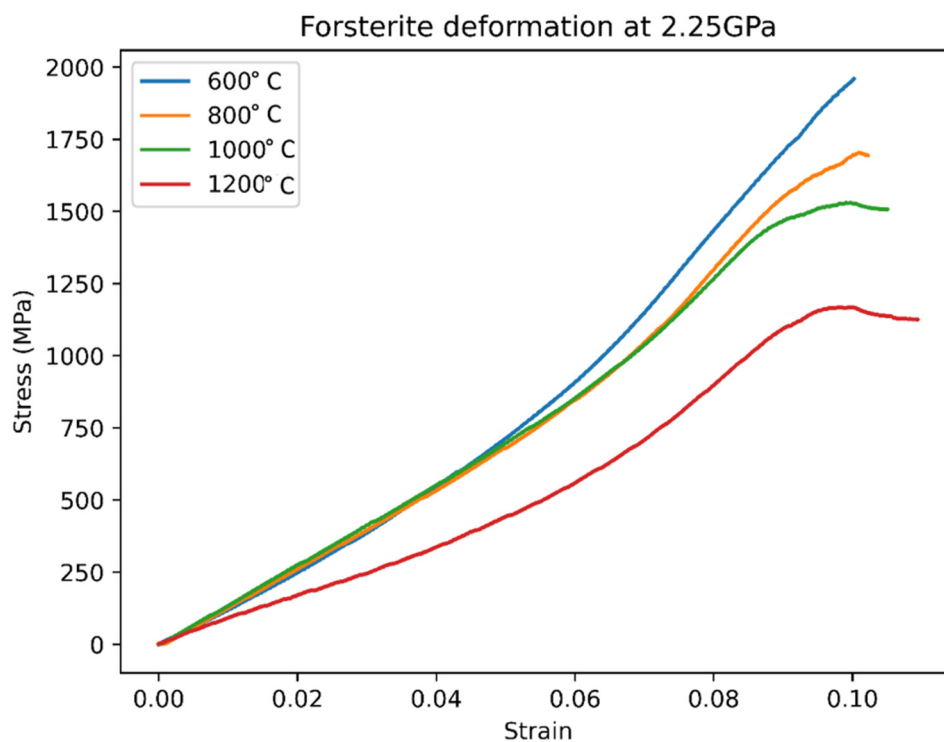


Fig. 3.8-13: Stress-strain plot of single crystal forsterite deformation experiments at 2.25 GPa and different temperatures conducted at BGI. The strength of the crystals decreases with increasing temperature reaching the yield point between 800 and 1000 °C at a strain of close to 0.1. Stresses were determined with the piezo-crystal technique.

Importantly, the experiments demonstrated our ability to measure stress effectively in both compression and tension modes, offering a more nuanced view of the behaviour of minerals under the complex conditions prevalent in the upper mantle and asthenosphere. The combination of synchrotron X-ray diffraction and piezoelectric stress measurement techniques in these experiments has been instrumental in capturing these dual-mode stress responses. The

insights gained from this research are invaluable, contributing significantly to our understanding of the geophysical processes and dynamics governing the Earth's interior, and highlighting the intricate interplay of temperature, pressure, and stress in these deep Earth regions.

j. *Setup and start of commissioning of the SAPHiR helium-3 detector system at FRM II (A. Howard, K. Zeitelhack and N. Walte/Garching and H. Keppler)*

SAPHiR is an instrument for neutron diffraction and radiography under extreme pressure and temperature conditions under construction at the MLZ neutron source in Garching (see previous annual reports). A pulsed, polychromatic neutron beam will be focused onto the sample position at the centre of the press using supermirror guides. A schematic diagram of the instrument is in Figure 3.8-14.

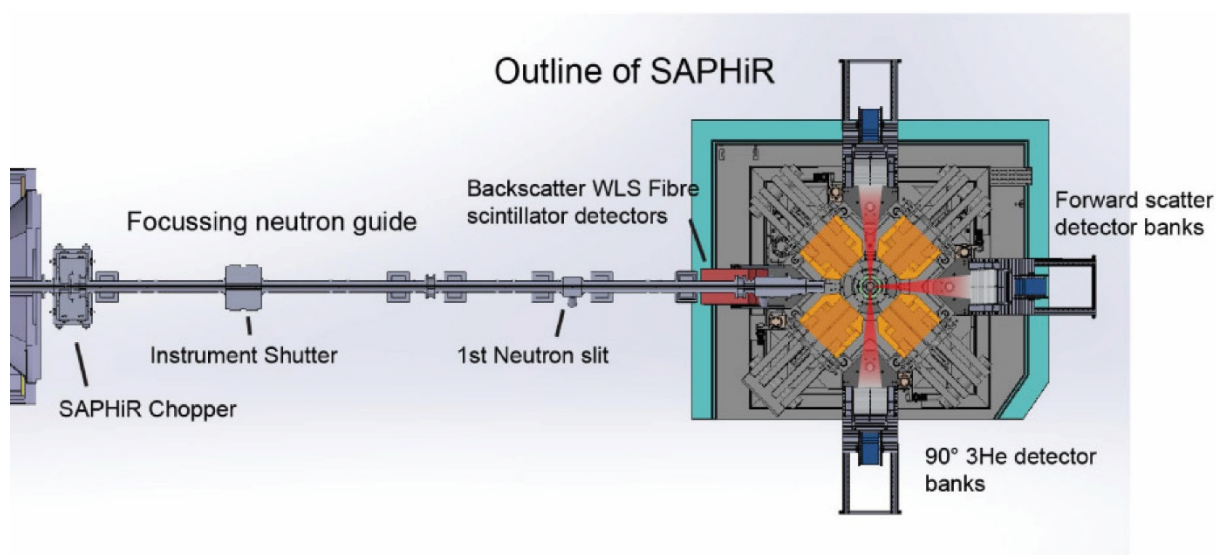


Fig. 3.8-14: Schematic diagram of the instrument SAPHiR at MLZ. The neutron beam has a time structure imprinted by the chopper and is focused onto the sample position at the press centre. The opening angle for outgoing neutrons scattered from the sample is shaded red. The outgoing neutrons are detected in arrays of position-sensitive ^3He detectors located perpendicular to the beam and in the forward scattering geometry.

Since the neutrons can only enter and exit the sample through the four vertical anvil gaps, the time-of-flight methodology is used for neutron diffraction, and large area detectors cover the solid angles where diffracted neutrons can exit the anvils. For the three detector banks perpendicular to the primary beam and in the forward scattering range (Fig. 3.8-14), a total of 648 position-sensitive ^3He detector tubes (PSD) are arranged along an arc with a radius of 1500 mm and the sample position at its centre.

While the individual elements of the detector system were produced by the FRM II detector group several years ago, only recently building progress in the new Eastern Guide Hall of the MLZ allowed the final installation at the instrument to take place. The mechanical mounting of the tubes on aluminium frames (see Fig. 3.8-15) ensures that they define precisely the desired arc around the sample position. A rail system provides freedom of movement for the detector banks in the radial direction and a series of precision screws at the base of the mechanics permits adjustments in all other directions. A laser level and range finder were used to fix the banks at the correct position and orientation relative to the sample position, defined as the geometric centre of the six anvils, to sub-mm precision.

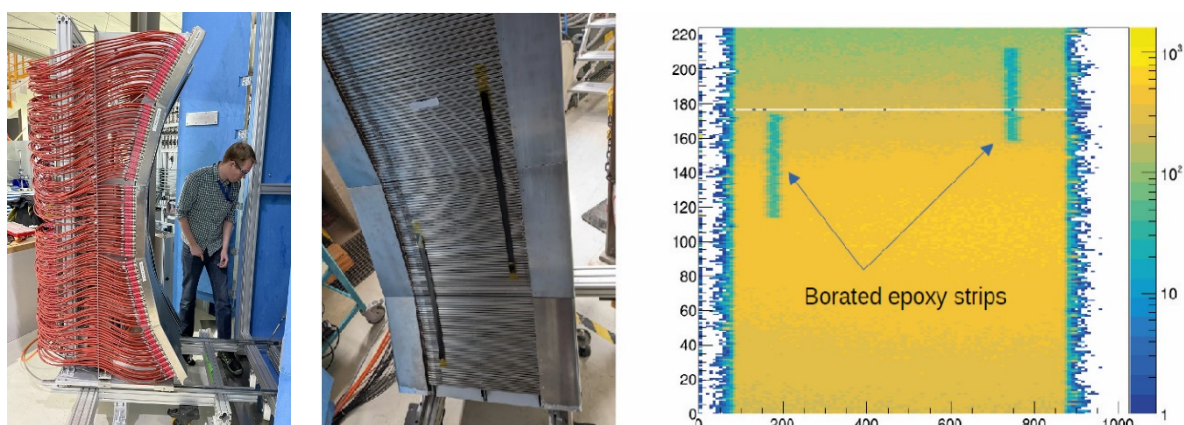


Fig. 3.8-15: (left) Assembled detector bank before installation into the SAPHiR press. The 224 detector tubes define an arc of radius 1500 mm around the sample. (centre) Front view of the detector bank with neutron absorbing borated epoxy strips (black) affixed to the surface as test masks. (right) Test measurement of the detectors with a ^{252}Cf source. Shown is the 2D position spectrum of detected neutrons (x-axis position resolution in mm, y-axis No. of PSD, each with a width of 8 mm). Note that both axes are mirrored. The fuzzy outline of the epoxy strips results from slight misalignments of the active length of the individual PSDs, which will be electronically corrected for in a later step. The white stripe in the top half results from a defective detector that has been replaced.

The detector tubes each have an active length of 400 mm, a diameter of 8 mm and are filled with 20 bars of ^3He gas. This gas filling is ionized by the $^3\text{He}(n,p)^3\text{H}$ reaction with the incoming neutrons. The efficiency of the detector is primarily governed by the probability of neutron capture and depends on both ^3He fill pressure and neutron wavelength. For the SAPHiR tubes, the efficiency varies between approximately 50 % at 1 Å and 70 % at 2.4 Å. A resistive anode wire (3 kΩ total resistance) is suspended along the central axis of each tube and held at high voltage (~ 1800 V). Both ends of the anode are connected to charge sensitive preamplifiers and the ratio of the two signal amplitudes gives the location along the tube at which the neutron was detected. A resolution of 3-mm has been confirmed in earlier test measurements using a slit screen.

Preliminary commissioning tests of the detectors plus associated electronics in their final configuration have now been carried out using a portable, polyethylene-moderated ^{252}Cf fission source. Due to the physical dimensions of the source (a cylinder of roughly 30 cm diameter), it cannot be placed at the sample position and hence only a single detector bank can be illuminated at once. The flux over the bank is non-homogeneous, due to both the source dimensions and placement inside of the sample radius, but provides a slowly varying flux over the entire bank with a measured rate of ~ 0.1 Hz per tube.

Figure 3.8-15 shows the 2D hit pattern from one of the 90° banks, obtained with borated epoxy masks to illustrate the position sensitivity. The resistive anode wires are suspended using springs and, due to the manufacturing process, the end points can be shifted by several mm between adjacent tubes. Combined with variations between the individual channels of the readout electronics, an independent position calibration of each tube is required. Without a calibration, a fuzzy outline as seen in the shadow of the masking strips in Figure 3.8-15 is produced. The installation of the two 90° banks is now complete and the forward bank is in the process of being cabled. A full commissioning of all three banks will take place in early 2024 with a view to being ready for the provision of first neutrons in the Guide Hall East, expected in the second half of 2024.

4. Publications, Conference Presentations, Seminars

4.1 Publications (published)

Supplement to **2022** (papers published at the end of 2022):

LANGHAMMER, D.; DI GENOVA G.; STEINLE-NEUMANN, G. (2022): Modelling viscosity of volcanic melts with artificial neural networks. *Geochem. Geophys. Geosyst.* 23, e2022GC010673, <https://doi.org/10.1029/2022GC010673>

ORIOLO, S.; SCHULZ, B.; HUECK, M.; OYHANTÇABAL, P.; HEIDELBACH, F.; SOSA, G.; VAN DEN KERKHOF, A.; WEMMER, K.; FOSSEN, H.; DRUGUET, E.; WALTER, J.; SIEGESMUND, S. (2022): The petrologic and petrochronologic record of progressive vs polyphase deformation: Opening the analytical toolbox. *Earth Science Reviews* 234, 104235, <https://doi.org/10.1016/j.earscirev.2022.104235>

2023

a) Refereed international journals

ABEYKOON, S.; HOWARD, C.; DOMINIJANNI, S.; EBERHARD, L.; KURNOSOV, A.; FROST, D.J.; BOFFA BALLARAN, T.; TERASAKI, H.; SAKAMAKI, T.; SUZUKI, A.; OHTANI, E.; SANO-FURUKAWA, A.; ABE, J. (2023): Deuterium content and site occupancy in iron sulfide at high pressure and temperature determined using *in situ* neutron diffraction measurements. *J. Geophys. Res. Solid Earth* 128 (9), e2023JB026710, <https://doi.org/10.1029/2023JB026710>

ABEYKOON, S.; LAURENZ, V.; FROST, D.J.; MIYAJIMA, N.; MCCAMMON, C. (2023): An experimental investigation of factors controlling the oxygen content of sulphide melts in the Earth's upper mantle. *Contrib. Mineral. Petrol.* 178 (2), 13, <https://doi.org/10.1007/s00410-023-01992-3>

AKBAR, F.Ia.; ASLANDUKOVA, A.; ASLANDUKOV, A.; YIN, Y.; TRYBEL, F.; KHANDARKHAEVA, S.; FEDOTENKO, T.; LANIEL, D.; BYKOV, M.; BYKOVA, E.; DUBROVINSKAIA, N.; DUBROVINSKY, L. (2023): High-pressure synthesis of dysprosium carbides. *Front. Chem.* 11, 1-9, <https://doi.org/10.3389/fchem.2023.1210081>

ASLANDUKOV, A.; JURZICK, P.L.; BYKOV, M.; ASLANDUKOVA, A.; CHANY SHEV, A.; LANIEL, D.; YIN, Y.; AKBAR, F.I.; KHANDARKHAEVA, S.; FEDOTENKO, T.; GLAZYRIN, K.; CHARITON, S.; PRAKAPENKA, V.; WILHELM, F.; ROGALEV, A.; COMBONI, D.; HANFLAND, M.; DUBROVINSKAIA, N.; DUBROVINSKY, L. (2023): Stabilization of the CN_3^{5-} anion in recoverable high-pressure $Ln_3O_2(CN_3)$ ($Ln = La, Eu, Gd, Tb, Ho, Yb$) oxoguanidates. *Angew. Chem. Int. Ed.* 62 (47), e202311516, <https://doi.org/10.1002/anie.202311516>

- ASLANDUKOVA, A.; ASLANDUKOV, A.; LANIEL, D.; KHANDARKHAEVA, S.; STEINLE-NEUMANN, G.; FEDOTENKO, T.; OVSYANNIKOV, S.V.; YIN, Y.; AKBAR, F.Ia.; GLAZYRIN, K.; HANFLAND, M.; DUBROVINSKY, L.; DUBROVINSKAIA, N. (2023): High-pressure *hP3* yttrium allotrope with CaHg₂-type structure as a prototype of the *hP3* rare-earth hydride series. *Phys. Rev. B*, 107 (1), 014103, <https://doi.org/10.1103/PhysRevB.107.014103>
- AUDÉTAT, A. (2023): A plea for more skepticism towards fluid inclusions: part II. Homogenization via halite dissolution in brine inclusions from magmatic-hydrothermal systems is commonly the result of postentrapment modifications. *Econ. Geol.* 118 (1), 43-55, <https://doi.org/10.5382/econgeo.4974>
- AUDÉTAT, A.; SCHMITT, A.; NJUL, R.; HARRIS, M.; BORISOVA, A.; LU, Y. (2023): New constraints on Ti diffusion in quartz and the priming of silicic volcanic eruptions. *Nat. Commun.* 14, 4277, <https://doi.org/10.1038/s41467-023-39912-5>
- BALLANTYNE, H.A.; JUTZI, M.; GOLABEK, G.J.; MISHRA, L.; CHENG, K.W.; ROZEL, A.; TACKLEY, P.J. (2023): Investigating the feasibility of an impact-induced Martian Dichotomy. *Icarus* 392, 115395, <https://doi.org/10.1016/j.icarus.2022.115395>
- BONDAR, D.; WITHERS, A.C.; WHITTINGTON, A.; FEI, H.; KATSURA, T. (2023): Dissolution mechanisms of water in depolymerized silicate (peridotitic) glasses based on infrared spectroscopy. *Geochim. Cosmochim. Acta* 342, 45-61, <https://doi.org/10.1016/j.gca.2022.11.029>
- BRAUN, P.M.; GREEN, R.J.; DUBROVINSKY, L.; OVSYANNIKOV, S.V.; MOEWES, A. (2023): The electronic structure of novel high-pressure and high-temperature phases of Mn₂O₃: Exploring perovskite and ilmenite-type structures. *J. Mater. Chem. C*, 11, 10864-10871, <https://doi.org/10.1039/D3TC00995E>
- CHAKRABORTI, A.; CHO, Y.; SJAKSTE, J.; BAPTISTE, B.; HENRY, L.; GUIGNOT, N.; LE GODEC, Y.; VAST, N. (2023): When carbon impurities trigger the synthesis of alpha boron at high pressure and high temperature. *Acta Materialia* 249, 118820, <https://doi.org/10.1016/j.actamat.2023.118820>
- CHANG, J.; AUDÉTAT, A. (2023): Experimental equilibrium and fractional crystallization of a H₂O, CO₂, Cl and S-bearing potassic mafic magma at 1.0 GPa, with implications for the origin of porphyry Cu (Au, Mo)-forming potassic magmas. *J. Petrol.* 64, 1-24, <https://doi.org/10.1093/petrology/egad034>
- CHANY SHEV, A.; FEI, H.; BONDAR, D.; WANG, B.; LIU, Z.; ISHII, T.; FARLA, R.; MCCAMMON, C.; KATSURA, T. (2023): Ferric iron substitution mechanism in bridgmanite under SiO₂-saturated conditions at 27 GPa. *ACS Earth Space Chem.* 7 (2) 471-478, <https://doi.org/10.1021/acsearthspacechem.2c00326>
- CRINITI, G.; ISHII, T.; KURNOSOV, A.; GLAZYRIN, K.; BOFFA BALLARAN, T. (2023): High-pressure phase transition and equation of state of hydrous Al-bearing silica. *Am. Mineral.* 108 (8), 1558-1568, <https://doi.org/10.2138/am-2022-8546>
- CRINITI, G.; ISHII, T.; KURNOSOV, A.; GLAZYRIN, K.; HUSBAND, R.J.; BOFFA BALLARAN, T. (2023): Structure and compressibility of Fe-bearing Al-phase D. *Am. Mineral.* 108 (9), 1764-1772, <https://doi.org/10.2138/am-2022-8559>

- CZAJA, A. D.; ZORZANO, M.-P.; KMINEK, G.; MEYER, M.A.; BEATY, D.W.; SEFTON-NASH, E.; CARRIER, B.L.; THIESSEN, F.; HALTIGIN, T.; BOUVIER, A.; *et al.* (MSR Campaign Science Group) (2023): Report of the science community workshop on the proposed first sample depot for the Mars sample return campaign. *Meteorit. Planet. Sci.* 58 (6), 885-896, <https://doi.org/10.1111/maps.13981>
- DALE, K.I.; RUBIE, D.C.; NAKAJIMA, M.; JACOBSON, S.; NATHAN, G.; GOLABEK, G.J.; CAMBIONI, S.; MORBIDELLI, A. (2023): An improved model of metal/silicate differentiation during Earth's accretion. *Icarus* 406, 115739, <https://doi.org/10.1016/j.icarus.2023.115739>
- DI GENOVA, D.; BONDAR, D.; ZANDONÀ, A.; VALDIVIA, P.; AL-MUKADAM, R.; FEI, H.; WITHERS, A.C.; BOFFA BALLARAN, T.; KURNOSOV, A.; MCCAMMON, C.; DEUBENER, J.; KATSURA, T. (2023): Viscosity of anhydrous and hydrous peridotite melts. *Chem. Geol.* 625, 121440, <https://doi.org/10.1016/j.chemgeo.2023.121440>
- EBERHARD, L.; FROST, D.J.; MCCAMMON, C.; DOLEJŠ, D.; CONNOLLY, J.A.D. (2023): Experimental constraints on the ferric Fe content and oxygen fugacity in subducted serpentinites. *J. Petrol.* 64 (10), 1-18, <https://doi.org/10.1093/petrology/egad069>
- EBERHARD, L.; PLÜMPER, O.; FROST, D.J. (2023): Early release of H₂O during subduction of carbonated ultramafic lithologies. *Contrib. Mineral. Petrol.* 178, 17, <https://doi.org/10.1007/s00410-023-01997-y>
- FACCINCANI, L.; CRINITI, G.; KURNOSOV, A.; BOFFA BALLARAN, T.; WITHERS, A.C.; MAZZUCHELLI, M.; NESTOLA, F.; COLTORTI, M. (2023): Sound velocities and single-crystal elasticity of hydrous Fo₉₀ olivine to 12 GPa. *Phys. Earth Planet. Inter.* 337, 107011, <https://doi.org/10.1016/j.pepi.2023.107011>
- FEI, H.; BALLMER, M.D.; FAUL, U.; WALTE, N.; CAO, W.; KATSURA, T. (2023): Variation in bridgmanite grain size accounts for the mid-mantle viscosity jump. *Nature* 620, 794-799, <https://doi.org/10.1038/s41586-023-06215-0>
- FUJIYA, W.; *et al.* with the Hayabusa2 Initial Analysis Chemistry Team (including BOUVIER, A.) (2023): Carbonate record of the change in oxygen fugacity and gaseous species in asteroid Ryugu. *Nat. Geosci.* 16, 675-682, <https://doi.org/10.1038/s41561-023-01226-y>
- GLAZYRIN, K.; ASLANDUKOV, A.; ASLANDUKOVA, A.; FEDOTENKO, T.; KHANDARKHAEVA, S.; LANIEL, D.; BYKOV, M.; DUBROVINSKY, L. (2023): High-pressure reactions between the pnictogens: the rediscovery of BiN. *Front. Chem.* 11, 1257942, <https://doi.org/10.3389/fchem.2023.1257942>
- GORELOVA, L.; KHANDARKHAEVA, S.; YUKHNO, V.; KRZHIZHANOVSKAYA, M.; VERESHCHAGIN, O.; DUBROVINSKY, L.S. (2023): Topologically prone or cation compression restricted phase transition: An example of feldspar-related SrGe₂B₂O₈. *J. Alloys Compd.* 938, 168642, <https://doi.org/10.1016/j.jallcom.2022.168642>
- GORELOVA, L.; VERESHCHAGIN, O.; ASLANDUKOV, A.; ASLANDUKOVA, A.; SPIRIDONOVA, D.; KRZHIZHANOVSKAYA, M.; KASATKIN, A.; DUBROVINSKY, L. (2023): Hydroxylherderite (Ca₂Be₂P₂O₈(OH)₂) stability under extreme conditions (up to 750 °C/100 GPa). *J. Am. Ceram. Soc.* 106, 2622-2634, <https://doi.org/10.1111/jace.18923>

- GREER, J.; ZHANG, B.; ISHEIM, D.; SEIDMAN, D.N.; BOUVIER, A.; HECK, P.R. (2023): 4.46 Ga zircons anchor chronology of lunar magma ocean. *Geochem. Persp. Lett.* 27, 49-53, <https://doi.org/10.7185/geochemlet.2334>
- HOUDE, V.; FLEMMING, R.L.; BOUVIER, A.; TERSKIKH, V. (2023): Cation ordering in spinel from calcium-aluminium-rich inclusions in carbonaceous chondrites NWA 2364 and NWA 6991 to quantify temperature in the Early Solar System. *The Canadian Journal of Mineralogy and Petrology* 61, 749-766, <https://doi.org/10.3749/2200051>
- HUANG, R.; BOFFA BALLARAN, T.; MCCAMMON, C.A.; FROST, D.J. (2023): The composition and redox state of hydrous partial melts generated at the top of the lower mantle. *Earth Planet. Sci. Lett.* 624, 118447, <https://doi.org/10.1016/j.epsl.2023.118447>
- IKEDA, O.; SAKAMAKI, T.; MITSUI, T.; FUJIWARA, K.; MCCAMMON, C.A.; SUZUKI, A. (2023): Magnetic spin-flop transition of ϵ -FeOOH at 8 GPa. *J. Phys. Soc. Jpn.* 92 (4), 043702, <https://doi.org/10.7566/JPSJ.92.043702>
- ISHII, T.; CRINITI, G.; WANG, X.; GLAZYRIN, K.; BOFFA BALLARAN, T. (2023): Synthesis and structural analysis of CaFe_2O_4 -type single crystals in the NaAlSiO_4 - MgAl_2O_4 - Fe_3O_4 system. *Am. Mineral.* 108 (1), 217-221, <https://doi.org/10.2138/am-2022-8748>
- ISHII, T.; MCCAMMON, C.; KATSURA, T. (2023): Iron and aluminum substitution mechanism in perovskite phase in the system MgSiO_3 - FeAlO_3 - MgO . *Am. Mineral.* 108 (4), 738-743, <https://doi.org/10.2138/am-2022-8457>
- ISHII, T.; FROST, D.J. KIM, E.J.; CHANY SHEV, A.; NISHIDA, K.; WANG, B.; BAN, R.; XU, J.; LIU, J.; SU, X.; HIGO, Y.; TANGE, Y.; MAO, H.-K.; KATSURA, T. (2023): Buoyancy of slabs and plumes enhanced by curved post-garnet phase boundary. *Nat. Geosci.* 16, 828-832, <https://doi.org/10.1038/s41561-023-01244-w>
- KISLYAKOVA, K.G.; NOACK, L.; SANCHIS, E.; FOSSATI, L.; VALYAVIN, G.G.; GOLABEK, G.J.; GÜDEL, M. (2023): Induction heating of planetary interiors in white dwarf systems. *Astron. Astrophys.* 677, A109, <https://doi.org/10.1051/0004-6361/202245225>
- KISS, D.; MOULAS, E.; KAUS, B.J.; SPANG, A. (2023): Decompression and fracturing caused by magmatically induced thermal stresses. *Journal of Geophysical Research: Solid Earth*, 128 (3), e2022JB025341, <https://doi.org/10.1029/2022JB025341>
- KLEIN, T.; ZULAUF, G.; EVANS, D.; GERDES, A.; GLODNY, J.; HEIDELBACH, F.; KIRST, F.; LINCKENS, J.; MÜLLER, W.; ÖZCAN, E.; PETSCHICK, R.; XYPOLIAS, P. (2023): Cenozoic evolution of the Tripolitza carbonate platform in the Tethyan realm: New age constraints on deposition, diagenesis, metamorphism and nappe emplacement based on U-Pb and Rb-Sr dating (External Hellenides, Crete). *Geological Magazine* 160 (7), 1282-1300, <https://doi.org/10.1017/S0016756823000377>
- KLEINSCHMIDT, U.; FRENCH, M.; STEINLE-NEUMANN, G.; REDMER, R. (2023): Electrical and thermal conductivity of fcc and hcp iron under conditions of the Earth's core from *ab initio* simulations. *Phys. Rev. B.* 107, 085145, <https://doi.org/10.1103/PhysRevB.107.085145>

- KOEMETS, I.; WANG, B.; KOEMETS, E.; ISHII, T.; LIU, Z.; MCCAMMON, C.; CHANYSHEV, A.; KATSURA, T.; HANFLAND, M.; CHUMAKOV, A.; DUBROVINSKY, L. (2023): Crystal chemistry and compressibility of $\text{Fe}_{0.5}\text{Mg}_{0.5}\text{Al}_{0.5}\text{Si}_{0.5}\text{O}_3$ and $\text{FeMg}_{0.5}\text{Si}_{0.5}\text{O}_3$ silicate perovskites at pressures up to 95 GPa. *Front. Chem.* 11, 1258389, <https://doi.org/10.3389/fchem.2023.1258389>
- LANIEL, D.; TRYBEL, F.; ASLANDUKOV, A.; KHANDARKHAEVA, S.; FEDOTENKO, T.; YIN, Y.; MIYAJIMA, N.; TASNÁDI, F.; PONOMAREVA, A.V.; JENA, N.; AKBAR, F.I.; WINKLER, B.; NÉRI, A.; CHARITON, S.; PRAKAPENKA, V.; MILMAN, V.; SCHNICK, W.; RUDENKO, A.N.; KATSNELSON, M.I.; ABRIKOSOV, I.A.; DUBROVINSKY, L.; DUBROVINSKAIA, N. (2023): Synthesis of ultra-incompressible and recoverable carbon nitrides featuring CN_4 tetrahedra. *Adv. Mater.* 2308030, <https://doi.org/10.1002/adma.202308030>
- LANIEL, D.; TRYBEL, F.; ASLANDUKOV, A.; SPENDER, J.; RANIERI, U.; FEDOTENKO, T.; GLAZYRIN, K.; BRIGHT, E.L.; CHARITON, S.; PRAKAPENKA, V.; ABRIKOSOV, I.A.; DUBROVINSKY, L.; DUBROVINSKAIA, N. (2023): Structure determination of $\zeta\text{-N}_2$ from single-crystal X-ray diffraction and theoretical suggestion for the formation of amorphous nitrogen. *Nat. Comm.* 14 (1), 6207, <https://doi.org/10.1038/s41467-023-41968-2>
- LANIEL, D.; TRYBEL, F.; YIN, Y.; FEDOTENKO, T.; KHANDARKHAEVA, S.; ASLANDUKOV, A.; ABRIKOSOV, A.I.; MASOOD, T.B.; GIACOBBE, C.; BRIGHT, E.L.; GLAZYRIN, K.; HANFLAND, M.; HOTZ, I.; ABRIKOSOV, I.A.; DUBROVINSKY, L.; DUBROVINSKAIA, N. (2023): Aromatic hexazine $[\text{N}_6]^{4-}$ anion revealed in the complex structure of the high-pressure potassium nitride K_9N_{56} . *Nat. Chem.* 15 (5), 641-646, <https://doi.org/10.1038/s41557-023-01148-7>
- LIAO, X.J.; DENK, J.; TRAN, T.; MIYAJIMA, N.; BENKER, L.; ROSENFELDT, S.; SCHAFFÖNER, S.; RETSCH, M.; GREINER, A.; MOTZ, G.; AGARWAL, S. (2023): Extremely low thermal conductivity and high electrical conductivity of sustainable carbon ceramic electrospun nonwoven materials. *Sci. Adv.* 9 (13), <https://doi.org/10.1126/sciadv.ade6066>
- MA, M.; OVERVEST, P.; HIJKEMA, A.; MANGOLD, S.; MCCAMMON, C.; VOEGELIN, A.; BEHRENDTS, T. (2023): Phosphate burial in aquatic sediments: Rates and mechanisms of vivianite formation from mackinawite. *Chem. Eng. J. Adv.* 16, 100565, <https://doi.org/10.1016/j.ceja.2023.100565>
- MELAI, C.; BOFFA BALLARAN, T.; UENVER-THIELE, L.; KURNOSOV, A.; CHUMAKOV, A.I.; BESSAS, D.; FROST, D.J. (2023): Compressibilities along the magnetite-magnesioferrite solid solution. *Phys. Chem. Minerals* 50, 1, <https://doi.org/10.1007/s00269-022-01217-2>
- MIYAJIMA, N.; BUCHEN, J.; KAWAZOE, T. (2023): Twinning in hydrous wadsleyite: symmetry relations, origin, and consequences. *Am. Mineral.*, 108 (11), 2096-2104, <https://doi.org/10.2138/am-2022-8596>
- MOROZOVA, N.V.; USIK, A.Y.; KOROBENNIKOV, I.V.; TITOV, A.N.; OVSYANNIKOV, S.V. (2023): Controlling the semiconductor-metal transition in Cu-intercalated TiSe_2 by applying stress. *J. Mater. Chem. C*, 11, 6071-6081, <https://doi.org/10.1039/D3TC00210A>

- NATHAN, G.; RUBIE, D.C.; JACOBSON, S.A. (2023): Constraining the origin of Mars with simulations of multi-stage core formation. *Icarus* 401, 115596, <https://doi.org/10.1016/j.icarus.2023.115596>
- NESTOLA, F.; REGIER, M.E.; LUTH, R.W.; PEARSON, D.G.; STACHEL, T.; MCCAMMON, C.; WENZ, M.D.; JACOBSEN, S.D.; ANZOLINI, C.; BINDI, L.; HARRIS, J.W. (2023): Extreme redox variations in a superdeep diamond from a subducted slab. *Nature* 613, 85-89, <https://doi.org/10.1038/s41586-022-05392-8>
- NEUMANN, W.; LUTHER, R.; TRIELOFF, M.; REGER, P.; BOUVIER, A. (2023): Fitting thermal evolution models to the chronological record of Erg Chech 002 and modeling the ejection conditions of the meteorite. *Planet. Sci. J.* 4 (10), 196-212, <https://doi.org/10.3847/PSJ/acf465>
- NGUYEN, A.; *et al.* with the Hayabusa2 Initial Analysis Chemistry Team (including BOUVIER, A.) (2023): Preservation of abundant presolar grains and primordial organic matter in asteroid Ryugu. *Sci. Adv.* 9 (28), eadh1003, <https://doi.org/10.1126/sciadv.adh1003>
- OVSYANNIKOV, S.V.; KARKIN, A.E.; KOROBAYNIKOV, I.V.; MOROZOVA, N.V.; BYKOV, M.; BYKOVA, E.; DUBROVINSKY, L. (2023): Electronic properties of single-crystalline Fe₄O₅. *Dalton Trans.* 52, 5563-5574, <https://doi.org/10.1039/D3DT00381G>
- PAQUET, M.; *et al.* with the Hayabusa2 Initial Analysis Chemistry Team (including BOUVIER, A.) (2023): Contribution of Ryugu-like material to Earth's volatile inventory by Cu and Zn isotopic analysis. *Nat. Astron.* 7, 182-189, <https://doi.org/10.1038/s41550-022-01846-1>
- PAUL, J.; CONRAD, C.P.; BECKER, T.W.; GHOSH, A. (2023): Convective self-compression of cratons and the stabilization of old lithosphere. *Geophys. Res. Lett.* 50 (4), e2022GL101842, <https://doi.org/10.1029/2022GL101842>
- PIANI, L.; *et al.* with the Hayabusa2 Initial Analysis Chemistry Team (including BOUVIER, A.) (2023): Hydrogen isotopic composition of water in asteroid Ryugu. *Astrophys. J.* 946, L43, <https://doi.org/10.3847/2041-8213/acc393>
- PUTAK JURICEK, M.; KEPPLER, H. (2023): Amphibole stability, water storage in the mantle, and the nature of the lithosphere-asthenosphere boundary. *Earth Planet. Sci. Lett.* 608, 118082, <https://doi.org/10.1016/j.epsl.2023.118082>
- REGER, P.M.; RÖBBERT, Y.; NEUMANN, W.; GANNOUN, A.; REGELOUS, M.; SCHWARZ, W.H.; LUDWIG, T.; TRIELOFF, M.; WEYER, S.; BOUVIER, A. (2023): Al-Mg and U-Pb chronological records of Erg Chech 002 ungrouped achondrite meteorite. *Geochim. Cosmochim. Acta* 343, 33-48, <https://doi.org/10.1016/j.gca.2022.12.025>
- ROESCHE, C.; BOFFA BALLARAN, T.; MIHAILOVA, B. (2023): Pressure-induced structural transformations in (1-x)Na_{0.5}Bi_{0.5}TiO₃-xBaTiO₃ at the morphotropic phase boundary. *Phys. Rev. B* 108, 094110, <https://doi.org/10.1103/PhysRevB.108.094110>
- ROGOWITZ, A.; THIELMANN, M.; KRAUS, K.; GRASEMANN, B.; RENNER, J. (2023): The effect of the garnet content on deformation mechanisms and weakening of eclogite: Insights from deformation experiments and numerical simulations. *Geochem. Geophys. Geosyst.* 24, e2022GC010743, <https://doi.org/10.1029/2022GC010743>

- SAHA, P.; MURAKAMI, M.; MCCAMMON, C.; LIEBSKE, C.; KRYMARYS, E. (2023): Ultrahigh-pressure sound velocities of aluminous silicate glass up to 155 GPa with implications for the structure and dynamics of the deep terrestrial magma ocean. *Geophys. Res. Lett.* 50 (14), e2023GL103614, <https://doi.org/10.1029/2023GL103614>
- SEMERIKOVA, A.; CHANY SHEV, A.D.; GLAZYRIN, K.; PAKHOMOVA, A.; KURNOSOV, A.; LITASOV, K.; DUBROVINSKY, L.; FEDOTENKO, T.; KOEMETS, E.; RASHCHENKO, S. (2023): Does it "rain" diamonds on Neptune and Uranus? *ACS Earth and Space Chemistry* 7 (3), 582-588, <https://doi.org/10.1021/acsearthspacechem.2c00343>
- SIERSCH, N.C.; CRINITI, G.; KURNOSOV, A.; BOFFA BALLARAN, T.; LIU, Z.; ISHII, T.; FROST, D.J.; YU, T.; WANG, Y. (2023): The influence of Al₂O₃ on the structural properties of MgSiO₃ akimotoite. *Am. Mineral.* 108 (1), 100-109, <https://doi.org/10.2138/am-2022-8257>
- SIERSCH, N.C.; CRINITI, G.; KURNOSOV, A.; GLAZYRIN, K.; ANTONANGELI D. (2023): Thermal equation of state of Fe₃O₄ magnetite up to 16 GPa and 1100 K. *Am. Mineral.* 108 (7), 1322-1329, <https://doi.org/10.2138/am-2022-8571>
- STAGNO, V.; BINDI, L.; BONECHI, B.; GREAU, S.; AULBACH, S.; IRIFUNE, T.; LUPI, S.; MARRAS, G.; MCCAMMON, C.; NAZZARI, M.; PICCIRILLI, F.; POE, B.T.; ROMANO, C.; SCARLATO, P. (2023): Cubic Fe-bearing majorite synthesized at 18-25 GPa and 1000 °C: Implications for element transport, subducted slab rheology and diamond formation. *Sci. Rep.* 13, 15855, <https://doi.org/10.1038/s41598-023-43037-6>
- TANG, H.; CHENG, Y.; YUAN, X.; ZHANG, K.; KURNOSOV, A.; CHEN, Z.; XIAO, W.; JEPPESEN, H.S.; ETTER, M.; LIANG, T.; ZENG, Z.; WANG, F.; FEI, H.; WANG, L.; HAN, S.; WANG, M.-S.; CHEN, G.; SHENG, H.; KATSURA, T. (2023): Toughening oxide glasses through paracrystallization. *Nat. Mater.* 22, 1189-1195, <https://doi.org/10.1038/s41563-023-01625-x>
- TIRABOSCHI, C.; MCCAMMON, C.; ROHRBACH, A.; KLEMME, S.; BERNDT, J.; SANCHEZ-VALLE, C. (2023): Preferential mobilisation of oxidised iron by slab-derived hydrous silicate melts. *Geochem. Persp. Lett.* 24, 43-47, <https://doi.org/10.7185/geochemlet.2304>
- TRAUTNER, V.E.; STACKHOUSE, S.; TURNER, A.R.; KOELEMMEIJER, P.; DAVIES, D.R.; MÉNDEZ, A.S.; SATTA, N.; KURNOSOV, A.; LIERMANN, H.P.; MARQUARDT, H. (2023): Compressibility of ferropicicase at high-temperature: Evidence for the iron spin crossover in seismic tomography. *Earth Planet. Sci. Lett.* 618, 118296, <https://doi.org/10.1016/j.epsl.2023.118296>
- VALDIVIA, P.; ZANDONÀ, A.; KURNOSOV, A.; BOFFA BALLARAN, T.; DEUBENER, J.; DI GENOVA, D. (2023): Are volcanic melts less viscous than we thought? The case of Stromboli basalt. *Contrib. Mineral. Petrol.* 178, 45, <https://doi.org/10.1007/s00410-023-02024-w>
- VLASOV, K.; AUDÉTAT, A.; KEPPLER, H. (2023): H₂-H₂O immiscibility in Earth's upper mantle. *Contrib. Mineral. Petrol.* 178, 36, <https://doi.org/10.1007/s00410-023-02019-7>
- WALTE, N.P.; HOWARD, C.M.; GOLABEK, G.J. (2023): Mantle fragmentation and incomplete core merging of colliding planetesimals as evidenced by pallasites. *Earth Planet. Sci. Lett.* 617, 118247, <https://doi.org/10.1016/j.epsl.2023.118247>

- WANG, B.; BUCHEN, J.; MÉNDEZ, A.S.J.; KURNOSOV, A.; CRINITI, G.; LIERMANN, H.-P.; MARQUARDT, H. (2023): Strong effect of stress on the seismic signature of the post-stishovite phase transition in the Earth's lower mantle. *Geophys. Res. Lett.* 50 (10), e2023GL102740, <https://doi.org/10.1029/2023GL102740>
- WANG, F.; FEI, H.; WANG, L.; MCCAMMON, C.; FROST, D.J.; KATSURA, T. (2023): A decrease in the $\text{Fe}^{3+}/\Sigma\text{Fe}$ ratio of bridgmanite with temperature at the top of the lower mantle. *Earth Planet. Sci. Lett.* 624, 118440, <https://doi.org/10.1016/j.epsl.2023.118440>
- WANG, L.; FEI, Y. (2023): A partially equilibrated initial mantle and core indicated by stress-induced percolative core formation through a bridgmanite matrix. *Sci. Adv.* 9 (7), eade3010, <https://doi.org/10.1126/sciadv.ade3010>
- WANG, L.; LIU, Z.; KOIZUMI, S.; BOFFA BALLARAN, T.; KATSURA, T. (2023): Aluminum components in bridgmanite coexisting with corundum and the CF-Phase with temperature. *J. Geophys. Res. Solid Earth* 128 (1), e2022JB025739, <https://doi.org/10.1029/2022JB025739>
- WOODLAND, A.B.; UENVER-THIELE, L.; BOFFA BALLARAN, T.; MIYAJIMA, N.; ROSBACH, K.; ISHII, T. (2023): Stability of Fe_5O_6 and its relation to other Fe-Mg-oxides at high pressures and temperatures. *Am. Mineral.* 108 (1), 140-149, <https://doi.org/10.2138/am-2022-8370>
- WU, J.; LI, H.; MATHUR, R.; BOUVIER, A.; POWELL, W.; YONEZU, K.; ZHU, D. (2023): Compositional variation and Sn isotope fractionation of cassiterite during magmatic-hydrothermal process. *Earth Planet. Sci. Lett.* 613, 118186, <https://doi.org/10.1016/j.epsl.2023.118186>
- YIN, Y.; ASLANDUKOVA, A.; JENA, N.; TRYBEL, F.; ABRIKOSOV, I.A.; WINKLER, B.; KHANDARKHAEVA, S.; FEDOTENKO, T.; BYKOVA, E.; LANIEL, D.; BYKOV, M.; ASLANDUKOV, A.; AKBAR, F.I.; GLAZYRIN, K.; GARBARINO, G.; GIACOBBE, C.; BRIGHT, E.L.; JIA, Z.; DUBROVINSKY, L.; DUBROVINSKAIA (2023): Unraveling the bonding complexity of polyhalogen anions: High-pressure synthesis of unpredicted sodium chlorides Na_2Cl_3 and Na_4Cl_5 and bromide Na_4Br_5 . *JACS Au*, 3, 1634-1641, <https://doi.org/10.1021/jacsau.3c00090>
- YOKOYAMA, T.; *et al.* with the Hayabusa2 Initial Analysis Chemistry Team (including BOUVIER, A.): Water circulation in Ryugu asteroid affected the distribution of nucleosynthetic isotope anomalies in returned sample. *Sci. Adv.* 9, eadi704, <https://doi.org/10.1126/sciadv.adi7048>
- YUAN, L.; STEINLE-NEUMANN, G. (2023): Hydrogen distribution between the Earth's inner and outer core. *Earth Planet. Sci. Lett.* 609, 118084, <https://doi.org/10.1016/j.epsl.2023.118084>
- ZHANG, B.; LIN, Y.; HAO, J.; SCHRADER, D.L.; WADHWA, M.; KOROTEV, R.L.; HARTMANN, W.K.; BOUVIER, A. (2023): SIMS U-Pb dating of micro-zircons in the lunar meteorites Dhofar 1528 and Dhofar 1627. *Meteorit. Planet. Sci.* 58, 1540-1551, <https://doi.org/10.1111/maps.14078>
- ZHANG, D.; AUDÉTAT, A. (2023): A plea for more skepticism towards fluid inclusions: part (I). Postentrapment changes in fluid density and fluid salinity are very common. *Econ. Geol.* 118 (1), 15-41, <https://doi.org/10.5382/econgeo.4966>

b) Non peer-reviewed publications

KIM, E.J.; ZANDONA, A.; HIRAGA, T.; KOIZUMI, S.; MIYAJIMA, N.; KATSURA, T.; SO, B.D. (2023): The effect of phases of starting materials on the grain size at high pressure: The comparison of grain size in the samples using glass and nano powder as starting materials. *Korean Journal of Mineralogy and Petrology* 36, 213-220, 2023. (in Korean)

4.2 Publications (submitted, in press)

ALÉON, J.; *et al.* with the Hayabusa2 Initial Analysis Chemistry Team (including BOUVIER, A.): Hydrogen in magnetite from asteroid Ryugu. *Meteorit. Planet. Sci.* (submitted)

ASLANDUKOV, A.; ASLANDUKOVA, A.; LANIEL, D.; KHANDARKHAEVA, S.; YIN, Y.; AKBAR, F.I.; CHARITON, S.; PRAKAPENKA, V.; BRIGHT, E.L.; GIACOBBE, C.; WRIGHT, J.; COMBONI, D.; HANFLAND, M.; DUBROVINSKAIA, N.; DUBROVINSKY, L.: Stabilization of N₆ and N₈ anionic units and 2D polynitrogen layers in high-pressure scandium polynitrides. *Nat. Comm.* (submitted)

ASLANDUKOVA, A.; ASLANDUKOV, A.; LANIEL, D.; YIN, Y.; AKBAR, F.I.; BYKOV, M.; FEDOTENKO, T.; GLAZYRIN, K.; PAKHOMOVA, A.; GARBARINO, G.; BRIGHT, E.L.; WRIGHT, J.; HANFLAND, M.; CHARITON, S.; PRAKAPENKA, V.; DUBROVINSKAIA, N.; DUBROVINSKY, L.: Diverse high-pressure chemistry in Y–NH₃BH₃ and Y–paraffin oil systems. *Sci. Adv.* (submitted)

BIZZARRO M.; *et al.* with the Hayabusa2 Initial Analysis Chemistry Team (including BOUVIER, A.): The magnesium isotope composition of samples returned from asteroid Ryugu. *Astrophys. J.* (accepted)

BOUVIER, A.; BERMINGHAM, K.R.; FÜRI, E.: Planetary materials: A record of early solar system events to planetary processes. *Treatise on Geochemistry*, 3rd Edition, Elsevier (submitted)

BYSTRICKY, M.; LAWLIS, J.; MACKWELL, S.; HEIDELBACH, F.: High-temperature deformation of enstatite-olivine aggregates. *J. Geophys. Res. Solid Earth* (in press)

CHANY SHEV, A.; MARTIROSYAN, N.; WANG, L.; CHAKRABORTI, A.; PUREVJAV, N.; WANG, F.; KIM, E.J.; TANG, H.; FEDOTENKO, T.; BHAT, S.; FARLA, R.; KATSURA, T.: Thermal equation of state of cubic silicon carbide at high pressures. *ChemPhysChem* (submitted)

CHENG, K.W.; BALLANTYNE, H.A.; GOLABEK, G.J.; JUTZI, M.; ROZEL, A.B.; TACKLEY, P.J.: Combined impact and interior evolution models in three dimensions indicate a southern impact origin of the Martian Dichotomy. *Icarus* (submitted)

CHENG, K.W.; ROZEL, A.B.; GOLABEK, G.J.; BALLANTYNE, H.A.; JUTZI, M.; TACKLEY, P.J.: Mars's crustal and volcanic structure explained by southern giant impact and resulting mantle depletion. *Geophys. Res. Lett.* (submitted)

CRINITI, G.; BOFFA BALLARAN, T.; KURNOSOV, A.; LIU, Z.; GLAZYRIN, K.; MERLINI, M.; HANFLAND, M.; FROST, D.J. (2023): Thermal equation of state and structural evolution of Al-bearing bridgmanite. *J. Geophys. Res. Solid Earth* (in press), <https://doi.org/10.1029/2023JB026879>

- FEI, H.; WANG, F.; MCCAMMON, C.; KATSURA, T.: The effects of trivalent cations (Al and Fe) on the grain growth rates of bridgmanite. *Earth Planet. Sci. Lett.* (submitted)
- FROSSARD, P.; BONNAND, P.; BOYET, M.; BOUVIER, A.: Role of redox conditions and thermal metamorphism in the preservation of Cr isotopic anomalies in components of non-carbonaceous chondrites. *Geochim. Cosmochim. Acta* (submitted)
- FUKUSHIMA, R.; TSUJIMORI, T.; MIYAJIMA, N.: Simulation of microtextural evolution in omphacite: Ordering transformation kinetics as an archive of convergent margin dynamics. *Phys. Earth Planet. Inter.* (submitted)
- GILLMANN, C.; ARNEY, G.N.; AVICE, G.; DYAR, M.D.; GOLABEK, G.J.; GÜLCHER, A.J.P.; JOHNSON, N.M.; LEFÈVRE, M.; WIDEMANN, T.: Venus. *Treatise on Geochemistry* (submitted)
- GÖTZE, J.; MACRAY, C.; PAN, Y.; WILSON, N.C.; TORPY, A.; AUDÉTAT, A.: The 450 nm (2.8 eV) cathodoluminescence emission in quartz and its relation to structural defects and Ti contents. *Am. Mineral.* (in press), <https://doi.org/10.2138/am-2022-8884>
- HAMANO, K.; GILLMANN, C.; GOLABEK, G.J.; LOURENÇO, D.; WESTALL, F.: The evolutionary divergence of Mars, Venus and Earth. *Treatise on Geochemistry* (submitted)
- HAMMOUDA, T.; FROSSARD, P.; BOYET, M.; BOUVIER, A.; NEWVILLE, M.; LANZIROTTI, A.: Mapping the redox state of the young solar system using ytterbium valence state. *Geochim. Cosmochim. Acta* (submitted)
- HU, X.; LI, H.; ZHU, D.; BOUVIER, A.; WU, J.-H.; MENG, Y.: Differentiating Jurassic Cu-, W-, and Sn (-W)-bearing plutons in the Nanling Range (South China): An integrated apatite study. *Ore Geol. Rev.* (submitted)
- HU, Y. *et al.*; with the Hayabusa2 Initial Analysis Chemistry Team (including BOUVIER, A.): Pervasive aqueous alteration in the early solar system revealed by potassium isotopic variations in Ryugu samples and carbonaceous chondrites. *Icarus* (submitted)
- HUANG, Y.; NAKATANI, T.; SAWA, S.; WU, G.; NAKAMURA, M.; MCCAMMON, C.: Effect of faceting on olivine wetting properties. *Am. Mineral.* (in press), <http://doi.org/10.2138/am-2022-8808>
- ISHII, T.; CRINITI, G.; PUREVJAV, N.; KATSURA, T.; OHTANI, E.: Hydrogen partitioning between stishovite and hydrous phase δ : Implications for water cycle and distribution in the lower mantle. *Prog. Earth Planet. Sci.* (submitted)
- KEPPLER, H.; OHTANI, E.; YANG, X.: The subduction of hydrogen: Deep water cycling, seismicity, and plate tectonics. *Elements* (submitted)
- KITA, N.; *et al.* with the Hayabusa2 Initial Analysis Chemistry Team (including BOUVIER, A.): Disequilibrium oxygen isotope distribution among aqueously altered minerals in Ryugu asteroid returned samples. *Meteorit. Planet. Sci.* (submitted)
- LIBON, L.; SPIEKERMANN, G.; BLANCHARD, I.; KAA, J.M.; DOMINIJANNI, S.; FÖRSTER, M.; SIEBER, M.J.; ALBERS, C.; MORGENROTH, W.; APPEL, K.; MCCAMMON, C.; SCHREIBER, A.; RODDATIS, V.; GLAZYRIN, K.; HUSBAND, R.; HENNET, L.; WILKE, M.: Re-evaluating the fate of subducted magnesite in the Earth's lower mantle. *Phys. Earth Planet. Inter.* (submitted)
- LIU, D.; PUREVJAV, N.; FEI, H.; WITHERS, T.; YE, Y.; KATSURA, T.: Temperature and compositional dependences of H₂O solubility in majorite. *Am. Mineral.* (submitted)

- LIU, S.; KEPPLER, H.: The mobility of Cu, Zn, Mo, and W in subduction zone fluids. *Geochim. Cosmochim. Acta* (submitted)
- MAN, L.; FEI, H.; KIM, E.J.; NERI, A.; XIE, L.; FROST, D.J.: Alumina solubility in periclase determined to lower mantle conditions and implications for ferropericlase inclusions in diamonds. *Geochim. Cosmochim. Acta* (submitted)
- MARRAS, G.; MIKHAILENKO, D.; MCCAMMON, C.A.; AGASHEVA, E.; STAGNO, V.: Ferric iron in eclogitic garnet and clinopyroxene from V. Grib kimberlite pipe: Implications for the redox state of the Arkhangelsk Diamondiferous Province (NW Russia) and evidence for a highly oxidized subducted slab. *J. Petrol.* (submitted)
- MCGREGOR, N.J.; NIMMO, F.; GILLMANN, C.; GOLABEK, G.J.; PLATTNER, A.M.; CONRAD, J.W.: Probing the viscosity of Venus's mantle from dynamic topography at Baltis Vallis. *J. Geophys. Res.* (submitted)
- MORITA, M.; *et al.* with the Hayabusa2 Initial Analysis Chemistry Team (including BOUVIER, A.): Analysis of cation composition in dolomites on the intact particles sampled from asteroid Ryugu, *Anal. Chem.* (submitted)
- MOSENFELDER, J.L.; BUREAU, H.; WITHERS, A.C.: Hydrogen in the deep Earth. *Elements Magazine* (submitted)
- NAKANISHI, N.; *et al.* with the Hayabusa2 Initial Analysis Chemistry Team (including BOUVIER, A.): Nucleosynthetic s-process depletion in Mo from Ryugu samples returned by Hayabusa2. *Geochem. Persp. Lett.* (accepted)
- NEAVE, D.A.; STEWART, A.G.; HARTLEY, M.E.; MCCAMMON, C.: Re-evaluating stoichiometric estimates of iron valence in magmatic clinopyroxene crystals. *Contrib. Mineral. Petrol.* (submitted)
- NÉRI, A.; MAN, L.; CHANTEL, J.; FARLA, R.; BAUER, G.; LINHARDT, S.; BOFFA BALLARAN, T.; FROST, D.J.: The development of internal pressure standards for in-house elastic wave velocity measurements in multianvil presses. *Rev. Sci. Instrum.* (submitted)
- PAUSCH, T.; JOACHIM-MROSKO, B.; LUDWIG, T.; WITHERS A.C.; VAZHAKUTTIYAKAM, J.; KONZETT, J.: The role of Ca-phosphates and silicates in the storage and transport of phosphorus at the upper-to-lower mantle transition: An experimental study to 25 GPa in a model peridotitic bulk composition. *Geochim. Cosmochim. Acta* (submitted)
- PUREVJAV, N.; FEI, H.; ISHII, T.; CRINITI, G.; LIN, Y.; MAO, H.K.; KATSURA, T.: Temperature dependence of H₂O solubility in Al-free stishovite. *Geophys. Res. Lett.* (submitted)
- PUREVJAV, N.; TOMIOKA, N.; YAMASHITA, S.; SHINODA, K.; KOBAYASHI, S.; SHIMIZU, K.; ITO, M.; FU, S.; GU, J.; HOFFMANN, C.; LIN, J.-F.; OKUCHI, T.: Hydrogen incorporation mechanism in aluminous-ferrous bridgmanite. *Am. Mineral.* (in press), <https://doi.org/10.2138/am-2022-8680>
- PUTAK JURICEK, M.; AUDETAT, A.; KEPPLER, H.: Trace element partitioning between saline aqueous fluids and subducted metasediments and the origin of the "sediment fingerprint" in arc magmas. *Geochem. Geophys. Geosyst.* (submitted)

- REGER, P.; SIMON, S.B.; VILLENEUVE, J.; PIRALLA, M.; GIBSON, J.M.; GREENWOOD, R.; QIN, L.; REGELOUS, M.; BOUVIER, A.: *In situ* ^{26}Al - ^{26}Mg isotopic evidence for early chondrule formation. *Geochem. Persp. Lett.* (in revisions)
- RUSTIONI, G.; WIEDENBECK, M.; MIYAJIMA, N.; CHANYCHEV, A.; KEPPLER, H.: Magnesiowüstite as a major nitrogen reservoir in Earth's lowermost Mantle. *Geochem. Persp. Lett.* (submitted)
- TORRANO, Z.; *et al.* with the Hayabusa2 Initial Analysis Chemistry Team (including BOUVIER, A.): The neodymium and samarium isotopic compositions of c-type asteroid (162173) Ryugu. *Meteorit. Planet. Sci.* (submitted)
- UENVER-THIELE, L.; WOODLAND, A.B.; MIYAJIMA, N.; BOFFA BALLARAN, T.; ALIG, E.; FINK, L.: High-*P-T* phase relations of Al-bearing magnetite: Post-spinel phases as indicators for *P-T* conditions of formation of natural samples. *American Mineralogist* (in press), <https://doi.org/10.2138/am-2023-8948>
- WANG, F.; FEI, H.; WANG, L.; MCCAMMON, C.; FROST, D.J.; KATSURA, T.: A decrease in the $\text{Fe}^{3+}/\Sigma\text{Fe}$ ratio of bridgmanite with temperature at the top of the lower mantle. *Earth Planet. Sci. Lett.* (in press), <https://doi.org/10.1016/j.epsl.2023.118440>
- WANG, L.; MIYAJIMA, N.; WANG, F.; KATSURA, T.: Davemaoite exists in the lower mantle. *Nature* (submitted)
- YAO, J.; CIOBANU, C.; COOK, N.J.; EHRIG, K.; DIMA, G.I.; STEINLE-NEUMANN, G.: *Ab initio* calculations and crystal structure simulations for mixed layer compounds from the tetradymite series. *Am. Mineral.* (in press), <https://doi.org/10.2138/am-2023-9018>
- YIN, Y.; ASLANDUKOV, A.; BYKOV, M.; LANIEL, D.; ASLANDUKOVA, A.; PAKHOMOVA, A.; FEDOTENKO, T.; ZHOU, W.; AKBAR, F.I.; HANFLAND, M.; GLAZYRIN, K.; GIACOBBE, C.; BRIGHT, E.L.; GARBARINO, G.; JIA, Z.; DUBROVINSKAIA, N.; DUBROVINSKY, L. (2023): Polytypism of incommensurately modulated structures of crystalline bromine upon molecular dissociation under high pressure. *Phys. Rev. Lett.* (submitted)
- YUI, H.; *et al.* with the Hayabusa2 Initial Analysis Chemistry Team (including BOUVIER, A.): Analysis of cation composition in dolomites on the intact particles sampled from asteroid Ryugu. *Anal. Chem.* (submitted)
- YUI, H.; *et al.* with the Hayabusa2 Initial Analysis Chemistry Team (including BOUVIER, A.): Pyrrhotites in asteroid 162173 Ryugu: The record of anoxic initial changes on their surfaces with aqueous alteration. *Geochim. Cosmochim. Acta* (submitted)
- ZHU, D.-P.; KONG, H.; ALGEO, T.J.; BOUVIER, A.; LIU, B.; WU, J.-H.; HU, X.-J.; WU, Q.-H.: Evolution of skarn to quartz-vein mineralization: Insights from the Tongshanling Cu–Pb–Zn deposit, South China. *Ore Geol. Rev.* (submitted)

4.3 Presentations at scientific institutions and at congresses

- AKBAR, F.I.: 27.-30.03.2023, 31st Annual Meeting of the Crystallographic society (DGK), Frankfurt a. M., Germany: "Novel dysprosium carbides synthesised at high pressures"

- ASLANDUKOV, A.; ASLANDUKOV, M.; DUBROVINSKY, L.; DUBROVINSKAIA, N.: 23.-28.07.2023, The Joint 28th AIRAPT and 60th EHPRG International Conference on High Pressure Science and Technology, Edinburgh, U.K.: "The discovery of novel high-pressure yttrium nitrides in laser-heated diamond anvil cells using the Domain Auto Finder (DAFi) program"
- AUDÉTAT, A.; CHANG, J.: 20.04.2023, Colorado School of Mines, Golden, USA (*invited*): "Magmatic controls on porphyry Cu (Mo, Au) formation"
- BELTRAME, M.; ZIBERNA, L.; MCCAMMON, C.; MASOTTA, M.; VENIER, M.; DE FELICE, A.; MAJGSUREN, Y.; DE MIN, A.: 02.-03.06.2023, DMG Sektionstreffen Geochemie & Petrologie/Petrophysik 2023, Bayreuth, Germany: "The lithospheric mantle beneath central Mongolia: constraints from spinel-bearing peridotite xenoliths and high-pressure experiments"
- BELTRAME, M.; ZIBERNA, L.; MCCAMMON, C.; MASOTTA, M.; VENIER, M.; DE FELICE, A.; MAJGSUREN, Y.; DE MIN, A.: 19.-21.09.2023, SIMP-SGI-SOGEI-AIV Joint Congress 'The Geoscience paradigm: Resources, risks and future perspectives', Potenza, Italy: "The lithospheric mantle beneath central Mongolia: constraints from spinel-bearing peridotite xenoliths and high-pressure experiments"
- BONDAR, D.; WITHERS, A.C.; DI GENOVA, D.; ZANDONÀ, A.; FEI, H.; VALDIVIA, P.; KATSURA, T.: 23.-28.07.2023, The Joint 28th AIRAPT and 60th EHPRG International Conference on High Pressure Science and Technology, Edinburgh, U.K.: "Speciation and effects of water on hydrous peridotitic glasses: insights into the early evolution of rocky planets"
- BONDAR, D.; WITHERS, A.C.; DI GENOVA, D.; KATSURA, T.: 11.-15.12.2023, AGU Fall Meeting 2023, San Francisco, USA & online: "Investigation of hydrous peridotitic glasses: Accomplishments and future prospects"
- BOUVIER, A.; REGER, P.M.; OBENGO, E.; NEUMANN, W.O.; SCHWARZ, W.H.; LUDWIG, T.; TRIELOFF, M.: 09.-14.07.2023, Goldschmidt 2023, Lyon, France (*invited*): "Early planetesimal accretion and magmatic records in achondrite meteorites", Abs. 16195
- BRASSER, R.; WERNER, S.C.; MOJZSIS, S.; BOUVIER, A.; FISCHER-GÖDDE, M.: 09.-14.07.2023, Goldschmidt 2023, Lyon, France: "Timeline and composition of lunar impactors", Abs. 15042
- BUCHEN, J.; WANG, B.; SATTA, N.; TRAUTNER, V.; CRINITI, G.; MENDEZ, A.S.J.; LIERMANN, H.-P.; MARQUARDT, H.: 12.-15.06.2023, EMPG 2023, Milano, Italy: "Partitioning of elastic strain in polycrystalline materials at high pressures and seismic frequencies"
- BUCHEN, J.; WANG, B.; SATTA, N.; TRAUTNER, V.; CRINITI, G.; MÉNDEZ, A.S.J.; LIERMANN, H.-P.; MARQUARDT, H.: 11.-15.12.2023, AGU Fall Meeting 2023, San Francisco, USA & online: "Stress and strain partitioning in polycrystalline materials at high pressures and seismic frequencies"
- BUCHEN, J.; PARDO, O.S.; DOBROSAVLJEVIC, V.V.; STURHAHN, W.; ISHII, T.; CHARITON, S.; GREENBERG, E.; TOELLNER, T.S.; JACKSON, J.M.: 09.-14.07.2023, Goldschmidt 2023, Lyon, France: "Linking water and ferric iron in Earth's lower mantle"

- CALOGERO, M.A.; HETLAND, E.; LANGE, B.: 30.01-03.02.2023, The IAVCEI Scientific Assembly 2023, Rotorua, New Zealand: "High-resolution numerical modelling of rhyolite melt generation and transport induced by basalt emplacement into the crust beneath Long Valley, CA"
- CALOGERO, M.A.; HIN, R.; NIMMO, F.: 13-17.03.2023, 54th Lunar and Planetary Science Conference, The Woodlands, USA: "Potassium isotope anomalies from evaporative mass loss in planetesimals"
- CALOGERO, M.A.; HIN, R.; NIMMO, F.: 11.-16.06.2023, Gordon Research Conference on Origins of Solar Systems, South Hadley, USA: "Potassium isotope anomalies from evaporative mass loss in planetesimals"
- CALOGERO, M.A.; HETLAND, E.; LANGE, B.: 10.-15.09.2023, Xth Hutton Symposium – Granites and Related Rocks, Baveno, Italy: "High-resolution numerical modelling of rhyolite melt generation and transport induced by basalt emplacement into the crust beneath Long Valley, CA"
- CALOGERO, M.A.; HIN, R.; NIMMO, F.: 11.-15.12.2023, AGU Fall Meeting 2023, San Francisco, USA & online: "Potassium isotope anomalies from evaporative mass loss in planetesimals"
- CALVO, L.; LABIDI, J.; KUBIK, E.; SIEBERT, J.: 02.-03.06.2023, DMG Sektionstreffen Geochemie & Petrologie/Petrophysik 2023, Bayreuth, Germany: "Tracing the origin of volatile elements with core formation experiments and sulfur isotopes"
- CALVO, L.; LABIDI, J.; KUBIK, E.; SIEBERT, J.: 09.-14.07.2023, Goldschmidt 2023, Lyon, France: "Tracing the origin of volatile elements with core formation experiments and sulfur isotopes"
- CHAKRABORTI, A.; FEI, H.; NISHIHARA, Y.; THIELMANN, M.; CHANYNSHEV, A.; TSUJINO, N.; HEIDELBACH, F.; KATSURA, T.: 23.-28.07.2023, The Joint 28th AIRAPT and 60th EHPRG International Conference on High Pressure Science and Technology, Edinburgh, U.K.: "How does surface tension affect the rheology of the Earth's lower mantle"
- CHANG, J.; AUDÉTAT, A.: 16.01.2023, FAU Erlangen-Nürnberg, Erlangen, Germany: "Source and evolution of magmas associated with postsubduction porphyry Cu (Mo, Au) deposits"
- CHANG, J.: 02.03.2023, Guangzhou Institute of Geochemistry, Chinese Academy of Sciences, online: "The origin of porphyry Cu-forming magmas in postsubduction settings"
- CRINITI, G.; BOFFA BALLARAN, T.; KURNOSOV, A.; GLAZYRIN, K.; ISHII, T.; FROST, D.J.: 12.-15.06.2023, EMPG 2023, Milano, Italy: "High-pressure and high-temperature equation of state of CaFe₂O₄-type aluminous silicates"
- CRINITI, G.; BOFFA BALLARAN, T.; KURNOSOV, A.; GLAZYRIN, K.; ISHII, T.; FROST, D.J.: 04-05.09.2023, Mineral Physics Research in Progress Meeting 2023, Bristol, U.K.: "Thermal equation of state of CaFe₂O₄-type aluminous silicates and the density of subducted basalt in the lower mantle"
- CZEKAY, L.; MIYAJIMA, N.; FROST: 23.-28.04.2023, EGU General Assembly 2023, Vienna, Austria: "Al, Si diffusion in bridgmanite to estimate the Earth's lower mantle rheology", Abstract EGU23-15214

DOLINSCHI, J.D.; NÉRI, A.; MAN, L.; FARLA, R.; FROST, D.J.: 26.01.2023, DESY User Meeting 2023: Satellite Workshop P61B, Hamburg, Germany: "Development of a method to measure *in situ* stress in large volume press deformation experiments: P61B report"

DOLINSCHI, J.D.; NÉRI, A.; MAN, L.; FROST, D.J.: 02.-03.06.2023, DMG Sektionstreffen Geochemie & Petrologie/Petrophysik 2023, Bayreuth, Germany: "A novel method to measure *in situ* stress of a sample in large volume presses"

DOLINSCHI, J.; NÉRI, A.; MAN, L.; FROST, D.J.: 12.-15.06.2023, EMPG 2023, Milano, Italy: "A novel method to measure *in situ* stress of a sample in large volume presses"

DOLINSCHI, J.D.; MAN, L.; FROST, D.J.: 11.-15.12.2023, AGU Fall Meeting 2023, San Francisco, USA & online: "First direct measurements of *in situ* deformation stress at high pressures utilizing a novel piezoelectric method"

DUBROVINSKY, L.; DUBROVINSKAIA, N.: 27.-30.03.2023, 31st Annual Meeting of the German Crystallography Society (DGK) e.V., Frankfurt a. M., Germany: "High-pressure chemical crystallography: From mineral physics to material sciences"

DUBROVINSKY, L.: 19.-23.06.2023, 23rd Biennial Conference of the APS Topical Group on Shock Compression of Condensed Matter, Chicago, USA: "High-pressure behaviour of Fe-O-C-H system and Earth oxygen cycle"

FACCINCANI, L.; CRINITI, G.; KURNOSOV, A.; BOFFA BALLARAN, T.; WITHERS, A.C.; MAZZUCHELLI, M.; NESTOLA, F.; COLTORTI, M.: 23.-28.04.2023, EGU General Assembly 2023, Vienna, Austria: "Elasticity of hydrous olivine at high pressure and seismic detectability of water in Earth's mantle", Abstract EGU23-14573

FEI, H.; FAUL, U.; BALLMER, M.; WALTE, N.; KATSURA, T.: 23.-28.04.2023, EGU General Assembly 2023, Vienna, Austria: "Grain growth kinetics of bridgmanite under topmost lower-mantle", Abstract EGU23-7732

FROST, D.; PÖPPELBAUM, M.; NERI, A.: 21.-26.05.2023, Japan Geoscience Union Meeting 2023, online: "The passage of water through mantle assemblages under subduction zone conditions"

FROST, D.; PÖPPELBAUM, M.; NERI, A.: 09.-14.07.2023, Goldschmidt 2023, Lyon, France: "Experimental determination of the rate of fluid flow through mantle rocks"

FROST, D.: 30.05.2023, PETRA III Science seminar, DESY, Hamburg, Germany: "The use of high-pressure and -temperature experiments to understand the composition of the Martian core"

FROST, D.: 05.12.2023, Department of Earth Sciences Seminar, ETH Zurich, Switzerland: "High-pressure mineral physics experiments on Mars: Constraining the evolution and composition of the Martian core"

FUKUSHIMA, R.; TSUJIMORI, T.; MIYAJIMA, N.: 18.-22.08.2023, Water-Rock Interaction (WRI-17), Sendai, Japan: "Formation of columnar antiphase domains in omphacite from low-temperature eclogites: A modeling study"

FUKUSHIMA, R.; TSUJIMORI, T.; MIYAJIMA, N.; BOFFA BALLARAN, T.; CRINITI, G.; MCCAMMON, C.: 14.-16.09.2023, 2023 Annual Meeting of Japan Association of Mineralogical Sciences, Osaka, Japan: "Electron diffuse scattering in omphacite from lawsonite eclogite xenolith in Colorado Plateau: A preliminary report"

- GIULIANI, G.; DI FIORE, F.; VALDIVIA, P.; MOLLO, S.; ROMANO, C.; DI GENOVA, D.; VONA, A.: 12.-15.06.2023, EMPG 2023, Milano, Italy: "Experimental determination of the effect of limestone and dolomite assimilation on the viscosity of a phonotephritic melt"
- GOLABEK, G.J.; LICHTENBERG, T.; TACKLEY, P.J.: 27.-30.08.2023, German-Swiss Geodynamics Workshop 2023, Haltern am See, Germany: "Magma oceanography of the dense, ultrashort-period sub-Earth GJ 367b"
- GOLABEK, G.J.; LICHTENBERG, T.; TACKLEY, P.J.: 11.-16.06.2023, Gordon Research Conference on Origins of Solar Systems, South Hadley, USA: "Magma oceanography of the dense, ultrashort-period sub-Earth GJ 367b"
- GOLABEK, G.J.; LICHTENBERG, T.; TACKLEY, P.J.: 23.-28.04.2023, EGU General Assembly 2023, Vienna, Austria: "Magma oceanography of the dense, ultrashort-period sub-Earth GJ 367b", Abstract EGU23-3592
- GOLABEK, G.J.; WALTE, N.P.; SOLFERINO, G.F.D.; NIMMO, F.; SCHMIDT, M.W.: 12.04.2023, ETH Zürich, Switzerland: "Impact origin of pallasite meteorites"
- GOLABEK, G.J.: 28.03.2023, Blaauw Workshop, Groningen, The Netherlands: "Outgassing and atmosphere formation on terrestrial bodies"
- HAMMOUDA, T.; FROSSARD, P.; BOYET, M.; BOUVIER, A.; NEWVILLE, M.; LANZIROTTI, A.: 09.-14.07.2023, Goldschmidt 2023, Lyon, France: "Mapping the redox state of the young solar system using ytterbium valence state", Abs. 16477
- HECKEL, C.; WITHERS, A.C.; WOODLAND, A.B.; GIBSON, S.A.; LUDWIG, T.: 09.-14.07.2023, Goldschmidt 2023, Lyon, France: "Low-T sheared peridotites from the Kaapvaal-craton: Record of hydrous metasomatism during deformation"
- HUANG, D.; MURAKAMI, M.; BRODHOLT, J.; MCCAMMON, C.; PETITGIRARD, S.: 12.-15.06.2023, EMPG 2023, Milano, Italy: "Pressure-induced smooth structural evolution in a terrestrial magma ocean"
- IKEDA, O.; SAKAMAKI, T.; MITSUI, T.; FUJIWARA, K.; MCCAMMON, C.A.; SUZUKI, A.: 23.-28.07.2023, The Joint 28th AIRAPT and 60th EHPRG International Conference on High Pressure Science and Technology, Edinburgh, U.K.: "Pressure-induced magnetic transition of ϵ -FeOOH at 8 GPa"
- ISHII, T.; CRINITI, G.; OHTANI, E.; FEI, H.; PREVJAV, N.; MAO, H.-K.; KATSURA, T.: 11.-15.12.2023, AGU Fall Meeting 2023, San Francisco, USA & online: "Water solubility of aluminous silicas at lower mantle conditions and their implication for water cycle in the deep mantle"
- KATSURA, T.; CHANYSHEV, A.; ISHII, T.; BONDAR, D.; KIM, E.J.; NISHIDA, K.; LIU, Z.; WANG, L.; BHAT, S.; FARLA, R.; HIGO, Y.; TANGE, Y.: 14.03.2023, Graduate University, Chinese Academy of Science, Beijing, P.R. China: "Depressed 660-km discontinuity caused by akimotoite-bridgmanite transition"
- KATSURA, T.; CHANYSHEV, A.; ISHII, T.; BONDAR, D.; KIM, E.J.; NISHIDA, K.; LIU, Z.; WANG, L.; BHAT, S.; FARLA, R.; HIGO, Y.; TANGE, Y.: 15.03.2023, Institute of Geology and Geophysics, Chinese Academy of Science, Beijing, P.R. China: "Depressed 660-km discontinuity caused by akimotoite-bridgmanite transition"

- KATSURA, T.; FEI, H.; DRUZHBIN, D.; KOIZUMI, S.; SAKAMOTO, N.; YURIMOTO, H.: 17.03.2023, Center for High Pressure Science and Technology Advanced Research (HPSTAR), Beijing, P.R. China: "H₂O-enhanced ionic conductivity of olivine: prediction from diffusivity and conductivity measurement"
- KATSURA, T.; FEI, H.; ISHII, T.; LIU, Z.; BONDAR, D.; ZAREI, A.; LI, Y.; WITHERS, A.: 21.03.2023, Guiyang Institute for Geochemistry, Chinese Academy of Science, Guiyang, P.R. China: "Some recent developments of multianvil technology"
- KATSURA, T.; CHANY SHEV, A.; ISHII, T.; BONDAR, D.; KIM, E.J.; NISHIDA, K.; LIU, Z.; WANG, L.; BHAT, S.; FARLA, R.; HIGO, Y.; TANGE, Y.: 21.03.2023, Guiyang Institute for Geochemistry, Chinese Academy of Science, Guiyang, P.R. China: "Depressed 660-km discontinuity caused by akimotoite-bridgmanite transition"
- KATSURA, T.; WANG, L.; CHANY SHEV, A.; BLAHA, S.; MIYAJIMA, N.; KAWAZOE, T.: 27.03.2023, Zhejiang University, Hanzhou, P.R. China: "Determination of the H₂O-content dependence on the dislocation mobility in olivine by means of the dislocation recovery technique"
- KATSURA, T.; ISHII, T.; CRINITI, G.; OHTANI, E.; PUREVJAV, N.; FEI, H.; MAO, H.-K.: 23.-28.04.2023, EGU General Assembly 2023, Vienna, Austria: "Hydrous aluminous silicas as major water hosts in the lower mantle", Abstract EGU23-2770
- KATSURA, T.: 28.-31.05.2023, Earth, Sea and Sky VIII: International Joint Graduate Program Workshop in Earth and Environmental Sciences hosted by the International Joint Graduate Program in Earth and Environmental Sciences (GP-EES), Tohoku University, Sendai, Japan: "A new hypothesis about the structure of the lowermost mantle, its origin, and the hotspot-feeding process"
- KATSURA, T.: 11.-15.12.2023, AGU Fall Meeting 2023, San Francisco, USA & online: "A new hypothesis about the structure and origin of the lowermost mantle and the hotspot-feeding process"
- KATSURA, T.; FEI, H.; BALLMER, M.; FAUL, U.; WALTE, N.; CAO, W.: 11.-15.12.2023, AGU Fall Meeting 2023, San Francisco, USA & online: "Grain growth kinetics of bridgmanite as a function of the fraction of coexisting ferropericlasite: A new interpretation for the mid-mantle viscosity jump"
- KUBIK, E.: 22.03.2023, Université de Lille, Unité Matériaux Et Transformation, Lille, France: "Étude expérimentale des conséquences géochimiques de la formation des noyaux planétaires"
- KUBIK, E.; SOSSI, P.; BOUVIER, A.: 02.-03.06.2023, DMG Sektionstreffen Geochemie & Petrologie/Petrophysik 2023, Bayreuth, Germany: "Iron isotopic fractionation during core formation in large terrestrial planets"
- KUBIK, E.; SOSSI, P.A.; BOUVIER, A.: 12.-15.06.2023, EMPG 2023, Milano, Italy: "Iron isotopic fractionation during core formation in large terrestrial planets"
- KUBIK, E.; SOSSI, P.A.; BOUVIER, A.: 09.-14.07.2023, Goldschmidt 2023, Lyon, France: "Iron isotopic fractionation during core formation in large terrestrial planets", Abs. 17622
- KUBIK, E.; SOSSI, P.A.; CREECH, J.; BLANCHARD, I.; NERI, A.; MAHAN, B.; SIEBERT, J.; MOYNIER, F.: 23.11.2023, Network Meeting of the Alexander von Humboldt-Foundation, Stuttgart, Germany: "The imprint of core formation on planetary isotopic signatures"

KUBIK, E.: 07.12.2023, Laboratoire de Planétologie et Géosciences, Nantes Université, Nantes, France: "The geochemical imprint of core formation: a window into planetary formation"

KURNOSOV, A.; BOFFA BALLARAN, T.; CRINITI, G.; WITHERS, A.C.; FROST, D.J.: 12.-15.06.2023, EMPG 2023, Milano, Italy: "The elastic properties of the Martian mantle"

MAN, L.; NÉRI, A.; CHANTEL, J.; BOFFA BALLARAN, T.; DOLINSCHI, J.; FARLA, R.; GUIGNOT, N.; HENRY, L.; WANG, Y.; FROST, D.J.: 11.-15.12.2023, AGU Fall Meeting 2023, San Francisco, USA & online: "Fe-S-O melting phase relations and elastic properties to the Martian core conditions"

MARRAS, G.; MIKHAILENKO, D.; MCCAMMON, C.; AULBACH, S.; LOGVINOVA, A.; DOMINIJANNI, S.; STAGNO, V.: 09.-14.07.2023, Goldschmidt 2023, Lyon, France: "Redox heterogeneities in the Archean mantle inferred from mineral inclusions in Siberian E-type diamonds: implications for volatile speciation and diamond formation"

MARRAS, G.; MIKHAILENKO, D.; MCCAMMON, C.; AULBACH, S.; LOGVINOVA, A.; DOMINIJANNI, S.; STAGNO, V.: 19.-21.09.2023, SIMP-SGI-SOGEI-AIV Joint Congress 'The Geoscience paradigm: Resources, risks and future perspectives', Potenza, Italy: "Mineral inclusions in eclogitic diamonds from Udachnaya pipe (Siberia) help to track the geochemical and redox evolution of the subducted ancient oceanic crust and the deep volatiles recycle"

MCCAMMON, C.: 23.-28.04.2023, EGU General Assembly 2023, Vienna, Austria: "European Research Council (ERC) Funding Opportunities in Geosciences"

MCCAMMON, C.: 30.05.2023, HPSTAR, Beijing, P.R. China: "Iron matters and how it influenced Earth history"

MCCAMMON, C.: 02.06.2023, HPSTAR, Shanghai, P.R. China: "Probing electronic structure and magnetic properties at high pressure"

MCCAMMON, C.: 05.-09.06.2023, The 6th International Conference on Matter and Radiation at Extremes, Zhuhai, P.R. China: "Pulsed laser heating with time-resolved analysis: A new tool to explore material properties at extreme conditions"

MELAI, C.; BOFFA BALLARAN, T.; FROST, D.J.; MCCAMMON, C.; MIYAJIMA, N.: 12.-15.06.2023, EMPG 2023, Milano, Italy: "Experimental constraints on the conditions of formation of ferropericlasite inclusions in diamonds"

MIYAJIMA, N.; WANG, L.; KATSURA, T.: 12.-15.06.2023, EMPG 2023, Milano, Italy: "The electron diffraction pattern of a quenched davemaoite at ambient conditions. The volume at ambient pressure"

NEAVE, D.A.; STEWART, A.; HARTLEY, M.E.; NAMUR, O.; MCCAMMON, C.: 09.-14.07.2023, Goldschmidt 2023, Lyon, France: "Iron valence systematics in clinopyroxenes from oceanic basalts: re-evaluating stoichiometric estimates of clinopyroxene ferric iron contents"

NÉRI, A.; MAN, L.; CHANTEL, J.; FARLA, R.; BOFFA BALLARAN, T.; FROST, D.J.: 12.-15.06.2023, EMPG 2023, Milano, Italy: "Development of internal pressure standards for in-house elastic wave velocity measurements"

NÉRI, A.; KUBIK, E.; GOLABEK, G.J.; BOUVIER, A.; WALTE, N.P.: 09.-14.07.2023, Goldschmidt 2023, Lyon, France: "Reproducing iron-rich phase textures in primitive achondrites: overcoming surface tension in solids", Abs. 17908

NEUMANN, W.; LUTHER, R.; TRIELOFF, M.; REGER, P.; BOUVIER A.: 01.-06.10.2023: 55th Annual Division for Planetary Sciences (DPS) Meeting joint with the Europlanet Science Congress (EPSC), San Antonio, USA: "Thermal history of the Erg Chech 002 parent body: Early accretion and early differentiation of a small-size planetesimal"

PÖPPELBAUM, M.; NÉRI, A.; FROST, D.J.: 12.-15.06.2023, EMPG 2023, Milano, Italy: "Experimental determination of the rate of fluid flow through mantle rocks"

PAUL, J.; TACKLEY, P.; GOLABEK, G.; ROZEL, A.; KATSURA, T.; FEI, H.: 23.-28.04.2023, EGU General Assembly 2023, Vienna, Austria: "Effect of grain-size evolution on the lower mantle dynamics", Abstract EGU23-9100

PAUL, J.; GHOSH, A.; CONRAD, C.P.; BECKER, T.W.; SPANG, A.; PICCOLO, A.: 27.-30.08.2023, German-Swiss Geodynamics Workshop 2023, Haltern am See, Germany: "Unraveling the stability and longevity of cratons: Traction patterns, weakening processes, and evolutionary dynamics"

PAUL, J.; GOLABEK, G.; ROZEL, A.; TACKLEY, P.; KATSURA, T.; FEI, H.: 27.-30.08.2023, German-Swiss Geodynamics Workshop 2023, Haltern am See, Germany: "Insignificant effect of grain size evolution in the lower mantle dynamics"

PAUL, J.; GOLABEK, G.; ROZEL, A.; TACKLEY, P.; KATSURA, T.; FEI, H.: 11.-15.12.2023, AGU Fall Meeting 2023, San Francisco, USA & online: "Negligible effect of bridgmanite-ferropericlasite grain growth in the lower mantle dynamics"

PAUL, J.; SPANG, A.; PICCOLO, A.; GHOSH, A.: 11.-15.12.2023, AGU Fall Meeting 2023, San Francisco, USA & online: "Craton weakening and destruction: A comparative analysis of North China and Indian Craton"

PAUSCH, T.; VAZHAKUTTIYAKAM, J.; WITHERS, A.C.; LUDWIG, T.; JOACHIMMROSKO, B.; KONZETT, J.: 02.-03.06.2023, DMG Sektionstreffen Geochemie & Petrologie/Petrophysik 2023, Bayreuth, Germany: "Phosphorus in the deep Earth: An experimental investigation of Ca-phosphates at upper- to lower-mantle P-T conditions"

PAUSCH, T.; VAZHAKUTTIYAKAM, J.; WITHERS, A.C.; LUDWIG, T.; JOACHIMMROSKO, B.; KONZETT, J.: 12.-15.06.2023, EMPG 2023, Milano, Italy: "The stability of tuite [γ -Ca₃(PO₄)₂] in a peridotitic bulk composition and its significance for the deep Earth phosphorus cycle"

PAUSCH, T.; VAZHAKUTTIYAKAM, J.; WITHERS, A.C.; LUDWIG, T.; JOACHIMMROSKO, B.; KONZETT, J.: 09.-14.07.2023, Goldschmidt 2023, Lyon, France: "Phosphorus in the deep Earth: An experimental investigation of Ca-phosphates at upper to lower mantle P-T conditions"

PICCOLO, A.; THIELMANN, M.; SPANG, A.: 23.-28.04.2023, EGU General Assembly 2023, Vienna, Austria: "Insights into slab detachment dynamics from 0D to 3D numerical experiments", Abstract EGU23-14144

PICCOLO, A.; THIELMANN, M.; SPANG, A.: 03.-07.09.2023, GeoBerlin 2023, Berlin, Germany: "Effects of upper mantle drag on slab detachment dynamics: insights from 0D and 3D experiments"

PICCOLO, A.; THIELMANN, M.; SPANG, A.: 25.-28.09.2023, Geomod 2023, Sorbonne University, Paris, France: "Slab detachment dynamics: insights from 0D to 3D numerical experiments"

- PICCOLO, A.; THIELMANN, M.; SPANG, A.: 04.-06.10.2023, 7th Annual AlpArray Scientific Meeting, Bad Hofgastein, Austria: "Slab detachment dynamics: Insights from 0D to 3D numerical experiments"
- PÖPPELBAUM, M.; NÉRI, A.; FROST, D.J.: 02.-03.06.2023, DMG Sektionstreffen Geochemie & Petrologie/Petrophysik 2023, Bayreuth, Germany: "The permeability of water in mineral assemblages under subduction zone conditions"
- PÖPPELBAUM, M.; NÉRI, A.; FROST, D.J.: 12.-15.06.2023, EMPG 2023, Milano, Italy: "Experimental determination of the rate of fluid flow through mantle rocks"
- PÖPPELBAUM, M.; FROST, D.J.: 09.-14.07.2023, Goldschmidt 2023, Lyon, France: "The speciation of sulphur released in fluids from sulphide-bearing serpentinite"
- PÖPPELBAUM, M.; NÉRI, A.; FROST, D.J.: 11.-15.12.2023, AGU Fall Meeting 2023, San Francisco, USA & online: "Experimental determination of the rate of fluid flow through mantle rocks at high pressure and temperature"
- PUTAK JURIČEK, M.; KEPPLER, H.: 12.-15.06.2023, EMPG 2023, Milano, Italy: "Amphibole stability, water storage in the mantle, and the nature of the lithosphere-asthenosphere boundary"
- REGER, P.; SIMON, S.; GANNOUN, M.; BOUVIER, A.: 13.-18.08.2023, 85th Meeting of the Meteoritical Society, Los Angeles, USA: "Lead isotope systematics of unequilibrated ordinary chondrite chondrules", Abs. 6278
- ROGMANN, E.-M.; CRINITI, G.; KURNOSOV, A.; WANG, X.; FROST, D.J.; BOFFA BALLARAN, T.: 12.-15.06.2023, EMPG 2023, Milano, Italy: "The variation with pressure of the elastic tensor of $\text{Na}_{0.62}\text{Mg}_{0.19}\text{Fe}^{2+}_{0.174}\text{Al}_{1.20}\text{Si}_{0.70}\text{Fe}^{3+}_{0.08}\text{O}_4$ calcium-ferrite type phase"
- ROSBACH, K.; WOODLAND, A.B.; UENVER-THIELE, L.; MELAI, C.; BOFFA BALLARAN, T.: 12.-15.06.2023, EMPG 2023, Milano, Italy: "Cr incorporation in post-spinel Mg-Fe³⁺ oxides"
- RUSTIONI, G.; WIEDENBECK, M.; CHANY SHEV, A.; KEPPLER, H.: 12.-15.06.2023, EMPG 2023, Milano, Italy: "Nitrogen solubility in bridgmanite"
- SCHUMANN, K.; UENVER-THIELE, L.; WOODLAND, A.; MELAI, C.: 12.-15.06.2023, EMPG 2023, Milano, Italy: "Cr incorporation in post-spinel Fe²⁺-Fe³⁺ oxides"
- SPANG, A.; THIELMANN, M.; KISS, D.: 23.-28.04.2023, EGU General Assembly 2023, Vienna, Austria: "GPU-based numerical models of rapid ductile strain localization due to thermal runaway", Abstract EGU23-11594
- SPANG, A.; THIELMANN, M.; KISS, D.: 27.-30.08.2023, German-Swiss Geodynamics Workshop 2023, Haltern am See, Germany: "1D and 2D numerical models of rapid ductile strain localization due to thermal runaway"
- SPANG, A.; THIELMANN, M.; KISS, D.: 25.-28.09.2023, Geomod 2023, Sorbonne University, Paris, France: "1D and 2D numerical models of rapid ductile strain localization due to thermal runaway"
- STEINLE-NEUMANN, G.; YAO, J.; FROST, D.J.: 06.-08.03.2023, Final meeting of DFG SPP 1833, Köln, Germany: "Lower mantle melting: Experiments and thermodynamic modeling in the systems MgO-SiO₂ and MgO-FeO-SiO₂"

STEINLE-NEUMANN, G.; LANGHAMMER, D.; DI GENOVA, D.: 25.-27.09.2023, 11th Joint Workshop on High Pressure, Planetary and Plasma Physics (HP4), Rostock, Germany: "Viscosity of volcanic melts from artificial neural networks"

STEINLE-NEUMANN, G.; YUAN, L.: 25.-27.09.2023, 11th Joint Workshop on High Pressure, Planetary and Plasma Physics (HP4), Rostock, Germany: "Hydrogen distribution between the Earth's inner and outer core from large-scale molecular dynamics simulations"

STEINLE-NEUMANN, G.; REDMER, R.: 15.-17.11.2023, Kickoff Meeting DFG SPP 2404 Tutzing, Germany: "The role of light elements at the core-mantle boundary – partitioning, demixing, and transport"

THIELMANN, M.; AHARONOV, E.; YAMATO, P.; DURETZ, T.: 23.-28.04.2023, EGU General Assembly 2023, Vienna, Austria: "Phase transition induced stresses and their implications for deep earthquakes", Abstract EGU23-13677

THIELMANN, M.; KAUS, B.J.P.; MEIER, T.: 27.-30.08.2023, German-Swiss Geodynamics Workshop 2023, Haltern am See, Germany: "The Geophysical Model Generator: a tool to unify and interpret geophysical datasets"

THIELMANN, M.; SPANG, A.; DURETZ, T.; YAMATO, P.; KISS, D.: 25.-28.09.2023, Geomod 2023, Sorbonne University, Paris, France (*keynote*): "Advances and challenges in modelling lithospheric strain localization"

THIELMANN, M.: 05.10.2023, 7th Annual AlpArray Scientific Meeting, Bad Hofgastein, Austria (*keynote*): "Processes and repercussions of slab detachment"

THIELMANN, M.: 20.11.2023, Geodynamics Seminar, Universität Halle, Germany: "From micro to macro: The rheological impact of rock heterogeneities on large-scale deformation"

TIRABOSCHI, C.; MCCAMMON, C.; ROHRBACH, A.; KLEMME, S.; BERNDT, J.; SANCHEZ-VALLE, C.: 09.-14.07.2023, Goldschmidt 2023, Lyon, France: "Preferential mobilisation of oxidised iron by slab-derived hydrous silicate melts"

TRYBEL, F.; MEIER, T.; STEINLE-NEUMANN, G.: 25.-27.09.2023, 11th Joint Workshop on High Pressure, Planetary and Plasma Physics (HP4), Rostock, Germany: "The O-H-O hydrogen bond symmetrization at high pressure"

UENVER-THIELE, L.; WOODLAND, A.B.; MIYAJIMA, N.; BOFFA BALLARAN, T.: 12.-15.06.2023, EMPG 2023, Milano, Italy: "High-*P* phase relations of Al-bearing magnetite: Implications for terrestrial and extraterrestrial samples"

VALDIVIA, P.; ZANDONA, A.; BONDAR, D.; KURNOSOV, A.; BOFFA BALLARAN, T.; MIYAJIMA, N.; DEUBENER, J.; DI GENOVA, D.: 12.-15.06.2023, EMPG 2023, Milano, Italy: "The viscosity of volcanic melts: Current knowledge, challenges, and future directions"

VALDIVIA, P.; BOFFA BALLARAN, T.; KURNOSOV, A.; ZANDONA, A.; DEUBENER, J.; DI GENOVA, D.: 23.-28.04.2023, EGU General Assembly 2023, Vienna, Austria: "Are volcanic melts less viscous than we thought? The case of Stromboli", Abstract EGU23-2366

WANG, B.; KULKA, B.; SATTA, N.; KOEMETS, E.; BUCHEN, J.; TRAUTNER, V.; MENDEZ, A.S.J.; CRINITI, G.; GLAZYRIN, K.; LIERMANN, H-P.; MARQUARDT, H.: 12.-15.06.2023, EMPG 2023, Milano, Italy: "Time-resolved X-ray diffraction during continuous compression of MgO using dynamic diamond anvil cells"

- WANG, L.; MIYAJIMA, N.; WANG, F.; KATSURA, T.: 23.-28.04.2023, EGU General Assembly 2023, Vienna, Austria: "Limited intersolubility of Ca and Mg between bridgmanite and CaSiO₃-perovskite in the lower mantle", Abstract EGU23-6782
- WANG, L.; KATSURA, T.; MIYAJIMA, N.; WANG, F.: 11.-15.12.2023, AGU Fall Meeting 2023, San Francisco, USA & online: "Davemaoite does exist in the lower mantle"
- YUAN, H.; MAN, L.: 09.-14.07.2023, Goldschmidt 2023, Lyon, France: " Water-triggered dissociation of iron-rich magnesium silicate in the deep lower mantle: implications for formation of UVLZs near the margins of LLSVPs via slab interaction"
- ZANDONÀ, A.; BONDAR, D.; VALDIVIA, P.; AL-MUKADAM, R.; FEI, H.; WITHERS, A.C.; BOFFA BALLARAN, T.; KURNOSOV, A.; MCCAMMON, C.; DEUBENER, J.; KATSURA, T.; DI GENOVA, D.: 12.-15.06.2023, EMPG 2023, Milano, Italy: "Measuring and parameterizing the room-pressure viscosity of ultramafic melts"
- ZHAO, R.; BOUVIER, A.; TRIELOFF, M.; SCHWARZ, W.; LUDWIG, T.: 02.-03.06.2023, DMG Sektionstreffen Geochemie & Petrologie/Petrophysik 2023, Bayreuth, Germany: "The origin and impact history of ordinary chondrite melt breccia Northwest Africa 12520"
- ZUCCHINI, A.; BOFFA BALLARAN, T.; MASOTTA, M.; FASTELLI, M.; MCCAMMON, C.; FRONDINI, F.; NAZZARI, M.; COMBONI, D.; HANFLAND, M.; COMODI, P.: 12.-15.06.2023, EMPG 2023, Milano, Italy: "Influence of disorder and Fe-content on the properties of ankerite"
- ZUCCHINI, A.; BOFFA BALLARAN, T.; MASOTTA, M.; FASTELLI, M.; MCCAMMON, C.; MICHELE, A.D.; FRONDINI, F.; NAZZARI, M.; COMBONI, D.; HANFLAND, M.; COMODI, P.: 19.-21.09.2023, SIMP-SGI-SOGEI-AIV Joint Congress 'The Geoscience paradigm: Resources, risks and future perspectives', Potenza, Italy: "Disorder and Fe-enrichment in thermally treated ankerite"
- ZUCCHINI, A.; BOFFA BALLARAN, T.; MCCAMMON, C.; FASTELLI, M.; COMBONI, D.; HANFLAND, M.; FRONDINI, F.; COMODI, P.: 13.-17.11.2023, The joint virtual event of the African Light Source AfLS-2023 (6th) and the African Physical Society AfPS2023, online: "The influence of cation disorder on the mineral physics of ankerite: new HP synchrotron X-ray diffraction data"

4.4 Lectures and seminars at Bayerisches Geoinstitut

- BALLMER, Maxim, University College London, Earth Sciences, London, U.K.: "Long-term thermo-chemical evolution of Earth's mantle", 05.06.2023
- BETHKENHAGEN, Mandy, École Polytechnique, Laboratoire pour l'Utilisation des Lasers Intenses (LULI), Palaiseau, France: "Exploring the deep interior of giant planets with atomistic simulations", 30.11.2023
- CHENNAOUI AOUDJEHANE, Hasnaa, Hassan II University of Casablanca, Department of Geology, Casablanca, Morocco: "Meteorites from Morocco, science, geoheritage and outreach", 09.05.2023
- CZEKAY, Laura, Bayerisches Geoinstitut, Bayreuth, Germany: "Al-Si interdiffusion under lower mantle conditions. Analytical TEM study of Al-bearing bridgmanite", 16.02.2023

- DE LIGNY, Dominique, Friedrich-Alexander-Universität, Department of Materials Science and Engineering, Erlangen, Germany: "Reading the temperature and pressure memory of glass", 09.11.2023
- GUIGNOT, Nicolas, Synchrotron SOLEIL, Saint-Aubin, France: "PSICHÉ beamline: innovative tools for high-pressure science", 19.01.2023
- HUANG, Dongyang, ETH Zurich, Institute of Geochemistry and Petrology, Zurich, Switzerland: "An anomalous layer atop Mars' core: insights from thermoelastic properties of liquid Fe-rich alloys", 06.07.2023
- HUNT, Alison, ETH Zurich, Institute of Geochemistry and Petrology, Zurich, Switzerland: "The IAB iron parent body: A unique insight into parent body evolution and solar system processes", 12.01.2023
- INCEL, Sarah, Imperial College London, Centre for Advanced Structural Ceramics, London, U.K.: "Deformation and reaction of crustal rocks under high-pressure, high-temperature conditions", 16.11.2023
- JOHN, Timm, Freie Universität Berlin, Arbeitsbereich Mineralogie-Petrologie, Berlin, Germany: "New insights on slab mantle dehydration", 26.01.2023
- KLAHR, Hubert, Max-Planck-Institut für Astronomie, Heidelberg, Germany: "Turbulence, pebbles and planetesimals: The origin of minor bodies in the solar system", 07.12.2023
- KUBIK, E.: Bayerisches Geoinstitut, Bayreuth, Germany: "Experimental isotopic fractionation during core formation on large terrestrial planets", *Academy Commission Business Meeting*, 11.05.2023
- LENHART, Eric, University of Western Ontario, Department of Earth Sciences, London, Canada: "Electrical resistivity of liquid Fe-S-Si alloys at high pressures with implications for heat flux through the cores of Vesta, Io and sub-Earth exoplanets", 22.05.2023
- LI, Yuan, Guangzhou Institute of Geochemistry, Chinese Academy of Sciences, Guangzhou, P.R. China: "Experimental constraints on the origin of Earth's volatiles", 22.08.2023
- LIANG, Chuntao, Chengdu University of Technology, Chengdu, P.R. China: "The growth mechanism of the Eastern Tibetan plateau revealed by the high resolution 3D seismic velocity and anisotropy", 02.05.2023
- LOBANOV, Sergey, Helmholtz-Zentrum Potsdam, Deutsches GeoForschungsZentrum, Potsdam, Germany: "What color is the mantle? Spectroscopy meets geodynamics", 25.05.2023
- LOURO LOURENÇO, Diogo, ETH Zurich, Institute of Geophysics, Zurich, Switzerland: "Influence of possible bulk compositions and tectonic regimes on the long-term evolution of Venus", 02.11.2023
- MOJZSIS, Stephen, Research Centre for Astronomy and Earth Sciences, Origins Research Institute (ORI), Budapest, Hungary: "Galactic evolution of planet-forming nuclides expressed in terrestrial exoplanet geodynamics", 20.04.2023
- MORARD, Guillaume, Université Grenoble Alpes, Institut des Sciences de la Terre (ISTerre), Gières, France: "Planetary differentiation studied by *in situ* time-resolved X-ray diagnostics", 22.06.2023

- MÜNKER, Carsten, Universität zu Köln, Institut für Geologie und Mineralogie, Köln, Germany: "The early geodynamic evolution of the Earth: new clues from novel isotope systems", 01.06.2023
- PETITGIRARD, Sylvain, ETH Zurich, Institute of Geochemistry and Petrology, Zurich, Switzerland: "Structure-density relationships in high-pressure glasses", 30.08.2023
- PIERRU, Rémy, Sorbonne Université, Institut de minéralogie, de physique des matériaux et de cosmochimie, Paris, France: "Mantle melting of Earth and Mars at high pressure and high temperature: From magma ocean crystallization to the formation of large igneous provinces", 05.05.2023
- POZZI, Giacomo, Istituto Nazionale di Geofisica e Vulcanologia, Roma, Italy: "Brittle rock fabrics and their control on fault slip behaviour", 23.11.2023
- SCHULZE, Maximilian, Universität zu Köln, Institut für Geologie und Mineralogie, Köln, Germany: "Carbonate and silicate melts in the Earth's mantle: Structure and transport properties studied by ab initio molecular dynamics simulations", 20.11.2023
- TRYBEL, Florian, Linköping University, Department of Physics, Chemistry and Biology (IFM), Linköping, Sweden: "High-pressure hydrides and nitrides: true technological opportunity or pure scientific challenge?", 02.02.2023
- VAN DER MAREL, Nienke, Universiteit Leiden, Leiden Observatory, The Netherlands: "The observational revolution of planet forming disks", 26.10.2023
- WANG, Chao, Institut de Physique du Globe de Paris, France: "The origin of abiotic organic compounds in the deep Earth: Constraints from petrological observations and high-pressure experimental simulations", 04.05.2023
- YAXLEY, Gregory, Australian National University, Research School of Earth Sciences, Canberra, Australia: "Petrogenesis of carbonates and their role in mantle metasomatism", 05.07.2023
- ZANDONA, Alessio, National Research Council of Italy, Institute of Environmental Geology and Geoengineering, Roma, Italy: "At the limits of glass formation: Exotic magmas and novel glass-ceramics", 29.06.2023
- ZHANG, Bidong, University of California, Earth, Planetary & Space Sciences, Los Angeles, USA: "Compositions of asteroidal cores across the early solar system", 14.12.2023

4.5 Conference organization

- 23.-28.04.2023, European Geosciences Union General Assembly 2023, Vienna, Austria: "Solving geoscience problems using mineralogy" (J. INGRIN, C. MCCAMMON, J. REYNES, M. SIEBER, J. MAJZLAN)
- 23.-28.04.2023, European Geosciences Union General Assembly 2023, Vienna, Austria: "Venus: Models, observations, exoplanet analogue" (G. GOLABEK)
- 23.-28.04.2023, European Geosciences Union General Assembly 2023, Vienna, Austria: "Dynamics, structure and evolution of Earth and rocky planets from formation to the present day" (G. GOLABEK)

- 02.-03.06.2023, Deutsche Mineralogische Gesellschaft, Section Meeting Petrology/
Petrophysics & Geochemistry, Bayreuth, Germany (A. BOUVIER, Organizer)
- 09.-14.07.2023, Goldschmidt 2023, Lyon, France: Session 1e, "Extraterrestrial and related
experimental samples: a window into the origin and evolution of the Solar System" (A.
BOUVIER, Co-Chair)
- 02.-03.09.2023 Short Course SC9 related to SGA 2023 Meeting in Zürich, Switzerland:
"Variations and processes in the epithermal environment: relations and transition to
intrusions" (A. AUDÉTAT, J. HEDENQUIST)
- 17.09.-21.09.23, MinWien23, Joint Mineralogical Meeting DMG-ÖMG-SMS, Vienna,
Austria: Chair of the 'Young Scientists' session (R. VOLKMANN, L. CZEKAY)

5. Visiting Scientists

5.1 Visiting scientists funded by the Bayerisches Geoinstitut

ARIF, Soukaina, Hassan II University of Casablanca, Department of Geology, Casablanca, Morocco: 08.05.-04.06.2023

BALLMER, Maxim, University College London, Earth Sciences, London, U.K.: 04.-07.06.2023

BELTRAME, Marco, Università degli Studi di Trieste, Department of Mathematics and Geosciences, Trieste, Italy: 15.02.-31.08.2023

BETHKENHAGEN, Mandy, École Polytechnique, Laboratoire pour l'Utilisation des Lasers Intenses (LULI), Palaiseau, France: 29.11.-01.12.2023

BOLFAN-CASANOVA, Nathalie, Université Clermont Auvergne, Laboratoire Magmas et Volcans, Aubière, France: 09.-13.10.2023

CHENNAOUI AOUDJEHANE, Hasnaa, Hassan II University of Casablanca, Department of Geology, Casablanca, Morocco: 08.05.-14.05.2023

CHRAPPAN SOLDAVINI, Benedetta, Università degli Studi di Milano, Dipartimento di Scienze della Terra, Milano, Italy: 17.04.-09.06.2023

DE LIGNY, Dominique, Friedrich-Alexander-Universität, Department of Materials Science and Engineering, Erlangen, Germany: 09.11.2023

DOLEJŠ, David, Universität Freiberg, Institut für Geo- und Umweltwissenschaften, Freiberg, Germany: 19.-23.02.2023

FANESI, Emanuele, Università di Camerino, Scuola di Studi Superiori "Carlo Urbani", Camerino, Italy: 20.11.-31.12.2023

GUIGNOT, Nicolas, Synchrotron SOLEIL, Saint-Aubin, France: 18.-20.01.2023

HUANG, Dongyang, ETH Zurich, Institute of Geochemistry and Petrology, Zurich, Switzerland: 04.-07.07.2023

HUNT, Alison, ETH Zurich, Institute of Geochemistry and Petrology, Zurich, Switzerland: 11.-13.01.2023

INCEL, Sahar, Imperial College London, Centre for Advanced Structural Ceramics, London, U.K.: 15.-17.11.2023

JOHN, Timm, Freie Universität Berlin, Arbeitsbereich Mineralogie-Petrologie, Berlin, Germany: 26.-27.01.2023

KLAHR, Hubert, Max-Planck-Institut für Astronomie, Heidelberg, Germany: 07.12.2023

LI, Yaozhu, University of Western Ontario, Department of Earth Sciences, London, Canada: 20.02.-23.04.2023

LI, Yuan, Guangzhou Institute of Geochemistry, Chinese Academy of Sciences, Goangzhou, P.R. China: 19.-28.08.2023

LOBANOV, Sergey, Helmholtz-Zentrum Potsdam, Deutsches GeoForschungsZentrum, Potsdam, Germany: 25.-26.05.2023

LOURO LOURENÇO, Diogo, ETH Zurich, Institute of Geophysics, Zurich, Switzerland: 31.10.-03.11.2023

MASOTTA, Matteo, Università di Pisa, Dipartimento di Scienze della Terra, Pisa, Italy: 19.-23.02.2023

MOJZSIS, Stephen, Research Centre for Astronomy and Earth Sciences, Origins Research Institute (ORI), Budapest, Hungary: 19.-22.04.2023

MORARD, Guillaume, Université Grenoble Alpes, Institut des Sciences de la Terre (ISTerre), Gières, France: 21.-24.06.2023

MÜNKER, Carsten, Universität zu Köln, Institut für Geologie und Mineralogie, Köln, Germany: 01.-03.06.2023

PETITGIRARD, Sylvain, ETH Zurich, Institute of Geochemistry and Petrology, Zurich, Switzerland: 28.-31.08.2023

PIERRU, Rémy, Sorbonne Université, Institut de minéralogie, de physique des matériaux et de cosmochimie, Paris, France: 04.-06.05.2023

POZZI, Giacomo, Istituto Nazionale di Geofisica e Vulcanologia, Roma, Italy: 22.-24.11.2023

PRANGER, Casper, Ludwig-Maximilians-Universität, Department of Earth and Environmental Sciences, Geophysics, München, Germany: 10.-14.07.2023

PUTAK JURICEK, Marija, Georg-August-Universität Göttingen, Department of Mineralogy, Göttingen, Germany: 29.05.-04.06.2023

SCHMITT-KOPPLIN, Philippe, Helmholtz Zentrum München, Analytical Biogeochemistry, München, Germany: 09.-10.05.2023

SCHNEIDER, Evelyn, Gymnasium Hilpoltstein, Germany: 31.07.-03.08.2023

SCHULZE, Maximilian, Universität zu Köln, Institut für Geologie und Mineralogie, Köln, Germany: 19.-21.11.2023

SHAW, Cliff, University of New Brunswick, Earth Sciences, Fredericton, Canada: 01.03.-30.04.2023

TRYBEL, Florian, Linköping University, Department of Physics, Chemistry and Biology (IFM), Linköping, Sweden: 02.-03.02.2023

UENVER-THIELE, Laura, Johann Wolfgang Goethe-Universität, Institut für Geowissenschaften, Frankfurt/M., Germany: 24.-28.04.2023

VAN DER MAREL, Nienke, Universiteit Leiden, Leiden Observatory, The Netherlands: 26.-27.10.2023

WALTE, Nico, TU München, Forschungs-Neutronenquelle Heinz Maier-Leibnitz (FRM II), Garching, Germany: 20.-23.02.2023, 11.-12.05.2023

WANG, Chao, Institut de Physique du Globe de Paris, France: 03.-06.05.2023

WEN, Shijie, University of Oxford, U.K.: 24.06.-26.07.2023

YAXLEY, Gregory, Australian National University, Research School of Earth Sciences, Canberra, Australia: 04.-06.07.2023

ZANDONA, Alessio, National Research Council of Italy, Institute of Environmental Geology and Geoengineering, Roma, Italy: 28.-30.06.2023

ZHANG, Bidong, University of California, Earth, Planetary & Space Sciences, Los Angeles, USA: 26.11.-22.12.2023

5.2 Visiting scientists supported by other externally funded BGI projects

WOODLAND, Alan, Johann Wolfgang Goethe-Universität, Institut für Geowissenschaften, Frankfurt/M., Germany: 29.03.2023 (DFG*)

* DFG: Deutsche Forschungsgemeinschaft

5.3 Visitors (externally funded)

ABEYKOON, Sumith, Université de Lorraine, Centre de Recherches Pétrographiques et Géochimiques, Vandœuvre les Nancy, France: 17.-21.07.2023

BRASSER, Ramon, Konkoly Observatory, Research Centre for Astronomy and Earth Sciences, Budapest, Hungary: 09.-14.10.2023

BRUGMAN, Kara, Arizona State University, Eyring Materials Center, Tempe, USA: 07.06.2023

BYKOV, Maxim, Universität Köln, Institut für Anorganische Chemie, Köln, Germany: 10.-13.02.2023, 14.-17.04.2023, 09.-12.06.2023, 23.06.2023, 26.-27.09.2023, 27.-30.10.2023

BYKOVA, Elena, Goethe Universität Frankfurt a. M., Mineralogie, Frankfurt a. M., Germany: 10.-13.02.2023, 05.-08.05.2023, 16.08.2023, 27.-30.10.2023

CALVO, Lucas, Institut de Physique du Globe de Paris, France: 24.05.-02.06.2023

FEDOTENKO, Timofey, DESY Hamburg, Germany: 09.-11.10.2023

FUKUSHIMA, Ryo, Tohoku University, Center for Northeast Asian Studies, Sendai, Japan: 16.01.-18.02.2023, 08.05.-10.06.2023

FURLONG, Eimear, Trinity College, Dublin, Ireland: 12.-14.09.2023

GIRANI, Alice, ETH Zurich, Institute of Geochemistry and Petrology, Zurich, Switzerland: 21.-28.08.2023

HIN, Remco, Università degli Studi di Milano, Dipartimento di Scienze della Terra 'Ardito Desio', Milano, Italy: 26.-30.06.2023, 18.-22.09.2023

HUPPERTZ, Hubert, Universität Innsbruck, Institut für Allgemeine, Anorganische und Theoretische Chemie, Innsbruck, Austria: 24.-25.04.2023

KULKA, Britany, University of Oxford, Department of Earth Sciences, Oxford, U.K.: 13.-24.03.2023, 20.06.-23.08.2023

LENHART, Eric, University of Western Ontario, Department of Earth Sciences, London, Canada: 22.-23.05.2023

LI, Xiang, Universität Münster, Institut für Mineralogie, Münster, Germany: 08.-11.02.2023, 10.-14.04.2023

LIANG, Chuntao, Chengdu University of Technology, Chengdu, P.R. China: 28.04.-05.05.2023

LIU, Zhiqiang, Chengdu University of Technology, Chengdu, P.R. China: 28.04.-05.05.2023

MEIER, Thomas, Center for High Pressure Science & Technology Advanced Research (HPSTAR), Beijing, P.R. China: 31.07.2023

MELAI, Caterina, Trinity College, Dublin, Ireland: 03.-22.09.2023, 05.-14.10.2023
NISHIYAMA, Norimasa, Sumitomo Electric Industries, Ltd., Advanced Materials Laboratory, Itami, Japan: 03.02.2023
NIU, Guoliang, Center for High Pressure Science & Technology Advanced Research (HPSTAR), Beijing, P.R. China: 15.05.-07.08.2023
RADOVSKAIA, Viktoriia, Radboud-Universität Nijmegen, The Netherlands: 04.-08.09.2023
RIDOLFI, Filippo, Leibniz Universität Hannover, Institut für Mineralogie, Hannover, Germany: 12.-26.03.2023
RÖSCHE, Costanze, Universität Hamburg, Mineralogisch-Petrographisches Institut, Hamburg, Germany: 22.-26.05.2023
ROGMANN, Elena-Marie, University of Bristol, School of Earth Sciences, Bristol, U.K.: 19.-22.09.2023
SAHA, Pinku, ETH Zurich, Institute of Geochemistry and Petrology, Zurich, Switzerland: 26.02.-04.03.2023
SCHUMANN, Katrin, Johann Wolfgang Goethe-Universität, Institut für Geowissenschaften, Frankfurt/M., Germany: 24.-28.04.2023
UENVER-THIELE, Laura, Johann Wolfgang Goethe-Universität, Institut für Geowissenschaften, Frankfurt/M., Germany: 16.08.2023
WANG, Biao, University of Oxford, Department of Earth Sciences, Oxford, U.K.: 11.-28.07.2023
WALTE, Nico, TU München, Forschungs-Neutronenquelle Heinz Maier-Leibnitz (FRM II), Garching, Germany: 11.-12.01.2023
WIDMANN, Ingo, Universität Innsbruck, Institut für Allgemeine, Anorganische und Theoretische Chemie, Innsbruck, Austria: 24.-25.04.2023
ZIPPOLI, Matteo, Università degli Studi di Milano-Bicocca, Italy: 25.05.2023

6. Additional scientific activities

6.1 Theses

Ph.D. theses

CRINITI, Giacomo: "Constraining the chemical and mineralogical composition of Earth's lower mantle through high-pressure crystallography and mineral elasticity"

CZEKAY, Laura: "Al-Si interdiffusion under lower mantle conditions. Analytical TEM study of Al-bearing bridgmanite"

MELAI, Caterina: "The stability field of ferropericlase with respect to oxygen fugacity in the Earth's mantle and the origin of superdeep diamonds"

6.2 Honours and awards

CRINITI, Giacomo Best Poster Award, 18th International Symposium on Experimental Mineralogy, Petrology and Geochemistry (EMPG-XVIII)

MCCAMMON, Catherine Harry H. Hess Medal of the American Geophysical Union

WITHERS, Anthony Fellow of the Mineralogical Society of America

ZHAO, Ran Best Poster Award, DMG Sektionstreffen Geochemie & Petrologie/Petrophysik 2023, Bayreuth, Germany

6.3 Editorship of scientific journals

AUDÉTAT, Andreas Associate Editor "Journal of Petrology"
Associate Editor "Economic Geology"

BOFFA BALLARAN, Associate Editor "European Journal of Mineralogy"
Tiziana

BOUVIER, Audrey Associate Editor "Geochimica et Cosmochimica Acta"

DUBROVINSKY, Leonid Member, Editorial Board "High Pressure Research"
Member, Advisory Board "Minerals"
Editor-in-Chief, "Minerals"

KEPPLER, Hans Editorial Board "Contributions to Mineralogy and Petrology"
Editorial Board "ACS Earth and Space Chemistry"

MCCAMMON, Catherine Editor in Chief "Physics and Chemistry of Minerals"

MIYAJIMA, Nobuyoshi Associate Editor "European Journal of Mineralogy"

6.4 Membership of scientific advisory bodies

BOUVIER, Audrey Chair, Section Geochemistry, Deutsche Mineralogische
Gesellschaft (DMG)
Member, Leonard medal, Nier prize and Fellows committee,
Meteoritical Society
Member, Science Working Team for Early Solar System
Evolution, Martian Moons eXploration (MMX) mission,
Japanese Aerospace Exploration Agency
Member, Mars Sample Return (MSR) Campaign Science Group,
European Space Agency

DUBROVINSKY, Leonid Member, Review Panel of Canadian Light Source Chair
Member, Subcommittee on Spectroscopy, Diffraction, and new
Instrumentations in Mineral Physics of the International
Mineralogical Association
Member, Review Panel of PETRA III
Lithuanian Research Council, Head of Evaluation Committee in
Civil Engineering

FROST, Dan Member, Royal Society
Member, Bavarian Academy of Sciences
Member, German National Academy of Sciences (Leopoldina)
Scientific Advisory Committee of the GeoForschungsZentrum
Potsdam
Member, Royal Society Fellows Sectional Committee SC5
Vice President of the European Association of Geochemistry

KATSURA, Tomoo Japan Association of Mineralogical Sciences Award Committee
Chair

KEPPLER, Hans Member, German National Academy of Sciences (Leopoldina)
Member, Bavarian Academy of Sciences

MCCAMMON, Catherine Member, Implementation Task Force, American Geophysical Union
Member, Project Review Panel P01, PETRA III
Member, Council, International Mineralogical Association
Member, Fellows Committee, VGP section, American Geophysical Union
Member, Award Committee of the International Board on the Applications of Mössbauer Spectroscopy

WITHERS, Anthony Member, Project Review Panel P02.2 and P61.B, PETRA III

7. Scientific and Technical Personnel

Name		Position	Duration in 2023	Funding source
AKBAR, Fariia Iasmin	M.Sc.	Wiss. Mitarbeiterin		DFG
ANDREIEVA, Daria	B.Sc.	Student. Hilfskraft		DFG
ANTUNES, Anaelle	B.Sc.	Student. Hilfskraft	from 01.10.	UBT
ASLANDUKOV, Andrii	M.Sc.	Wiss. Mitarbeiter	to 30.06.	DFG
ASLANDUKOVA, Alena	M.Sc.	Wiss. Mitarbeiterin		DFG
AUDÉTAT, Andreas	Dr.	Akad. Oberrat		BGI
BAUER, Gerald	Dipl.-Ing. (FH)	Techn. Angestellter		BGI
BOFFA BALLARAN, Tiziana	Dr.	Akad. Oberrätin		BGI
BONDAR, Dmitry	Dr.	Wiss. Mitarbeiter		EU
BOUVIER, Audrey	Prof. Dr.	Professorin		BGI
BUBMANN, Daniela		Techn. Angestellte		BGI
BUCHEN, Johannes	Dr.	Juniorprofessor	from 20.05.	BGI
BUCHERT, Petra		Fremdsprachen- Sekretärin		BGI
CALOGERO, Meredith	Dr.	Wiss. Mitarbeiterin		EU
CHAKRABORTI, Amrita	Dr.	Wiss. Mitarbeiterin	to 31.08.	DFG
			from 01.09.	EU
CHANG, Jia	Dr.	Wiss. Mitarbeiter	to 14.01.	DFG
			from 15.01.	BGI/VP
CHANYSHEV, Artem	Dr.	Wiss. Mitarbeiter	to 30.09.	EU
			from 01.10.	DFG
CRINITI, Giacomo	M.Sc.	Wiss. Mitarbeiter	to 14.10.	Leibniz
CZEKAY, Laura	M.Sc.	Wiss. Mitarbeiterin	to 28.02.	DFG
			01.03.-31.05.	BGI/VP
	Dr.	Wiss. Mitarbeiterin	from 01.06.	DFG
DELL, Serghius		Elektrotechniker		BGI
DINIUS, Anna		Verwaltungsangestellte	to 18.08.	BGI
DOLINSCHI, Jonathan	M.Sc.	Wiss. Mitarbeiter		Leibniz
DUBROVINSKY, Leonid	Apl. Prof. Dr.	Akad. Direktor		BGI
FEI, Hongzhan	Dr.	Wiss. Mitarbeiter	to 31.01.	BGI
FISCHER, Heinz		Mechaniker		BGI
FROST, Daniel	Prof. Dr.	Stellvertr. Leiter		BGI
GASPERT, Olga		Verwaltungsangestellte	from 18.09.	BGI
GOLABEK, Gregor	Prof. Dr.	Professor		BGI
HAMADI, Muhammad	M.Sc.	Student. Hilfskraft	to 30.09.	EU
		Wiss. Mitarbeiter	from 01.12.	Leibniz

HAN, Kui	Dr.	Stipendiat	from 15.02.	CSC
HEIDELBACH, Florian	Dr.	Wiss. Mitarbeiter		BGI
HIN, Remco	Dr.	Akad. Rat (auf Zeit)	to 01.05.	BGI
HIRSCHMANN, Marc	Prof. Dr.	Forschungspreisträger	to 31.05.	AvH
HLEDE, Matej	B.Sc.	Student. Hilfskraft		DFG
JEMAL, Ibrahim Jibril	B.Sc.	Student. Hilfskraft	from 01.10.	DFG
KATSURA, Tomoo	Prof. Dr.	Professor		BGI
KEPPLER, Hans	Prof. Dr.	Leiter		BGI
KIM, Eun Jeong	Dr.	Stipendiatin	to 28.02.	AvH
KRAUßE, Detlef	Dipl.-Inform. (FH)	Techn. Angestellter		BGI
KRIEGL, Holger		Haustechniker		BGI
KUBIK, Edith	Dr.	Wiss. Mitarbeiterin	to 28.02. from 01.03.	BGI/VP AvH
KURNOSOV, Alexander	Dr.	Wiss. Mitarbeiter		DFG
LANGHAMMER, Dominic	M.Sc.	Wiss. Mitarbeiter	to 30.06.	DFG
LINHARDT, Sven		Elektrotechniker		BGI
MAN, Lianjie	M.Sc.	Wiss. Mitarbeiter		Leibniz
MARTIROSYAN, Naira	Dr.	Wiss. Mitarbeiterin		DFG
MATTHÄUS, Rebecka		Chem.-Techn. Assistentin		BGI
MCCAMMON, Catherine	PD Dr.	Akad. Direktorin	to 31.07.	BGI
		Wiss. Mitarbeiterin	from 01.08.	DFG
MIYAJIMA, Nobuyoshi	Dr.	Akad. Oberrat		BGI
MINCHENKOVA, Anastasiia	B.Sc.	Student. Hilfskraft	from 15.04.	DFG
NÉRI, Adrien	Dr.	Wiss. Mitarbeiter	to 30.04. 01.05.-31.08.	Leibniz BGI
NJUL, Raphael		Präparator		BGI
OVSYANNIKOV, Sergey	Dr.	Wiss. Mitarbeiter	from 01.11	DFG
PAUL, Jyotirmoy	Dr.	Wiss. Mitarbeiter	to 30.09. from 01.10.	EU BGI/VP
PICCOLO, Andrea	Dr.	Wiss. Mitarbeiter		DFG
PÖPPELBAUM, Melanie	M.Sc.	Wiss. Mitarbeiterin	to 14.05. from 15.05.	DFG Leibniz
POSNER, Esther	Dr.	Wiss. Mitarbeiterin	to 07.01.	DFG
POTZEL, Anke		Chem.-Techn. Assistentin		BGI
PUREVJAV, Narangoo	Dr.	Wiss. Mitarbeiterin	to 12.01.	BGI/VP
RAUSCH, Oliver		Mechaniker		BGI
ROTHER, David Alexander		Präparator	to 31.10.	BGI
RUSTIONI, Greta	Dr.	Wiss. Mitarbeiterin		DFG

SCHARNAGEL, Janina		Sekretärin		BGI
SIKDAR, Jinia	Dr.	Wiss. Mitarbeiterin		EU
SILVA SOUZA, Danielle	M.Sc.	Wiss. Mitarbeiterin	from 01.12.	DFG
SONG, Yunke	M.Sc.	Stipendiat	from 15.11.	CSC
SPANG, Arne	Dr.	Wiss. Mitarbeiter		DFG
STEINLE-NEUMANN, Gerd	PD Dr.	Akad. Oberrat		BGI
THIELMANN, Marcel	Dr.	Wiss. Mitarbeiter		DFG
TIMONER BOSCH, Cristian	B.Sc.	Student. Hilfskraft		DFG
TRENZ, Ulrike		Biol.-Techn. Assistentin		BGI
ÜBELHACK, Stefan		Mechaniker		BGI
VALDIVIA MUNOZ, Pedro Antonio	M.Sc.	Wiss. Mitarbeiter		DFG
WANG, Fei	Dr.	Wiss. Mitarbeiter		EU
WANG, Lin	Dr.	Wiss. Mitarbeiter	to 01.08. from 02.08.	EU BGI
WEILER, Tatjana	M.Sc.	Wiss. Mitarbeiterin	from 01.12.	DFG
WIESNER, Dorothea		Techn. Assistentin		BGI
WITHERS, Antony	Dr.	Wiss. Mitarbeiter		BGI
YUAN, Liang	Dr.	Wiss. Mitarbeiter	to 31.10.	DFG
ZHAO, Ran	M.Sc.	Stipendiat		CSC
ZHU, Da-Peng	M.Sc.	Stipendiat	from 01.03.	CSC
ZIPPOLI, Matteo	B.Sc.	Student. Hilfskraft	from 01.10.	DFG

Abbreviations/explanations:

AvH	Alexander von Humboldt Foundation
BGI	Staff Position of Bayerisches Geoinstitut
BGI/VP	Visiting Scientists' Program of Bayerisches Geoinstitut
CSC	China Scholarship Council
DFG	German Science Foundation
EU	European Union
Leibniz	Leibniz-Preis der Deutschen Forschungsgemeinschaft Prof. Frost
UBT	Universität Bayreuth

Index

Abeykoon, S.	51
Akbar, F.I.	133, 134, 135
Andrić-Tomašević, N.	30
Arif, S.	39
Aslandukov, A.	77, 133, 134, 135
Aslandukova, A.	77, 133, 134, 135
Audétat, A.	53, 54, 56, 59
Beltrame, M.	66
Boffa Ballaran, T.	70, 72, 73, 81, 88, 90, 91, 93, 94, 113, 137, 142
Bondar, D.	148
Bouvier, A.	23, 25, 27, 39, 43, 62, 96
Buchen, J.	141
Bureau, H.	148
Bykov, M.	134, 135
Bykova, E.	134
Calvo, L.M.	46
Chakraborti, A.	125, 154
Chang, J.	54, 56
Chanyshv, A.	75, 100, 112, 125, 135
Chariton, S.	133, 135
Chennaoui Aoudjehane, H.	39
Chrappan, B.	90
Claussmann, B.	30
Comboni, D.	135
Couffignal, F.	126, 148
Criniti, G.	81, 88, 90, 91, 93, 94, 106, 141, 142
Czekay, L.	76
De Min, A.	66
Deubener, J.	113
Di Fiore, D.	113
Di Genova, D.	113, 115, 148
Dohmen, R.	126
Dolinschi, J.D.	154
Dubrovinskaia, N.A.	77, 133, 134, 135, 136
Dubrovinsky, L.S.	77, 133, 134, 135, 136
Ehlers, T.A.	30
Eskens, L.H.J.	30
Farla, R.	75, 154
Fedotenko, T.	77, 91, 135
Fei, H.	68, 80, 106, 112, 122, 125, 126, 148

French, M.	32
Frost, D.J.	51, 80, 88, 91, 93, 94, 107, 111, 154
Fukushima, R.	81
Gannoun, A.	37
Glazyrin, K.	77, 91, 93, 135
Golabek, G.J.	22, 96, 122
Greer, J.	25
Hamadi, M.I.	51, 121
Han, K.	75, 152
Hanfland, M.	88, 133, 135, 136
Heck, P.R.	25
Heidelbach, F.	125, 142, 146
Hin, R.	153
Hirschmann, M.M.	47, 144
Hlede, M.	58
Howard, A.	157
Huang, Y.	86
Isheim, D.	25
Ishii, T.	91, 93, 106
Jurzick, P.L.	135
Katsura, T.	75, 80, 81, 106, 112, 122, 125, 126, 148, 152
Keppler, H.	53, 58, 76, 100, 157
Khandarkhaeva, S.	77, 135
Khodja, H.	148
Kim, E.J.	68
Kiss, D.	119
Kleinschmidt, U.	32
Kubik, E.	41, 43, 44, 46, 96, 153
Kurnosov, A.	88, 90, 91, 93, 94, 113, 142
Labidi, J.	46
Lejri, M.	30
Langhammer, D.	115
Laniel, D.	77, 134, 135
Li, H.	62
Lichtenberg, T.	22
Liermann, H.-P.	141
Lin, Y.	106
Löschmann, J.	113
Ludwig, T.	23, 37
Man, L.	68, 154
Mao, H.K.	106
Marquardt, H.	141
Marras, G.	79

Martirosyan, N.	75, 112
Masotta, M.	66
Mathur, R.	62
McCammon, C.A.	66, 79, 80, 81, 86, 113
Melai, C.	70, 72, 88
Méndez, A.S.J.	141
Merlini, M.	90
Mihailova, B.	137
Mikhailenko, D.	79
Minchenkova, A.	88
Miyajima, N.	73, 80, 81, 82, 100, 128, 150
Nakamura, M.	86
Nakatani, T.	86
Néri, A.	51, 68, 96, 107, 153
Neumann, W.	37
Nishihara, Y.	125
Ovsyannikov, S.V.	131
Pakhomova, A.	133
Paul, J.	27, 122
Pettke, T.	54
Piccolo, A.	27, 29, 30
Pöppelbaum, M.	107, 111
Powell, W.	62
Prakapenka, V.	133, 135
Purevjav, N.	106
Rabin, S.	41
Redmer, R.	32
Regelous, M.	37
Reger, P.M.	37
Roebbert, Y.	37
Rösche, C.	137
Rogalev, A.	131, 135
Romano, C.	113
Rosbach, K.	72
Rozel, A.	122
Rustioni, G.	53, 100
Satta, N.	141
Sawa, S.	86
Schumann, K.	70
Schwarz, W.H.	23, 37
Seidman, D.N.	25
Shaw, C.	52
Siebert, J.	46

Sikdar, J.	44
Sossi, P.A.	43
Spang, A.	27, 29, 119, 120, 121
Stagno, V.	79
Steinle-Neumann, G.	32, 102, 115
Tackley, P.J.	22, 122
Thielmann, M.	29, 30, 119, 120, 121, 125
Timoner, C.	59, 150
Trautner, V.	141
Trieloff, M.	23, 37
Tsujimori, T.	81
Tsujino, N.	125
Uenver-Thiele, L.	70, 72, 73
Valdivia Munoz, P.	113
Walte, N.P.	96, 157
Wang, B.	141
Wang, F.	75, 80
Wang, J.	126
Wang, L.	80, 81, 126, 154
Wen, S.	128
Weyer, S.	37
Whitney, D.L.	146
Wiedenbeck, M.	100, 126, 148
Wilhelm, F.	131, 135
Wilke, M.	146
Withers, A.C.	104, 148
Woodland, A.B.	70, 72, 73
Wu, G.	86
Wu, J.	62
Wu, W.	125
Yin, Y.	77, 134, 135
Yonezu, K.	62
Yuan, L.	102
Zandonà, A.	113
Zeitlhack, K.	157
Zhang, B.	25
Zhang, H.L.	144
Zhao, R.	23
Zhou, W.	88, 136
Zhu, D.	62
Ziberna, L.	66